

**Development of novel liquid and gel polymer
electrolytes for room temperature sodium-sulfur
batteries**

Von der Fakultät Chemie der Universität Stuttgart

zur Erlangung der Würde eines

Doktors der Naturwissenschaften (Dr. rer. nat.)

genehmigte Abhandlung

Vorgelegt von

Saravanakumar Murugan

Aus Indien

Hauptberichter: Prof. Dr. Michael R. Buchmeiser

Mitberichter: Prof. Dr. Oliver Clemens

Prüfungsvorsitzender: Prof. Dr. Johannes Kästner

Tag der mündlichen Prüfung: 25.10.2022

Institut für Polymerchemie der Universität Stuttgart

2022

To my family,
with love and gratitude

“No research without action, no action without research.”

- Kurt Lewin

Erklärung über die Eigenständigkeit der Dissertation

Hiermit versichere ich, dass die Arbeit mit dem Titel

“Development of novel liquid and gel polymer electrolytes for room temperature sodium-sulfur batteries”

eigenständig verfasst wurde und keine anderen als die gekennzeichneten Quellen und Hilfsmittel benutzt wurden; die digitale Version stimmt mit den anderen Exemplaren überein.

Declaration of Authorship

Hereby, I certify that the dissertation entitled

“Development of novel liquid and gel polymer electrolytes for room temperature sodium-sulfur batteries”

has been written independently except stated otherwise. Ideas and passages from other sources have been indicated. The digital version is identical to all hard copies.

Name/Name: Saravanakumar Murugan

Unterschrift/Signed: _____

Datum/Date: _____

Danksagung

An erster Stelle möchte ich meinem Doktorvater Herrn Prof. Dr. Buchmeiser für die Doktorandenstelle in seiner Forschungsgruppe, die Betreuung, die Forschungsunterstützung und das Korrekturlesen der Manuskripte danken. Ich bin dankbar für die ausgezeichneten Laborbedingungen und den günstigen elektrochemischen Versuchsaufbau, die zu einer schnellen Analyse und damit zu besseren Ergebnissen führten. Ich möchte Professor Clemens für seine Rolle als Zweitgutachter und Professor Kästner für seine Rolle als Drittgutachter danken.

Ich möchte Dr. Dongren Wang für seine Hilfe bei der Bestellung von Chemikalien und der Klärung von Zweifeln in allen fachlichen Fragen danken. Ich möchte Herrn Juilan Kappler für eine großartige Unterstützung während meiner ersten Monate danken, für die geduldige Beantwortung all meiner Fragen und für eine nette, professionelle und freundliche Begleitung. Ich möchte mich bei Dr. Hagen Altman, Dr. Mathis Benedikter, Dr. Felix Ziegler, Dr. Mohasin Momin und Dr. Pradeed Panyam, Dr. Abdul Wasif für ihre Diskussionen und Unterstützung bei der Salzsynthese bedanken. Ich danke Herrn Dr. Janis Musso, Herrn Stefan Niesen und Herrn Julian Kappler für den freundlichen Umgang miteinander, kurze Reisen, viele Abendessen und erfolgreiche Diskussionsrunden. Herrn Noah Keim danke ich für seinen Beitrag während seiner Masterarbeit. Ein besonderer Dank geht an meine Familie für ihre unermüdliche Unterstützung während meiner Forschungszeit.

Table of Contents

Erklärung über die Eigenständigkeit der Dissertation	V
Danksagung	VII
Table of Contents	IX
List of Abbreviations	XI
Zusammenfassung	XV
Abstract.....	XIX
1 Introduction.....	1
1.1 Motivation	1
1.2 State-of-the-art technology.....	3
1.3 Metal-ion batteries (MIB)	8
1.3.1 Working mechanism	10
1.3.2 Cathodes, anodes, and electrolytes	11
1.3.3 Limitations of MIBs.....	13
1.4 Alternate cathode materials for high-energy batteries	14
1.5 High-temperature sodium-sulfur batteries	17
1.5.1 Working principle	19
1.5.2 Challenges of high-temperature sodium-sulfur batteries.....	20
1.6 Room temperature sodium-sulfur battery	21
1.6.1 Mechanism.....	22
1.6.2 Technical difficulties inhibiting the development of room temperature sodium-sulfur batteries	24
1.6.3 Cathode, anode, and separator modifications	26
1.6.4 Organic liquid electrolytes for RT SSB	31
1.6.5 Polymer-based electrolytes	39
1.6.6 Solid electrolyte interface on sodium metal anodes	43
2 Background on the electrochemical terms used in this study.....	47

Table of Contents

2.1	Charging and discharging	47
2.2	Overpotential	47
2.3	Voltammetric techniques	47
2.4	Ionic conductivity and transference number	49
2.5	Electrochemical impedance spectroscopy	51
2.6	Galvanostatic intermittent titration technique	55
3	Electrolytes based on sodium salt of weakly coordinating anion.....	57
3.1	Introduction	57
3.2	Publication “Ultra-Stable Cycling of High Capacity Room Temperature Sodium-Sulfur Batteries Based on Sulfurated Poly(acrylonitrile)”	63
3.3	Publication “A sodium bis(perfluoropinacol) borate-based electrolyte for stable, high-performance room temperature sodium-sulfur batteries based on sulfurized poly(acrylonitrile)”	88
4	Gel polymer electrolyte for sodium sulfur batteries	103
4.1	Introduction	103
4.2	Publication “Stable Cycling of Room-Temperature Sodium-Sulfur Batteries Based on an In Situ Crosslinked Gel Polymer Electrolyte”	111
5	References	153
6	Curriculum Vitae	165

List of Abbreviations

AC	Alternating current
ALD	Atomic layer deposition
BETA	Bis(pentafluoroethanesulfonyl)amide
BMS	Battery management system
CE	Coulombic efficiency
CPE	Constant phase element
CSPE	Composite solid polymer electrolytes
CV	Cyclic voltammetry
DCP	Discharge cut-off potential
DEC	Diethyl carbonate
DFT	Density functional theory
DMC	Dimethyl carbonate
DME	1,2-Dimethoxyethane
DMT	<i>N, N</i> -Dimethyl triflimide
DOL	1,3-Dioxolane
DPT	<i>N, N</i> -dipropyl triflimide
EC	Ethylene carbonate
EIS	Electrochemical impedance spectroscopy
ES	Ethylene sulfide
EV	Electric vehicle
FEC	Fluoroethylene carbonate
FIA	Fluoride ion affinity
GITT	Galvanostatic intermittent titration technique
GPE	Gel polymer electrolyte
HC	Hollow carbon
HF	Hydrogen fluoride
HOMO	Highest occupied molecular orbital
HT-SSB	High-temperature sodium-sulfur battery
IL	Ionic liquid
KOH	Potassium hydroxide
LCO	Lithium cobalt oxide

List of Abbreviations

LE	Liquid electrolyte
LED	Light-emitting diode
LFP	Lithium iron phosphate
LIB	Lithium-ion battery
LiFSI	Lithium bis(fluorosulfonyl)imide
LiOTf	Lithium triflate
LiTFSI	Lithium bis(trifluoromethanesulfonyl)imide
LMO	Lithium manganese oxide
LSB	Lithium-sulfur battery
LSV	Linear sweep voltammetry
LTO	Lithium-titanium-oxide
LUMO	Lowest occupied molecular orbital
MCP	Microporous carbon
MH	Metal hydride
MIB	Metal-ion battery
MLD	Molecular layer deposition
MSB	Metal sulfur battery
Na-Bhfip	Sodium tetrakis(hexafluoroisopropoxy)borate
NaOH	Sodium hydroxide
Na-PPB	Sodium bis(perfluoropinacol) borate
NASICON	Sodium super ion conductor
NCO	Sodium cobalt oxide
NMC	Nickel manganese oxide
OCV	Open-circuit voltage
OCV	Open-circuit voltage
PAA	Poly(acrylic acid)
PC	Propylene carbonate
PED	Portable electronic devices
PEGDE	Poly(ethylene glycol) diglycidyl ether
PEO	Poly(ethylene oxide)
PETA	Pentaerythritol triacrylate
PMMA	Poly(methyl methacrylate)

PPE	Plasticized polymer electrolytes
PS	Polysulfide
PVA	Poly(vinyl alcohol)
PVDF	Poly(vinylidene fluoride)
PVDF-HFP	Poly(vinylidene fluoride-co-hexafluoropropylene)
RT-SSB	Room-temperature sodium-sulfur battery
SEI	Solid electrolyte interface
SEM	Scanning electron microscope
SHE	Standard hydrogen electrode
SIB	Sodium-ion battery
SIC	Single ion conducting
SPAN	Sulfurized poly(acrylonitrile)
SPE	Solid polymer electrolytes
SSB	Solid state battery
SSB	Sodium sulfur battery
TEGDME	Tetra(ethylene glycol) dimethyl ether
TFMA	Trifluoroethyl methacrylate
VC	Vinylene carbonate
VFT	Vogel-Tammann-Fulcher
WCA	Weakly coordinating anion
WCS	Weakly coordinating solvents
XPS	X-ray photoelectron spectroscopy

Zusammenfassung

Der ständig wachsende Energiebedarf erfordert die Untersuchung einer nächsten Generation von vielversprechenden Energiespeichersystemen. Sekundärbatterien sind ein unverzichtbarer Bestandteil des Energiespeichersmarktes, wobei Lithium-Ionen-Batterien (LIB) mehr als 85 % des Marktanteils ausmachen. Der wachsende Markt für Elektrofahrzeuge (BEV) erfordert kostengünstige Batterien mit hoher Reichweite. Die unsicheren Preise für Lithium-Rohstoffe, die Kapitalkosten für Energiespeichersysteme im Netz, der schnelle Materialabbau und Umweltbedenken führen zu einem zunehmenden Interesse an nicht-lithiumbasierten Batterien. Batterien auf Natriumbasis gelten aufgrund ihres stabilen und günstigen Preises und des hohen Anteils von Natrium in der Erdkruste (Li-20 mg kg^{-1} ; $\text{Na-28400 mg kg}^{-1}$) als mögliche Alternative für LIBs. Die für Lithiumbatterien weit verbreitete Interkalationschemie auf Basis geschichteter Metalloxidverbindungen zeigt für Natriumbatterien allerdings eine geringe Speicherkapazität und Energiedichte. Daher wurde kostengünstiger und leicht verfügbarer Schwefel mit einer theoretischen Kapazität von 1675 mAh g^{-1} als Kathodenmaterial für Natriumbatterien untersucht, um eine gesteigerte Energiedichte zu erreichen.

Hochtemperatur-Natrium-Schwefel-Batterien (HT-SSB) werden bei $300\text{-}350 \text{ }^\circ\text{C}$ betrieben, wobei sowohl Natrium als auch Schwefel in geschmolzenem Zustand vorliegen, was zu großen Sicherheitsproblemen, einschließlich Explosionen, führen kann. Es wurden mehrere Versuche unternommen, die Betriebstemperatur der Batterie zu senken und Natrium-Schwefel-Batterien, die bei Raumtemperatur (RT-SSB) betrieben werden können, zu entwickeln. Die Wahl des richtigen Elektrolyten spielt dabei eine entscheidende Rolle für eine hohe Kapazität, hohe Zyklenstabilität und die Sicherheit der Batterie. Die wichtigsten Kriterien für einen idealen Elektrolyten sind eine hohe Dissoziation des Salzes, hohe Ionenleitfähigkeit, niedrige Aktivierungsenergie und chemische Stabilität gegenüber den Elektroden. Die Wahl eines Elektrolytsalzes für RT-SSBs erfolgt analog zu den Salzen, die in LIBs verwendet werden. Diese Salze haben jedoch mehrere Nachteile, wie z.B. Feuchtigkeitsempfindlichkeit, eingeschränktes elektrochemisches Fenster, geringe Oxidationsbeständigkeit, Korrosivität für den Stromabnehmer, Explosivität und Toxizität. Um eine hohe Kapazität und stabile Zyklen zu erreichen, wurden in dieser Arbeit drei Arten von Elektrolyten synthetisiert und sowohl chemisch als auch elektrochemisch charakterisiert. Im ersten Teil dieser Arbeit

wurden zwei verschiedene schwach koordinierende Anionen (WCA) auf der Basis von Natriumtetrakis(hexafluorisopropoxy)borat ($\text{Na}[\text{B}(\text{hfip})_4]$; hfip = Hexafluorisopropoxid, Na-Bhfip) und Natriumbis(perfluoropinacol)borat (Na-PPB); $\text{NaB}[\text{O}_2\text{C}_2(\text{CF}_3)_4]_2$ in einfachen einstufigen Reaktionen synthetisiert. Beide Salze weisen ein hohes Oxidationspotenzial gegen verschiedene Stromsammler in einem Elektrolyten auf Carbonatbasis auf. Die hohe Ionenleitfähigkeit des Na-Bhfip-Elektrolyten zeigte eine ausgezeichnete Ratenfähigkeit und ermöglichte stabile Zyklen bis zu 1000 Zyklen bei einer hohen C-Rate von 3 C. Das Entladungs-Cut-off-Potenzial (DCP) begrenzt die Natriumsulfidbildung während der Reduktion, die sich direkt auf die Entladekapazität auswirkt. Verschiedene elektrochemische Techniken wie die galvanostatische intermittierende Titrationstechnik (GITT) und die Röntgenphotoelektronenspektroskopie (XPS) wurden angewandt, um die Auswirkungen des DCP auf die Reaktionskinetik zu analysieren. Bei niedrigem DCP wies die Zelle eine langsame Reaktionskinetik (zyklische Voltammetrie, CV), einen niedrigen Diffusionskoeffizienten (GITT) und eine hohe Umwandlung in endgültige Sulfide (XPS) auf. Der Na-PPB-Elektrolyt hingegen wies eine niedrige Barriere für die Neuorientierung des Na^+ -Ions um das Anion herum auf, was zu einer höheren Ionenleitfähigkeit und einer besseren elektrochemischen Leistung als Na-Bhfip führte. Darüber hinaus zeigte Na-PPB, auch nach einer 2-tägigen Exposition zu Raumluft eine hohe elektrochemische Rate. Diese Ergebnisse deuten darauf hin, dass zweizählige anionische Liganden chemisch stabiler sind als Leitsalze mit einzähligen Anionen.

Indem der flüssige Elektrolyt in einer Polymermatrix eingeschlossen wird, weisen Gelpolymerelektrolyte (GPE) Elektrolyteigenschaften von Festkörper, wie auch flüssigen Elektrolytssystemen auf. Im zweiten Teil dieser Arbeit wurde ein GPE auf Basis von Pentaerythritoltriacyrlat (PETA) synthetisiert und charakterisiert, um eine sichere und hocheffiziente SSB zu demonstrieren. Das GPE zeigte eine ausgezeichnete Oxidationsstabilität (>6 V) gegenüber dem Aluminium-Stromabnehmer, was der höchste bisher berichtete Wert ist. Berechnungen des molekularen elektrostatischen Potenzials ergaben, dass das Na^+ -Ion mit dem Poly-PETA über mehrere schwache Koordinationen interagiert und eine niedrige Aktivierungsenergie aufweist, wodurch die Ionenleitfähigkeit des Elektrolyten verbessert wird. Das Polymernetzwerk schränkt die Bewegung des sterisch anspruchsvollen Anions ein, indem es mit seinen delokalisierten Ladungen interagiert, was zu einer hohen Na^+ -Ionen-Übertragungszahl und einer geringeren Zellpolarisation führt. DFT-Berechnungen zeigten, dass die starke

Bindungsenergie zwischen PETA und Polysulfiden die Polysulfidauflösung hemmt und dadurch das Selbstentladungsverhalten verringert. Der synthetisierte GPE zeigte eine verbesserte Reaktionskinetik, indem er die Produkte des Entladungsprozesses effektiv lokal einschränkt. GPE ermöglichte Niedrigtemperatur-Zyklen der Zelle bei 0 °C, während das GPE bei Raumtemperatur eine hervorragende Zyklenstabilität von bis zu 2500 Zyklen bei 2 C aufwies. Die Einschließungseigenschaft von GPE wurde weiter analysiert, indem der Bindemittelgehalt in der Kathode reduziert wurde. Die GITT-Analyse ergab, dass die Zelle bei einem sehr geringen Binderanteil von 2 Gew.-% eine schnellere Na⁺-Ionendiffusion aufweist. Aufgrund des sehr guten Grenzflächenkontakts waren die GPE-haltigen Pouch-Zellen in der Lage selbst unter mechanischer Deformation stabile Zyklen bei 1 C zu liefern. Außerdem konnte die Pouch-Zelle eine Leuchtdiode (LED) betreiben, wenn sie mechanisch verformt oder geschnitten wurde.

Abstract

The ever-growing energy consumption requires promising next-generation advanced energy storage systems. Secondary batteries are an indispensable part of the energy storage market, with lithium-ion batteries (LIB) holding more than 85% of the market share. The booming electric vehicle (EV) market demands low-cost and long-range batteries. Uncertainty in the price of lithium raw materials, capital costs in grid energy storage systems, rapid material degradation, and environmental concerns are driving the increasing interest in non-lithium-based batteries. Sodium-based batteries are considered to be an alternative for LIBs due to their stable, low price, and high natural abundance of Na in the Earth's crust (Li - 20 mg kg⁻¹; Na - 28400 mg kg⁻¹). However, intercalation chemistry limits the storage capacity and energy density of Na batteries. Therefore, low-cost, and highly abundant sulfur with a theoretical capacity of 1675 mAh g⁻¹ has been studied as a conversion type cathode material to enhance the energy density of the battery.

High-temperature sodium-sulfur batteries (HT-SSB) operate at 300-350 °C, where both sodium and sulfur exist in a molten state, which leads to serious safety issues, including explosions. Multiple attempts have been made to reduce the operating temperature of the battery and develop room-temperature sodium-sulfur batteries (RT-SSB). The right choice of electrolyte plays a vital role in achieving high capacity, stable cycling, and safety of the battery. The most important criteria for an ideal electrolyte are high dissociation of the salt, high ionic conductivity, low activation energy, and chemical stability against all electrodes. The choice of an electrolyte salt for RT-SSBs is analogous to the salts used in LIBs. However, these salts have several disadvantages, such as moisture sensitivity, reduced electrochemical window, poor resistance against oxidation, corrosiveness to the current collector, explosiveness, and toxicity. Therefore, in this work, to achieve high capacity and stable cycling, three types of electrolytes were synthesized and characterized both chemically and electrochemically. In the first section of this thesis, two distinct weakly coordinating anion (WCA) based salts of sodium tetrakis(hexafluoroisopropoxy)borate (Na[B(hfip)₄]; hfip = hexafluoroisopropoxide, Na-Bhfip) and sodium bis(perfluoropinacol)borate, (Na-PPB); NaB[O₂C₂(CF₃)₄]₂ were synthesized in facile one-step reactions. Both salts exhibit a high oxidation potential against various current collectors in a carbonate-based electrolyte. The high ionic conductivity of the Na-Bhfip electrolyte displayed excellent rate capability and maintained stable cycling up to 1000 cycles at a high C-rate of 3 C. The discharge cut-off

potential (DCP) limits sodium sulfide formation during reduction, which directly affects the discharge capacity. Various electrochemical techniques, such as the galvanostatic intermittent titration technique (GITT), and X-ray photoelectron spectroscopy (XPS), were applied to analyze the impact of DCP on the reaction kinetics. At low DCP, the cell exhibited slow reaction kinetics (cyclic voltammetry, CV), low diffusion coefficient (GITT), and high conversion to final sulfides (XPS). A Na-PPB electrolyte, on the other hand, exhibited a low barrier for re-orientation of Na⁺ ions around the anion, resulting in higher ionic conductivity and better electrochemical performance than Na-Bhfip. Moreover, Na-PPB was able to maintain high-rate capability even after exposing it to atmospheric conditions for 2 days. These results suggest that the bidentate ligand containing anion salts is chemically more stable than their monodentate anion counterparts.

By trapping the liquid electrolyte in a polymer matrix, gel polymer electrolytes (GPE) exhibit both solid and liquid electrolyte properties. In the second part of this thesis, a GPE based on pentaerythritol triacrylate (PETA) was synthesized and characterized to demonstrate a safe and highly efficient SSB. The GPE showed excellent oxidation stability (>6 V) against an aluminum current collector, which is the highest value reported so far. Molecular electrostatic potential calculations revealed that the Na⁺ ion interacts with poly-PETA through multiple weak coordination and has low activation energy, thereby improving the ionic conductivity of the electrolyte. The polymer network restricts the movement of the bulky anion by interacting with its delocalized charges, resulting in a high Na⁺ ion transference number and reduced cell polarization. DFT calculations showed that the strong binding energy between PETA and polysulfides inhibits the polysulfide dissolution, thereby decreasing the self-discharge behavior. GPE demonstrated enhanced reaction kinetics by effectively confining discharged products locally. GPE enabled low-temperature cycling of the cell at 0 °C whereas, at room temperature, the GPE maintained outstanding cycle stability of up to 2500 cycles at 2 C. The confinement properties of GPE were further analyzed by reducing the binder content in the cathode. GITT analysis revealed that at an extremely low binder amount of 2 wt.% the cell exhibits faster Na⁺ ion diffusion. Owing to enhanced interfacial contact, the GPE-containing pouch cells were able to deliver stable cycling at 1 C even when they were bent. Additionally, the pouch cell was able to light the light-emitting diode (LED) when it was mechanically deformed or cut.

1 Introduction

1.1 Motivation

World energy demand is in multifold increase due to higher living standards linked to a growing population. Moreover, carbon footprint and fossil fuel depletion pose an enormous challenge to attaining the energy production target. Figure 1 shows the projection of future energy consumption vs. population growth.^[1] Electricity production is by far dependent on fossil fuels, which are responsible for CO₂ emissions, climate change, water pollution, air pollution, etc. Thus, the benign way of electricity production by renewable energy gained a lot of attention in recent years. Currently, solar and wind power generation technologies are the forerunners in renewable energies.^[2]

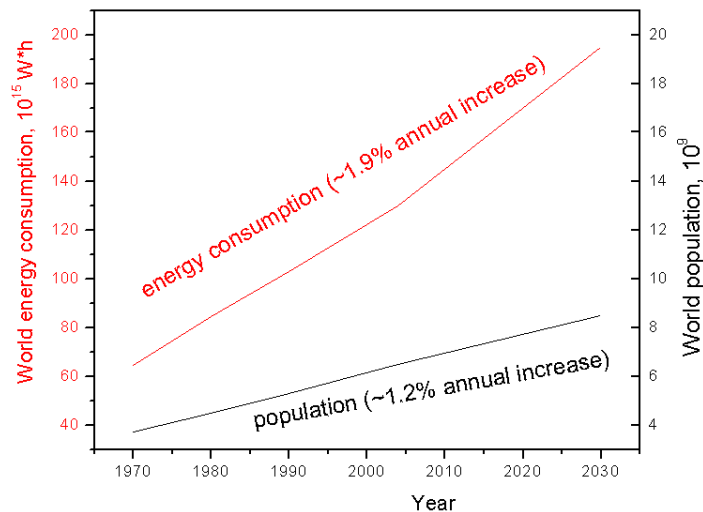


Figure 1: Population growth vs. energy consumption calculation.^[1]

Figure 2 shows that the energy storage technologies are also developing promptly in order to store the electrical energy produced via renewable technologies. The more prominent way of storing electricity is by using rechargeable batteries. Batteries store electricity in the form of chemical energy where the bond formation between different chemical compounds occurs. Batteries are an indispensable part of today's world with the market expected to grow up to \$152 billion by 2025. These electrochemical devices made their way to mobiles, stationary energy storage devices, commercial & small-scale appliances, and electric vehicles (EVs). For electric vehicles, the market hugely depends on the energy density of the batteries, which directly affects the performance. Different cell chemistries were utilized for the applications that require minimum energy such as portable electronic devices (PED), sensors, etc. The maximum achievable energy density

1.1. Motivation

of modern Li-ion batteries is $<500 \text{ Wh kg}^{-1}$, which is insufficient for long-range mobility.^[3]

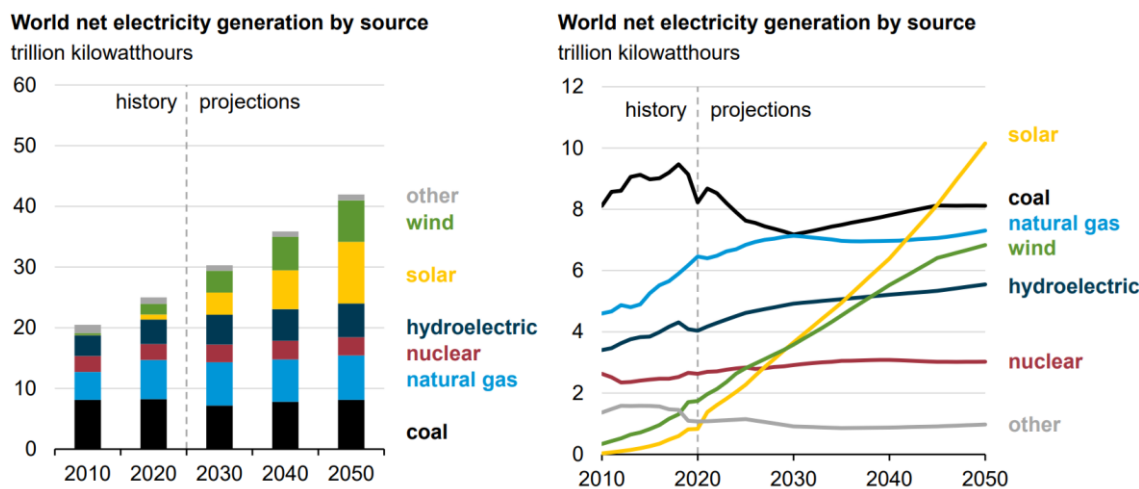


Figure 2: World electricity production based on sources (reproduced with permission from Ref. ^[2], open-access).

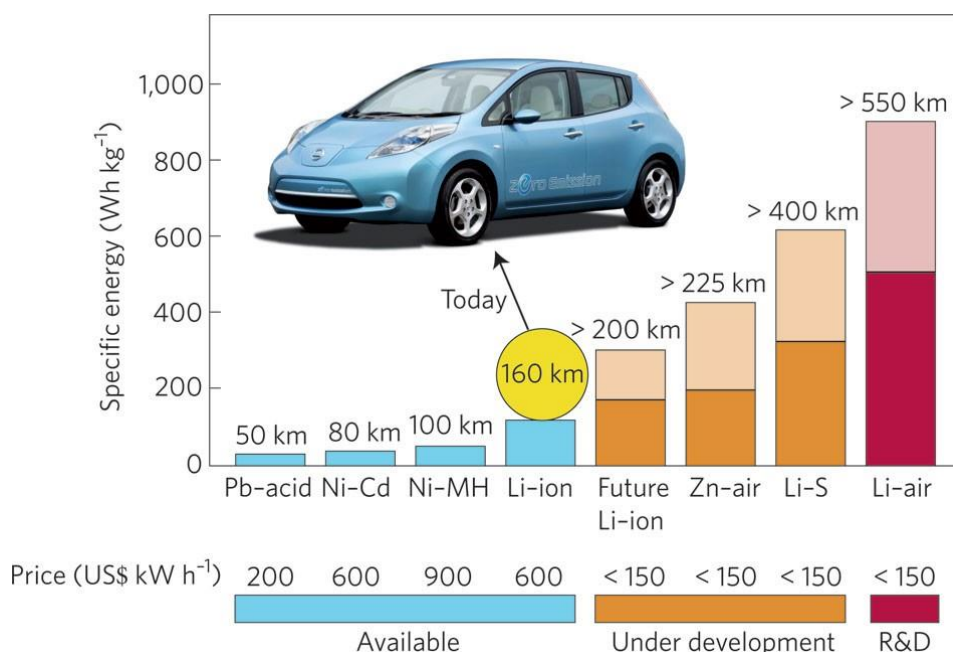


Figure 3: Specific energy density vs. different types of cell chemistry combined with projected driving range for electric vehicles (reproduced with permission Ref. ^[4]).

Thus, an advanced battery with different cell chemistry (including solid-state electrolytes) and high energy density ($>500 \text{ Wh kg}^{-1}$) should be developed in near future to fulfill the growing expectations. Additionally, the price mentioned in Figure 3 for various types of cells is simply too high for stationary energy storage applications where a substantial number of batteries are required. Alternatively, sulfur-based chemistry such as sodium-

sulfur and lithium-sulfur batteries can be utilized to achieve an economical solution for large-scale energy storage systems. Sodium is an inexpensive metal compared to its lithium counterpart, thanks to its abundance in the earth's crust. Therefore, an electrochemical cell consisting of a Na anode and sulfur cathode could provide a considerable capacity with cost-effective maintenance. High-temperature sodium-sulfur batteries (HT SSB) were first introduced by Neill Weber and J. T. Kummer at the Ford Motor Company in the 1960s for vehicles while the modern/commercial HT SSB technology was developed by Tokyo Electric Power Co, in collaboration with NGK insulators. These cells operate at 300 – 350 °C to ensure good ionic conductivity of the solid-state electrolyte. The battery's lifetime was claimed to be 15 years or 4500 cycles with an efficiency of around 85%.^[5] Due to their high practical energy density (760 Wh kg⁻¹), HT SSBs can be compared to current lithium-ion battery (LIB) technology.^[6] However, operating at 300-350 °C, both sodium and sulfur exist in a molten state, which presented a huge risk to be used in an electric vehicle. Therefore, room temperature sodium sulfur batteries (RT SSB) were developed to address safety issues and to achieve high energy densities (1274 Wh kg⁻¹). The electrolyte plays an important leading role in cell chemistry, and cell performance. RT SSBs employ commercial electrolyte salts, which are analogous to that of lithium. Therefore, it is important to gain a deeper knowledge of the effect of electrolytes on the cell's kinetics and electrochemical process to enhance its performance. Hence, this work was motivated by developing and employing a novel type of salts and electrolyte system to understand the electrochemical process occurring in RT SSBs.

1.2 State-of-the-art technology

The very first electrochemical cell, named “Voltaic pile” was fabricated by Alessandro Volta (at the University of Pavia, Italy) in 1800. The cell consisted of a series of alternately stacked zinc and silver wafers separated by a cloth, which was wetted with NaCl solution.^[7] The fundamental concept for modern carbon-zinc batteries was developed in 1866 by the French engineer Georges-Lionel Leclanche.^[8] He patented the galvanostatic energy storage device consisting of a zinc anode, carbon mixed manganese oxide cathode, and ammonium chloride as an electrolyte solution. The electrochemical cell can be divided into two main sectors based on the cell chemistry namely, primary, and secondary batteries.

Primary cell:

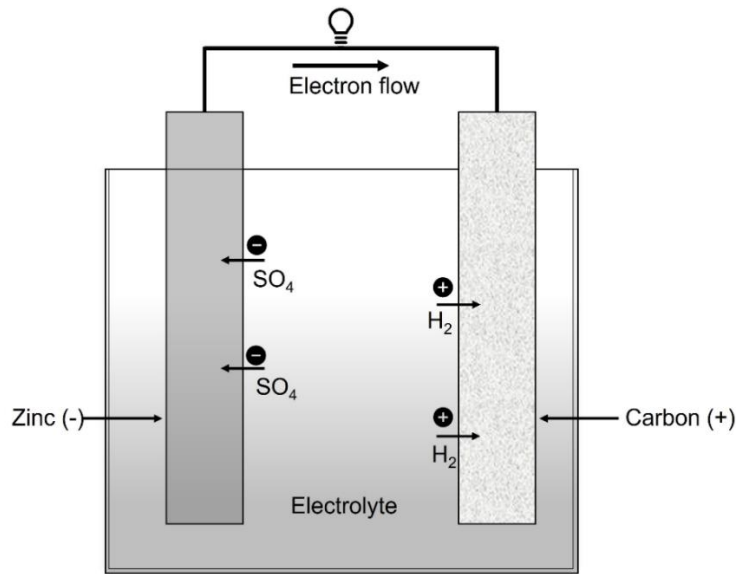


Figure 4: Zinc-carbon primary cell chemistry (based on Ref. [9, 10]).

The galvanic cell consists of electrodes with different potentials. Figure 4 shows the simplest known cell (galvanic cell) consists of zinc and carbon (wet cell). Carbon and zinc electrodes are suspended in an electrolyte solution consisting of water and sulfuric acid in a container. The current flows from the negative electrode to the positive electrode across the load. Carbon and zinc electrodes attract hydrogen ions and SO_4 ions from the electrolyte, respectively. This migration of ions results in the formation of zinc sulfate in the negative electrode. On the other hand, hydrogen gas is released in the positive electrode. Eventually, the zinc electrode dissolves into zinc sulfate, which is an irreversible chemical reaction.

Unlike primary cell chemistry, the chemical reactions are reversible in the secondary cells. For example, a lead-acid battery (Pb-acid) contains a cathode and anode made of sponge lead and lead peroxide, respectively. Figure 5a-d shows Pb-acid batteries at different charge-discharge states. During discharge (Figure 5b), the electrons flow from the cathode to the anode as in a primary cell but contrastingly the discharged product lead sulfate is chemically reversible and forms a sponge-like structure. On the anode side, the lead peroxide is converted to lead sulfate by the electrolyte. The amount of lead sulfate and sponge lead varies during discharge and charging and forms maximum lead sulfate when the cell is completely discharged. The reaction is controlled by the amount of sulfuric acid that remains in the electrolyte. During recharge, the chemical reaction is

reversed and forms sponge lead. This chemical reaction cycle can be repeated several times.^[10]

Secondary cell:

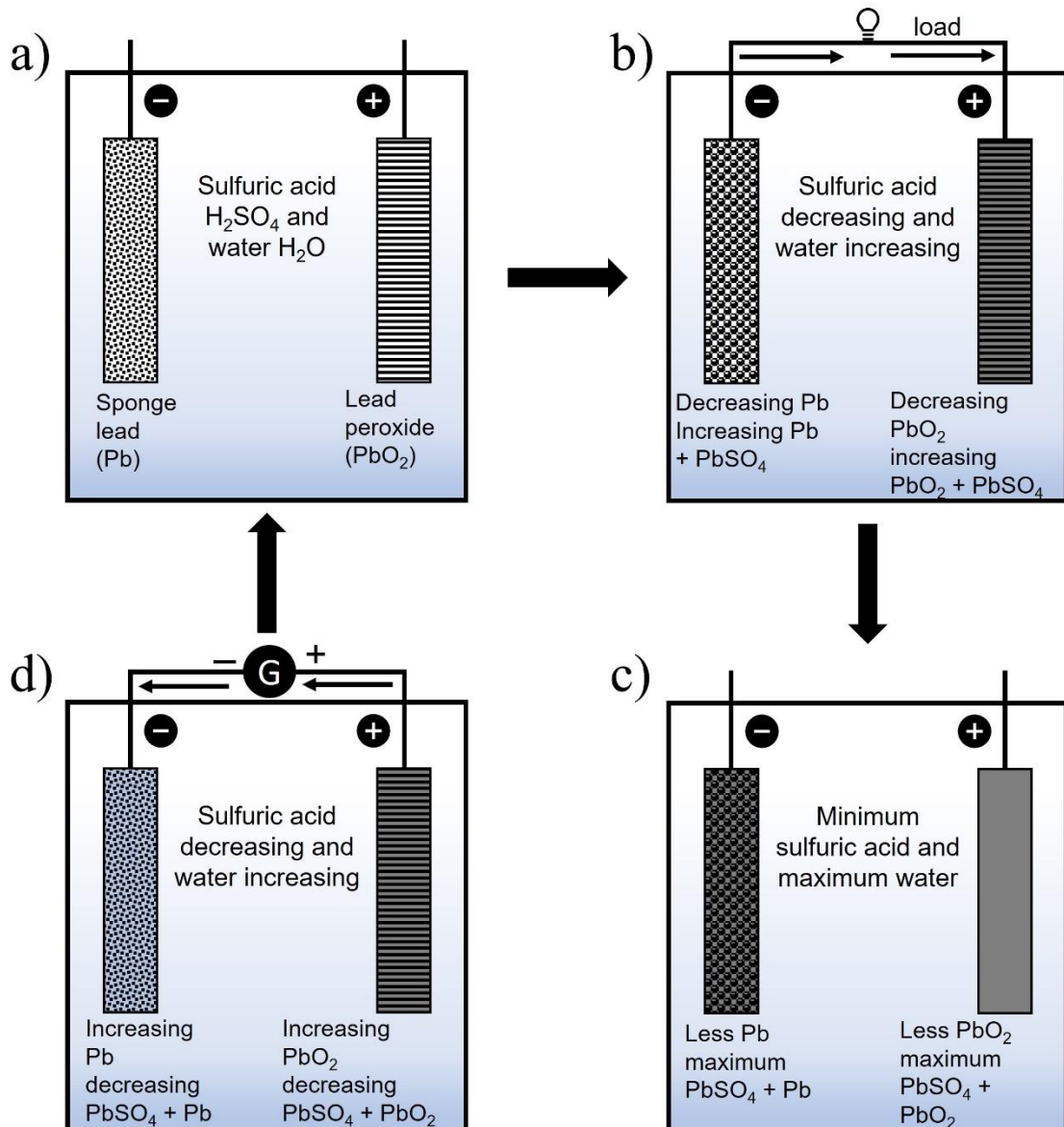


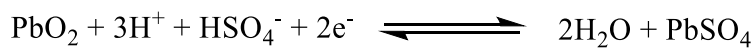
Figure 5: Typical lead-acid battery during, a) fully charged; b) discharging; c) fully discharged; d) charging (based on Ref. ^[11]).

Apart from PEDs, secondary rechargeable batteries are highly sought for EVs. The critical need to cut carbon emissions due to climate change is forcing the transportation sector to get electrified and store solar and wind energy in large storage grids. There are different types of secondary rechargeable batteries based on their chemical reactions. The batteries used in automobiles and grid energy storage applications are:

1) Lead-acid

Lead-acid batteries were invented in 1859 by Gaston Plante. They are widely used in automobile vehicles such as golf cars and forklifts and stationary applications (standby emergency power for telephone exchange) due to their low cost, low self-discharge, and low-temperature tolerance. However, disadvantages such as low cycle life (50-500 cycles), low energy density (30-40 Wh kg⁻¹), and safety hazards limit their application.^[11] The nominal voltage of a Pb-acid battery is 2 V and the open-circuit voltage (OCV) ranges from 2.05 – 2.125 V. As mentioned previously, the lead acid is a rechargeable secondary battery, and the following chemical reactions take place during charging/discharging:

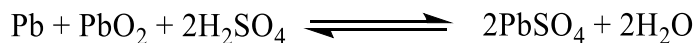
Cathode:



Anode:



Overall reaction:



2) Nickel-cadmium

Cadmium as a negative electrode and nickel oxide hydroxide as a positive electrode contains KOH or NaOH as an electrolyte solution. At the cathode, nickel oxyhydroxide is reduced to nickel hydroxide by taking up the electron. On the other hand, at the anode, cadmium metal oxidizes into cadmium hydroxide by losing electrons. The average voltage of the cell is 1.2V, less than in Pb-acid batteries. It was used in standby power sources and electric vehicles due to its longer lifetime and low-temperature performances. However, the toxicity of cadmium and the high self-discharge rate replaced Ni-Cd batteries with Li-ion batteries (LIB).^[9, 11]

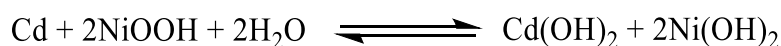
Cathode:



Anode:



Overall reaction:



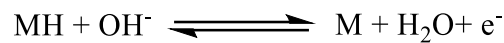
3) Ni-metal hydride

Ni-MH batteries are commercially used in hybrid-electric vehicles. As of 2018 Ni-MH batteries sustained a \$1.2 B market with 10% shares in all secondary batteries. The longer cycle life (3000) of Ni-MH batteries and their high energy density and fast charging compared to Ni-Cd batteries facilitated its use in a hybrid-electric vehicle (Toyota Prius). The cell voltage is similar to that of Ni-Cd batteries (1.2 V) High self-discharge of >50 %, three times higher than in Ni-Cd batteries, limits its usage in PEDs. The cell chemistry is comparable to that of Ni-Cd batteries, where the cathode is the same for both batteries. The toxic Cd was replaced by a metal hydride in the anode.

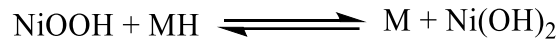
Cathode:



Anode:



Overall reaction:



Even though aqueous electrolyte cells such as Pb-acid, Ni-Cd, and Ni-MH achieved significant improvement in performance over a few decades, the energy density of these cells has indeed been the limiting factor for use in modern electronics or EVs.

Thus, to increase the energy density of the battery, it is necessary to develop anodes based on alkali metals, such as lithium, sodium, and magnesium due to their high reactivity, theoretical specific capacity, and reduced potentials.^[9, 12] Figure 6 represents the theoretical and practical energy density of various secondary batteries. Metal-ion batteries (MIBs) based on Li and Na have higher gravimetric energy density than aqueous cells, thus these are the obvious choice for high-energy batteries for PED to EV.

1.3. Metal-ion batteries (MIB)

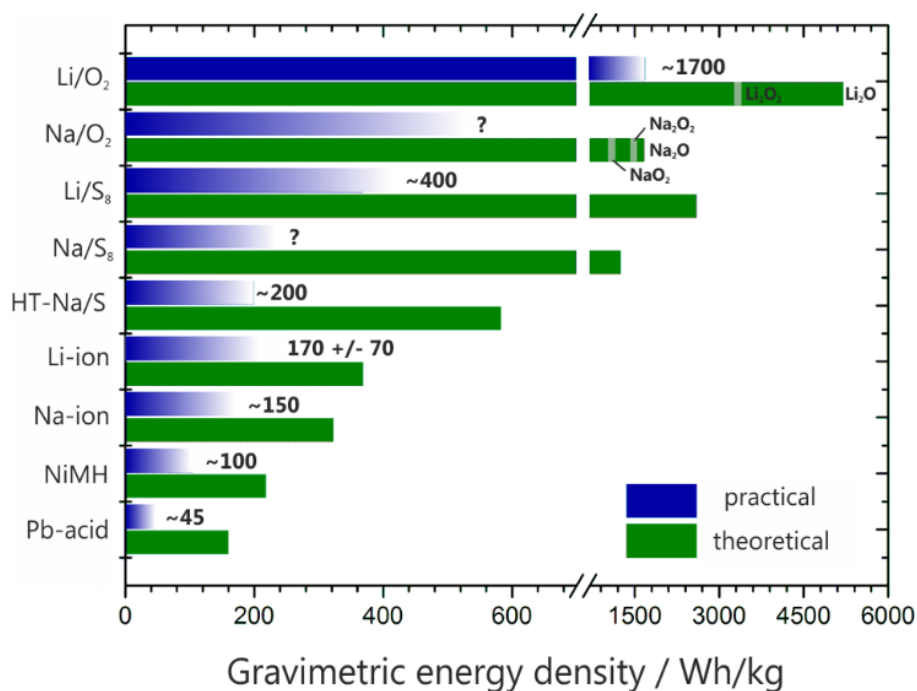


Figure 6: Energy density comparison of different types of batteries (reproduced with permission from Ref. ^[13], open access).

1.3 Metal-ion batteries (MIB)

Two major MIBs (Li and Na) are indeed in development for today's stationary energy storage and automotive sector. LIBs are commonly used in all types of grid & industry energy storage and also in the transportation sector due to their high energy efficiency. One of the major advantages of Li-ion compared to any other battery technology existing today is their high energy density of 160-260 Wh kg⁻¹ with an average cell voltage of around 3.6 V. Moreover, lithium is a lightweight material and exists at the bottom of the electrochemical series with the highest negative reduction potential (-3.05 V vs. SHE), which provides high energy density to the batteries.^[14, 15] Due to the smaller size of lithium, it holds more energy per unit of an atom. Thus, Li is the preferable choice for battery applications. Despite the improvements in LIBs, the increase in lithium consumption over the years in PEDs and other medium-scale storage devices will increase the price of the battery and render it impossible to utilize in large-scale energy storage applications.^[16] The high price of lithium also emerges from the low earth abundance of raw material in the earth's crust, and the uneven distribution of Li mining urges researchers to quest for an alternate metal. Recently, extensive focus has been given to other alkali metals such as Na, Al, and Mg for their application in batteries. Sodium can be an excellent alternative metal for lithium considering its reduction potential (-2.74 V), which is close to that of Li. In recent years, Na-ion batteries attracted massive attention,

thanks to their similar chemistry to Li, natural abundance in earth's crust, low cost (Na_2CO_3 , $\$150 \text{ ton}^{-1}$ vs. Li_2CO_3 , $\$5000 \text{ ton}^{-1}$) long cycle life, and high power.^[17, 18] Additionally, a higher conductivity of sodium salt (20% more than Li), ability to discharge 100% (vs. 80% discharge in lithium), and small desolvation energy (30% less than Li)^[19], and the possibility to use aluminum as a current collector (lithium alloys with Al) makes sodium an attractive alternate to Li. Many research attempts to develop sodium-ion batteries for the commercial EV market made them promising for future battery technology "beyond Li-ion". Though the energy density of sodium-ion battery (SIB) is less than the commercially available {lithium cobalt oxide (LCO), lithium manganese oxide (LMO), lithium nickel cobalt manganese oxide (NCM)} LIBs, it can be compared to lithium iron phosphate (LiFePO_4) (LFP) based LIB.^[3]

Table 1. The comparative description of the physical properties of lithium and sodium atoms (reproduced with permission Ref. ^[20]).

	Li⁺	Na⁺
relative atomic mass	6.94	23
mass-to-electron ratio	6.94	23
Shannon's ionic radii (Å)	0.76	1.02
E° (vs SHE) (V)	-3.04	-2.71
melting point (°C)	180.5	97.7
the theoretical capacity of metal electrodes (mAh g^{-1})	3861	1166
the theoretical capacity of metal electrodes (mAh cm^{-3})	2062	1131
theoretical capacity of ACoO_2 (mAh g^{-1})	274	235
the theoretical capacity of ACoO_2 (mAh cm^{-3})	1378	1193
molar conductivity in AClO_4/PC ($\text{S cm}^2 \text{ mol}^{-1}$)	6.54	7.16
desolvation energy in PC (kJ mol^{-1})	218	157.3
coordination preference	octahedral and tetrahedral	octahedral and prismatic

1.3.1 Working mechanism

MIBs contain a cathode and anode that allow intercalation/deintercalation of the alkali metal cations during charging/discharging. Since the alkali metal ions move back and forth between electrodes, these batteries are known as ‘rocking-chair’ batteries. Among many other MIBs (Mg, Al, K, and Ca), lithium and sodium ions are discussed in detail below.

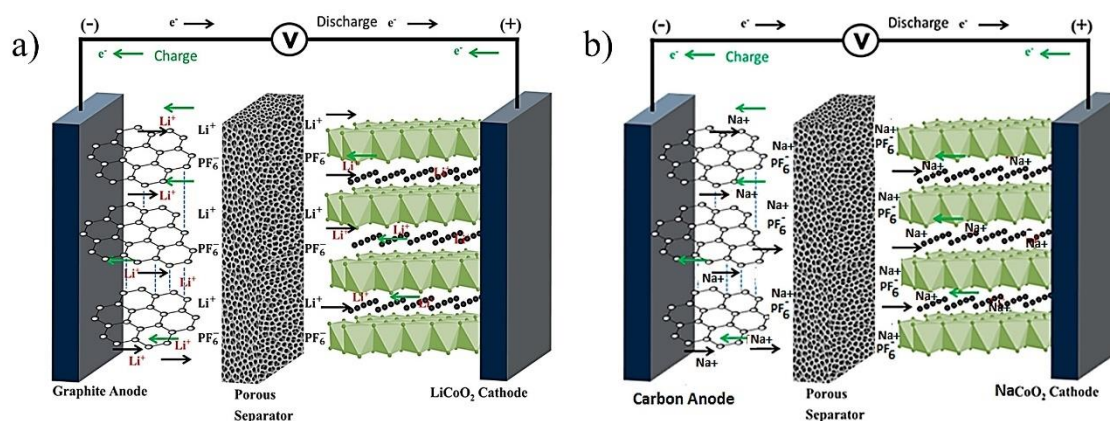


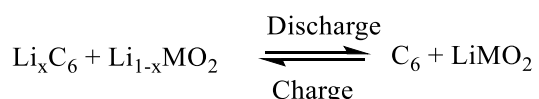
Figure 7: Schematic of working principles of non-aqueous a) Li-ion; and b) Na-ion battery (reproduced with permission Ref. [21, 22]).

Figure 7a, b shows the working mechanism of the Li and Na ion battery during charging and discharging. Both LIB and SIB consist of a current collector, cathode, anode, separator, and electrolyte. The anode materials can be segregated depending on their working principle namely, insertion reaction by carbon materials, conversion by sulfides or transition metal oxides, and alloying by Si or Sn.

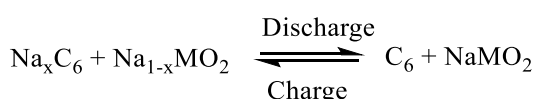
A general working concept for both LIB and SIB can be explained with the help of Figure 7a, b. In recent years, intercalation-based anodes are used to avoid dendrite formation by the negative metal electrodes. During charge, electrons flow from the cathode to the anode externally by releasing ions (Na or Li) into the electrolyte, which then combine with the electron and react with the anode material.

Electrode reaction:

LIB:



SIB:



1.3.2 Cathodes, anodes, and electrolytes

The commonly used cathode components in LIB are cobalt oxide, nickel oxide, manganese oxide, iron phosphate, and titanate. Graphite and $\text{Li}_4\text{Ti}_5\text{O}_{12}$ are used as anode materials. Transition metal oxide cathodes were developed by J. B. Goodenough's group in 1980 with the aim of increasing the cell potential. Eventually, layered, spinel, and polyanion-type cathodes were explored as novel cathode material.^[23] LiCoO_2 (LCO) cathode remains one of the best cathodes due to its structural stability, high potential (3.8 V) with good electrical and Li-ion conductivity. However, high cost and oxygen release from the crystal lattice upon charging to more than 50% impedes any safe operation of LIB.^[24, 25] Replacing cobalt with environmentally benign and abundant material Mn and Ni ($\text{LiNi}_{1-y-z}\text{Mn}_y\text{Co}_z\text{O}_2$, NMC) exhibits high capacity at low cost. Spinel oxide cathode LiMn_2O_4 (LMO) offers a high voltage of 4.1 V with high electrical and ionic conductivity and offers fast charging/discharging.^[26] Polyanion-based cathodes (LiFePO_4 , LFP) can increase thermal stability, and safety and contain non-toxic materials.^[27, 28, 29]

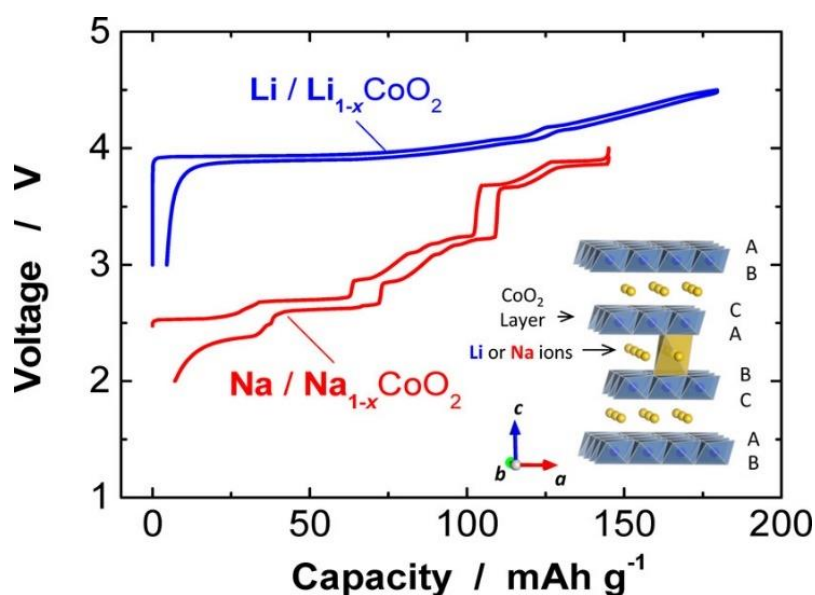


Figure 8: Comparison of transition metal oxide (Li and Na-based) cathode charging/discharging cycle against lithium metal anode (reproduced with permission Ref. [22]).

Intercalation cathodes for SIBs are analogous to LIB, which can be categorized into polyanions ($\text{Na}_3\text{V}_2(\text{PO}_4)_3$, NaFePO_4), oxides (O3 type – $\text{Na}(\text{Ni}_{0.6}\text{Co}_{0.05}\text{Mn}_{0.35})\text{O}_2$, and P2 type – $\text{Na}_{0.67}(\text{Ni}_{1/3}\text{Mn}_{2/2})\text{O}_2$), and organic ($\text{Na}_2\text{C}_6\text{O}_6$) compounds.^[30] The NaCoO_2 (NCO) cathode can reversibly intercalate Na ions similar to LiCoO_2 . Comparing the

1.3. Metal-ion batteries (MIB)

charge/discharge of both cathode materials from Figure 8, it is evident that the LCO shows higher potential (>1.0 V) compared to NCO. During discharge, NCO exhibits a reduction in potential as the Na content in the cathode increases. This results in lower available energy density for Na systems than LCO.^[31, 32]

In the early days, lithium metal was used as an anode material in LIBs. However, dendrite formation and subsequent short circuits lead to thermal runaways and fires which inhibited the deployment of Li metal in modern LIBs.^[33] Commonly used anodes for LIB are graphite, $\text{Li}_4\text{Ti}_5\text{O}_{12}$ (LTO), and conversion-based Si anodes. Lithium intercalates between the graphite planes given their good electrical conductivity and Li-ion transportation. The theoretical capacity of the graphite is 372 mAh g^{-1} , higher than many cathode materials.^[34] In presence of propylene carbonate (PC), graphite anodes show capacity loss due to the exfoliation of the graphitic planes caused by the intercalation of PC.^[35] Hard carbon was also investigated in LIB due to its small graphitic grains with a disordered structure, increasing structural stability. Nevertheless, nanovoids reduce the density of the particle, thereby decreasing the volumetric capacity.^[36] LTO has high thermal stability, high volumetric capacity, and good cycle life, but the low capacity (175 mAh g^{-1}) and high cost of Ti limit its use in many applications.^[37]

Anodes for SIB were synthesized from various carbonaceous materials (hard carbon, graphene), metal alloys (Sn, Ge, Sb), and organic compounds ($\text{Na}_2\text{C}_{10}\text{H}_2\text{O}_4$). The most common anode for SIB is the hard carbon due to the thermodynamic instability of Na-intercalated graphite compounds. A plausible reason could be that the size of the Na ion restricts the intercalation into graphite.^[38, 39, 40]

Electrolytes in both LIB and SIB can be classified into six major types: 1) organic liquid electrolytes,^[41, 42] 2) ionic liquids,^[43, 44] 3) aqueous electrolytes,^[45, 46] 4) gel/quasi solid polymer electrolytes,^[47, 48] 5) solid polymer electrolytes,^[49, 50] and 6) inorganic solid electrolyte.^[51, 52] The commonly used electrolytes are organic solvents based on carbonates or ethers with suitable Li or Na salts. Out of these, ether-based electrolytes are seldomly used in LIB due to their poor passivation of the anode and instability towards >4 V class cathode.^[53] However, fluorinated ethers are found to be flame-retardant for LCO and LMO cathodes.^[54, 55] On the other hand, ether-based electrolytes have been used in SIB due to their high reduction resistance and high coulombic efficiency (CE).^[56] For example, in commercial LIB, an electrolyte composition consists of a LiPF_6 salt (lithium hexafluorophosphate) dissolved in mixtures of EC, DMC, PC, DEC, and EMC. This

electrolyte composition delivers high ionic conductivity, and good stability, and prevents Al current collector corrosion.^[57]

The popular choice of EC has its own merits such as high solubility of salts due to its high dielectric constant, and the formation of a robust SEI layer on various electrodes in both LIB and SIB. However, the high melting point (36 °C) and high viscosity of EC prevent its usage as a single component electrolyte. On the other hand, linear carbonates (DMC, DEC, EMC) have low viscosity but suffer from poor solvation power of Li or Na salts. Thus, the combination of both solvents displays a synergetic effect, resulting in enhanced ionic conductivity of the electrolyte, reduced viscosity, and a wide electrochemical potential window. PC solvent is compatible with SIBs (hard carbon anode) unlike its counterpart LIBs due to co-intercalation into graphite anode.^[58]

The typical salts used in LIBs are LiPF₆, lithium trifluoromethanesulfonate (LiOTf), lithium bis(trifluoromethylsulfonyl)-imide (LiTFSI), lithium tetrafluoroborate (LiBF₄), and lithium perchlorate (LiClO₄). Nevertheless, the main drawback of LiPF₆ is its poor thermal stability (>55 °C) and moisture sensitivity. At high temperatures, LiPF₆ decomposes to PF₅, which reacts with solvents to produce highly toxic fluoro-organic gas and also polymerizes the solvents.^[59] When it comes in contact with moisture, LiPF₆ decomposes readily and generates toxic hydrogen fluoride (HF), which forms a highly resistive lithium fluoride (LiF) layer thereby, increasing the cell impedance.^[60, 61]

Since room temperature sodium-sulfur batteries (RT SSB) employ similar salts and solvents, the detailed study of the salt structure and its influence on ionic conductivity, solid electrolyte interphase, and the effect of additives on cell chemistry will be discussed further in the following section (1.6).

1.3.3 Limitations of MIBs

As mentioned previously, SIBs are still in the early research period, thus only LIB limitations are explained in this chapter.

Even though LIBs are more mature in technology, the high energy density required for the growing market demands an urgent development of next-generation batteries.^[62, 63] In general, intercalation chemistry in MIBs limits its charge storing capacity and energy density. Increasing the energy density can be achieved by increasing the charge storage of the electrodes or improving the cell potential. Increasing the cathode voltage above ~4.3 V results in electrolyte decomposition due to the limited electrochemical stability

1.4. Alternate cathode materials for high-energy batteries

window.^[64] Numerous potential anodes and cathodes were still discovered in recent times but the capacities of an anode (graphite) and cathode are capped at ~ 370 and ~ 250 mAh g^{-1} , respectively.^[65] For example, LFP cathodes can hold one Li^+ per $LiFePO_4$ molecule and the graphite anode can accommodate a maximum of LiC_6 .

Anode materials such as Sn and Si provide excellent theoretical capacities of 960 and 3579 mAh g^{-1} , respectively. However, the huge volume expansion (Sn – 257 %, Si – 400 %,) pulverizes the anode during cycling, which eventually leads to poor performance.^[66, 67] On the other hand, renewing the usage of pure alkali metal anodes is gaining increased attention in recent times due to its enhancement in the energy density of secondary batteries. Out of many metals, lithium provides the highest theoretical capacity of 3862 mAh g^{-1} with the lowest reduction potential of $-3.05V$ vs. SHE.^[68] By addressing the issues regarding the unstable anode-electrolyte interface, which leads to the formation of dendrites and dead lithium, rechargeable batteries with Li metal can replace LIBs in various applications.^[33, 69] Considering cathodes, LCO contains cobalt, a toxic, environmentally unfriendly, and expensive metal. On the other hand, LFP is inexpensive but exhibits low capacity. Though the use of Li metal anode increases the capacity, the overall limiting factor is the cathode capacity. Thus, an alternate cathode material with high theoretical capacity is essential to utilize the full potential of Li metal anode.^[70]

1.4 Alternate cathode materials for high-energy batteries

Sulfur and oxygen would be the potential choice for the cathode material in lithium-based batteries due to their high theoretical energy density of 2510 and 3500 Wh kg^{-1} (based on Li_2O_2), respectively. $Li-O_2$ batteries consist of a porous carbon cathode, electrolyte, separator, and Li metal as an anode.^[71] Contrary to the intercalation mechanism, the $Li-O_2$ battery operates due to the reaction between Li with oxygen molecules. Thus, the specific energy density is 10 times greater than the commercial LIBs.^[72, 73] The first high-temperature Na- O_2 batteries at 105 °C using polymer electrolytes were investigated in 2011, by Peled et al. The molten Na helps to decrease the cell impedance, elimination of dendrite formation, and acceleration of cathode kinetics.^[74, 75] However, $Li-O_2$ and Na- O_2 batteries face several disadvantages such as high charging overpotential, low efficiency, pure O_2 source, and component stability.

Another potential high-energy-density cathode material is based on the conversion reaction between Li ions and sulfur.^[76] Elemental sulfur is non-toxic, low cost, earth-

abundant, and holds a high theoretical capacity (1675 mAh g^{-1} , with a two-electron transfer per atom). It exists in sulfur allotrope octasulfur (S_8). Sulfur melts at $112 \text{ }^\circ\text{C}$ and has a density of 1.819 g cm^{-3} (liquid). Despite the first lithium-sulfur cell being patented in 1962, lithium-sulfur batteries (LSB) have seen a huge surge in popularity within the last two decades, foreseeing sulfur as the potential alternate to LIB technology. Figure 9 shows the different cathode materials and a comparison of their energy densities. It is evident that intercalation-based cathodes underperform sulfur and oxygen-based cathodes. LSB can deliver more than five times the theoretical energy density (2600 Wh kg^{-1}) of LIBs ($\sim 420 \text{ Wh kg}^{-1}$). Continuous improvement on the material and cell level in both Li- O_2 batteries and LSBs helps to achieve the practical energy density needed ($>500 \text{ Wh kg}^{-1}$) for EVs.^[77]

Due to the moderate atomic weight of sulfur and less dense lithium metal, high-energy batteries with less weight can be realized. All these advantages of sulfur-based batteries make them a potential candidate for a wide range of applications. Apart from LSBs, sulfur cathodes were researched for various alkali metal anode batteries such as Na, Mg, Ca, K, and Al. The two most popular alkali metals (Na and Li) have similar physical and chemical properties and thus similar redox mechanisms. Sodium-sulfur batteries (SSB) operate in a similar mechanism to that of LSB. Despite the merits mentioned above, sulfur-based cathodes face serious challenges: 1) the insulating nature of sulfur and final sulfide leads to poor utilization of the active material,^[78, 79, 80] 2) long-chain polysulfide dissolution in ether-based solvents such as 1,3-dioxolane (DOL), 1,2-dimethoxyethane (DME), and tetra(ethylene glycol) dimethyl ether (TEGDME) controls the redox shuttling, which is responsible for the detrimental effect on cells performance,^[81, 82, 83, 84] 3) polysulfides react with most of the carbonate solvents thus forming thioethers,^[85, 86, 87] 4) volume expansion of discharged sulfides ($\sim 80\%$ for Li_2S and $\sim 170\%$ for Na_2S) pulverizes the cathode, leading to capacity loss.^[88, 89, 90] A lot of efforts were taken to alleviate the drawbacks of the sulfur cathode, such as 1) nanostructured/porous carbon framework to increase the conductivity and accommodate volume expansion, 2) adsorption of the polysulfides by polar host material, 3) modified separators or blocking interface, and 4) electrolyte additives or solid electrolytes to avoid polysulfide dissolution.^[91, 92, 93, 94, 95]

1.4. Alternate cathode materials for high-energy batteries

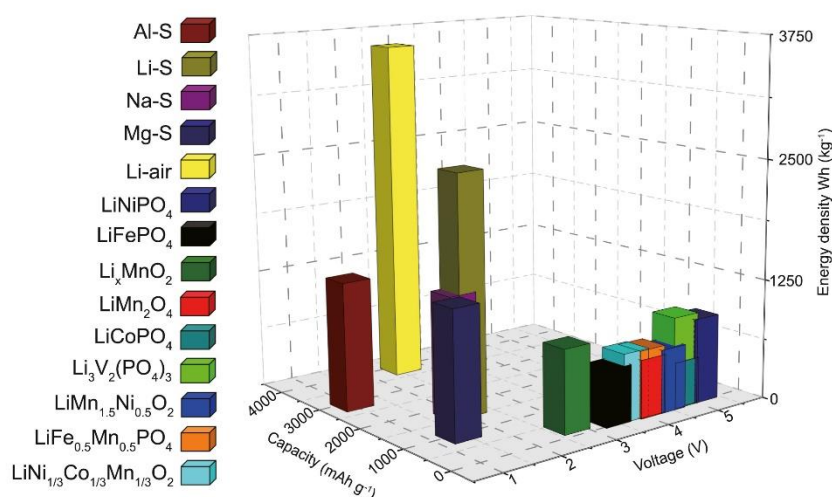


Figure 9: Comparison of capacity vs. potential vs. theoretical specific energy density of different cathode materials (reproduced with permission from Ref. [96], open access).

However, most of the above-mentioned methods can only delay polysulfide diffusion to some degree, yet, during long-term cycling, complete elimination of polysulfide (PS) dissolution is the cornerstone to achieving shuttle-free cycling. Thus, developing a cathode that cannot form long chain polysulfides during redox reactions would solve this issue. One reasonable methodology is to restrain the small sulfur allotropes (S_{2-4}) into microporous carbon with ~ 0.5 nm. In this way, the solid-liquid transition from S_8 to S_4^{2-} is completely neglected with only one discharge plateau appearing at ~ 1.9 V (vs. Li/Li⁺). However, some researchers believe that a nonpolar carbon host cannot efficiently contain polar PS species, which explains the low coulombic efficiency and fast capacity decay observed during long-term cycling.^[97, 98, 99]

Another approach to avoid PS dissolution is by trapping sulfur atoms in a polymer network by covalent bonding. Sulfurized poly(acrylonitrile) (SPAN) composite cathode was first proposed by Wang et al. for both lithium and sodium batteries.^[100, 101] Heating sulfur with poly(acrylonitrile) above 300 °C under inert conditions resulted in a cyclized structure where sulfur is covalently bound to the polymer backbone. It is well known that in SPAN sulfur exists in short chains ($-S_x-$, $x \leq 3$), thus eliminating the possibility of PS dissolution in carbonate electrolytes.^[97, 102, 103] However, in an ether-based electrolyte, long-chain polysulfide formation is inevitable since short-chain PS oxidizes to elemental sulfur during charging.^[103] Figure 10 shows two different voltage profiles for cathodes based on elemental sulfur and SPAN. The sulfur cathode has two distinct discharge plateaus at ~ 2.3 V and ~ 2.1 V, representing the conversion of S_8 into long-chain PS and

of PS into subsequent short-chain polysulfides, respectively. In contrast to elemental sulfur, SPAN cathode shows a huge potential drop during the first cycle, indicating the high energy needed to break S-C covalent bond and S-S bonds. Also, in the elemental sulfur cathode, the conversion reaction proceeds as solid-liquid-solid transformation, which requires a high volume of electrolyte to ensure smooth cycling. A high electrolyte to sulfur ratio significantly reduces the energy density of the cell.^[104] On the other hand, SPAN exhibits one plateau at ~ 1.7 V, indicating that sulfur exists in a short-chain ($C-S_x-C$, $x = 2-3$), which undergoes a solid-solid transformation.^[103, 105] Moreover, SPAN exhibits a stable operation in carbonate-based electrolytes with high coulombic efficiency.

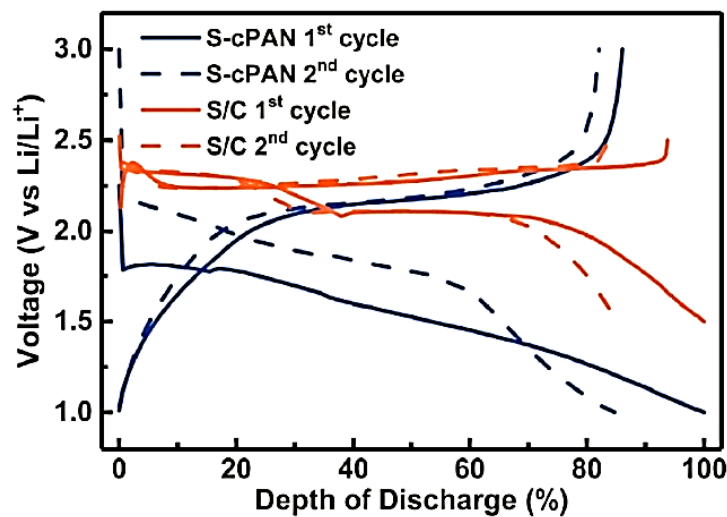


Figure 10: Comparison of voltage profiles comparison of an elemental sulfur-based cathode (in ether electrolyte) and an SPAN cathode (in carbonate electrolyte) for LSB (reproduced from Ref. ^[106] with permission from Elsevier).

Overview of their advantages, SPAN-based cathodes were used in this research. SSB working principles, limitations, and improvements will be discussed in the following sections.

1.5 High-temperature sodium-sulfur batteries

Figure 11a shows the current state-of-the-art batteries and their power output based on the application. Among many other battery technologies applied in utility-scale grid energy storage applications, LIB and HT SSBs have a significant market share. LIB technology is the economic solution for fast response frequency regulation, and short-term (30 minutes) spinning reserve applications. Currently, it holds >60 % of shares in batteries applied for grid connections. However, toxic gas releases during thermal runaway

and environmental risks raise concerns over full-fledged commercialization for the growing market.

On the other hand, HT SSB holds only 19% of the shares but it is non-toxic and inexpensive. Additionally, it exhibits high energy density, ~100% coulombic efficiency, high cycle life (~15 years), and has one of the longest storage durations in the current market.^[107] The high theoretical specific capacity of 760 Wh kg⁻¹ is three times more than the commercial lead-acid battery and more than the state-of-the-art LIBs. There are no external pumps or valves attached, thus the maintenance is limited to periodic cleaning. Despite the low cost of raw materials, the price of the SSB (per kWh) is still comparable to that of LIB. However, 99 wt.% of the SSB materials can be recycled thereby significantly reducing the overall price of the battery.^[108] A typical HT SSB operation is shown in Figure 11b. The cell contains Na and sulfur in a molten state, and a ceramic solid separator (β – alumina or β – Al₂O₃). The liquid sodium acts as a negative electrode and the outer shell which is in contact with sulfur acts as a positive electrode. The cylindrical cell is enclosed by a steel casing covered in chromium and molybdenum to avoid corrosion.^[109]

The electrolyte plays a key role in the operation of the battery such as ion conduction and capacity retention. A crystalline compound β – alumina has a general structure of (Na₂O) xAl₂O₃ where x ranges from 11 (β – Al₂O₃, hexagonal) to 5 (β'' – Al₂O₃, rhombohedral).^[110] The unit cell consists of three sets of loosely packed Na⁺ and O²⁻ in the spinel blocks. The main difference between β and β'' – alumina arises from the stacking sequence of O²⁻ through the conduction plane. The stacking disparity between two different structures causes a 50% increase in unit cell volume of β'' – Al₂O₃. Thus, it exhibits higher Na⁺ ionic conductivity, which is suitable for HT SSB applications. The β'' – alumina demonstrates higher ionic conductivity than β – alumina ranging from 0.2 – 0.4 S cm⁻¹ at 300 °C, making it suitable for HT SSB applications.^[110, 111, 112, 113] Additionally, substituting mono or divalent (Mg²⁺ or Li⁺) cations for the aluminum ions in the spinel block results in a single crystal with a stable ion-rich phase.^[114]

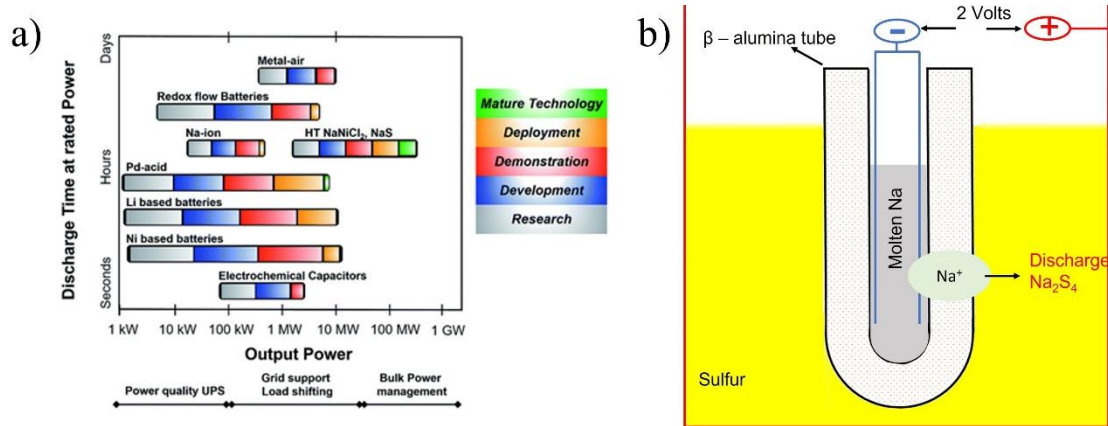


Figure 11: a) comparison of different battery energy storage devices based on their output power (open access Ref. ^[115], reproduced from the Royal Society of Chemistry), b) schematic diagram of HT SSB (reproduced with permission Ref. ^[116]).

1.5.1 Working principle

The working principle of an HT SSB is based on a reversible chemical conversion process during discharge/charge. During discharge, Na oxidized at the anode/electrolyte interface, and the resulting Na⁺ diffuses through the electrolyte towards the sulfur container by giving off one electron which travels through the external circuit. This electron then combines with sulfur and sodium to form sodium polysulfide (S_x^{2-}). The discharge profile can be separated into three regions based on the state of discharge and the products formed (Figure 12).

During the initial discharge at 2.075 V, the melt consists of Na₂S₅ ($T_m = 253\text{ }^\circ\text{C}$), which is immiscible with β-S₈ ($T_m = 115\text{ }^\circ\text{C}$) therefore the two-phase system is formed at the cathode. The sulfur content varies from 78 to 100 wt.%.^[11, 115]



Continuous discharge extends the two-phase zone throughout the catholyte thereby reducing the β-S₈ concentration. Further discharging the cell leads to a reaction between the remaining sulfur and the sodium to form Na₂S₄ ($T_m = 290\text{ }^\circ\text{C}$).



The cell potential is decreased linearly, and the continuous reaction leads to the formation of Na₂S₃ ($T_m = 235\text{ }^\circ\text{C}$) further driving the potential to 1.74 V.

1.5. High-temperature sodium-sulfur batteries



According to DFT calculations, larger dianions (S_x^{2-} , $x > 4$) are thermally unstable at $> 300^\circ\text{C}$, thus only small dianions, and radical monoanionic ions paired with sodium (NaS_x^- , $\text{NaS}_x^{\cdot-}$ where $x = 2, 3$) exists during cycling. It is known that discharging further than Na_2S_3 leads to the formation of Na_2S_2 which is favored by the Gibbs energy.^[117] However, Na_2S_2 ($T_m = 475^\circ\text{C}$) adversely affects the battery efficiency by depositing on the carbon felt matrix in form of small crystals. This solid product increases the resistance of the cell, decreases its electronic conductivity, and hinders further recharging of the cell.

Overall cell reaction:^[118]

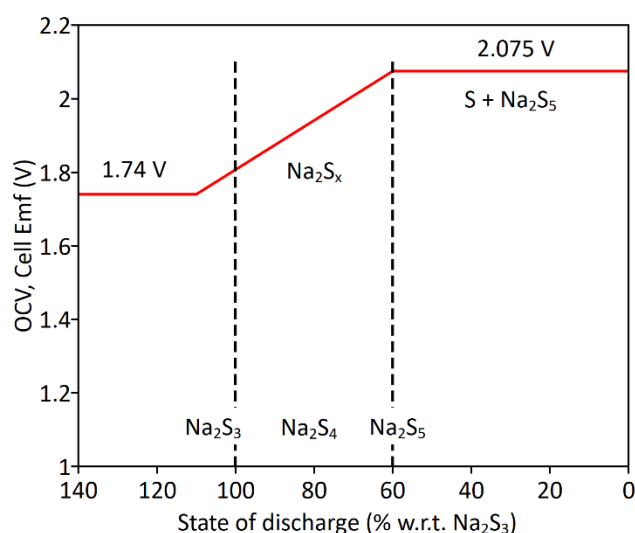
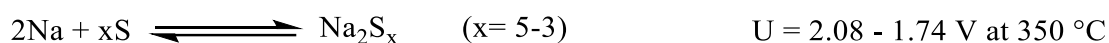


Figure 12: Discharge potential profile vs. state-of-discharge of HT SSB (reproduced with permission Ref. ^[119])

1.5.2 Challenges of high-temperature sodium-sulfur batteries

Besides all the advantages, a wide acceptance of HT SSB still faces several challenges. The main concern is the elevated temperature (300°C) required to enable the high conductivity of the solid electrolyte. Thus, a fraction of the produced current is constantly consumed to maintain the temperature of the battery, thereby, reducing overall efficiency. The solid electrolyte, β – alumina, would slowly develop a crack and eventually break during cycling, which results in short-circuiting due to contact between molten sodium and sulfur. This failure of the electrolyte would possibly cause fire or even an explosion. Temperature maintenance by the battery management system (BMS) is mandatory since

the sulfur ($T_b = 444\text{ }^\circ\text{C}$) vapor can rupture the cell at $600\text{ }^\circ\text{C}$.^[120] Moreover, the molten polysulfides are corrosive to the current collectors and the cell capsules, which requires perfect sealing. The cell is discharged only up to $\sim 33\%$ (Na_2S_3 , 558 mAh g_s^{-1}) of the capacity of the sulfur due to the formation of insulating Na_2S_2 and Na_2S . All these shortcomings irrefutably restrict the use of HT SSB in EV applications.^[11, 121, 122]

1.6 Room temperature sodium-sulfur battery

The research on RT SSBs, a potential alternative for HT SSB was first proposed in 2006.^[123] The first cell delivered a specific capacity of 489 mAh g_s^{-1} at the beginning of the discharge and eventually decreased drastically to 40 mAh g_s^{-1} after 20 cycles. In recent years, RT SSB research is gaining increased attention for large-scale energy storage applications and also for EVs.^[90] It has analogous cell chemistry to the lithium-sulfur battery but is not identical.

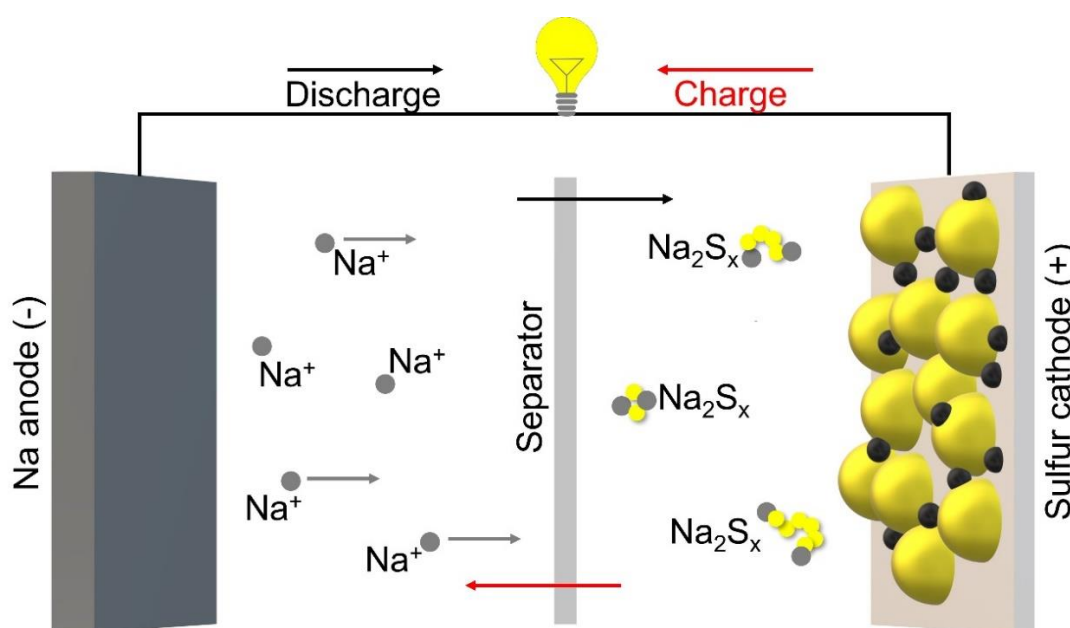


Figure 13: Schematic diagram of RT sodium-sulfur battery

In general, RT SSB contains sodium metal as an anode, sulfur/carbon mixture as a cathode, and a liquid/gel/solid composition as an electrolyte. The electrolyte contains one or two types of sodium salt dissolved in two or more solvents. The sulfur cathode can be modified to improve cycle stability, rate capability, and coulombic efficiency.^[124] During discharge, the electron travels through an external circuit by releasing Na^+ into the electrolyte by powering the device connected to the circuit. This Na^+ ion travels towards the cathode and reduces the sulfur by combining with the electrons. During charging, the opposite reaction occurs by drawing current from the power source. Figure 13 represents

the schematic diagram of RT SSB during charging/discharging. This section focuses on explaining the principles and mechanism behind RT SSB.

1.6.1 Mechanism

As denoted previously, the resemblance with LSB working principles helps to understand the discharge and charge mechanism of RT SSBs. Even though the reaction path is comparable, the major difference between Li and Na arises from its reduction potential (-3.04 V for Li, -2.71 V for Na (vs. SHE)). The sulfur cathode and additional interlayer (commercial carbon foam) between cathode and separator were fabricated and tested by Yu et al.^[125] The calculated theoretical capacity of the sulfur and the practical capacity were compared as shown in Figure 14.

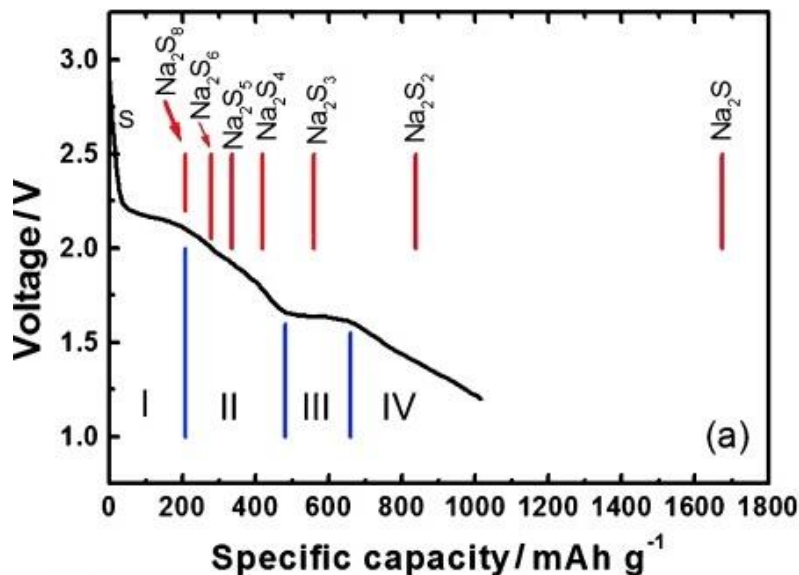


Figure 14: Theoretical and practical data comparison on potential vs. capacity curve for RT SSB (red lines – theoretical values, blue lines – practical values) (reproduced with permission Ref. ^[125]).

The potential curve exhibits two plateaus at ~2.20 V and ~1.65 V, indicating multiple complicated reduction processes. The first slope of discharge potential ranges from 2.20 to 1.65 V and the second slope begins from 1.60 to 1.20 V.^[125] From the thermodynamical point of view, the capacity values were calculated based on sulfur reduction. The curve in Figure 14 can be segregated into four sections with each step representing the reduction from elemental sulfur to sodium sulfides. The theoretical capacity (Q) was calculated based on the following equation:

$$Q_T = \frac{nF}{M_w} \quad \text{Equation 1}$$

where n is the number of electrons involved in the charge transfer, F is the Faraday constant, and M_w indicates the molecular weight of the active material.

Table 2: Electrochemical reactions of RT SSB. ^[125, 126]

	Reduction reactions	description	Q_T, mAh g_s^{-1}
I	$2\text{Na}^+ + \text{S}_8 + 2\text{e}^- \rightleftharpoons \text{Na}_2\text{S}_8$	Plateau at 2.20 V, Solid (S_8) \rightarrow liquid (Na_2S_8)	209
II	$2\text{Na}^+ + \text{Na}_2\text{S}_8 + 2\text{e}^- \rightleftharpoons 2\text{Na}_2\text{S}_4$	Sloping region from 2.20 to 1.65 V, Liquid (Na_2S_8) \rightarrow liquid (Na_2S_4) (Includes other minor reactions)	279
	$2/3\text{Na}^+ + \text{Na}_2\text{S}_8 + 2/3\text{e}^- \rightleftharpoons 4/3\text{Na}_2\text{S}_6$		335
	$2/5\text{Na}^+ + \text{Na}_2\text{S}_6 + 2/5\text{e}^- \rightleftharpoons 6/5\text{Na}_2\text{S}_5$		418
	$1/2\text{Na}^+ + \text{Na}_2\text{S}_5 + 1/2\text{e}^- \rightleftharpoons 5/4\text{Na}_2\text{S}_4$		
III	$2/3\text{Na}^+ + \text{Na}_2\text{S}_4 + 2/3\text{e}^- \rightleftharpoons 4/3\text{Na}_2\text{S}_3$	Plateau at 1.65 V, Liquid (Na_2S_4) \rightarrow coexisting solid (Na_2S_3 , Na_2S_2 , and Na_2S)	558
	$2\text{Na}^+ + \text{Na}_2\text{S}_4 + 2\text{e}^- \rightleftharpoons 2\text{Na}_2\text{S}_2$		837
	$6\text{Na}^+ + \text{Na}_2\text{S}_4 + 6\text{e}^- \rightleftharpoons 4\text{Na}_2\text{S}$		
IV	$2\text{Na}^+ + \text{Na}_2\text{S}_2 + 2\text{e}^- \rightleftharpoons 2\text{Na}_2\text{S}$	Sloping region from 1.65 to 1.20 V, Solid (Na_2S_2) \rightarrow solid (Na_2S)	1675

Table 2 shows the detailed description of discharge reactions that occurs during battery cycling. It is supposed that in section II, where dissolved polysulfides react with one another is the most complicated reaction mechanism and it is easily affected by the

1.6. Room temperature sodium-sulfur battery

chemical equilibrium between polysulfide species. The final capacity depends on the competition between the formation of the final sulfide species (Na_2S_3 , Na_2S_2 , and Na_2S) in section III. Owing to their insoluble nature and insulating properties, Na_2S_2 and Na_2S formation reactions suffer from sluggish kinetics and increased polarization.

Based on the stepwise reduction process, the overall reaction between sodium and sulfur in SSB can be written as:



RT SSB has an overall specific energy density of 1274 Wh kg^{-1} , corresponding to an increase of 60% compared to HT SSB. This is due to the final discharge product being Na_2S instead of Na_2S_3 (in HT SSBs).^[127, 128]

1.6.2 Technical difficulties inhibiting the development of room temperature sodium-sulfur batteries

Though RT SSB has many advantages, its drawbacks are similar to that of LSB, which hinder their development. Multiple challenges associated with this type of technology hinder its application. For example, the insulating nature of the sulfur and polysulfides restricts the utilization of full cell capacity. Polysulfide dissolution remains one of the main causes of capacity fading by shuttling. Dissolution of polysulfide also affects the cell's self-discharge phenomenon. Another major cause for poor cycling capacity is the volume expansion caused by discharged products. Moreover, the sluggish nature of Na results in low-capacity retention. The issues regarding dendrite formation, polysulfide migration, sluggish nature of Na, and volume changes are exacerbated in SSB due to the high reactivity and larger ion radius of Na compared to those of Li. All these demerits ultimately compromise cells' safety, stability, capacity, energy density, and coulombic efficiency.

1.6.2.1 Poor utilization of active material

As mentioned earlier, sulfur is the right choice for high energy and economic cathode due to its high theoretical capacity (1675 mAh g^{-1}) low cost, and environmental benignity. However, sulfur has a very low electrical conductivity of $5 \times 10^{-30} \text{ S cm}^{-1}$ at room temperature, which is unfavorable for battery performance.^[129, 130] Also the final discharge products such as Na_2S_2 and Na_2S have poor electrical conductivity.^[131] During cycling, the electron should reach the active material from the anode while discharging and vice versa to facilitate the conversion reaction.^[132] Thus, usually, a high amount of

electrically conductive matrix (ex: carbon) is mixed with sulfur to ensure electronic transport throughout the cathode. Overall, the conductive matrix and the binder reduce the amount of sulfur in the cathode which adversely affects the energy density of the cell.

1.6.2.2 Shuttling

The sulfur reduction contains multiple complicated steps involving both long chain and short chain polysulfides. Out of those, short-chain polysulfides Na_2S_x ($x \leq 2$) are insoluble in the electrolyte,^[133, 134] whereas long-chain polysulfides Na_2S_x ($x = 4$ to 8) are intermediate in polarity, and dissolve well in liquid electrolytes (LEs). This dissolution leads to the depletion of active material from the cathode, which results in poor capacity retention of the battery.^[135] Moreover, during charging, the long-chain polysulfides in the electrolyte migrate towards the sodium and are reduced on the surface, where electrons are readily available. Then the reduced short-chain polysulfides migrate back to the cathode and oxidize to high-order polysulfides. The current produced during this reaction does not contribute to charging the electrodes. This action is repeated numerous times until the active material is completely depleted. This phenomenon is called shuttling, which is detrimental to the cell's performance by inflicting low coulombic efficiency and a high self-discharge rate. Shuttling can be identified during charging, where the charging curve seemingly appears 'infinite' with the voltage plateau below the cut-off potential.^[132] Additionally, low-order polysulfides also deposit on the anode surface, leading to interfacial deterioration.^[136, 137]

1.6.2.3 Volume expansion

During discharge, the sulfur molecules transfer from S_8 to Na_2S , while during charge the opposite conversion reaction occurs. These structural and morphological changes also include intermediate polysulfides but due to identical density between various polysulfides, there is little to no volume change in the cathode. A huge volume change occurs when the final sodium sulfides are formed.^[138] The formation of Na_2S_x ($x = 1$ to 3) leads to a huge volume expansion, which can be severe and unfavorably affects the cathode morphology. The density difference between sulfur (1.96 g cm^{-3}) and Na_2S (1.86 g cm^{-3}) indicates that the volume change of the cathode will be 170 % at the end of the discharge.^[139] The colossal volume change in the cathode affects the mechanical strength and leads to capacity fade. Additionally, the expansion and contraction of the active material forces away from the carbon and binder matrix next to it. This creates a loss in contact between the primary active material and the secondary carbon particle, indicating an inefficient electronic conduction path. Lack of electrical conductivity in the cathode

1.6. Room temperature sodium-sulfur battery

might accelerate capacity fading. Hence, the volume change of the sulfur cathode in the sodium system is one of the biggest challenges, even more, severe than in the Li-S system. Thereby, it is essential to develop a cathode that can accommodate huge volume changes and contain the cathode materials together.^[124]

1.6.2.4 Sluggish kinetics

Even though long-chain polysulfides are soluble in most of the non-aqueous electrolytes Na_2S_x ($x = 4$ to 8) the short-chain and final sulfides Na_2S_x ($x = 1$ to 4) are insoluble in nature. The non-conductive and slow kinetics of Na_2S_2 and Na_2S cause capacity to fade, resulting in an incomplete reduction of Na_2S in the subsequent cycle.^[140] Moreover, the practical capacity of the cell is much lower than the theoretical capacity due to the insulating nature of the sulfur and the sluggish reactivity of the sodium with sulfur.^[137]

1.6.2.5 Challenges of metallic Na anode

Apart from the above-mentioned issues, one of the major hindrances in the development of RT SSB is the metallic sodium anode. Metallic sodium is electrically conductive and a strong reducing agent, which is ideal to be used as an anode material. Nevertheless, similar to LSBs, Na anodes develop dendrites, an unstable SEI layer, high reactivity towards electrolytes, volume expansion during cycling, sluggish kinetics, etc.^[141, 142] The major concern with metallic sodium is the needle-like or mossy dendrite formation during cycling. This dendrite formation is caused by an uneven deposit of Na atoms on the surface of the anode, leading to the rapid growth of a needle-like structure.^[143] Those needles can penetrate through the separator and contact the cathode, resulting in short-circuiting of the cell, thermal runaway, fire, or explosion. Additionally, an unstable SEI and repeated reaction with the electrolyte increase the impedance of the cell, resulting in cell failure.^[144]

1.6.3 Cathode, anode, and separator modifications

To tackle the above-mentioned drawbacks of RT SSBs, research has been carried out to develop potential methods to optimize the cell components. The battery components and their morphology, chemical composition, and physical interaction play a significant role in cell performance. Extensive research has been carried out starting from the cathode, separators, electrolyte design, and anode morphology. The proposed solutions for the technical challenges faced by RT SSB are:

- a) Carbon materials, oxides, and other conductive materials were coated onto the sulfur particle to increase the electronic conductivity and speed up the charging/discharging rate.
- b) Adding additives in the electrolyte solution to assist the film formation on the anode and to improve the electrolyte performance.
- c) Mechanical or chemically formed solid electrolyte interphase (SEI) layer on sodium anode to prevent dendrite formation.
- d) Modification of the separator by ion-selective methods or solid electrolytes to eliminate the polysulfide shuttle.

1.6.3.1 Cathode

In the cathode, the insulating nature of the sulfur reduces its electrical conductivity. Additionally, polysulfide shuttle and volume expansion lead to a major failure of the cell. Xin et al.^[128] developed a sulfur microporous carbon composite with a coaxial morphology containing a carbon nanotube core and a microporous carbon (MCP) sheath. The sulfur molecules penetrate the MCP and exist in form of metastable sulfur allotropes (S_{2-4}). This confinement strategy enhances the electrochemical reactivity of the sulfur with Na^+ . The nanometer-sized MCP (0.5 nm) restricts the formation of higher-order polysulfides, thereby eliminating polysulfide dissolution. The corresponding Na-S battery displayed a high specific energy density of 750 Wh kg^{-1} and a specific capacity of $>1000 \text{ mAh g}_s^{-1}$ for 200 cycles. Zhang et al.^[132] improved the sulfur reactivity and eliminated polysulfide shuttle by immobilizing polysulfide species on atomic cobalt (Co) clusters. These atomic Co molecules are supported by hollow carbon (HC) nanospheres, which encapsulate the sulfur molecules. The cell with sulfur@Co-HC cathode delivers 508 mAh g_s^{-1} even after 600 cycles. The Co could electrocatalytically convert Na_2S_4 into Na_2S rapidly, avoiding polysulfide dissolution and shuttling. Similarly, Zheng et al.^[145] used nano-copper (n-Cu) to anchor the sulfur by forming n-Cu polysulfide clusters. Due to the strong interaction between n-Cu and sulfur, the cell delivers a remarkable reversible capacity of 610 mAh g_s^{-1} with 100% coulombic efficiency. Using metal oxides in the cathode resolves multiple issues concerning volume expansion, polysulfide dissolution, and catalytic conversion to final sodium sulfides.^[146, 147, 148, 149]

Qiang et al.^[150] synthesized a hierarchical porous carbon doped with nitrogen and sulfur from low-cost materials. The high concentration of N and S successfully confines the sodium polysulfides in the nanopores via electrostatic interaction between the pore wall,

sodium-nitride, and sulfur. This interaction effectively inhibits the side reaction between polysulfides and carbonate electrolytes. The cell showed ultra-long cycling over 10000 cycles with coulombic efficiency >99.5% and 20% capacity decay. Carbon materials with high porosity and high surface area act as perfect host materials for the sulfur cathodes. Carbon nanotubes (CNTs) have excellent conductivity and flexibility. Combining CNTs with active material can be useful to fabricate a highly conductive binder-free flexible cathode. Yu et al.^[138] proposed a binder-free electrode using CNTs for Na/liquid phase catholyte to investigate the reaction mechanism in RT SSB. CNTs not only act as a high surface area current collector but also significantly contribute towards localizing the polysulfides and accommodating the volume expansion. Though the performance of the sulfur cathode is effectively improved by adding metal, metal oxides, and intermediate polysulfides, the weight ratio of the sulfur in the cathode has to be increased to achieve the desired energy density. One way of achieving high sulfur amount is by increasing the pore volume of the host material to lodge more sulfur.

Apart from the carbonaceous materials, sulfur can react with organic polymer to produce sulfur-polymer composite cathode. These sulfur-polymer composites eliminate the formation of long-chain polysulfides, resulting in the shuttle-free cycling of SSBs. Poly(acrylonitrile) is one of the polymers that can react with sulfur at high temperatures to form covalent bonds. A sulfurized poly(acrylonitrile) (SPAN) cathode was used by Wang et al.^[101] for RT SSBs. During the discharge process, the sulfur is reduced completely to Na₂S with a capacity exceeding 650 mAh g⁻¹ and coulombic efficiency maintained at 100%. Similarly, Hwang et al.^[151] synthesized one-dimensional SPAN fibers by electrospinning poly(acrylonitrile) solutions and later reacting it with sulfur. The fibers produced had a diameter of ~150 nm which improved the reaction kinetics of the cathode. At the end of the 500th cycle, the coulombic efficiency was >99.84%.

1.6.3.2 Anode

Thin metallic sodium foil is used in SSB as an anode material unlike in SIB where intercalation-based anodes are employed. Na possesses a high theoretical specific capacity of 1166 mAh g⁻¹ and low redox potential of -2.713 V (*vs.* SHE). Na metal in liquid electrolytes causes safety concerns such as the formation of dendrites, emerging from irregular nucleation of Na at the surface of the anode. This needle-like structure pierces the separator which leads to an internal short-circuit of the cell. Moreover, solvents in the electrolyte can react with the fresh Na surface, resulting in low coulombic

efficiency and the formation of Na dendrites. Various methods have been used to protect the Na surface from detrimental reaction with the electrolyte and prevent dendrite formation.

Seh et al.^[152] reported simple glyme (mono-, di-, tetra-) based electrolyte solvents with NaPF₆ formed an SEI layer comprised of inorganic compounds such as Na₂O and NaF, which are impermeable to the electrolyte solvents. The cell exhibited a coulombic efficiency of 99.9% for 300 cycles at 0.5 mA cm⁻². Subsequently, Zhao et al.^[153, 154] found an effective way to protect the Na anode surface by covering it with Al₂O₃ by atomic layer deposition (ALD) and molecular layer deposition (MLD). An ultrathin (up to 7 nm) Al₂O₃ layer suppressed the dendrite growth and mossy Na deposition on the anode surface. Both techniques showed an increased lifetime of the cell but MLD exhibits a stable polarization curve and longer cycling than ALD. Luo et al.^[155] prepared a stable Na anode by integrating it into the carbonized wood channels. This technique resulted in a mechanically stable high surface area anode. These Na-wood composite anodes showed low overpotential and stable cycling over 500 h at 1 mA cm⁻² in a carbonate electrolyte.

Similar to the composite lithium anode made of graphene oxide, Wang et al.^[156] introduced sodium-infused reduced graphene oxide (r-GO) as an anode for Na-based batteries. Anodes based on pure metallic Na are difficult to process due to the malleable nature of Na. Addition of a 4.5% percent r-GO composite increases the hardness and stability of the anode compared to pure Na metal. The plating/stripping in ether and carbonate-based electrolytes demonstrated extended cycle stability and less dendrite formation of the composite anode. Apart from protecting the Na metal surface, Na can also be stored as an alloyed material. Lee et al.^[157] stated that alloying of Na with Sn could enhance cycle stability. The anode nano-Na-Sn-C alloy displayed a reversible capacity of 550 mAh g⁻¹ over more than 120 h.

1.6.3.3 Separator

β-alumina can be used both as a separator and electrolyte, however, it operates only at 300 °C.^[158] On the other hand, RT-SSB with LE requires a separator that allows only positive ions through the pores. Separators are an indispensable part of metal-sulfur batteries (MSB) due to their role in polysulfide shuttle inhibition. Currently, room temperature SSBs often use separators made of polyethylene, polypropylene, and glass fiber. Besides the commercially available separators, Nafion or modified Nafion was also used to suppress the shuttle effect. The low binding energy between the glass fiber

1.6. Room temperature sodium-sulfur battery

separator and the polysulfides leads to the migration of polysulfides to the anode, resulting in the poor performance of the battery.^[159, 160]

Owing to its large pore size and thickness, a glass fiber separator can take up a huge volume of LE, which reduces the energy density, increases the dissolution of polysulfides and ultimately increases the risk of flammability. Additionally, the large pore size is ineffective in hampering Na dendrite penetration, resulting in short-circuit and cell failure. However, a glass fiber separator coated with Fe³⁺/poly(acrylamide) nanospheres (FPNs)-graphene physically blocked and chemically anchored the polysulfides as demonstrated by Li et al.^[161] Through vacuum filtration, the glass fiber separator was coated with FPNs and placed inside the cell facing the cathode side. The FPNs chelate with adsorbed polysulfides due to the polarity of Lewis acid-base, thereby hindering the polysulfide shuttle. Additionally, the graphene layer improves the mechanical fragility of FPNs and also acts as a physical barrier for the polysulfide shuttle. The FPNs containing Na-S cells showed a high discharge capacity (639 mAh g⁻¹ at 0.1 C) and excellent rate capability (228 mAh g⁻¹ at 2 C).

Similarly, polyolefins separators such as poly(ethylene) and poly(propylene) are widely used in several types of batteries due to their low cost, easy handling, low thickness, and good mechanical strength. It requires a low amount of electrolyte compared to the glass fiber separators. Polyolefin separator alone suffers from dendrite penetration, thus modification of a poly(propylene) separator results in improved cell stability and high discharge capacity. Zhou et al.^[162] modified the poly(propylene) separator by a “graft-filtering” strategy to graft a single-ion conducting polymer on one side and coat a functional low-dimensional material on the other side. The single ion-conducting polymer-coated side had a reduced static contact angle of 45.5° compared to the bare separator. This type of Janus separator performed better than the glass fiber separator and delivered a highly reversible capacity and longer cycle life than the bare poly(propylene) separator. A Nafion separator can transport cations selectively and also effectively confine polysulfides at the cathode when used in SSBs. Kaskel et al.^[143] experimented with a modified poly(propylene) separator coated with Nafion. The negatively charged sulfonic group in the Nafion coating repels the negatively charged polysulfides, thereby inhibiting the polysulfide's movement, leading to enhanced coulombic efficiency. Similarly, an Al₂O₃ modified Nafion delivered a discharge capacity of ~250 mAh g⁻¹ even after 100 cycles. The Al₂O₃ particles can bind to the polysulfides whereas the Nafion

membrane repels the polysulfides S_n^{2-} due to its SO_3^- groups.^[163] Together with different separator materials, the addition of an intermediate layer has proven to be beneficial for the battery. Yu et al.^[164] proposed that an interlayer made of carbon nanofoam can be added between the separator and the sulfur cathode that can efficiently confine the soluble polysulfides and prevent migration. In conclusion, the choice of the separator in RT SSBs is important in obtaining high Na^+ passage, preventing sodium polysulfides shuttle, and preventing electron movement across the separator.

1.6.4 Organic liquid electrolytes for RT SSB

Electrolytes are the main component of the battery systems. They act as a conduit between electrodes by ensuring smooth movements of ions which are essential for achieving high cycle efficiency, cycle life, and safety. The electrolyte should meet a particular set of conventional requirements:^[165]

- a) Inert towards battery components during cycling (e.g., cell package, current collectors, separator, binder, etc.).
- b) Wide electrochemical window: large separation between lowest and highest onset potential for electrolyte decomposition, contributing to increased cell potential.
- c) Electrolyte solvents should have a low vapor pressure to achieve high efficiency, and safety.
- d) Should allow facile transport of Na^+ but electrons to avoid self-discharge of the battery.
- e) Environmentally benign solvents and salts for safer batteries.
- f) Easily available, cost-effective, earthly abundant materials, facile synthesis, and scaling processes.
- g) Solid electrolyte interphase should form on both electrodes in a controlled way to ensure a stable, insulating, ionically conducting interface.

The overall purpose of the electrolyte is to transfer ions across the electrodes. However, in reality, electrode/electrolyte solid interphase affects ion motion, and subsequently, battery performance. The electrolytes used for RT SSBs can be divided into three segments, i.e., liquid, gel, and solid electrolytes. Though research for sodium battery electrolytes is still in its initial stages, the different compositions of electrolyte systems are derived from its analogous LIBs. Usually, an electrolyte contains single or binary conductive salts and one/more solvent mixtures. This section discusses the liquid and polymer electrolyte components and the effect of an interphase layer in detail.

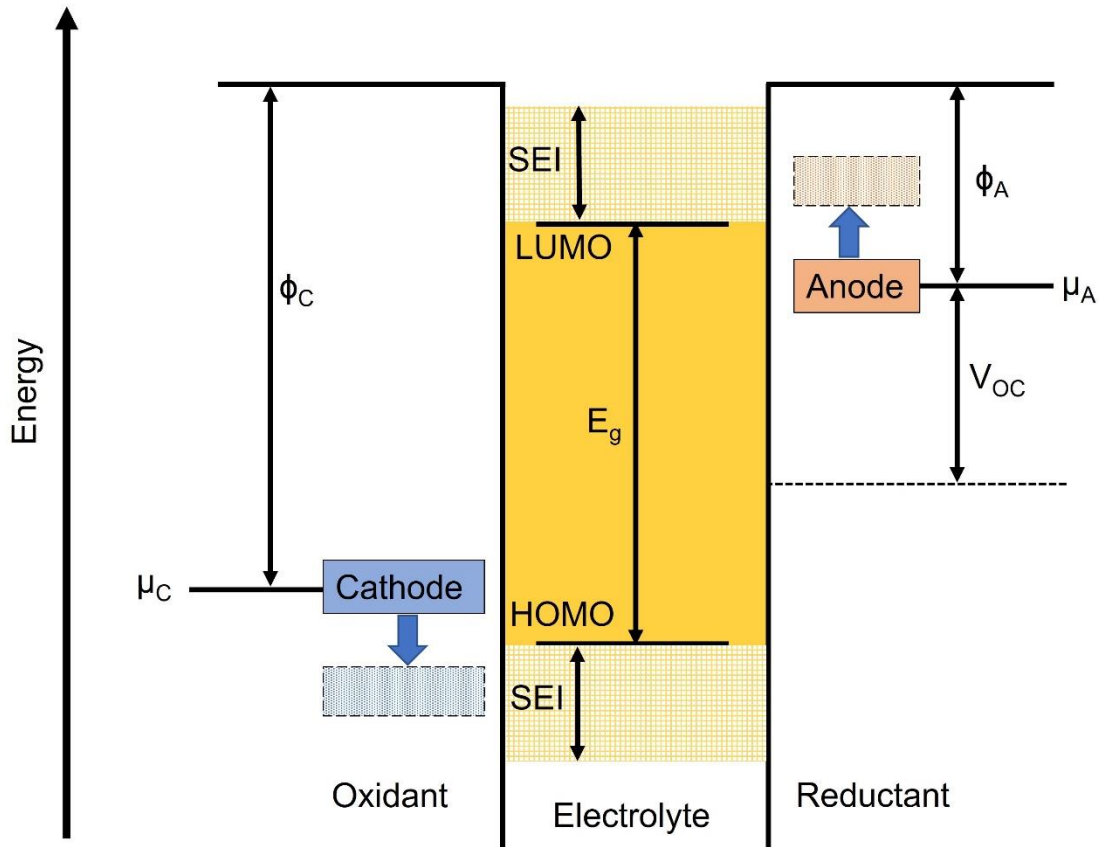


Figure 15. Graphic representation of open-circuit energy diagram of a battery with liquid electrolyte.^[64]

A thermodynamically stable battery with relative electron energies in the electrode and electrolyte is depicted in Figure 15. ϕ_A and ϕ_C represent the anode and cathode work functions, respectively. E_g is the thermodynamic stability “window” for the liquid electrolyte separated by HOMO (highest occupied molecular orbital) and LUMO (lowest occupied molecular orbital). μ_A and μ_C are the anodes and cathode electrochemical potentials, respectively. μ_A should be less than the LUMO to avoid reduction of the electrolyte unless a protected SEI layer is formed to prevent electron transfer from the anode to the electrolyte LUMO. Similarly, μ_C should be above the HOMO to prevent oxidation of the electrolyte unless the SEI layer is formed on the cathode to avoid the transfer of the electron from the electrolyte HOMO to the cathode. Hence, to maintain thermodynamic stability, both electrode potentials μ_A and μ_C should remain within the electrolyte stability “window”. This constricts the open circuit potential (V_{OC}) of the cell to:

$$eV_{OC} = \mu_A - \mu_C \leq E_g \quad \text{Equation 2}$$

where e is the electron charge magnitude. To obtain a large V_{OC} with good kinetic stability, the SEI layer should be formed at the electrolyte/electrode interface where $eV_{OC} - E_g$ is not too large. The capacity of the battery decreases with the rate of charge/discharge, i.e., electronic current flow in the external circuit should match with the ionic current flow inside the battery. However, the rate of ion transfer at the interface and the current density of the electrode and electrolyte is way smaller than the electronic current density. At high current densities, ionic movement within the electrode and at the interface is too slow to attain equilibrium, resulting in a decrease in discharge capacity.

A non-aqueous solvent can increase the E_g of the electrolytes. For example, the electrolyte stability window of the LIB electrolyte needs to be determined to design high-capacity electrodes with their chemical potentials matching HOMO and LUMO. Elemental Li^0 can be used as an anode unless an SEI layer is formed at the interface because μ_A lies above the LUMO of the commercial non-aqueous electrolytes. During repeated cycles, the SEI layer might break, which results in the formation of dendrites that can increase the risk of short-circuiting the cell.

1.6.4.1 Sodium salts

Electrolyte salts are responsible for the overall performance of the battery. Sodium salts should meet the following criteria to be utilized as an electrolyte component in batteries.

- a) Should be able to completely dissociate in the presence of the electrolyte solvents to provide high ion mobility.
- b) High ion diffusivity in the electrolyte solvent with less activation energy.
- c) Wide electrochemical potential window, which is enough to resist oxidation and reduction of the electrolyte.
- d) Chemically stable towards electrodes, separators, and current collectors.
- e) Environmentally benign, facile synthesis, and low cost.

Unfortunately, the above-mentioned properties (a, and c) already exclude a large portion of the available salt candidates. The counter-anion for Na^+ alters the electrochemical stability and ionic conductivity of the salt. Anions control the upper voltage limit during redox reactions due to the weak oxidation resistance of the anions in the electrolyte. Additionally, the strength of ion-pairing in the electrolyte solvent affects the ionic conductivity of the electrolyte.

Ion movement in the electrolyte is majorly affected by the choice of solvents. High viscosity solvents inhibit the faster ion movement, as a rule of thumb, viscosity is

1.6. Room temperature sodium-sulfur battery

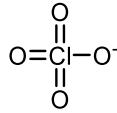
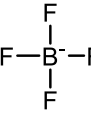
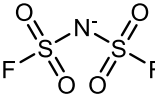
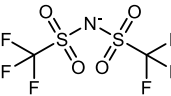
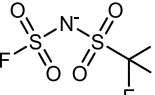
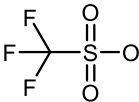
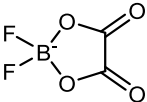
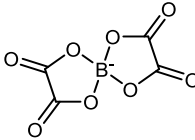
inversely proportional to the ionic conductivity. The ionic conductivity of the electrolyte is the sum of the number of charge carriers (n_i), mobility (μ_i), and charge (z_i). However, the amount of charge carried by the particular ion (cation and anion) is also of interest. The transference number (t_{Na}), which calculates the number of charges carried by the Na^+ cation, is given as follows:

$$t_{\text{Na}} = \frac{\mu_{\text{Na}}}{\sum \mu_i} \quad \text{Equation 3}$$

The solvation energy of the ions determines the transference number that can directly affect the polarization of the electrodes. Anions with weaker solvation shells affect ion mobility in an undesirable means. Cations have a more stable solvation shell than anions, resulting in a slow movement of the cations. In an ideal case, t_{Na} should be equal to one to achieve a high transference number. Sodium salts have weak solvated shells compared to their lithium counterparts. A high C-rate operation of the battery requires fast ion transport across the electrodes and reduced polarization. Both lithium and sodium cations experience similar solvent coordination in the solution. However, a reduced charge/radius ratio of Na^+ results in reduced ion-pairing by $\sim 15 - 20\%$ than Li^+ cations.^[19, 32]

The addition of an electron-withdrawing ligand in the center atom of the anion reduces the HOMO energy levels, resulting in the increased oxidative stability of the salt. This electron-withdrawing group delocalizes the negative charges around the anion, reducing anion-cation interaction, thereby forming weakly coordinating anions (WCAs). The most commonly used salts in RT-SSBs are listed in Table 3. Sodium perchlorate (NaClO_4) is often used, followed by sodium hexafluorophosphate (NaPF_6), sodium trifluoromethanesulfonate (NaOTf), sodium bis(trifluoromethanesulfonyl)imide (NaTFSI), and sodium bis(fluorosulfonyl)imide (NaFSI). Other sparsely used salts are sodium tetrafluoroborate (NaBF_4), sodium bis(oxalate)-borate (NaBOB), and sodium-difluoro(oxalato)borate (NaDFOB). Out of these, ClO_4^- , a strong oxidizing agent, which can cause fire or explosion, and is extremely hygroscopic (reported water content of > 40 ppm even after vacuum drying it overnight); OTf^- and BF_4^- have a lower ionic conductivity due to strong anion-cation interactions; PF_6^- , though it is the popular choice of electrolyte in LIBs, is sensitive to moisture and produces HF, PF_5 , and POF_3 ; TFSI^- and FSI^- salts corrode the aluminum current collector.

Table 3. Basic properties of sodium salts (reproduced with permission Ref. [165]).

Salt	Chemical structure	M _w (g mol ⁻¹)	T _m (°C)	Anodic stability (V vs. Na/Na ⁺)	Refs.
NaClO ₄		122.4	468	4.7	[166, 167]
NaPF ₆		167.9	300 (dec.)	5	[166] [168]
NaBF ₄		109.8	384	5	[167]
NaFSI		203.3	118	3.4 (Al)	[166]
NaTFSI		303.1	257	3.4 (Al)	[166, 168]
NaFTFSI		241.1	160	3.4 (Al)	[166]
NaOTf		172.1	248	-	[166]
NaDFOB		159.8	-	5.51	[169]
NaBOB		209.8	345	-	[170]

Despite adverse aluminum corrosion, NaFSI and NaTFSI are gaining attention due to their higher conductivity compared to NaOTf, non-toxicity, and higher thermal stability compared to NaPF₆ and NaBF₄. Bhide et al.^[171] compared the ionic conductivities of

1.6. Room temperature sodium-sulfur battery

different Na salts using the similar solvent matrix, EC:DMC, by varying the salt concentration. The ionic conductivity of the electrolyte increased with salt concentration and reached a threshold at certain concentrations. The maximum ionic conductivity values obtained were 6.8 mS cm^{-1} (0.6 M NaPF₆), 5.0 mS cm^{-1} (1 M NaClO₄), and 3.7 mS cm^{-1} (0.8 M NaOTf). LiBOB (lithium bis(oxalate) borate salt delivered promising results for lithium-ion batteries due to its excellent thermal stability at 70 °C.^[171, 172, 173] Hence, NaBOB (sodium bis(oxalate) borate) salt, which has a similar structure, might possess similar properties to that of LiBOB. The as-synthesized NaBOB and NaFBOB exhibited enhanced ionic conductivity and good thermal and chemical stability.^[169, 170]

1.6.4.2 Electrolyte solvents

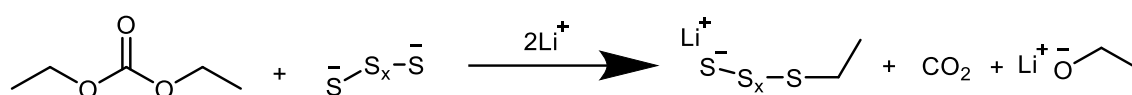
Non-aqueous liquid electrolyte solvents are chosen from the following groups: carbonate esters, ethers, and ionic liquids. Since strongly reducing positive electrodes and oxidizing negative electrodes require solvents with a high electrochemical stability window, aprotic solvents or non-aqueous solvents are suitable for RT SSBs. The solvents should be non-toxic for processing, less expensive, stable against redox reactions, dissolve Na salts, and, be compatible with Na anode.

Commonly, ester and ether-based solvents are used for sodium-based batteries. In carbonate solvents, two diverse types of esters are employed: cyclic (ethylene carbonate (EC), propylene carbonate (PC)) and linear carbonates (dimethyl carbonate (DMC), ethyl methyl carbonate (EMC)). Diglyme, triglyme, and DME are used as solvents in an ether-based electrolyte. The physical-chemical properties of the carbonate and ether-based solvents are given in Table 4. EC is the most used carbonate solvent due to its high dielectric constant, resulting in a high solubility of the salts. Owing to strong dipole-dipole intermolecular forces, EC can effectively interact with sodium salts. Even though EC is a good solvent, due to its high melting point of 36 °C, one or more solvents mixtures are used in the electrolyte. PC is a practical choice for a solvent due to its high dielectric constant (κ , 65) which increases the ionic conductivity and electrochemical stability window. Alternatively, DMC and DEC can be used as co-solvent to reduce the viscosity of the solution. The first Na-S battery used NaClO₄ with EC-DMC as an electrolyte solution.^[101] The battery exhibited a discharge capacity of 650 mAh g^{-1} with a coulombic efficiency of 100%. 1 M of NaClO₄ in EC-PC with small sulfur molecules trapped in microporous carbon delivered a discharge capacity of 1000 mAh g^{-1} over 200 cycles. This entrapment of sulfur allotropes facilitates the complete conversion to Na₂S, thereby

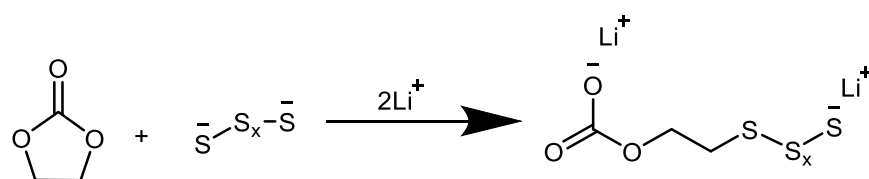
avoiding polysulfide reactions towards carbonate electrolytes.^[128] Untrapped or unmodified sulfur cathode produces polysulfides, which eventually react with carbonate solvents. Highly nucleophilic sulfide anions (with Na^+ or Li^+) react with common solvents such as DEC, EC, etc., to produce methylated thiols and thioether, respectively.^[85] This side reaction can be alleviated by cathode architecture modification such as confining sulfur in mesoporous carbon, the use of composite sulfur cathodes, and encapsulation of sulfur.

Polysulfide reaction with carbonates:

DEC:



EC:



Owing to the high reactivity of carbonates with sodium metal results in the formation of unstable SEI which adversely affects the coulombic efficiency, cycle life, and dendrite formation. Therefore, alternate ether-based solvents compatible with sodium metal have been investigated. For example, di-, tri-, tetra-glyme, 1,2-dimethoxyethane, and dioxolane solvents are widely used in SSBs due to their resistance against reduction. However, ether-based electrolytes result in low capacity compared to carbonate solvents. Even though the final discharge product delivers a theoretical capacity of 1675 mAh g^{-1} , a discharge capacity of only 550 mAh g^{-1} was observed, implying the incomplete reaction of sulfur with Na, possibly Na_2S_x ($3 \leq x \leq 5$). Additionally, the higher solubility of long-chain polysulfides in ether-based electrolytes leads to the shuttling phenomenon, thereby reducing the capacity, which is well described in lithium-sulfur batteries.^[174, 175]

During charging, the dissolved long-chain polysulfides are reduced at the Na anode due to the ready availability of the electrons. Later, short chain polysulfides migrate back to the sulfur electrode and then become oxidized again. The overall electron flow involved

1.6. Room temperature sodium-sulfur battery

in these side reactions does not contribute to the charging current, resulting in overcharging, low coulombic efficiency, and rapid capacity decay.^[176, 177]

Table 4: Physicochemical properties of commonly used solvents in Na-based batteries.^[58, 60]

Solvent	Dielectric constant at 25 °C	Viscosity at 25 °C (cP)	Heat of vaporization (kJ mol ⁻¹)	HOMO (eV)	LUMO (eV)
Ethylene carbonate (EC)	89.78	1.90 (40 °C)	51.68	-0.2585	-0.0177
Propylene carbonate (PC)	64.92	2.53	45.73	-0.2547	-0.0149
Dimethyl carbonate (DMC)	3.107	0.59	36.53 - 38.56	-0.2488	-0.0091
Ethyl methyl carbonate (EMC)	2.958	0.65	34.63	-0.2457	-0.0062
Diethyl carbonate (DEC)	2.805	0.75	41.96 - 44.76	-0.2426	-0.0036
Diethyleneglycol dimethylether (Diglyme)	7.4	1.06	-	-	-
Triethylene glycol dimethyl ether (Triglyme)	7.53	3.39	-	-	-
Tetraethylene glycol dimethyl ether (Tetraglyme)	7.8	3.25	-	-	-
1,3-Dioxolane (DOL)	7.10	0.59			
1,2-Dimethoxyethane (DME)	7.2	0.46	-	-	-

The polysulfide shuttle can be suppressed by modification of separators, and confinement of sulfur in the cathode.^[143] Ryu et al. employed TEGDME with NaOTf in a sulfur-carbon cathode together with a Na anode. The cell delivered an initial capacity of 538 mAh g⁻¹, which decreased rapidly to 240 mAh g⁻¹ after 10 cycles.^[176] Apart from TEGDME, DME/DOL electrolytes were also reported for RT SSBs.^[178]

Ionic liquid (IL) electrolytes are gaining increased attention due to their non-flammability, low vapor pressure, and thermal and electrochemical stability.^[179] Despite their high thermochemical stability, ILs show limited conductivity and discharge capacity compared to organic electrolytes. Depending on the type of ILs, the cation can be either Na or Li. Owing to several advantages, IL electrolytes have been used in LSBs.^[180] However, until now, only a few reports are available on IL electrolytes for RT SSBs. Wei et al. proposed a novel method to modify the silica nanoparticle with ionic liquid (SiO₂-IL-ClO₄) in a carbonate electrolyte (NaClO₄ in EC/PC). An IL in silica particles helps to form a robust, stable SEI layer thereby preventing side reactions of the Na metal with liquid electrolytes.^[181] Moreover, the anchoring of an anion (ClO₄⁻) by SiO₂ can effectively suppress the electric field by the tethered anion effect.^[182, 183, 184] Polysulfide dissolution in IL electrolytes depends on their lewis basicity. For example, IL-containing anions with high donor numbers (donicity) such as triflate (OTf⁻) exhibit stronger interaction with Li⁺, resulting in high solubility of Li₂S_n compared to typical ether-based electrolytes. Polysulfide dissolution reduces with decreasing donicity of the anion, (OTf⁻) > (TFSI⁻) > (BETA⁻) > (FSI⁻).^[185, 186] Polysulfide solubility is reduced in the IL containing larger cations.^[180] Nonetheless, the poor ionic conductivity of the ILs prevents their wider use.^[187, 188] To improve the ionic conductivity of the ILs, cations are solvated by solvents (triglyme, tetraglyme).^[189, 190] By controlling the free solvent in the electrolyte, polysulfide dissolution can be eliminated.^[191] The ether solvation of Li⁺ cation and weakly coordinating anion results in a similar diffusion coefficient of solvent and Li⁺.^[192] A similar technique can be applied to RT SSBs to realize high capacity, reduced polysulfide formation, and high coulombic efficiency.

1.6.5 Polymer-based electrolytes

Conventional organic non-aqueous LEs (ethers and carbonates) pose serious safety issues such as fire, explosion, and electrolyte leakage, which are impeding the development of batteries.^[193] During the thermal runaway of the battery, the temperature inside the cell is raised to higher levels within milliseconds; this converts the electrolyte solvents to a

1.6. Room temperature sodium-sulfur battery

gaseous state, which eventually causes fire and explosion. [194, 195] These issues are prominent for post-LIBs such as Li-metal, Na-metal, and alkali MSBs. [196] Substituting LEs with polymer electrolytes might enhance the safety of Li and Na-based batteries. Polymer electrolytes can be divided into three main categories, such as a) solid polymer electrolytes (SPEs), [197] b) gel (GPEs) [198], and plasticized polymer electrolytes (PPEs), and c) composite solid polymer electrolytes (CSPEs). [199, 200, 201] SPEs consist of a polymer as a solvent matrix wherein the conductive salts are dissolved. SPEs contain no flammable solvents in the polymer matrix, resulting in a safe operation of the battery even at high rates. GPE contains >50 wt.% of liquid plasticizers whereas PPEs contain less than 50 wt.% of plasticizers. GPEs are inherently flexible and have high ionic conductivity like liquid electrolytes and maintain good mechanical stability such as solid electrolytes. CSPE comprise an inorganic filler or ceramics incorporated into SPEs to increase the ionic conductivity of the electrolytes.

Figure 16 shows the relative performance of various types of electrolytes. Electrolyte leakage, ionic conductivity, and dendrite suppression are the important electrolyte parameters to meet the requirement for commercial applications. Another class of solid-state electrolytes (SSEs) is based on a wide range of inorganic ceramic, amorphous glasses, and glass-ceramic electrolytes. These SSEs are most appropriate for rigid battery applications where high elastic modulus, strong chemical/thermal resistance, and safety are vital. [202, 203, 204, 205] Despite their high safety standards, SSEs suffer from low ionic conductivity, narrow electrochemical windows (sulfide electrolytes), and poor interfacial contact with the electrodes. On the other hand, SPEs can form a good interfacial contact with the electrodes, thereby reducing the interfacial resistance. SPEs can also be suitable for flexible thin-film batteries where complex geometries are required. Compared to inorganic electrolytes, SPEs possess several advantages such as a facile synthesis process, shortened processing time, and low costs. [206, 207] However, the ionic conductivity of SPEs is lower than that of the SSEs. By combining the SPEs and SSEs, good thermal/electrochemical properties and good mechanical strength of the polymer-ceramic electrolytes can be achieved. [208, 209]

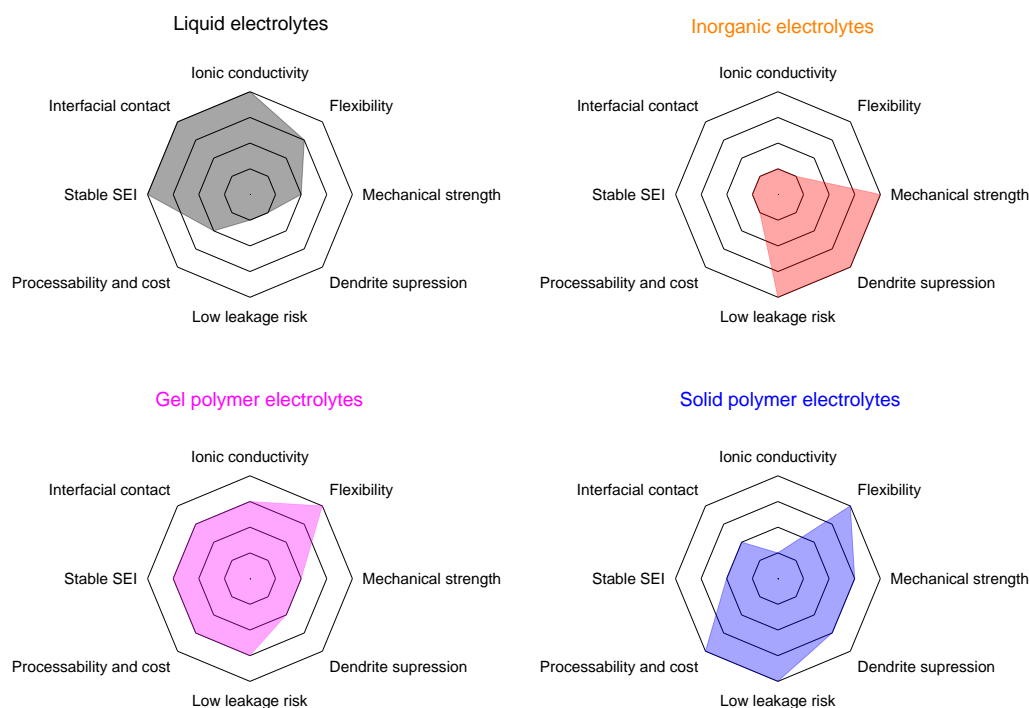


Figure 16. Comparative performance of various types of electrolytes (based on Ref. ^[210]).

Ion movement in inorganic solid electrolytes occurs due to point defects that facilitate ion conduction.^[211] Therefore, the ionic conductivity of the SSEs strongly depends on the vacancies, available hopping sites, and the activation barrier for hopping.^[212, 213, 214] Among all SPEs, polyethylene oxide (PEO) is the most popular host to be used as a polymer matrix. The transport mechanism of Li^+ inside the PEO matrix was first proposed by MacGlashan et al.^[215] The ion conductive mechanism in PEO polymer is shown in Figure 17. The dissociated cations from the conductive salt coordinate with the “electron-donor” group in the PEO chain. During the application of electric field, the cations tend to hop from one coordinating site to another. The ion hopping is enabled due to the polymer segmental motion or an ion-cluster supporting function where the temporary ion-pairing occurs before being solvated by the electron-donating groups.^[216]

At low salt concentrations, the polymer segmental motion governs the ion motion whereas, at high salt concentrations, the ions could self-diffuse in the polymer matrix due to the restricted polymer segmental motion. It is believed that ion conductivity in the polymer matrix occurs in the amorphous region. Therefore, the ion conductivity of the electrolyte depends on the ratio of the crystalline phase to the amorphous phase. PEO possesses high crystallinity phases below 65 °C, thus at room temperature, the ionic

1.6. Room temperature sodium-sulfur battery

conductivity ranges between 10^{-9} to 10^{-6} S cm $^{-1}$. By increasing the temperature to 80 °C, the ionic conductivity of the electrolyte can be increased substantially (10^{-4} to 10^{-3} S cm $^{-1}$).

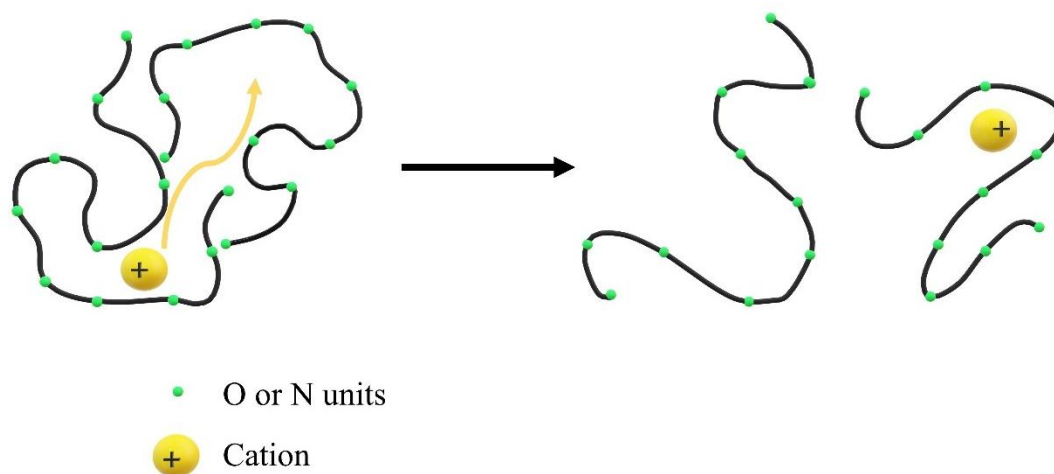


Figure 17. Ion conduction mechanism in PEO-based SPEs.

Anions such as FSI $^{-}$, and TFSI $^{-}$ interact with PEO chains, thereby reducing crystallinity and increasing Na $^{+}$ movement.^[217] As highlighted earlier, SPEs suffer from poor ionic conductivity at room temperatures (Figure 18). Consequently, inorganic fillers (inactive) such as TiO $_2$, SiO $_2$, and BaTiO $_3$ can be added to improve the ionic conductivity of the polymer matrix (CSPEs).^[49, 218, 219, 220, 221, 222] These ceramic nanoparticles interact well with oxygens in the polymer chain and the anions of the conductive salt through the oxygen vacancies on the ceramic particle surface. The chemical interaction with the filler prevents crystallization of the polymer and also the interaction with the salt leads to immobilization of the anions and release of free Na $^{+}$ ions. Apart from the inactive fillers, inorganic active fillers can be incorporated into SPEs to achieve ceramic-polymer composite electrolytes. This combination could ultimately provide good mechanical properties, increased ionic conductivity, and excellent thermal stability compared to SPEs. For example, the PEO-NASICON (Na Super Ion Conductor) composite electrolyte was able to withstand 150 °C with high flexibility.^[208] The ion motion in ceramic-polymer composite occurs not only due to the reduction in crystallinity of the polymer but also due to the ion movement within the active ceramic particle and at the polymer-ceramic interface. The room temperature ionic conductivity within the active ceramic particles and at the polymer-ceramic interface could reach up to $\sim 10^{-3}$ to 10^{-4} S cm $^{-1}$ and 10^{-4} S cm $^{-1}$, respectively. The ionic conductivity of the polymer-ceramic composite can

be increased by increasing the ceramic loading in the polymer host. However, due to the agglomeration of the ceramic particles, the conductivity decreases after a specific loading of ceramic fillers.

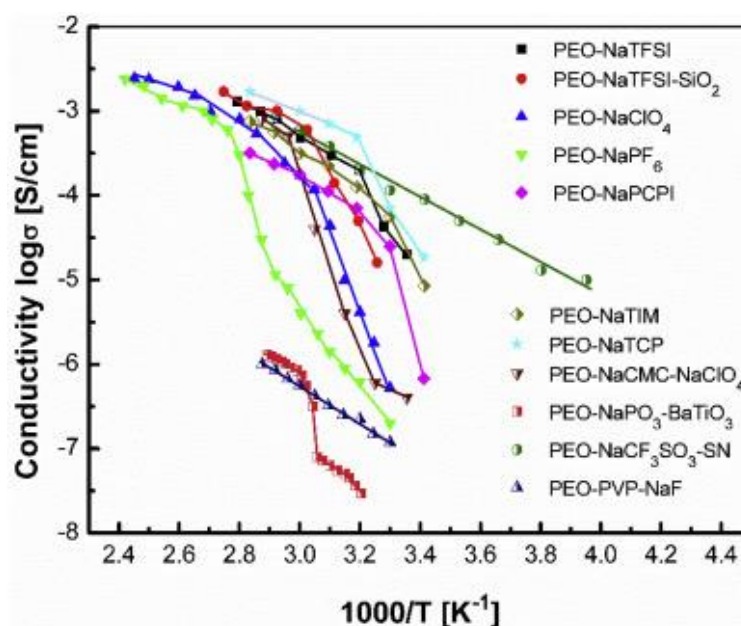


Figure 18. Ionic conductivity of SPEs based on PEO and various Na salts (reproduced with permission Ref. [52]).

1.6.6 Solid electrolyte interface on sodium metal anodes

An SEI layer forms when the electrolyte comes in contact with an alkali metal. The thickness of the SEI ranges from 15-25 Å. This SEI layer consists of insoluble products which act as a solid electrolyte by preventing electron flow.^[223] Interface reactions in alkali metal anodes have a huge impact on cell chemistry and performance. The reaction of the electrolyte with highly reactive metal anodes results in the formation of the interphase layer, which prevents the electrolyte from further decomposition. However, during cycling, the interphase layer (SEI) undergoes severe volume change, stress, and pulverization of the materials. This ultimately leads to the breakage of the layer, which again facilitates the SEI formation in subsequent cycling. On the other hand, the formation of the thick SEI layer occurs by continuous decomposition, resulting in the blocking of Na ions, thereby promoting dendrite growth. The dendrite formation on the anode seriously challenges the safety of the cell. As shown in Figure 19, a highly reactive sodium metal forms an unstable SEI layer due to the formation of a thick SEI layer, dead Na, gas evolution, etc.^[224, 225]

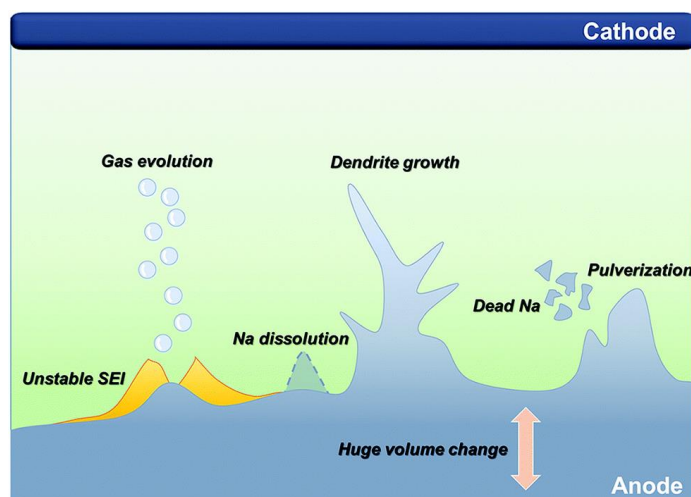


Figure 19. Graphical representation of key challenges in a sodium metal anode for sodium metal batteries (reproduced with permission from Ref. ^[226], open access).

Compared to sodium, lithium forms relatively more stable organometallic compounds in the interphase, which act as an anionic polymerization initiator.^[227] Therefore, the dissolution of the SEI in Na electrolytes is much higher than for Li electrolytes. Even under OCV, the Na cell containing NaPF₆ in EC:DMC showed an increase in impedance of the cell compared to LiPF₆-based electrolyte.^[228] This indicates that the Na metal continuously consumes the electrolyte, eventually resulting in unstable SEI layer formation. There are several methods proven to alleviate unstable SEI formation on Na anodes. The dendrite formation on Na metal is not identical to that of Li dendrite growth. Na metal nucleation thermodynamics and kinetics are different since the binding of Na with inorganic, metallic, and carbon structures are different from that of Li. Electrolyte additives are added to suppress dendrite growth and to form a stable SEI layer. The commonly added additives for Na metal-based batteries are fluoroethylene carbonate (FEC), vinylene carbonate (VC), and ethylene sulfide (ES). FEC and PC electrolytes are advantageous for improving coulombic efficiency but ES and VC are not as efficient.^[229, 230] For Na metal-based batteries, FEC additive plays an important role in the formation of a stable SEI layer. FEC readily accepts electrons from the Na anode and forms an interlayer, which reduces the interfacial resistance.^[231] Rodriguez et al. demonstrated the effect of FEC on Na metal during cycling by *in situ* optical imaging. The FEC-containing cell showed an increase in cycling efficiency and performance by forming a NaF-rich SEI layer. This SEI layer suppresses the reaction of organic and salt anion reduction products.^[232] Figure 20 shows the HOMO and LUMO energy diagram of a Na cell with conventional carbonate solvents, FEC, and DME.

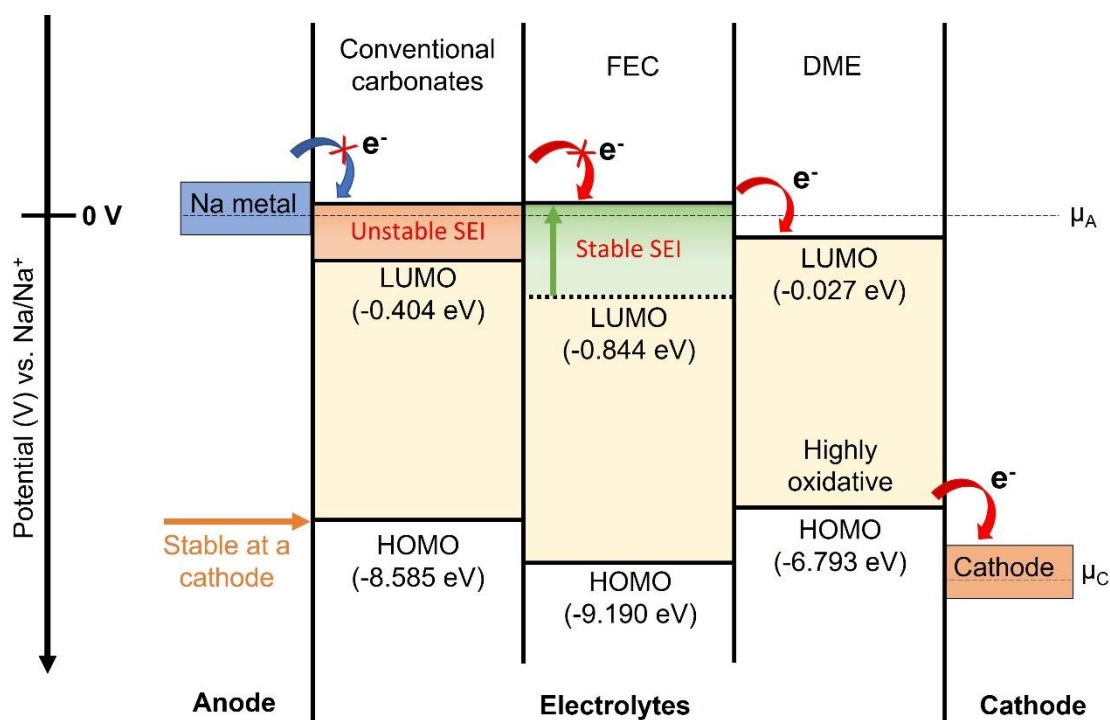


Figure 20. HOMO-LUMO energy-level diagram of a sodium anode, a sodium-containing cathode, and conventional carbonates, FEC, and DME-containing electrolytes (reproduced with permission Ref. ^[233]).

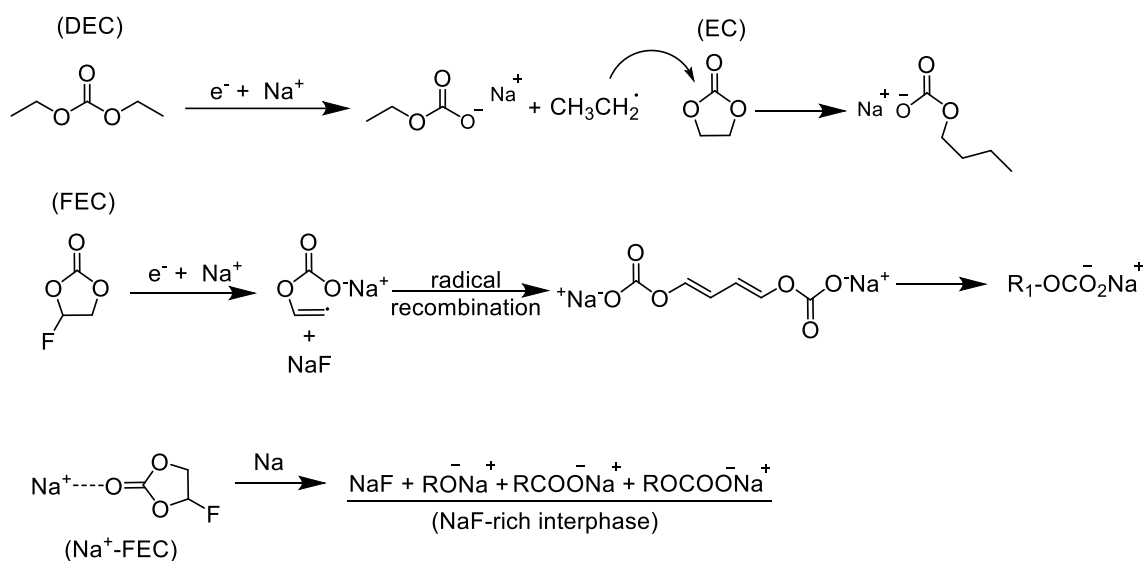
Conventional carbonate solvents form unstable interlayers with less ionic conductivity, resulting in the irreversible cycling of Na anodes. On the other hand, DME possesses a high HOMO level, which can be readily oxidized with high voltage cathodes. Among these, FEC has a low LUMO, thus the electrons accumulated in the Na anode are consumed by FEC during initial Na plating, thereby forming an interlayer by reductive decomposition of FEC. This interlayer prevents further electron transfer and decomposition of the electrolyte. Generally, fluorine-containing molecules lower the HOMO energy level, therefore, FEC-containing electrolytes are stable against oxidation at the cathode during cycling.^[233]

Lee et al.^[234] demonstrated highly stable SIBs with a conventional carbonate electrolyte containing 5 wt.% FEC as an additive. DEC, one of the carbonate solvents, reacts with Na metal to form radicals and sodium alkyl carbonates. When FEC is present in the electrolyte, it can form a stable interlayer due to its low LUMO. Similarly, FEC reduction occurs due to the catalytic effects of Na metal that formed during plating, which leads to the formation of NaF, R₁-OCO₂Na, and Na₂CO₃.^[233] Another possible FEC-based electrolyte reduction mechanism was proposed by Lu et al. with the help of *ab initio*

1.6. Room temperature sodium-sulfur battery

molecular dynamics simulation. Na⁺-FEC could be reduced by Na metal easily due to their low LUMO energy level than pure FEC. The simulation revealed that pure FEC heterocycle is broken at 84 fs and the C-F bond breaks at 117 fs. Contrarily, breakage of the C-F bond occurs at 80 fs for Na⁺-FEC, implying the rapid formation of the interlayer.^[235]

The proposed decomposition reaction of carbonates with Na metal:^[233, 234]



2 Background on the electrochemical terms used in this study

2.1 Charging and discharging

The charging process is applied only to the secondary cells. During charging, the ions are oxidized on the positive side and reduced on the negative side. The charge voltage is higher than the discharge voltage. During discharge, the electrons are released from the anode where oxidation occurs. This electron flow to the cathode side where the ions are reduced.

2.2 Overpotential

In equilibrium conditions, the current in both anodic and cathodic directions is the same. If the electrode area is considered, these are called exchange current densities (j_0 , A cm⁻²). While discharging, the current flows, thereby disrupting the equilibrium conditions. A shift in a single half-cell is considered to be an overpotential, η . The overpotential of the cell can arise from different origins. The speed of the charge transferring between electrode/electrolyte interphase depends on the electrode material, electrolyte condition, and the reacting substance. This phenomenon limits the charge transfer, which gives rise to the charge transfer overpotential. The application of the high current densities (j) at the electrodes results in the depletion of the reaction substances. This causes concentration polarization where the reaction kinetics can only be measured by the diffusion process through this zone, called the Nernst layer. Other than the above-mentioned overpotentials, adsorption and desorption processes of the electrode govern the reaction kinetics, this is known as reaction overpotential. Metal deposition on the negative side during charging of the battery leads to crystallization overpotential.^[236, 237]

2.3 Voltammetric techniques

Linear sweep voltammetry (LSV) and cyclic voltammetry (CV)

In LSV, the potential is scanned from one point to another point either in a forward or reverse direction. Whereas a CV includes scanning between two fixed potentials and subsequent current observation by the redox reactions. Figure 21a, b shows the waveform and its resultant current-potential curve (voltammogram) for LSV and CV.

For a reversible system, a CV works based on the principles of the Nernst equation.^[238]

$$E = E^0 - \frac{RT}{nF} \ln \frac{(\text{Red})}{(\text{Ox})} \quad \text{Equation 4}$$

2. Background on the electrochemical terms used in this study

For a simple reversible redox process, the application of a scan rate (v) results in the redox reactions at the electrode/electrolyte interface, which can be observed by measuring the I vs. E curve (Figure 21). The initial cathodic scan starts from OCV where only capacitive current flows (non-faradic current). This is due to the higher initial potential compared to the actual reduction potential. As the reduction begins, the reaction species are consumed at the electrode surface and form a diffusion layer made of reduced species. Therefore, the concentration gradient forms between the electrode surface and the bulk solution which leads to diffusion. This diffusion flux of ions generates a cathodic current that is proportional to the concentration gradient. As the potential sweep progresses, all of the surface species are consumed, and the flux attains a peak. Further scanning results in an increase in diffusion layer thickness which slows down the mass transport, resulting in a decrease in the current. During oxidation, a similar peak current response is observed in an opposite direction.^[239]

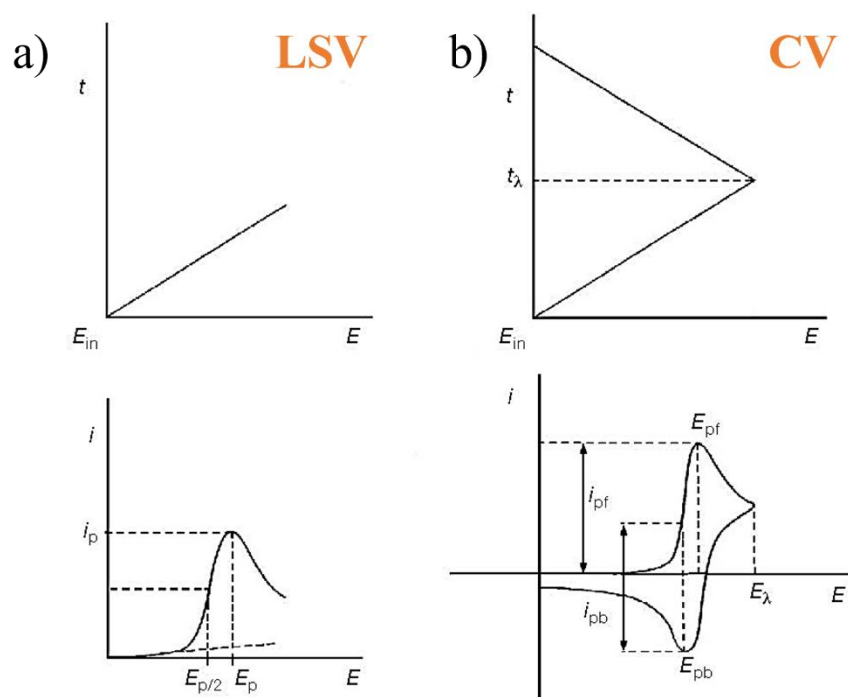


Figure 21. Potential waveforms and corresponding voltammograms for a) LSV; and b) CV, respectively (reproduced with permission Ref. ^[240]).

The scan rate of the potential in the experiment governs the electrochemical reaction at the electrodes. When the scan rate is faster, the thickness of the diffusion layer decreases, resulting in higher currents. For an electrochemically reversible system, the current (i) is proportional to the square root of the scan rate (\sqrt{v}). The peak current (i_p) can be described by the Randles-Sevcik equation:

$$i_p = 268600 n^{\frac{3}{2}} A \sqrt{D} C \sqrt{v} \quad \text{Equation 5}$$

Where n is the number of electrons involved in the reaction, C (mol cm^{-3}) is the bulk concentration of the active species, v (V s^{-1}) is the scan rate, and D ($\text{cm}^2 \text{sec}^{-1}$) is the diffusion coefficient of the oxidized species. For a reversible electron transfer reaction, the redox species must be diffusing freely (indicated by the Randles-Sevcik equation) thus the i_p vs. \sqrt{v} is linear. Whereas linear i_p vs. v indicates that the redox reaction is also controlled by the adsorption process. Based on the values from slopes, equation 5 is used for calculating the diffusion coefficient of the redox species. The values from the double logarithmic plots of i_p vs. v provide an idea about diffusion-controlled (slow semi-infinite-diffusion controlled faradaic process, slope - 0.5) or surface adsorbed reactions (fast near-surface activities, slope - 1) in the cathode.^[241, 242, 243, 244, 245]

2.4 Ionic conductivity and transference number

The ionic conductivity of the electrolyte can be calculated from the blocking electrode configuration. The bulk resistance of the electrolyte can be obtained from the impedance curve. The ionic conductivity can be calculated from the following equation:^[246]

$$\sigma = \frac{l}{R_b \cdot A} \quad \text{Equation 6}$$

Where σ is the ionic conductivity (S cm^{-1}), R_b is the bulk resistance (Ω), l is the thickness of the electrolyte, and A is the area of the specimen. Temperature-dependent ionic conductivity in the electrolytes is divided into two types: ion transport in solid and polymeric materials. For crystalline materials, the ionic conductivity follows the Arrhenius type and for amorphous materials, it follows Vogel-Tammann-Fulcher (VTF) model.^[247, 248, 249]

Arrhenius equation:

$$\sigma(T) = \sigma_0 \cdot \exp\left(-\frac{E_a}{RT}\right) \quad \text{Equation 7}$$

VTF equation:

$$\sigma(T) = \sigma_0 \cdot T^{-0.5} \cdot \exp\left(-\frac{E_a}{R(T-T_0)}\right) \quad \text{Equation 8}$$

Here, σ_0 ($\text{S}^{-1} \text{cm}^{-1} \text{k}^{-0.5}$) denotes the number of charge carriers, E_a (eV) represents the activation energy for the conductivity,^[250] R is the gas constant, T is the temperature, T_0

2. Background on the electrochemical terms used in this study

correlates to the glass transition temperature, T_g , of the material (usually about 10 – 50 k lower than T_g). The Arrhenius equation with a linear relationship between conductivity and inverse of temperature plot indicates a simple ion hopping mechanism decoupled from the polymer chain relaxation, whereas a non-linear curve for the VTF plot shows that the ion hopping motion coupled with relaxation and/or segmental motion of the polymeric chains.^[251] The VTF curve is bent due to the reason that diffusion is only possible when the diffusing species move from one free volume space to another. The availability of the free volume is indicated by $T-T_0$. The main ion conductive mechanism in a polymer electrolyte is dependent on the coupling between ion transport and polymer chain relaxation. Ratner et al.^[252] proved that a conductive polymer relaxes more rapidly than a non-conductive one. The data revealed that, when the polymer relaxes quickly, the ionic conductivity increases. Based on this “coupling” mechanism, diffusion of the ion occurs only when the relaxation process is active. Below the glass transition temperature, the relaxation is arrested, therefore the ionic conductivity decreases rapidly.^[253, 254]

On the other hand, non-blocking electrodes are used to measure the transference number of the electrolytes. Determination of a.c. impedance, before and after d.c. polarization can be used to calculate the transference number of the electrolyte. This method was developed by Bruce and Vincent.^[255, 256, 257] When a small constant potential is applied to the non-blocking electrodes with conductive electrolyte, the current is decreased and a steady state is attained that is only due to the cations. The current decrease arises from the concentration gradient developed across the cell. When a small potential difference is introduced in the symmetric cell, the ions start to move across the electrodes due to oxidation (at the positive electrode) and reduction (at the negative electrode) reactions. Together with cations, the anions tend to move in the opposite direction. However, the anions are not engaged with the electrodes, which causes anion accumulation near the electrode surface. The cations follow the anions to keep the charge in equilibrium. Due to the concentration gradient, diffusion of the ions takes place to neutralize the salt concentration in the electrolyte. At the initial state ($t=0$), both cations and anions move to produce current but at the steady state, only the cations move to induce current across the electrodes.^[258, 259, 260]

$$t_+ = \frac{I_{ss}(\Delta V - I_0 R_0)}{I_0(\Delta V - I_{ss} R_{ss})} \quad \text{Equation 9}$$

where t_+ indicates the cation transference number, V is the applied potential, I_0 is the initial current, I_{ss} is the steady-state current, R_0 is the bulk resistance before polarization, and R_{ss} is the bulk resistance after polarization.

2.5 Electrochemical impedance spectroscopy

Electrochemical impedance spectroscopy (EIS) is an important electroanalytical technique for batteries where the impedance is measured in Ohms (Ω). A small potential perturbation is applied to the electrode (~ 10 mV) and the resulting electrode response can be measured near the equilibrium. This method can be used to probe electrodes without inflicting any irreversible reactions on the electrodes. Since the electrode is measured close to equilibrium, EIS can be combined with other common electrochemical techniques to study the electrode under different conditions. EIS is measured by applying sinusoidal AC (alternating current) potential to the cell and the resulting sinusoidal AC current signal is monitored (Figure 22).^[261]

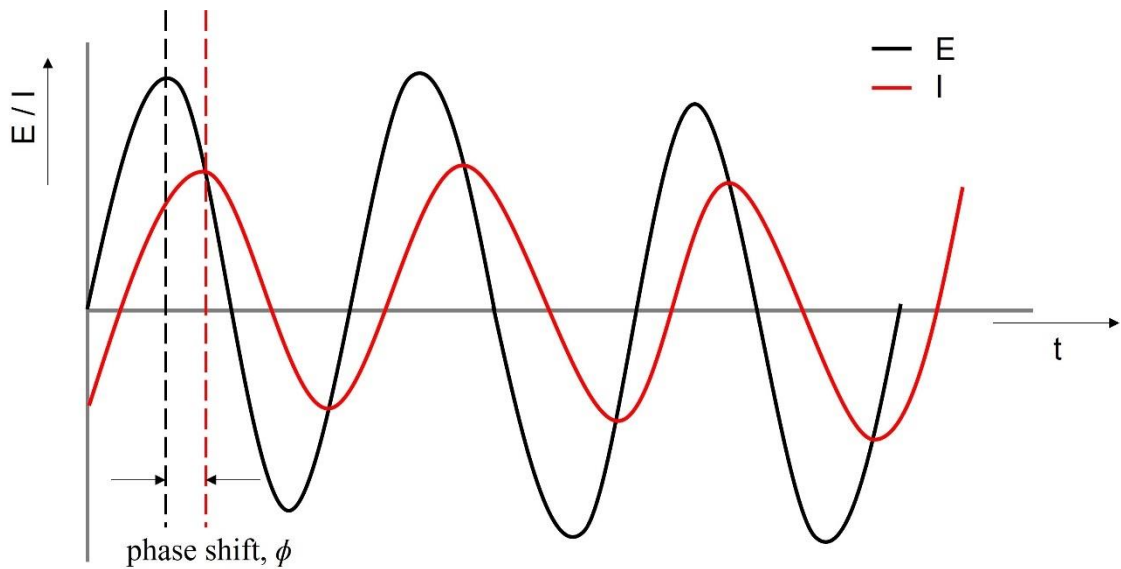


Figure 22. Sinusoidal current response.^[262]

The shape of the sinusoidal potential and current response curve can be expressed as the following:

$$E_t = E_0 \sin(\omega t) \quad \text{Equation 10}$$

$$I_t = I_0 \sin(\omega t + \phi) \quad \text{Equation 11}$$

Based on Euler's relationship

$$\exp(i\phi) = \cos(\phi) + i\sin(\phi) \quad \text{Equation 12}$$

2. Background on the electrochemical terms used in this study

the impedance can be described as a complex function

$$E_t = E_0 \sin(i\omega t) \quad \text{Equation 13}$$

$$I_t = I_0 \sin(i\omega t + \phi) \quad \text{Equation 14}$$

$$Z = \frac{E(t)}{I(t)} = Z_t \cdot e^{i\phi} = Z_t (\cos \phi + i \sin \phi) = Z^{\text{real}} + iZ^{\text{im}} \quad \text{Equation 15}$$

Where E_t and I_t are the potential and current at time t , respectively, E_0 is the maximum amplitude of the signal in the current wave, and ω is the radial frequency where $\omega = 2\pi f$, and ϕ is the phase shift in the sinusoidal current signal. The impedance is divided into real (X-axis) and imaginary (Y-axis) parts and plotted as the "Nyquist Plot". However, to visualize the impedance at a particular frequency, a "Bode plot" is utilized, which plots $\log Z^{\text{real}}$, $\log Z^{\text{im}}$, $\log |Z|$ and ϕ vs. $\log f$. The resistors and capacitor's impedance response in the battery can be defined as follows.

Figure 23a-d shows the impedance spectra of the resistor and capacitor. The resistor follows Ohm's law, resulting in a single point in impedance spectra without any reactive part (phase shift). Ideal capacitors have a reactive impedance with zero resistance. When the AC voltage is applied through the capacitor, the current leads the voltage by -90° (phase angle). The impedance is inversely proportional to the frequency.^[263] Combining resistor and capacitor can be defined by adding impedance of the capacitor and the resistor. The equivalent circuit can be considered as a blocking electrode (i.e.) an inert electrode immersed in an electrolyte. R in the equivalent circuit represents the ionic resistance of the bulk electrolyte and the C represents the capacitance of the electrode surface arising from the double layer. On the other hand, parallelly connecting resistor and capacitor result in admittances (reciprocal to the impedance). When the $\omega \rightarrow \infty$, the impedance becomes zero; the circuit behaves like an ideal capacitor. Adversely, when $\omega \rightarrow 0$, the impedance is equal to the ideal resistor. Additional non-ideal circuit elements (Figures 23e and f) are required to represent the complex system such as constant phase element (CPE) and Warburg diffusion (W). Where Q and σ represent the CPE and Warburg coefficient, respectively. For a real equivalent circuit model, a non-intuitive circuit element called the "constant phase element" was introduced to fit the circuit models. The CPE circuit element symbol is slightly different from that of the capacitor. This is due to variations in surface roughness, distribution of reaction rates, thickness, and compositions being considered in real systems.^[264, 265]

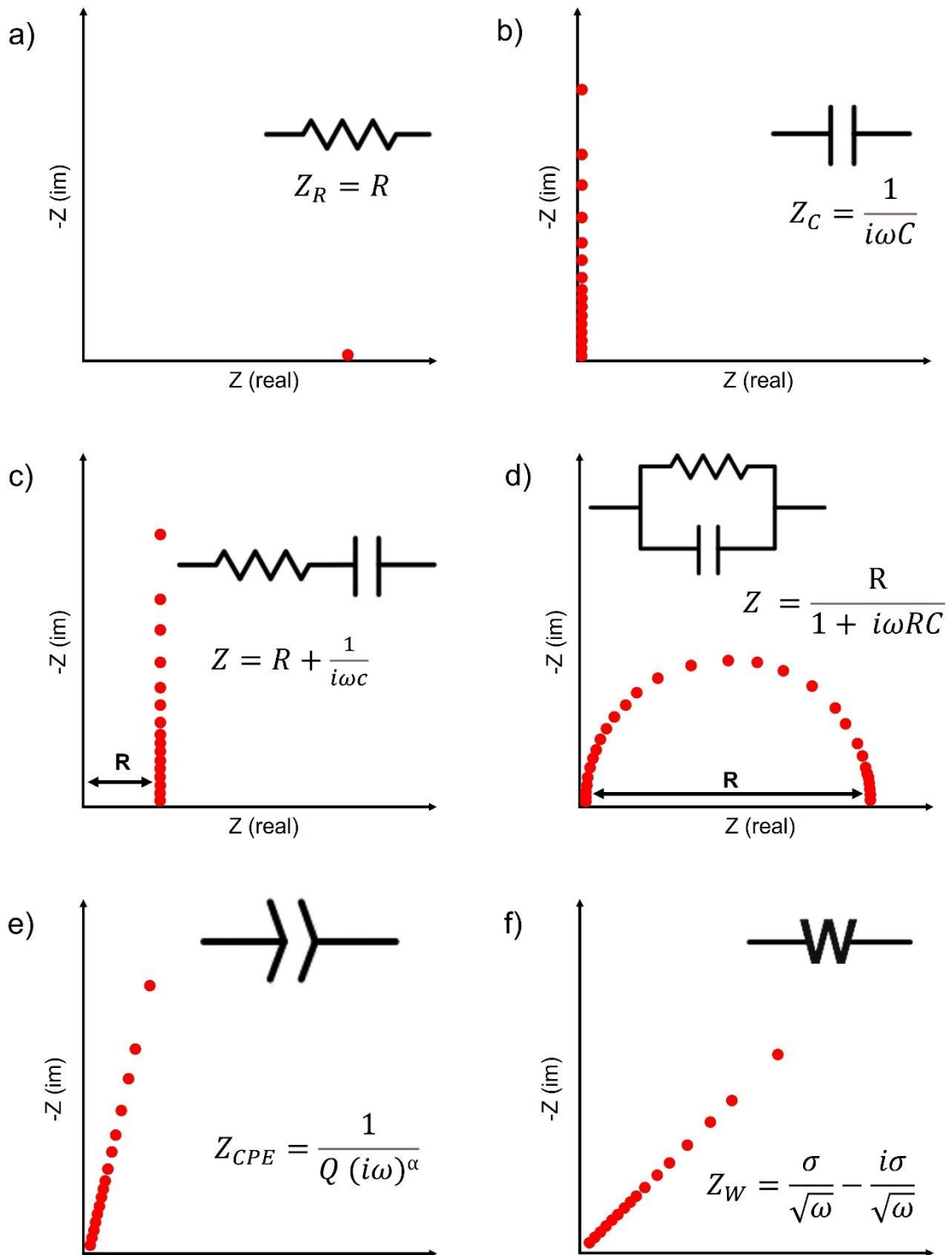


Figure 23. The Nyquist plot, equivalent circuit, and mathematical derivation of a) resistor; b) capacitor; c) resistor and capacitor in series; d) resistor and capacitor in parallel; e) constant phase element; f) Warburg impedance.

The Warburg impedance models the semi-infinite linear diffusion: diffusion along one direction, which is bound to a planar electrode on one side. The Nyquist plot for Warburg

2. Background on the electrochemical terms used in this study

impedance shows a straight line with an incline of 45°. For an infinitely thick diffusion layer, the Warburg coefficient can be defined as:

$$\sigma_w = \frac{RT}{n^2 F^2 A \sqrt{2}} \left[\frac{1}{C_O \sqrt{D_O}} + \frac{1}{C_R \sqrt{D_R}} \right] \quad \text{Equation 16}$$

where D_O and D_R are the diffusion coefficient of the oxidant and reductant, respectively. Similarly, C_O and C_R are the concentration of the oxidant and reductant, respectively. F – Faraday constant, A – electrode area R – gas constant, and T – temperature.

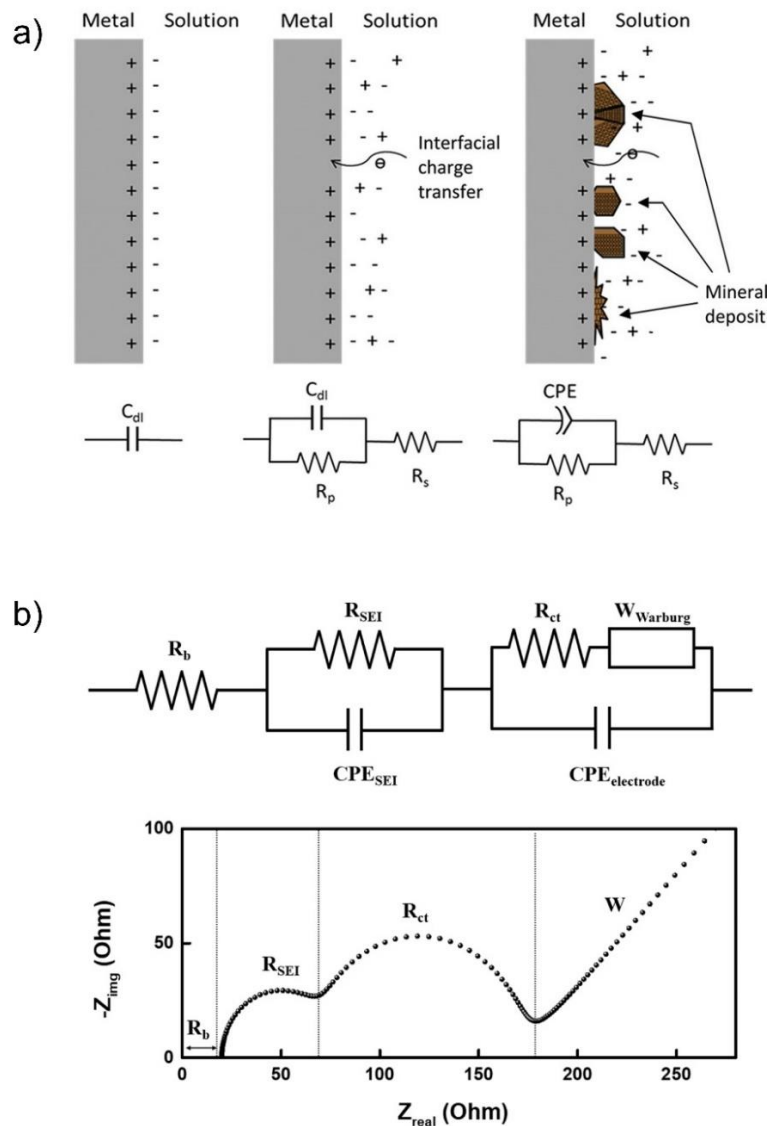


Figure 24. a) Equivalent circuit model at the metal-solution interface corresponding to the formed electrical double layer: C_{dl} = double-layer capacitance, R_p = polarization resistance; R_s = solution resistance (reproduced with permission Ref. [266]); b) an example circuit model and its corresponding Nyquist plot of a Li-ion half cell (reproduced with permission Ref. [267]).

The equivalent circuit model of a metal in a solution is represented in Figure 24a. The electrical double layer is formed at the metal-solution interface due to the difference in chemical energy.^[268] Application of a sinusoidal potential wave at the interface results in capacitive behavior of the response signal (varying current). Therefore, the circuit can be modeled close to a pure capacitor. During electrochemical reactions, the subtle changes in the interface can be envisaged using a combination of resistors, capacitors, and inductors. Figure 24a shows the circuit model for ionic diffusions and charge transfer approximated by R_s , and R_p , respectively. This type of equivalent circuit model is called the Randle circuit model. When the cell is covered by the surface deposits the circuit model gets complicated. The deposition results in frequency dispersion, which can be attributed to the capacitance dispersion represented as a CPE in the Randle circuit model.^[261, 269, 270] An example (Li-ion half cell) of a simplified equivalent circuit model for a mixed kinetic and semi-infinite linear diffusion is shown in Figure 24b. The corresponding Nyquist plot indicates the bulk resistance (R_b), which is connected to two parallel R/CPE elements representing the resistance and capacitance of the SEI layer (R_{SEI}/CPE_{SEI}) and charge transfer reaction ($R_{ct}/CPE_{electrode}$) at the electrode/electrolyte interphase. In an extremely low frequency, the Warburg element (45° straight line) can be observed due to semi-infinite diffusion conditions.^[271]

2.6 Galvanostatic intermittent titration technique

The galvanostatic intermittent titration technique (GITT) is used to determine transport kinetics and other thermodynamic parameters in ion-insertion electrodes.^[272] Batteries rate capability is limited by the rate of ion transport in the electrodes, which can be calculated by the diffusion coefficient of the ion by GITT. With the help of GITT, Lacey et al.^[273, 274] demonstrated that the LSB failure is related to its rapidly increasing internal resistance. GITT theory, originally developed for dense planar electrodes can be transferred to porous electrodes by considering the electrode area as the electrochemically active area.^[275, 276] GITT can be measured by applying a series of current pulses with a long relaxation step between each pulse. This process is repeated until the battery is fully charged/discharged. As shown in Figure 25a, b, during the application of negative current (during discharge), the cell potential drops suddenly to the value proportional to iR , where R is the sum of uncompensated and charge transfer resistance. Then, the potential decreases gradually for the defined amount of time, due to the galvanostatic discharge reactions. At the beginning of the relaxation period, the cell potential rises rapidly similar to the ohmic resistance and then increases slowly until the electrode reaches equilibrium

2. Background on the electrochemical terms used in this study

(i.e., $dE/dt \sim 0$) and open circuit potential (V_{oc}). This sequence is continued until the cell's potential reaches the discharge cut-off potential. The same process is repeated with a positive current pulse for charging. The chemical diffusion coefficient can be calculated as follows:^[277, 278]

$$D = \frac{4}{\tau\pi} \left(\frac{n_m V_m}{S} \right)^2 \left(\frac{\Delta E_s}{\Delta E_t} \right)^2 \quad \text{Equation 17}$$

where τ is the duration of the current pulses (s), n_m is the number of moles (mol), V_m is the molar volume of the active material (cm^3/mol), S is the active electrode contact area, ΔE_s is the steady-state voltage change, and ΔE_t is the voltage variation during the application of the current pulses (without iR drop).

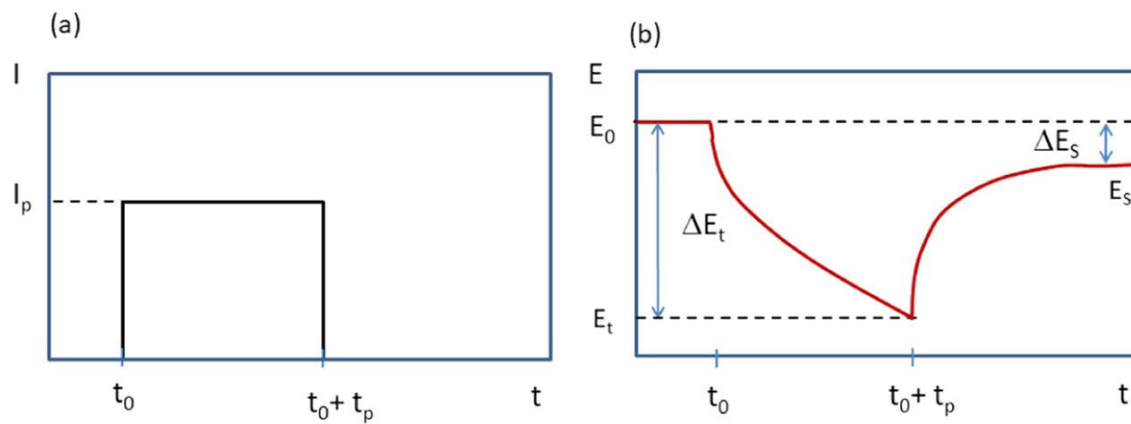


Figure 25. Schematic representation of the application of the current pulse and relaxation during the GITT experiment by a) current (I); b) potential (E) at the working electrode (reproduced with permission Ref. ^[279]).

3 Electrolytes based on sodium salt of weakly coordinating anion

3.1 Introduction

The ability of an anion to coordinate to a metal cation partially depends on the solvent nature and other bases present in the electrolyte solution, steric hindrance, and activation energy restrictions. A coordinating anion approaches the metal cation more closely compared to a non-coordinating anion. This coordination certainly alters the cation's magnetic moment and spectral properties which will be significantly different from a non-coordinated one. It was found that the alleged noncoordinating anions such as BF_4^- , NO_3^- were coordinating when the water was excluded from the system. "It is clear that the notion of non-coordinating anion should put to rest alongside the notion of the non-coordinating solvent", was concluded by Rosenthal in 1973.^[280] In recent years researchers continue to report it as non-coordinating anions and non-coordinating solvents. It would be meaningful to use weakly coordinating anions (WCA) and weakly coordinating solvents (WCS).^[281] WCAs should possess a few ideal properties such as a) low overall charge, and b) high degree of charge delocalization. The overall charge in the anion should be delocalized over the entire anion (i.e.) no single atom or a group of atoms carries a high concentration of charges. This suggests that the larger the anion, the more delocalization of the charge and the more weakly coordinating of the anion. Another important property would be the existence of very weak basic sites on the boundary of the anion (i.e.) anions with hydrogen or fluorine atoms are more weakly coordinating than the anions with oxygen or chlorine atoms, respectively. For example, BF_4^- is more weakly coordinating than ClO_4^- .^[282, 283] While choosing WCAs, two important issues need to be addressed. First, some exceptionally large anions tend to dissociate into smaller fragments, which could at least in part act as a strongly coordinating molecule. This phenomenon was observed even in small molecules such as BF_4^- , and PF_6^- . The stability of the WCA against the strong electrophilic cations should be high enough to avoid oxidation.^[284, 285] The good WCA allows only very minimal interaction between cation-anion. WCAs can be designed based on the following principles:

- a) The charge should be low (univalent) at the anion to reduce the coulombic interaction. An increase in the size of an anion reduces the electrostatic interaction and facilitates the dissolution in low polarity solvent.
- b) Charge delocalization should be over the entire anion and no basic or nucleophilic sites should be present.

3. Electrolytes based on sodium salt of weakly coordinating anion

- c) The moieties should be robust and withstand highly reactive cations.
- d) The anion surface should be less polarizable.
- e) The WCA should exhibit high fluoride ion affinity (FIA) and ligand affinity (LA) values.

WCAs can stabilize highly electrophilic, organometallic cations for use in catalysis. Particularly good cations such as $[\text{SiR}_3]^+$ ($\text{R}=\text{organyl}$) are extremely electron-deficient and highly Lewis acidic. Therefore, they tend to coordinate with almost all known WCAs. This can be prevented only by the combination of a bulky ligand R at the cationic center, which prevents the accessibility to the Si^+ center, and a chemically robust WCA that blocks ion pairing. If the ligand is only weakly bound to the metal cation acceptor M^+ , the possibility of repelling the ligands out of the metal ion coordination sphere and then substituting it with cation or the solvent is high. WCA should be stable against oxidations is one of the important parameters. A moderately oxidizing cation such as $[\text{NO}]^+$ is not compatible with good WCA, $[\text{B}(\text{C}_6\text{F}_5)_4]^-$ due to its aromatic system.

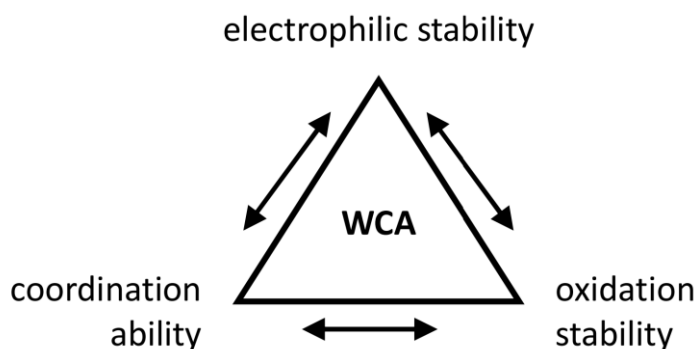


Figure 26. A triangle summarizing the most important criteria for the selection of WCAs (reproduced with permission Ref. ^[286]).

Based on the basic requirements shown in Figure 26, fluorinated moieties can be chosen as construction units for WCAs since they fulfill all requirements. Examples are fluorinated borates and aluminates such as $[\text{B}(\text{CF}_3)_4]^-$, $[\text{B}(\text{C}_6\text{F}_5)_4]^-$, $\{\text{Al}[\text{OC}(\text{CF}_3)_3]_4\}^-$. Anions such as BF_4^- have intense competition between its decomposition and coordination leading to the expansion of less basic and more stable WCAs. Modification of the BF_4^- anion with larger phenyl groups to obtain BPh_4^- further makes it susceptible to hydrolysis and bond cleavage.^[287] Thus, the BPh_4^- anion is an obvious development from the initial “non-coordinating anion” tetrafluoroborate, however, BPh_4^- is unstable against both chemical and electrochemical oxidation.^[288] To overcome these issues, the phenyl groups

were fluorinated and attached to the central boron atom. Much larger ligands were added by modification of existing ligands which leads to a reduction in coordination and high solubility in hydrocarbon solvents. Tetrakis(3,5-bis(trifluoromethyl)phenyl)borate [$\text{BAr}^{\text{F}}_4^-$], $[\{3,5\text{-(CF}_3)_2\text{C}_6\text{H}_3\}_4\text{B}]^-$, is mainly used in catalytic systems where an active site needs a weakly coordinating anion to the metal center and negligible anion contribution in the catalytic cycle.^[289, 290, 291, 292, 293]

Similar to borate, a highly electropositive aluminum, a strong bond between oxygen and aluminum, and an easy one-step synthesis from LiAlH_4 renders alkoxyaluminate-based anions one of the most widely used anions in the WCA community.^[294, 295] It was first reported by Strauss in 1966, and as of now wide varieties of anions were reported. Ex: $\{\text{Al}[\text{OC}_6\text{F}_5]_4\}^-$, $\{\text{Al}[\text{OCH}_2\text{CF}_3]_4\}^-$, $\{\text{Al}[\text{OC}(\text{Ph})_2\text{CF}_3]_4\}^-$, $\{\text{Al}[\text{OCR}(\text{CF}_3)_2]_4\}^-$, $\text{R} = \text{H, Me, CF}_3$ etc.).^[296, 297, 298, 299, 300] The most stable WCA is carborane, which is even stable against fierce electrophiles (e.g. small silylium anions) than $[\text{Al}(\text{OR}^{\text{F}})_4]^-$. However, synthesis requires explosive LiC_6F_5 and toxic HOTeF_5 precursors and thus makes it less attractive in real applications.^[301, 302, 303] Due to its facile scalable synthesis, easy conversion to other WCA-precursors and very weak coordinating strength makes $[\text{Al}(\text{OR}^{\text{F}})_4]^-$ ($\text{R}^{\text{F}} = \text{C}(\text{CF}_3)_3$) one of the most famous WCAs. The anion also demonstrates excellent stability against Bronsted acids, it is stable towards highly electrophilic cations such as $[\text{CX}_3]^+$ ($\text{X} = \text{Cl, Br, I}$) or with larger silylium cations. As mentioned, the easy conversion from its lithium salt to other useful WCA starting materials is of significant importance in synthesizing multigram scale metathesis reactions (Figure 27). Several advantages associated with alkoxyaluminate anions make it an effective alternative to borate-based anions, especially in the field of homogeneous catalysis where very weak anion-cation coordination is significant. Generally, alkoxyaluminates are easily hydrolyzed but the perfluorinated alkoxyaluminate anion is stable in 6 N nitric acid. This excellent stability arises from the effective shielding of the oxygen atoms by the bulky $\text{C}(\text{CF}_3)_3$ group and also the electronic stabilization from the fluorination. The acidity of the fluorinated alcohols determines the electron-withdrawing effect of the fluorinated ligands in the anion, usually calculated from its pK_a value. The $\text{HOC}(\text{CH}_3)_3$ has a $\text{pK}_a=19.3$, whereas perfluorinated alcohol $\text{HOC}(\text{CF}_3)_3$ has a pK_a value of 5. Therefore, perfluorinated ^tbutanol is 14 orders of magnitude more acidic than its non-fluorinated companion. The rate of reaction for asymmetric hydrogenation is high for $[\text{Al}(\text{OR}^{\text{F}})_4]^-$ compared to other WCAs and also exhibits very good oxygen and moisture resistance.^[304]

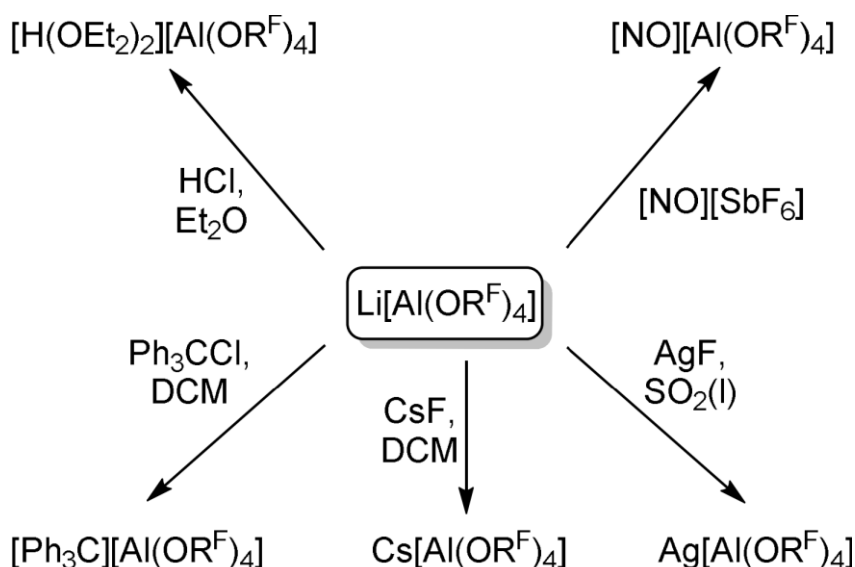


Figure 27. Synthesis of other WCA reagents from $\text{Li}[\text{Al}(\text{OR}^{\text{F}})_4]$ (reproduced with permission Ref. ^[286]).

Bridged WCAs form a larger anion complex where the host anion binds to another similar Lewis acid. Bridged anions can be derived from the modern WCA precursor (example shown in Figure 28) which is connected by a single monoanionic bond. The delocalization of the negative charge is spread over many numbers of atoms, reducing its coordination strength. The decomposition of $[\text{Al}(\text{OR}^{\text{F}})_4]^-$ by very small electrophiles such as $[\text{SiCl}_3]^+$, $[\text{PCl}_2]^+$ leads to the formation of $[(\text{R}^{\text{F}}\text{O})_3\text{Al-F-Al}(\text{OR}^{\text{F}})_3]^-$; $[\text{Al-F-Al}]^-$, which is even less coordinating. In fact, this is titled the “least coordinating anion”, it is resistant to even smaller cations and withstands fiercer conditions. The systematic synthesis of $[\text{Al-F-Al}]^-$ requires a two-step procedure from $\text{Ag}[\text{Al}(\text{OR}^{\text{F}})_4]$ with the loss of Ag^+ and OR^{F} moieties. Exceedingly small cations such as Li^+ can still coordinate to $[\text{Al}(\text{OR}^{\text{F}})_4]^-$ through the oxygen atoms. However, due to its steric hindrance, similar coordination with oxygen was not observed in $[\text{Al-F-Al}]^-$ compounds. The distribution of negative charge over 55 fluorine atoms (Figure 28) and also a partial localization of negative charges at the bridging fluorine atom make bridged WCA, $[\text{Al-F-Al}]^-$ more stable against F^- and $[\text{R}^{\text{F}}\text{O}]^-$ abstraction than regular WCA, $[\text{Al}(\text{OR}^{\text{F}})_4]^-$.^[305]

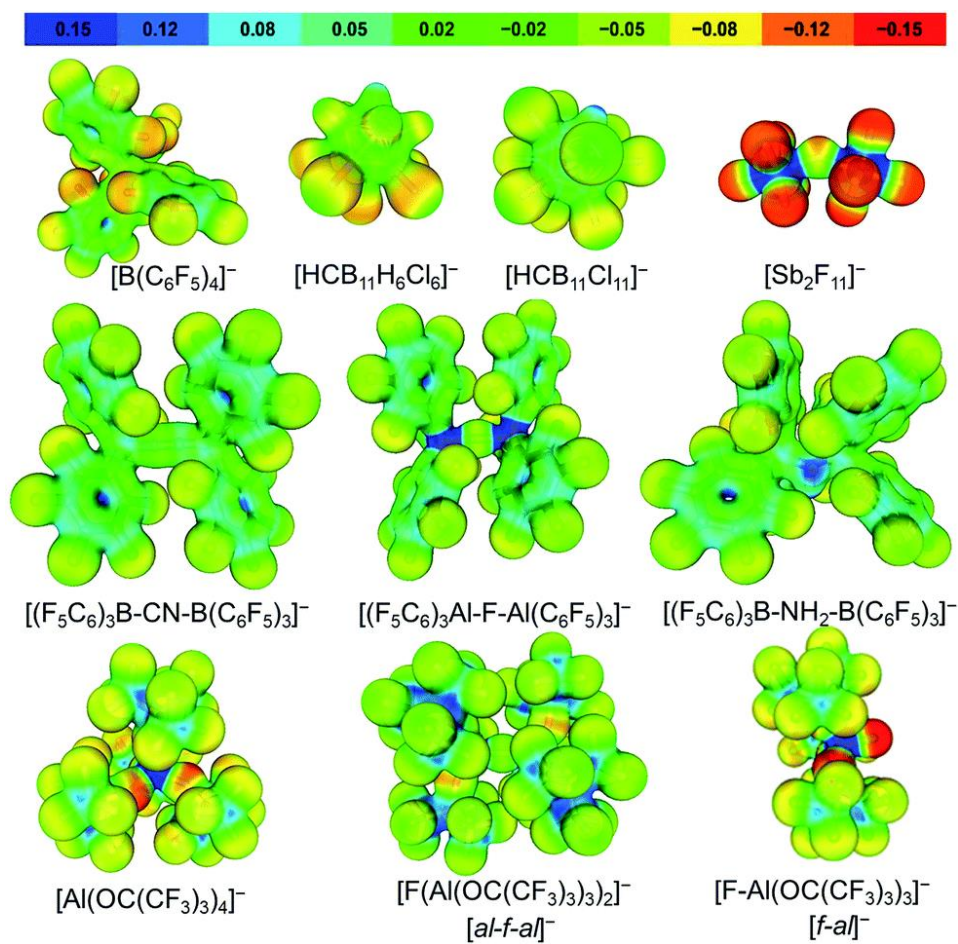


Figure 28. Calculated electrostatic potential of commonly used WCAs and their bridged WCAs (reproduced from Ref. ^[306] with permission from the Royal Society of Chemistry).

Due to weak interaction between cation and anion in the WCA system, there is a low propensity for ion-pairing in solution, making it useful for battery electrolyte applications.^[307] Alkoxyaluminates and borates can be considered promising electrolytes due to their synthetic adjustability, versatility, and compatibility with various cathodes. Like borates, aluminate-based WCAs also possess high ionic conductivity, high dielectric constant, and high oxidation stability. However, differences in their chemical properties affect the electrochemical stability and kinetics of the cell.^[308, 309] The disadvantage of aluminate salt is their sensitivity toward water than its borate counterpart. When exposed to air, aluminate salts readily decompose in the presence of humidity. A more polar and long bond length between Al-O causes the bond cleavage. The analogous boron central atom salt demonstrates a higher melting point, high viscosity, and good stability against water due to shorter and less polar B-O bonds. $[\text{Al}(\text{OR}^{\text{F}})_4]^-$ anion shows high ionicities, indicating that the ion pairing is very low, which leads to the free movement of the ions

3. Electrolytes based on sodium salt of weakly coordinating anion

in the electrolyte. Interestingly, WCAs containing salts and ionic liquids have found numerous applications in lithium-based batteries due to their good solubility in organic solvents, high ionic conductivity, good chemical and electrochemical stability, and facile synthesis methods, etc. WCAs such as PF_6^- bonds are susceptible to hydrolysis but $[\text{B}(\text{CF}_3)_4]^-$ is exceptionally stable even in anhydrous HF and can stabilize highly reactive cations. This superior stability of the anion towards hydrolysis is due to steric shielding and charge delocalization around the anion.^[53, 310, 311]

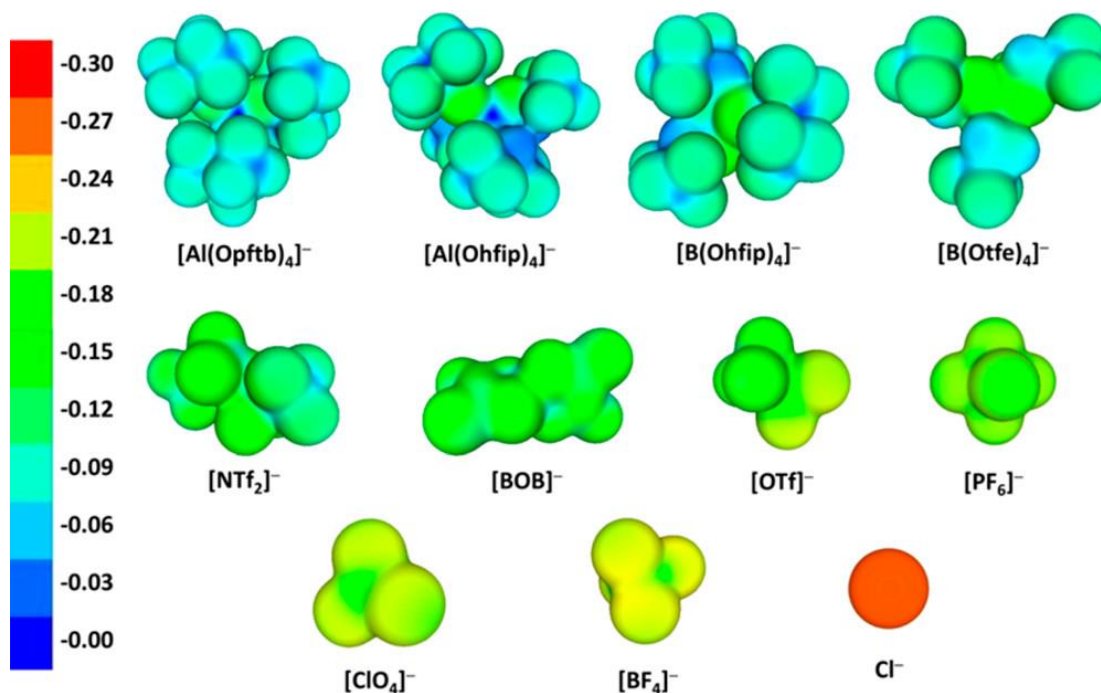


Figure 29. Calculated electrostatic potentials of various anions (reproduced with permission Ref. ^[312]).

A commonly used WCA salt in LIBs; bistrifluoromethanesulfonyl imide $[(\text{CF}_3\text{SO}_2)_2\text{N}]^-$; it provides high ionic conductivity due to the presence of the sulfonyl group which ensures the charge delocalization. Shyamsunder et al. successfully demonstrated LSB with “eliminated polysulfide shuttle” by combining $[\text{Al}(\text{Ohfip})_4]^-$; hfip = hexafluoroisopropoxide) anion and non-polar triflamide solvent as an electrolyte with as-synthesized non-polar solvents such as *N, N*-dimethyl triflamide (DMT), and *N, N*-dipropyl triflamide (DPT) where the electron-withdrawing triflyl group is attached to the nitrogen atom.^[313] The larger anion reduces the electrostatic interaction whereas the fluorine atom minimizes the ion-pairing and increases the stability against oxidation (reduction in HOMO). The DMT and DPT electrolytes exhibit oxidation stability of 5.6 V and 5.4 V and ionic conductivities of 1.25 and 0.24 mS cm^{-1} , respectively. The commonly

used anions and their calculated electrostatic potentials are shown in Figure 29. The color-coding represents the coordination status, red color = negatively charged, blue = positively charged. It is evident that a small anion shows a high accumulation of negatively charged surface. In bulky anions such as $[\text{Al}(\text{Ohfip})_4]^-$, where the basic oxygen sites are protected by fluorinated groups represented by a color closer to blue.

3.2 Publication “Ultra-Stable Cycling of High Capacity Room Temperature Sodium-Sulfur Batteries Based on Sulfurated Poly(acrylonitrile)”

Research on a novel electrolyte salt is the least explored topic in the field of RT SSBs due to the fact that existing sodium salts such as NaPF_6 , NaTFSI , and NaClO_4 show good cell performance. These traditional salts exhibit high ionic conductivity, good cycling stability, and rate performance. However, the advantages of WCAs on facile ion dissociation and quick ion mobility in the solvent could further enhance the ionic conductivity and rate capability of the cell. The facile one-pot synthesis of $\text{Na}[\text{B}(\text{hfip})_4]$; hfip = hexafluoroisopropoxide, and good compatibility with Na metal renders it a good candidate for RT SSB. As shown in Figure 30, the bulk synthesis was carried out under inert conditions and the salt purity was analyzed by NMR.

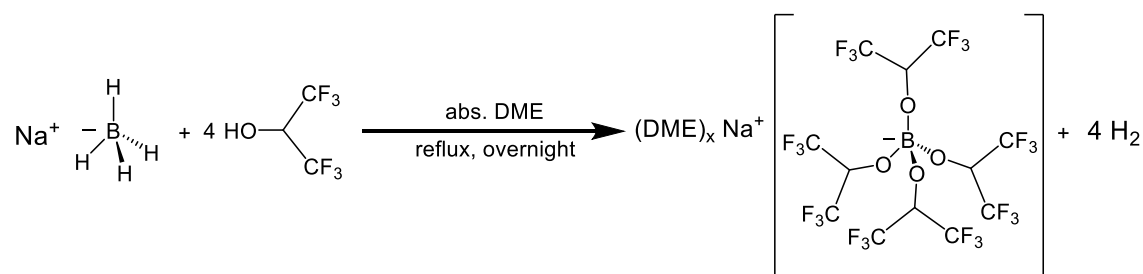


Figure 30. Bulk one-pot synthesis route of $\text{Na}[\text{B}(\text{hfip})_4]$ salt.

In this research, the WCA based on $\text{Na}[\text{B}(\text{hfip})_4]$ salt was combined with EC, DMC (1 : 1, vol. : vol.), and 13 wt.% FEC as an additive. The electrochemical properties such as oxidation stability, overpotential, and cycling stability were analyzed either by a full cell or symmetric cell. Moreover, SPAN was proven to be a suitable cathode for RT SSBs, therefore combining it with fluoroalkoxy borate WCA salt might enhance the reaction kinetics at the cathode side and also an overall improvement in cells performance. The cell was able to deliver $1072 \text{ mAh g}_s^{-1}$ at 3 C up to 1000 cycles. Moreover, the discharge cut-off study revealed that the formation of Na_2S is favored at 0.2 V.

Publication:

Murugan, S.; Niesen, S.; Kappler, J.; Küster, K.; Starke, U.; Buchmeiser, M. R., Ultra-Stable Cycling of High Capacity Room Temperature Sodium-Sulfur Batteries Based on Sulfurated Poly(acrylonitrile). *Batter. Supercaps* **2021**, *4*, 1636-1646.

Author Contributions: **Saravanakumar Murugan**: Conceptualization, Data curation, Formal analysis, Investigation, Methodology, Validation, Visualization, Writing - original draft, Writing - review & editing. **Stefan Niesen**: Data curation, Validation, Writing - review & editing. **Julian Kappler**: Data curation, Validation. **Kathrin Küster**: Investigation (XPS measurements), Data curation. **Ulrich Starke**: Resources, Supervision. **Michael R. Buchmeiser**: Funding acquisition, Methodology, Project administration, Resources, Supervision, Validation, Writing - review & editing.

Reprinted with permission from Ref. ^[314], (open access).

Ultra-Stable Cycling of High Capacity Room Temperature Sodium-Sulfur Batteries Based on Sulfurated Poly (acrylonitrile)

Saravanakumar Murugan,^[a] Stefan Niesen,^[a] Julian Kappler,^[a] Kathrin Küster,^[b] Ulrich Starke,^[b] and Michael R. Buchmeiser^{*[a, c]}

We report on a room temperature (RT) sodium-sulfur (Na–S) battery based on a sodium anode, a sulfurated poly (acrylonitrile) (SPAN) cathode and an electrolyte containing sodium tetrakis(hexafluoroisopropoxy) borate (Na[B(hfip)₄]; hfip = hexafluoroisopropoxide) in a mixture of ethylene carbonate (EC), dimethyl carbonate (DMC) and fluoroethylene carbonate (FEC). The hfip anion as a weakly coordinating anion (WCA) provides high anodic stability, high ionic conductivity, and superior electrochemical performance in carbonate-based solvents. The Na-SPAN cell exhibits an initial discharge capacity

of 1360 mAh g_s⁻¹ and a remarkable reversible capacity of 1072 mAh g_s⁻¹ after 1000 cycles at 3 C (C = C-rate, 5.025 A g_s⁻¹) with an insignificant average capacity decay of less than 0.021 % per cycle. A careful choice of the discharge cut-off potential (DCP) reveals that a DCP of 0.2 V allows for stable cycling for more than 500 cycles while a DCP of 0.5 V results in a constant capacity decay. The excellent cycle stability at a DCP of 0.2 V is likely to be caused by the high conversion of the SPAN-bound sulfur into Na₂S.

1. Introduction

To date, lithium-ion batteries are widely used for energy storage in portable electronic devices and electric vehicles.^[1–2] Apart from the growing electric vehicle market, lithium-ion batteries are also increasingly employed in large-scale stationary energy storage applications. In view of that, new materials with high energy density and good cycle stability that can be produced at low costs are of significant importance. Therefore, the use of inexpensive and environmentally benign materials such as sodium and sulfur has attracted substantial interest in recent years. Particularly the raw material costs of lithium compared to sodium (25000 \$/ton vs. 2100 \$/ton), a consequence of the natural abundance of these metals in the earth's crust (Li: 20 mg kg⁻¹; Na: 28400 mg kg⁻¹), makes sodium an economic choice for electrode materials.^[3–5]

Sulfur is a low-cost, highly abundant raw material with a high theoretical capacity of 1675 mAh g_s⁻¹. Consequently, high-

temperature (HT) Na–S batteries based on a solid-state β-alumina electrolyte are already widely used in energy storage for large-scale grid applications.^[1,6] Such batteries are operated at 300–350 °C to ensure adequate conductivity of the electrolyte and contain both Na and S in the molten state. Clearly, the use of such batteries entails severe disadvantages such as increased safety risks and the presence of corrosive polysulfides.^[7] Therefore, room temperature (RT) Na–S batteries have moved into the center of interest. However, RT Na–S batteries so far suffered from a severe capacity decay due to the formation of soluble polysulfides in the electrolyte, which shuttle to the anode.^[8]

Cathode materials, which avoid polysulfide shuttling such as sulfurated poly(acrylonitrile) (SPAN), have been developed by Wang et al. and show excellent performance in lithium-sulfur batteries using a carbonate-based electrolyte.^[9] The structure and electrochemistry of SPAN within the context of Li–S batteries have been studied in detail.^[10–17] By contrast, the use of SPAN for RT Na–S batteries so far resulted in limited success. Though a remarkable initial discharge capacity of 655 mAh g_{cathode}⁻¹ was observed, however, it dropped to 500 mAh g_{cathode}⁻¹ within 20 cycles.^[18]

Until now, various salts and different combinations of ether and/or carbonate-based solvents have been used for RT Na–S batteries. The choice of electrolyte highly depends on the compatibility with the sodium electrode. Since sodium is highly reactive and forms an unstable solid electrolyte interface (SEI) layer by reacting with the electrolyte, the choice of electrolyte is crucial. So far, sodium salts such as commercially available NaPF₆, NaTFSI, NaClO₄, NaFSI, and NaBF₄ (TFSI = bis(trifluoromethylsulfon)imide; FSI = bis(fluoromethylsulfonimide) have been used for Na–S cells.^[19] Even though weakly coordinating anions (WCAs) possess a wide potential window,

[a] S. Murugan, S. Niesen, J. Kappler, Prof. M. R. Buchmeiser
Institute of Polymer Chemistry
University of Stuttgart
70569 Stuttgart, Germany

[b] K. Küster, Prof. U. Starke
Max Planck Institute for Solid State Research
70569 Stuttgart, Germany

[c] Prof. M. R. Buchmeiser
German Institutes of Textile and Fiber Research (DITF) Denkendorf
73770 Denkendorf, Germany
E-mail: michael.buchmeiser@poc.uni-stuttgart.de

Supporting information for this article is available on the WWW under <https://doi.org/10.1002/batt.202100125>

© 2021 The Authors. Batteries & Supercaps published by Wiley-VCH GmbH. This is an open access article under the terms of the Creative Commons Attribution License, which permits use, distribution and reproduction in any medium, provided the original work is properly cited.

high ionic conductivity and allow for high coulombic efficiency, they have been limited so far to Li and Mg batteries.^[20–25] In view of the attractiveness of WCAs and SPAN as a cathode material, we were interested in the question of whether Na fluoroalkoxy borates, which have been reported to be stable against moisture and have high ionic conductivity as well as low viscosity,^[26–27] would allow for creating long-time stable Na–S cells. To the best of our knowledge, the concept of using fluoroalkoxy borates as WCAs in combination with SPAN for RT Na–S batteries has not been reported so far. And indeed, the use of sodium tetrakis(hexafluoroisopropoxy) borate (NaB[hfip]₄) in a mixture of ethylene carbonate (EC), dimethyl carbonate (DMC), and fluoroethylene carbonate (FEC) results in an electrolyte with high room temperature ionic conductivity (6.135 mS cm⁻¹). Variations in the discharge cut-off potential (DCP) provide valuable insights into the cycle stability of the cell. Cyclic voltammetry (CV), galvanostatic intermittent titration technique (GITT), and X-ray photoelectron spectroscopy (XPS) reveal that a DCP of 0.2 V allows for maintaining a stable discharge capacity by promoting the formation of Na₂S and reducing the formation of nucleophilic oligosulfides (S₂²⁻), thereby suppressing their reaction with carbonate-based solvents.^[28]

2. Results and Discussion

2.1. Electrochemical Stability of the Electrolyte

Na[B(hfip)₄]₃DME (DME = 1,2-dimethoxyethane) was synthesized as described in the literature.^[27] Its purity was confirmed by ¹H and ¹⁹F nuclear magnetic resonance (NMR) and by combustion elemental analysis (Figure S1, S2, Table S1). 1 M Na[B(hfip)₄] in EC : DMC (1:1) + 13 wt. % FEC was chosen as electrolyte. FEC can form a NaF-rich, stable SEI on Na, which prevents further electrolyte decomposition and allows dendrite-free cycling.^[29] Furthermore, FEC has lower binding energy with sodium polysulfides and can thus suppress polysulfide shuttling.^[30] The electrolyte was tested for its stability vs. oxidation with different current collectors to identify the potential window within which the cells could be cycled.^[31–32] Results from linear sweep voltammetry (LSV) of different working electrodes such as carbon-coated aluminum (typically used as a current collector for sulfur cathodes), copper, and platinum are shown in the I–U polarization curve (Figure 1). While the decomposition of the electrolyte on copper started at 3.21 V, the electrolyte was stable up to 4.65 V and 4.6 V using Pt and carbon-coated Al, respectively, demonstrating the compatibility of the electrolyte with conventional Al current collectors.

2.2. Electrochemical Performance

Since the sulfur is covalently bound to the carbon backbone in SPAN, long-chain polysulfide dissolution, which is responsible for the polysulfide shuttle effect and capacity fading, can be

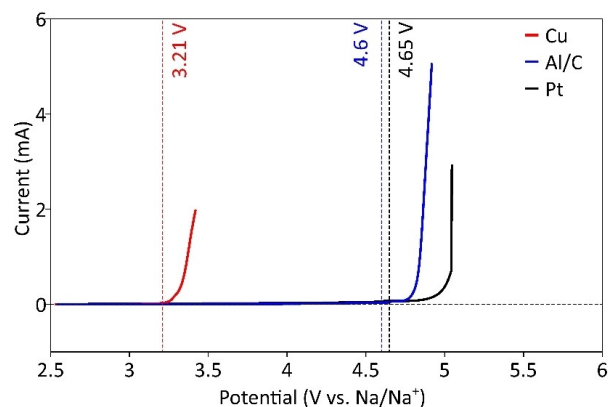


Figure 1. Stability of the electrolyte vs. oxidation as determined by LSV at a scan rate of 2 mV s⁻¹ with Pt, Cu, and Al/C and Na, both as a reference and counter electrode.

avoided. Fourier-transform infrared spectroscopy (FTIR) shows the cyclization chemistry and sulfur incorporation during SPAN synthesis (Figure S3).

Different electrochemical tests were performed to evaluate the compatibility of the electrolyte with the Na anode and the SPAN cathode. First, galvanostatic cycling tests were conducted with Swagelok-type cells to assess the performance and electrochemical properties of Na-SPAN batteries. Cells were cycled between 0.2–3 V vs. Na/Na⁺ at alternating C rates. Figure 2a and Figure 2b show the galvanostatic cycling of the cell and the corresponding voltage curve at a C-rate of 0.2 C (340 mA g_s⁻¹). Notably, the experimentally determined capacity of the Na-SPAN cell (> 1500 mAh g_s⁻¹) is near the theoretical capacity of the final discharge product Na₂S, indicating sulfur is reduced to sulfide (S²⁻). Also, the capacity decay was as low as 0.033% per cycle, resulting in good reversibility of the system with virtual 100% coulombic efficiency as calculated from the ratio of discharge over charge capacities at the corresponding cycle. The voltage vs. capacity curve provides insights into the redox reactions and the corresponding potential plateaus (Figure 2b). The first complete discharge curve shows the highest capacity of 2341 mAh g_s⁻¹, attributable to electrolyte decomposition and SEI formation.^[33] The capacity loss and voltage hysteresis in the first cycle is caused by irreversible reactions occurring at the anode and the poor electrical contact between SPAN and the carbon particles.^[34] The overall capacity decreases slightly at the beginning of the cycling but fully recovers up to the 50th cycle, which indicates that the activation process occurred in the cathode during continuous cycling. During the 2nd discharge, the plateau shows a two-step reduction reaction at 1.84 V and 1.08 V (Figure 2b, green curve), corresponding to the formation of Na polysulfides (Na₂S_x; 2 ≤ x ≤ 4) and Na₂S, respectively.^[35] Due to the sluggish redox kinetics of Na₂S, a steeper curve appears at the end of the discharge plateau, indicative for slow solid-state reaction kinetics.

A similar deep discharge cut-off potential (0.1 V) was already reported for Na–S batteries based on an FEC-containing electrolyte and also in hybrid Na-ion-sulfur cells.^[36] As outlined

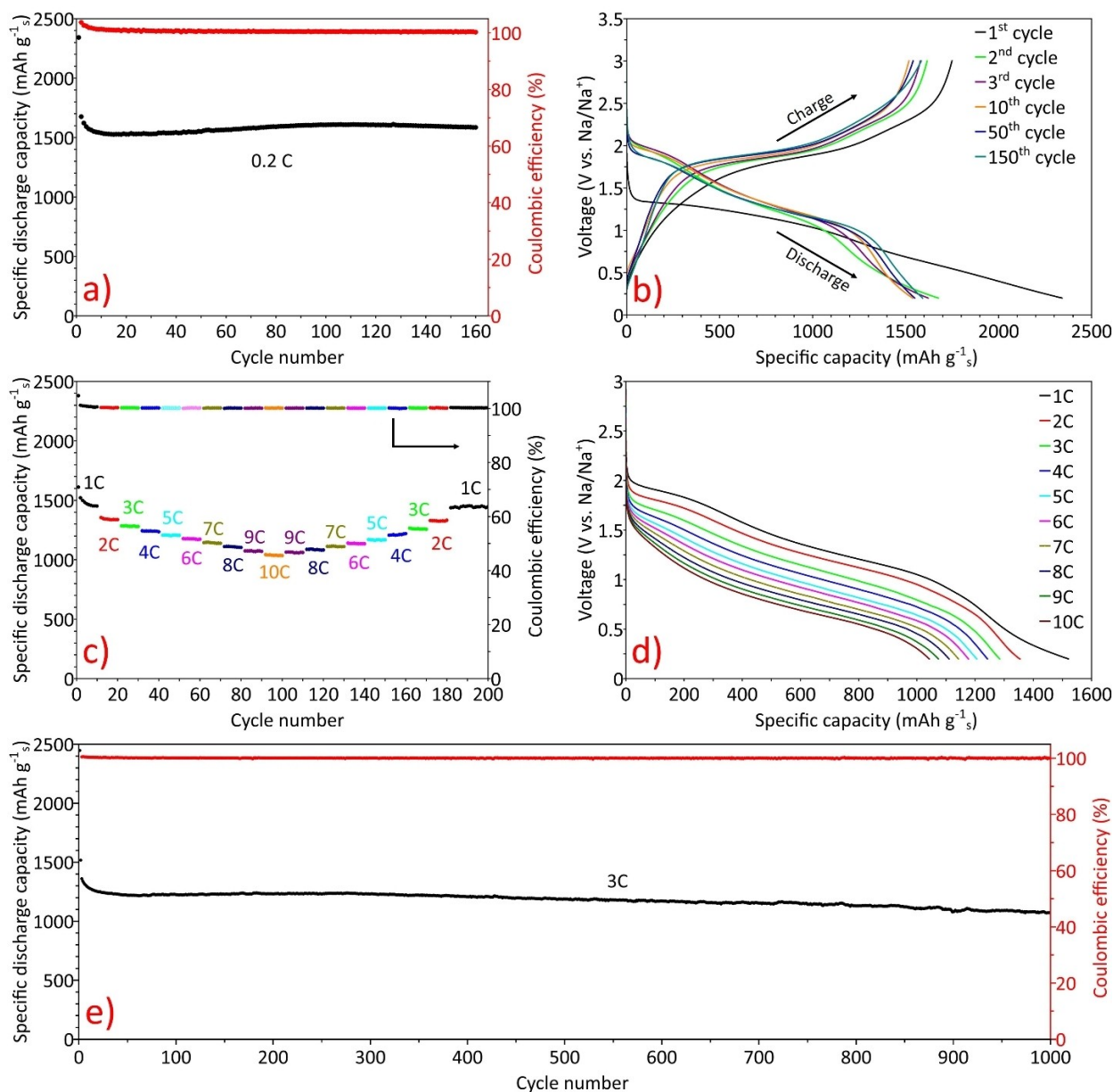


Figure 2. Electrochemical performance of a $\text{Na}[\text{B}(\text{hfp})_4]$ -based electrolyte in a Na-SPAN cell, a) galvanostatic cycling stability (black) and coulombic efficiency (red) at 0.2 C for 160 cycles; b) charge/discharge voltage profiles at 0.2 C during the 1st (black), 2nd (green), 3rd (purple), 10th (orange), 50th (blue) and 150th cycle (light blue); c) rate performances of the cathode ranging from 1 C to 10 C; d) voltage profiles at various C rates (1 C – 10 C) extracted from the rate capability test (Figure 2c); e) long-term galvanostatic cycling stability (black) and coulombic efficiency (red) at 3 C (5.025 A g_s^{-1}) over 1000 cycles.

earlier, the FEC additive plays an important role in stabilizing the anode surface, thereby preventing undesirable side reactions.^[29,37]

Figure 2c and Figure 2d show the high-rate capability of Na-SPAN cells with different current densities ranging from 1–10 C and their respective voltage profiles. Capacities of 1450, 1337, 1279, 1235, 1204, 1172, 1138, 1102, 1069, 1034 mAh g_s^{-1} were obtained at 1, 2, 3, 4, 5, 6, 7, 8, 9, and 10 C, respectively, with virtually 100% coulombic efficiency. Upon returning to a discharge rate of 1 C after 180 cycles, the discharge capacity almost fully restored, demonstrating excellent stress endurance of the SPAN cathode. The cell also exhibits exceptionally good rate performance at a high current density of 10 C, maintaining

1034 mAh g_s^{-1} . The high capacity at higher current, e.g. at 16.75 A g_s^{-1} , is a result of the high conversion rate both during charging and discharging. To the best of our knowledge, such high capacity and cycle stability of a Na–S cell have not been reported before.

A long-term cycling test (Figure 2e) was conducted with a high current density of 5.025 A g_s^{-1} (3 C). The cell showed stable cycling over 1000 cycles while maintaining a high coulombic efficiency of virtual 100%. The Na-SPAN cell displayed an initial stable capacity of $1360 \text{ mAh g}_s^{-1}$ and maintained a capacity of $1072 \text{ mAh g}_s^{-1}$ at the end of the 1000th cycle with only 0.021% capacity decay per cycle. High reversibility and high capacity for longer cycling ascertain that

the electrolyte is compatible with the SPAN cathode. Commercially available salts such as sodium bis(trifluoromethylsulfonyl) imide (NaTFSI) and sodium trifluoromethanesulfonate (NaOTf) were compared with NaB(hfip)₄ to demonstrate the potential of salts with a WCA in Na–S batteries. Figure S4a and Figure S4c show a comparison of long-term cycling and rate capability of cells based on NaB(hfip)₄, NaTFSI and NaOTf, respectively. Overall, cells based on NaB(hfip)₄ show high capacity, stable capacity retention at an extremely high C-rate, and low overpotential (Figure S4b).

To assess the electrolyte compatibility with the sodium anode, a cycling test was carried out by assembling symmetrical Na || Na cells (Figure 3a). Current density and capacity

were maintained at 0.565 mA cm⁻² and 0.285 mAh cm⁻², respectively. The symmetric cells showed stable plating and stripping for at least 280 h. The initial perturbation in voltage during the first few Na-dissolution and -deposition steps are attributable to some electrolyte decomposition and SEI formation.^[38] In the first few cycles, the deposition/dissolution overpotential (Figure 3b) of the cell reached 0.27 V/0.28 V, decreasing to 0.19 V and 0.13 V, respectively, at the end of the 280th cycle. This decrease in overpotential points towards low activation energy needed for Na-deposition and -dissolution. Electrochemical impedance spectroscopy (EIS) of the symmetrical cells during cycling was used to get insight into the origin of the cell resistance. During the initial stage open-circuit voltage (OCV)

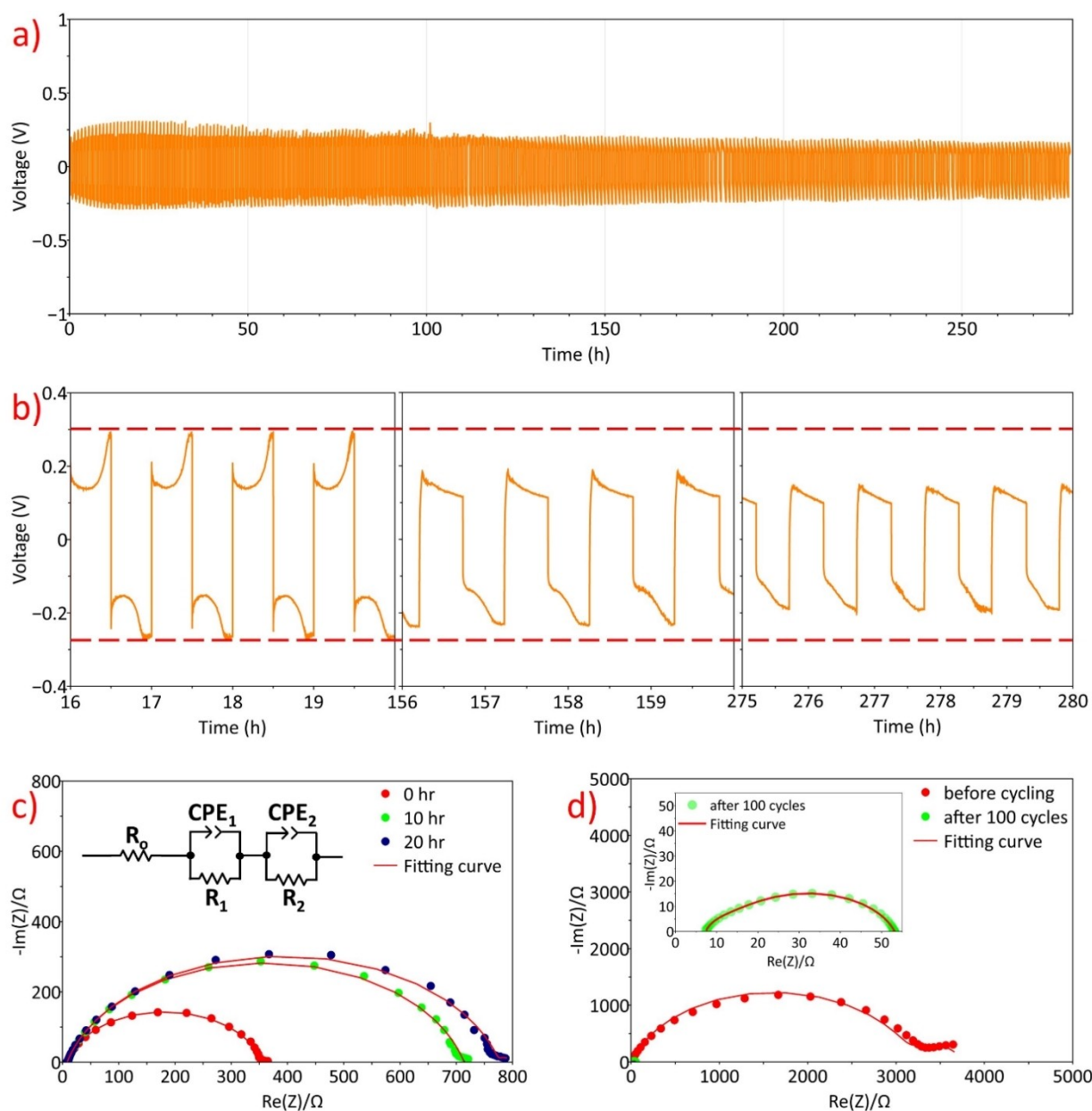


Figure 3. Electrochemical measurements of a symmetric Na || Na cell, a) Galvanostatic cycling voltage profiles at 0.565 mA cm⁻² (0.285 mAh cm⁻²); b) overpotential voltage profile at various times; c) impedance spectroscopy of a symmetric Na || Na cell at different OCV period (0th (red), 10th (green), 20th (blue)) (inset: equivalent circuit model); d) impedance before cycling (red) and after 100 cycles (green) (inset: zoom-in picture of impedance after 100 cycles).

period, the cell resistance increased due to the formation of the passivation (SEI) layer on the sodium surface. Freshly prepared cells showed a surface resistance (Figure 3c) of 350 Ω , 702 Ω , and 768 Ω after 0 h, 10 h and 20 h, respectively. This increase in cell resistance is directly related to the increase in SEI layer thickness with time. The equivalent circuit model used to fit the impedance data (shown in the inset of Figure 3c) contains R_0 , two constant phase elements CPE_1 and CPE_2 connected parallelly to the respective resistor (R_1 , R_2), with the two pairs ($i=1,2$) in series. The electrolyte/bulk resistance (R_0) together with the surface resistance ($R_1 + R_2$) describes both the SEI layer formation and charge-transfer resistance. Constant phase elements (CPE_1 and CPE_2) are used to describe the capacitance of the electrochemical double layer. Diffusion of Na^+ through the SEI layer at low frequency was avoided to fit the model accurately. Figure 3d shows the impedance of a symmetric Na | Na cell before the first cycle and after 100 cycles. Before cycling, the cell possesses a considerable surface resistance of 3221 Ω . However, after 100 cycles, a dramatically reduced surface resistance of 46.6 Ω was observed, attributable to an increase of the anode's surface area. This decrease in surface resistance suggests that the subsequent breakage and reformation of the SEI layer results in a larger surface area, which in turn helps to decrease the energy needed for stripping and plating. The rate performance of the symmetric cells was measured by applying current densities of 0.5, 1, 2, 3, and 4 mA cm^{-2} (Figure S5). A stable overpotential of 0.27, 0.31, 0.35 and 0.39 V, respectively, was observed for each current density. Only at higher current density (4 mA cm^{-2}), the overpotential increases rapidly, pointing towards the formation of an unstable SEI layer.^[39–40]

2.3. Impact of Discharge Cut-Off Potential on the Electrochemical Stability of the Cell

The oxidation and reduction potential as well as the reversibility and electrolyte stability of a Na-SPAN cell were deduced from CV applying a low scan rate of 0.1 mVs^{-1} .^[41] Concomitantly, the CV curves provide insights into the reaction kinetics based on the voltage applied and the corresponding current

density. The CV curves displayed in Figure 4a and Figure 4b reveal major differences during the sodiation/desodiation process when the DCP limits were fixed to 0.2 V and 0.5 V, respectively. During the first cycle applying a DCP of 0.2 V, two cathodic peaks are observed at 1.12 V and 0.51 V; these are shifted to higher potential, i.e. to 1.84 V and 1.08 V in the subsequent cycle. Similarly, applying a DCP of 0.5 V, one single reduction peak, though at a lower voltage (0.96 V), is observed during the first cycle. In a subsequent cycle, this peak shifted to 1.79 V and a second weak peak is observed at 1.25 V. The peak shifts during the second cycle go along with a considerable reduction in the polarization of the electrodes during cycling. During discharge, the peak at higher potential with both DCPs is attributable to the formation of Na_2S_x from SPAN, while the second peak indicates the formation of a mixture of Na_2S_2 and Na_2S .^[42] Upon charging, Na_2S is reconverted into polysulfides ($-\text{S}_x-$) at ca. 1.9 V and all sulfur is bound to SPAN in the fully charged state above 2.28 V vs. Na/Na^+ .^[34,43] Elemental analysis (Table S2) allows for calculating an atomic ratio between carbon and sulfur, revealing that SPAN contains C- S_x bonds with $x=3$ on average. Based on the atomic ratio between C and S, it can well be assumed that during discharge the intermediary-formed S_x -species predominantly exist in form of short-chain Na-polysulfides Na_2S_x ($2 \leq x \leq 3$). The main anodic peak current (2nd cycle, Figure 4a) at a DCP of 0.2 V (0.45 mA) is higher compared to the one at a DCP of 0.5 V (2nd cycle, 0.29 mA, Figure 4b). This can be explained by a high conversion rate during oxidation at low DCP. It is also reasonable to assign the small anodic peak at 2.32 V to the final conversion reaction to C- S_x . Since the same cathodic peak current is observed at both DCPs, very similar electrode kinetics must exist during the reduction of sulfur.

Next, the influence of different DCPs on mass transfer during cycling was investigated by CV applying different scan rates (Figure 5a, Figure 5b). Both graphs show that an increase in the scan rate results in an increase in the peak current. With increasing scan rate, the cathodic and anodic peaks shift towards a more negative and more positive potential (i.e., overpotential), respectively, pointing towards a mixed mass transfer mechanism comprising both a diffusion-controlled and a charge-transfer controlled process.^[44] At higher scan rates and

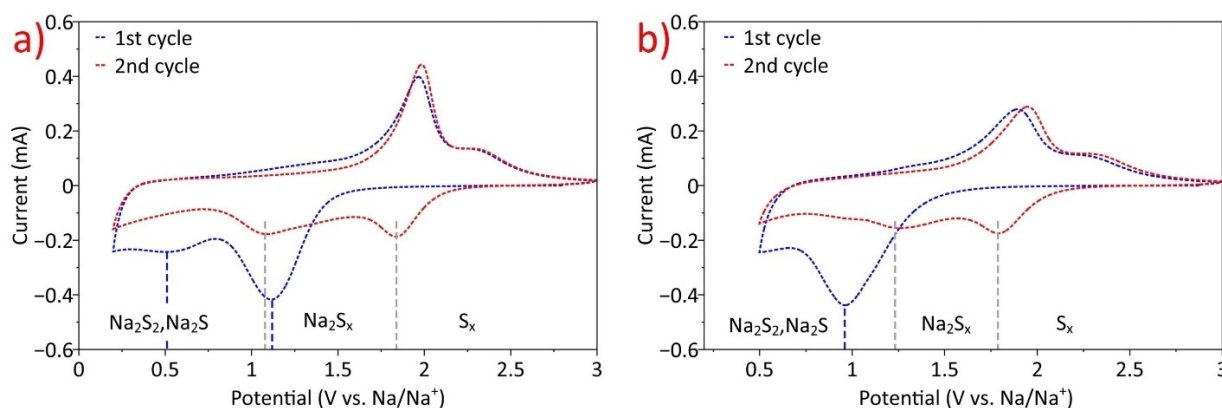


Figure 4. Cyclic voltammograms of a Na-SPAN cell recorded at the scan rate of 0.1 mVs^{-1} with different voltage windows, a) 0.2–3 V; b) 0.5–3 V.

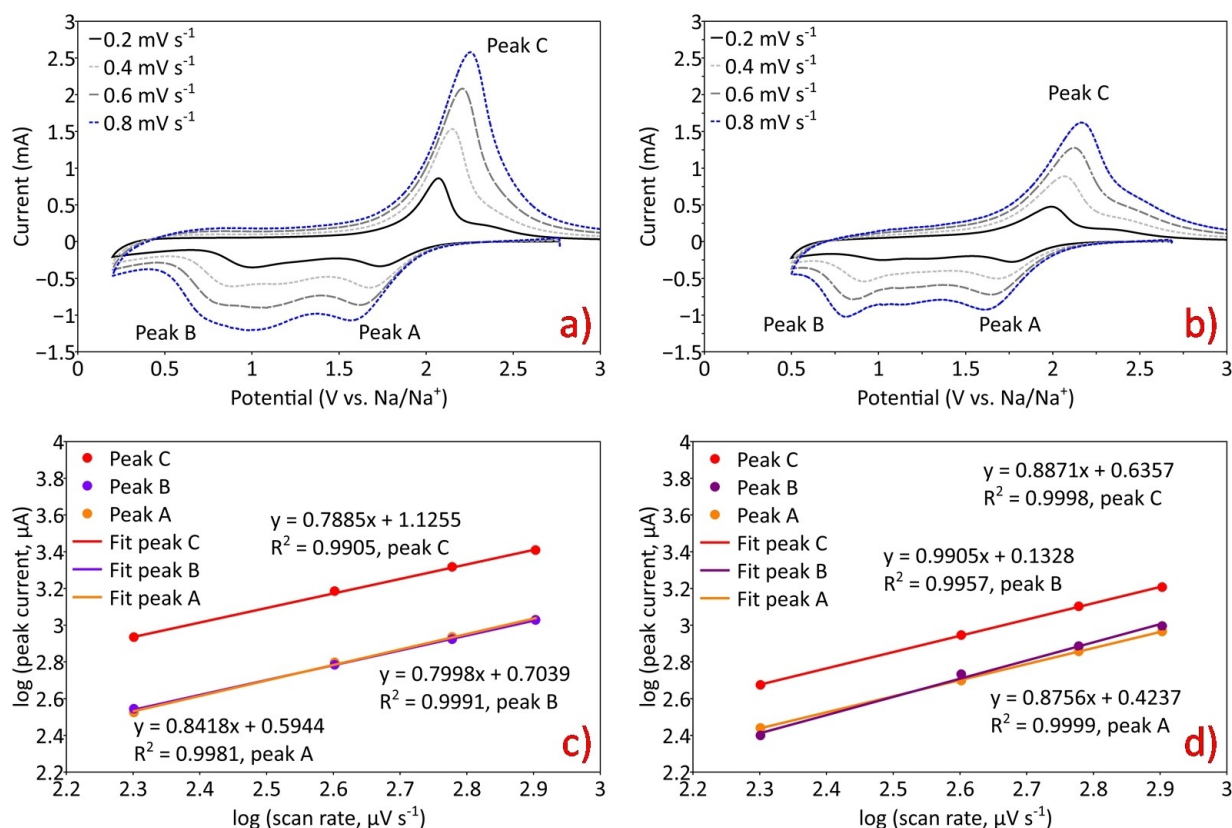


Figure 5. Cyclic voltammograms of Na-SPAN cells with different cut-off potentials, a) 0.2–3 V; b) 0.5–3 V at varying scan rates. Double logarithmic plots of current vs. scan rate for (peak A (orange), peak B (purple), peak C (red)), c) 0.2–3 V; and d) 0.5–3 V.

a DCP of 0.2 V, despite having a wide reduction potential at peak B, the current increases significantly compared to a DCP of 0.5 V (Figure 5a and Figure 5b). We tentatively ascribe this to a predominant solid-state conversion of intermediary Na-polysulfides into Na₂S.^[45–46] At a higher scan rate (0.8 mV s⁻¹), CV measurements with a DCP of 0.5 V show a larger potential gap between the main anodic and cathodic peak (157 mV) than CV measurements carried out at a DCP of 0.2 V (143 mV). An increase in the reduction onset potential and a decrease in the oxidation onset potential towards lower polarization and accelerated polysulfide conversion at the peak voltage.^[47] Vice versa, an insufficient conversion of sulfur leads to a lower anodic peak current (peak C, Figure 5b) at a DCP of 0.5 V, whereas a sharp peak at a DCP of 0.2 V is a result of high conductivity and high conversion (Peak C, Figure 5a). The oxidation peak at 2.35 V becomes insignificant as the scan rate increases, suggesting mass transfer limitations.

Since the DCP is of particular interest in this study, peak B in Figure 5a and Figure 5b was chosen to compare the reaction kinetics near the DCP. Using the Randles-Ševčík equation (Eq. S1),^[48] the electrode processes can be determined through the relation between the peak current and the scan rate. Figure S6a and Figure S6b show a plot of the peak current, I (mA) vs. the square root of the scan rate, $\nu^{1/2}$ (V^{1/2} s^{-1/2}) with a good linear fit without intercepting origin, which is typical for a diffusion-controlled reaction.^[49] The slope of the peak B at a DCP of 0.5 V (Figure S6b) was higher than the one at a DCP of 0.2 V

(Figure S6a), suggesting fast electrochemical kinetics. Nevertheless, a double logarithmic plot of I vs. ν (Figure 5c and Figure 5d) shows a linear relationship, indicating that the redox reaction is also controlled by adsorption processes.^[50] The gradient of the linear curve from the double logarithmic plot can be used to assess the contribution of the diffusion-controlled and surface-adsorption mass transfer process. Generally, mass transfer in a diffusion-controlled process is slower than the surface adsorption process. On the base of the semi-infinite diffusion-based Randles-Ševčík equation, the gradient close to 0.5 is indicative for a diffusion-controlled process. However, this slope can vary up to 1.0 for an adsorption process or a surface reaction, which is not uncommon for SPAN composites in which a redox reaction occurs with surface-bound S-moieties.^[51–52] And indeed, for peak B, at a DCP of 0.2 V, the slope was 0.8 (Figure 5c), indicating mixed diffusion and interface-controlled mass transfer reactions. By contrast, for peak B at a DCP of 0.5 V (Figure 5d), a slope of 0.99 was observed, strongly suggesting that the redox reactions occur virtually solely with surface-bound C–S_x/S–S species. Moreover, the slope near unity reconfirms that the reaction kinetics emerge from fast Na⁺ ion transfer near the cut-off potential. This fast kinetics are a result of the fast reaction of electrode surface-adsorbed species that react immediately upon application of the potential step, whereas bulk species would have to diffuse to the electrode surface prior to reaction. This is also

supported by the sharp cathodic peak (Figure 5b) at a DCP of 0.5 V (peak B).

Figure 6a shows the galvanostatic cycling of two Na-SPAN cells at a DCP of 0.2 V and 0.5 V, respectively. Long-term battery tests with these two DCPs illustrate the stability of the cells and the high reversibility at 3 C. Even though both cells have high coulombic efficiencies of virtually 100%, cycling at a DCP of 0.5 V unveils a constant capacity decay from the beginning resulting in a specific discharge capacity of 541 mAh g⁻¹ after 500 cycles. This corresponds to an average capacity decay of 0.091% per cycle, which is almost four times higher than the average capacity decay observed at a DCP of 0.2 V (1187 mAh g⁻¹ at the end of the 500th cycle), which was 0.025% per cycle. This fast decay in capacity can be attributed to the formation of larger amounts of intermediary polysulfides such as S₂²⁻, S₄²⁻ at a DCP of 0.5 V while mostly stable/inert Na₂S forms at a DCP of 0.2 V, respectively. Figure 6b shows the 5th cycle of a charge-discharge curve at two different DCPs. Specific discharge capacities of 977 and 1314 mAh g⁻¹, corresponding to the formation of Na₂S₂ and Na₂S,^[53] respectively, were obtained at a DCP of 0.5 and 0.2 V. Since Na₂S formation is sluggish, the voltage curve at a DCP of 0.2 V shows a small bump at 0.75 V (indicated by the dotted oval in Figure 6b) and then converges steeply at the end of the discharge. This behavior is well supported by the CV results suggesting that the broad peak at the end of the discharge (peak B, Figure 5a) is indeed related to the formation of Na₂S. Using a DCP of 0.2 V also results in a reduced polarization, demonstrated by improved redox reactions during cycling as compared to a DCP of 0.5 V. In contrast to a DCP of 0.2 V in Figure 2c, the rate capability at a DCP of 0.5 V (Figure S7) results in a very sharp decrease in specific discharge capacity at a high current. At high current density (16.75 A g⁻¹) mass transfer limitation rather leads to the formation of short-chain polysulfides than of Na₂S. These short-chain polysulfides are responsible for the fast capacity decay since they can react with the carbonate-based solvent.^[28,54–55]

Next, GITT was used to acquire kinetic data of the sodiation and desodiation process. The diffusion coefficient of Na⁺ in the cathode at DCPs of 0.2 V and 0.5 V, respectively, can be

determined by applying current pulses followed by relaxation for a defined time (Figure S8a). Initial pre-formation cycles ensured full interface wetting of the electrodes of the Na-SPAN full cell with electrolyte. Figure 7a shows the sodiation and desodiation process for depths-of-discharge (DOD) and states-of-charge (SOC) between zero and 100%. The GITT equilibrium discharge curve shows two reduction potential plateaus, corroborating the results from CV and voltage vs. capacity curves (Figure 4a and Figure 6b). The relaxation voltage (V_{relax}) (Figure S8b) during discharge shows a peak at 0.65 V and then gradually decreases. An increase in relaxation voltage near 0.5 V potentially points towards compositional inhomogeneity (Figure S8b), which can indeed be hypothesized by the surface-controlled reaction at a DCP of 0.5 V (Figure 5d).^[56] This might initiate the conversion of surface-bound or adsorbed species at first, which eventually forces the inner domain species to react later during galvanostatic cycling. The diffusion coefficient of Na⁺ (D_{Na^+}) at different charge/discharge states can be determined by the transient voltage response theory using the Weppner and Huggins equation [Equation (S1)].^[57] From Figure 7b, we deduce that at a discharge potential (U) of 0.5 V the cell exhibits a D_{Na^+} value of $2.6 \cdot 10^{-12}$ cm² s⁻¹. On the other hand, a D_{Na^+} value of $4.7 \cdot 10^{-13}$ cm² s⁻¹ was obtained at $U = 0.2$ V, which is about one order of magnitude lower than at $U = 0.5$ V. This higher diffusion coefficient at a discharge potential of 0.5 V supports a surface-controlled reaction as suggested by the double logarithmic plot (peak B, Figure 5d). From the consolidated data on diffusion, D_{Na^+} at a discharge potential of 0.2 V is the lowest in the entire discharge process. One can speculate that Na₂S crystals that form upon discharge to 0.2 V block the ion channels, thereby impeding the diffusion of Na⁺ into the cathode. Figure 7c also shows that during charging high diffusion values for Na were noticed at 2.2 V ($D_{Na^+} = 3.6 \cdot 10^{-12}$ cm² s⁻¹), indicating intermediate polysulfide conversion (peak C, Figure 5a and Figure 5b).

EIS at different charge and discharge voltages during cycling provides further evidence that Na₂S formation is responsible for the decrease in D_{Na^+} . As can be seen in Figure S9a, the charge transfer resistance (R_{ct}) decreases during charging due to the fact that Na₂S/Na₂S₂ are converted back to

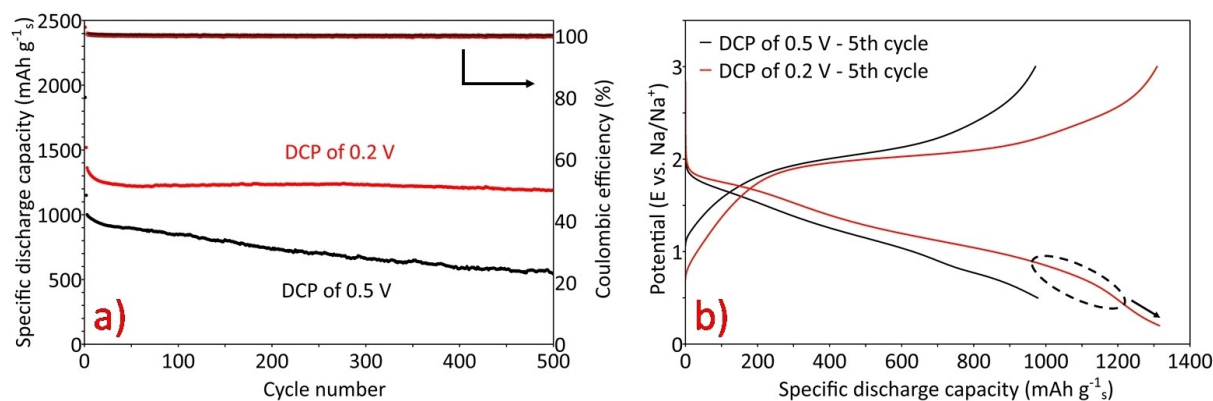


Figure 6. Galvanostatic cycling stability of a Na-SPAN cell (at 3 C) with two different DCPs, a) 0.2 V (red), 0.5 V (black), and b) the corresponding voltage profiles (charging and discharging) after the 5th cycle (dotted oval shows voltage bump at 0.75 V).

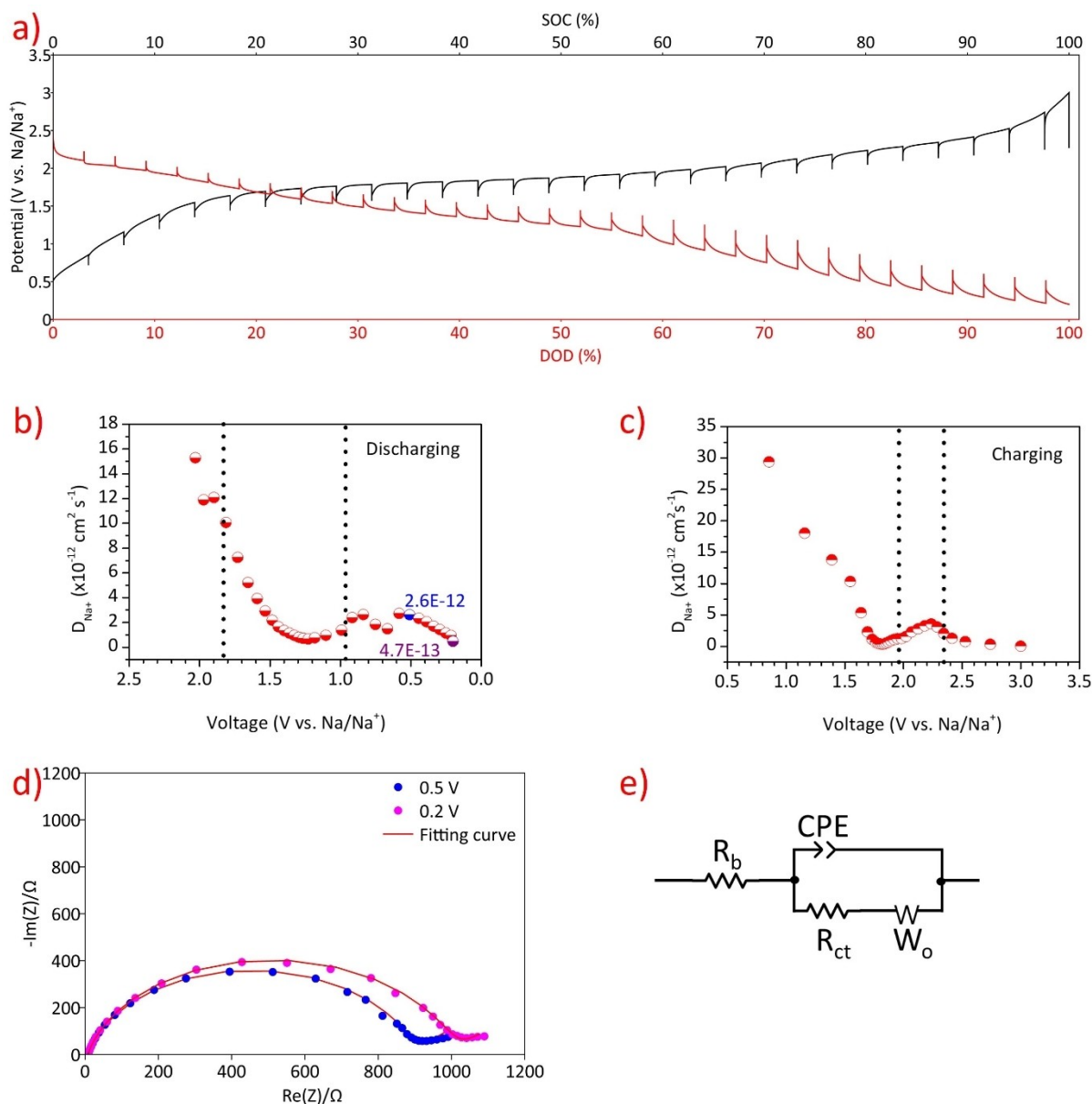


Figure 7. a) GITT pulses applied for 20 min at 0.1 C followed by 2 h relaxation. b, c) calculated diffusion coefficient at various potentials (b) during discharge (the values for 0.5 V and 0.2 V are indicated in blue and purple, respectively) and c) during charging, d) EIS of the discharged cathode at 0.5 V (purple) and 0.2 V (pink) and e) their equivalent circuit model (R_b -bulk resistance, CPE-constant phase element, R_{ct} -charge transfer resistance, W_o -Warburg impedance).

polysulfides and then to SPAN-bound sulfur, C-S_x. By contrast, the electrolyte or bulk resistance (R_b) of the cell is almost the same (8.1 Ω), both during charge and discharge. Discharge of the cell leads to an increase in R_{ct} since C-S_x moieties are converted into electronically insulating solid Na₂S (Figure S9b). The impedance of two voltage points at 0.5 V and 0.2 V during discharge and their corresponding equivalent circuit are shown in Figure 7d and Figure 7e. Impedance at 0.5 V shows a lower R_{ct} (884.6 Ω) than at 0.2 V (R_{ct} =993.3 Ω , Table 1). This difference in impedance can be attributed to the comparably large amount of polysulfides, which have a lower R_{ct} than electrically insulating solid Na₂S, which accumulates on the cathode, leading to poor charge transfer of the ions.

Table 1. Bulk resistance (R_b) and charge transfer resistance (R_{ct}) of Na-SPAN cell at a different discharge potential.

Discharge voltage [V]	R_b [Ω]	R_{ct} [Ω]
0.5	8.1	884.6
0.2	8.1	993.3

To evaluate the surface species formed on the cathode after cycling, ex situ XPS measurements were carried out under ultra-high vacuum conditions. Figure 8a-d and Table 2 show the S 2p spectra and binding energies of four separate SPAN cathodes in the pristine, charged, and two discharged states (DCP=0.5 V and 0.2 V). Due to spin-orbit splitting, every sulfur species exhibits a 2p_{3/2} and 2p_{1/2} component. In the following,

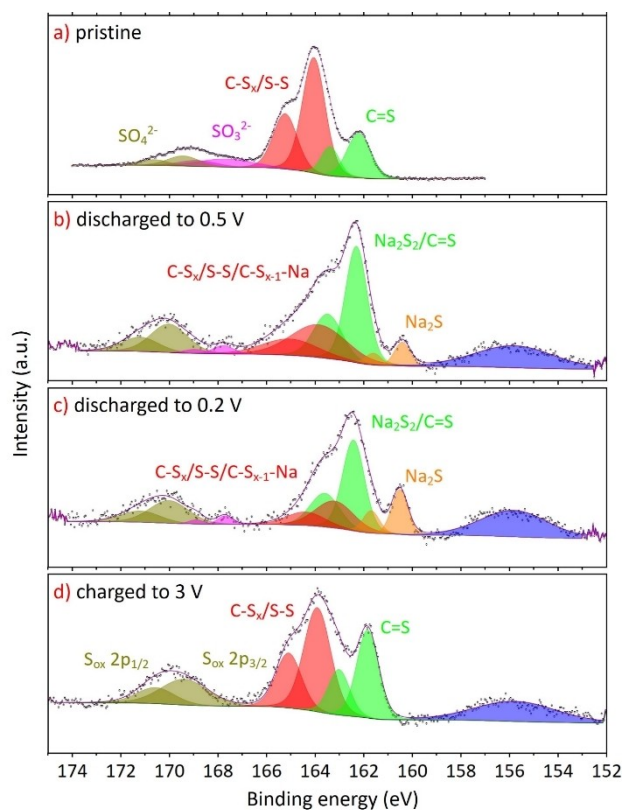


Figure 8. Sulfur S 2p ex situ XPS spectra of SPAN cathodes at different states (from top to bottom): pristine, discharged to 0.5 V, discharged to 0.2 V and charged to 3 V.

	Na ₂ S	C=S, Na ₂ S ₂	C-S _x , S-S, C-S _x -Na	SO ₃ ²⁻	SO ₄ ²⁻	S _{ox}
Pristine	–	162.2	164.0	167.7	169.5	–
Charged 3 V	–	161.8	163.9	–	–	169.4
Discharged 0.5 V	160.4	162.3	163.7	167.8	169.9	–
Discharged 0.2 V	160.5	162.4	163.3	167.7	169.9	–

we only discuss the position of the S 2p_{3/2} peaks (note that the fitted components for both angular momenta are included in the figure). The pristine SPAN cathode (Figure 8a) showed the typical signals for C=S, C-S_x/S-S bonds. The S 2p_{3/2} signals at 162.2 eV can be assigned to C=S and the peak at 164.0 eV can be assigned to S-S/C-S_x moieties.^[11,35, 58] Sulfate or thiosulfate species are observed at 166–172 eV.^[30,59–60] The charged cathode (Figure 8d) shows similar sulfur components except for the thiosulfates, which were probably oxidized to sulfate during charging.

Figure 8b and Figure 8c show the S 2p regions for discharged cathodes at 0.5 V and 0.2 V. The same chemical components for the two cathodes are visible although their relative intensities differ. It is obvious that a new component at the low binding energy side (160.5 eV) appears for the discharged cathodes. We relate this to the formation of Na₂S.^[43,61] Please note that the peak between 152 and 158 eV

observed on the cycled cathodes can be related to the Si 2s signal, which stems from the glass fiber.^[62]

The signal of Na₂S₂, which formed upon discharge, is overlapping with the C=S signal (binding energy around 162 eV). Since we cannot exclude that parts of the SPAN did not react with the Na upon discharge it is impossible to discriminate between these two different species. The same holds true for the polysulfide species around 164 eV which might be bound to C or Na. However, a shift towards lower binding energies and an increase of the full width at half maximum for the cathode discharged to 0.5 V and 0.2 V might indicate that this peak contains different chemical species like C-S_{x-1}-Na and C-S_x/S-S. Nonetheless, it is clearly visible that the amount of Na₂S (peak colored orange at 160.5 eV) for the sample discharged at 0.2 V is higher than for the sample discharged at 0.5 V (15.6% of the whole S 2p intensity for DCP of 0.2 V and 6.1% for DCP of 0.5 V). Figure S10 shows the absence of a Na-C bond, indicating that sodiation of carbon is not preferred even at a low DCP of 0.2 V.

Scanning electron microscopy (SEM) images (Figure S11a and Figure S11b) show the differences between a pristine and an SPAN cathode discharged to 0.2 V. The pristine cathode contains smaller particles with large pore space in-between. Poor dispersibility of carbon particles is visible in form of large agglomerates. The discharged cathode shows less pore space with larger crystals, indicating Na₂S formation. Energy-dispersive X-ray spectroscopy (EDX) measurements (Figure S12) reveal a high intensity of the sulfur signal in the pristine cathode and high intensity of sodium in the discharged cathode. To detect any potential formation of elemental sulfur after charging, the SPAN cathode was cycled 10 times and then analyzed by powder X-ray diffraction (XRD). Figure S13a and Figure S13b show both pristine and cycled SPAN cathodes (10 cycles) with no sign of crystalline sulfur formation. A broad signal between 2θ = 15° to 25° stems from the turbostratic structure of the carbon (002) backbone in carbonized PAN. A small reflection at 2θ = 20.1° indicates the limited crystalline nature of Na-CMC (binder).^[63] Orthorhombic S₈ (2θ = 23°, 222) embedded in the PAN structure loses its crystallinity during sulfurization. From Figure S13c, it is evident that both the cycled and pristine samples showed no additional reflections that would indicate the formation of another crystalline phase. Notably, both pristine and cycled SPAN have a broad signal at 2θ = 20°, however, its intensity is higher in the pristine sample than in the cycled cathode, indicating some structural changes of SPAN during the first discharge. Alternatively, differences in intensity can be attributed to differences in cathode binder distribution.

3. Conclusions

In summary, a cycle stable room temperature Na-S battery was developed using a Na anode, a SPAN cathode and a carbonate-based electrolyte containing the WCA salt Na[B(hfip)₄]. The electrolyte based on 1 M Na[B(hfip)₄] in EC : DMC + 13 wt. % FEC showed a high ionic conductivity of 6.1 mS cm⁻¹ and high

anodic stability of 4.6 V on an Al/C current collector. Na-SPAN cells employing a WCA-based electrolyte exhibited superior rate capability and delivered a discharge capacity of 1072 mAh g_s⁻¹ at 3 C (5.025 A g_s⁻¹) after cycling for 1000 cycles. The GITT measurements revealed a high conversion from polysulfides to solid and non-conductive Na₂S at 0.2 V compared to 0.5 V, which was confirmed by a lower diffusion coefficient of Na⁺ (D_{Na^+}) at lower potential (0.2 V). The favored formation of Na₂S at a DCP of 0.2 V compared to a DCP of 0.5 V was also confirmed by XPS measurements. The capacity decay at a DCP of 0.5 V is likely a result of the reaction between the carbonate-based electrolyte with the polysulfides formed when the cell is cycled between 0.5–3 V. We strongly believe that the use of other non- or weakly-coordinating anions in RT Na–S batteries will open new directions in the development of high energy density, high capacity and fast-charging batteries.

Experimental Section

3.1. Synthesis of Na[B(hfip)₄]

A slightly modified synthetic protocol was used for the synthesis of Na[B(hfip)₄].^[26] 3.0 g (79 mmol) of NaBH₄ were placed in a Schlenk flask filled with 250 ml of DME and the solution was cooled to 0 °C. 56.0 g (333 mmol) of hexafluoroisopropanol were added dropwise over 1 h via a dropping funnel under constant stirring. After the addition was completed, the solution was warmed to room temperature and stirred for another 1 h. Then, the temperature was increased slowly to 40 °C until H₂ evolution seized. To ensure complete conversion, the solution was refluxed overnight under vigorous stirring and then cooled to room temperature. The solvent was removed under vacuum, pentane was added and co-evaporated twice to remove most of the DME. Finally, the salt was dried at room temperature under vacuum (10⁻³ mbar) for 48 h and 24 h under ultra-high vacuum (10⁻⁹ mbar) at 30 °C. NMR (CD₃CN) and elemental analysis confirmed sufficient purity (see Figure S1, Figure S2 and Table S1).

3.2. Synthesis and Fabrication of SPAN Cathodes

1.5 g of poly(acrylonitrile) powder (PAN, $M_w = 150,000$ g/mol, Sigma-Aldrich, Germany) was placed inside a quartz tube containing sulfur (ca. 20 g, Carl Roth) and degassed with nitrogen. The tube was heated to 160 °C until all sulfur was molten. Next, the mixture was heated from room temperature to 550 °C for 3 h and then cooled to room temperature. A nitrogen flow of 200 L/h was applied during the entire process. The SPAN was then subjected to Soxhlet extraction in toluene for 48 h to remove all unreacted sulfur. Elemental analysis revealed a sulfur content of 38.18 ± 0.17 wt. % (see Table. S2). Next, a cathode slurry was prepared by mixing SPAN, carbon super C65 (MTI Corporation, USA), and Na-CMC binder (High viscosity, Sigma-Aldrich, Germany; 70:20:10, wt. %) in water using a planetary mixer (Thinky, Japan) at 2000 rpm for 5 min. The as-prepared slurry was coated on carbon-coated aluminum foil (16 μm, MTI Co., USA) with a wet thickness of 300 μm using doctor blading (Erichsen, Germany). The coating was dried overnight at 60 °C. Finally, cathodes 12 mm in diameter were punched out. The obtained average sulfur content per cathode was 0.6 mg.

3.3. Electrochemical characterization

Electrochemical tests were performed in Swagelok-type cells assembled in an Ar-filled glovebox (O₂, H₂O < 0.1 ppm). The electrolyte was prepared by dissolving 1 M Na[B(hfip)₄] in EC : DMC (1 : 1, vol. : vol.) and 13 wt. % FEC in a vial under stirring overnight followed by filtration and storage over 4 Å molecular sieves. The ionic conductivity of the electrolyte was measured with an InLab Sensor Conductometer (Mettler Toledo). Freshly cut sodium was pressed and rolled on a polyethylene surface and then cut into 12 mm disks. The cell was assembled in the following order: sodium foil, 120 μl of electrolyte, two wetted Whatman glass fiber separators (Ø = 13 mm), and the SPAN cathode.

Linear sweep voltammetry (LSV), cyclic voltammetry (CV), potentiostatic electrochemical impedance spectroscopy (PEIS), galvanostatic intermittent titration technique (GITT), and overpotential measurements were conducted using a Biologic VMP3 integrated frequency response analyzer (France). LSV was conducted in a three-electrode set-up applying a scan rate of 2 mV s⁻¹ with platinum, copper, and carbon-coated aluminum as working electrode and sodium as the reference and counter electrode. CV measurements were performed between 0.2–3 V and 0.5–3 V, respectively, using SPAN as working electrode and sodium as reference and counter electrodes. PEIS was performed at a constant voltage of 10 mV alternating current with frequencies ranging from 800 kHz to 100 mHz and the resulting impedance curves were fitted using the built-in Zfit library. GITT was performed by cycling the cells first at the C-rate of 0.5 for 5 cycles (0.2–3 V) followed by 0.1 C for 20 mins, followed by a 2 h relaxation period until the battery was fully charged/discharged. Symmetric Na || Na cells were used in overpotential measurements applying different current densities. Long-term cycling and rate performance testing of the cells was conducted on BasyTec XCTS-LAB systems (Germany). Galvanostatic cycling was performed at different C rates (1 C = 1672 mAh g_s⁻¹) with a voltage window between 0.2–3 V vs. Na/Na⁺. Unless mentioned otherwise, all cells were subjected to one preformation cycle at 0.3 C before testing. Rate capability testing was performed at varying C rates with ten cycles each between 1 C–10 C. For the analysis of the cut-off voltage effect on cycling, two different discharge cut-off potentials were chosen, i.e., 0.2–3 V and 0.5–3 V, respectively.

3.4. Material Characterization

XPS measurements were carried out after cycling the SPAN cathode-based cells for 30 cycles. Cathodes were washed with dimethyl carbonate (DMC) to remove excess electrolyte and then dried under vacuum at 40 °C. The samples then were transferred to the XPS system via an argon-filled transfer box to avoid exposure to air. A Kratos Axis Ultra system mounted with a monochromatic Al K_α X-ray source was used. High-resolution data were acquired with a pass energy of 20 eV. Peak fitting and calculation of the atomic concentrations of the sulfur were carried out using the CasaXPS processing software. For fitting the spin-orbit split of the S 2p_{3/2} and 2p_{1/2} peaks, the binding energy separation and area ratios were constrained to 1.18 eV and 2 : 1, respectively. SEM of the SPAN samples was performed with an Auriga-type field emission scanning electron microscope (Zeiss) equipped with EDX. XRD measurements were conducted on a Rigaku SmartLab using a 3 kW sealed Cu-tube (monochromatic K_{α1} emission, λ_{Cu} = 1.5406 Å) in the transmission mode.

Acknowledgments

We thankfully acknowledge funding and support from the German Federal Ministry for Economic Affairs and Energy (BMWi, project no. S50400, FiMaLiS). We thank Mr. J.V. Musso and Mr. Peter Schützendübe (MPI) and Mr. Jean-Louis Hoslauer (XRD measurement - Institute of Inorganic Chemistry) for fruitful discussions and Mr. U. Hageroth from the German Institute of Textile and Fiber Research (DIFT) Denkendorf for the SEM measurements. Open Access funding enabled and organized by Projekt DEAL.

Conflict of Interest

The authors declare no conflict of interest.

Keywords: sulfurated poly(acrylonitrile) (SPAN) · room-temperature sodium-sulfur battery · electrochemistry · weakly coordinating anions · X-ray photoelectron spectroscopy

- [1] B. Dunn, H. Kamath, J.-M. Tarascon, *Science* **2011**, *334*, 928.
- [2] L. Gaines, *Sustain. Mater. Technol.* **2014**, *1–2*, 2–7.
- [3] G. Nikiiforidis, M. C. M. van de Sanden, M. N. Tsampas, *RSC Adv.* **2019**, *9*, 5649–5673.
- [4] P. Adelhelm, P. Hartmann, C. L. Bender, M. Busche, C. Eufinger, J. Janek, *Beilstein J. Nanotechnol.* **2015**, *6*, 1016–1055.
- [5] P. K. Nayak, L. Yang, W. Brehm, P. Adelhelm, *Angew. Chem. Int. Ed.* **2018**, *57*, 102–120; *Angew. Chem.* **2018**, *130*, 106–126.
- [6] Z. Yang, J. Zhang, M. C. Kintner-Meyer, X. Lu, D. Choi, J. P. Lemmon, J. Liu, *Chem. Rev.* **2011**, *111*, 3577–3613.
- [7] Y.-X. Wang, B. Zhang, W. Lai, Y. Xu, S.-L. Chou, H.-K. Liu, S.-X. Dou, *Adv. Energy Mater.* **2017**, *7*, 1602829.
- [8] R. Mukkablá, M. R. Buchmeiser, *J. Mater. Chem. A* **2020**, *8*, 5379–5394.
- [9] J. Wang, J. Yang, J. Xie, N. Xu, *Adv. Mater.* **2002**, *14*, 963–965.
- [10] J. Fanous, M. Wegner, J. Grimming, M. Rolff, M. B. M. Spera, M. Tenzer, M. R. Buchmeiser, *J. Mater. Chem.* **2012**, *22*, 23240–23245.
- [11] M. Frey, R. K. Zenn, S. Warneke, K. Müller, A. Hintennach, R. E. Dinnebie, M. R. Buchmeiser, *ACS Energy Lett.* **2017**, *2*, 595–604.
- [12] J. Fanous, M. Wegner, J. Grimming, Å. Andresen, M. R. Buchmeiser, *Chem. Mater.* **2011**, *23*, 5024–5028.
- [13] J. Fanous, M. Wegner, M. B. M. Spera, M. R. Buchmeiser, *J. Electrochem. Soc.* **2013**, *160*, A1169–A1170.
- [14] J. Xiang, Z. Guo, Z. Yi, Y. Zhang, L. Yuan, Z. Cheng, Y. Shen, Y. Huang, *J. Energy Chem.* **2020**, *49*, 161–165.
- [15] J. Ye, F. He, J. Nie, Y. Cao, H. Yang, X. Ai, *J. Mater. Chem. A* **2015**, *3*, 7406–7412.
- [16] T. Leberher, M. Frey, A. Hintennach, M. R. Buchmeiser, *RSC Adv.* **2019**, *9*, 7181–7188.
- [17] S. Warneke, A. Hintennach, M. Buchmeiser, *J. Electrochem. Soc.* **2018**, *165*, A2093–A2095.
- [18] J. Wang, J. Yang, Y. Nuli, R. Holze, *Electrochem. Commun.* **2007**, *9*, 31–34.
- [19] M. S. Syali, D. Kumar, K. Mishra, D. K. Kanchan, *Energy Storage Mater.* **2020**, *31*, 352–372.
- [20] A. Shyamsunder, W. Beichel, P. Klose, Q. Pang, H. Scherer, A. Hoffmann, G. K. Murphy, I. Krossing, L. F. Nazar, *Angew. Chem. Int. Ed.* **2017**, *56*, 6192–6197; *Angew. Chem.* **2017**, *129*, 6288–6293.
- [21] K.-C. Lau, T. Seguin, E. Carino, N. Hahn, J. Connell, B. Ingram, K. Persson, K. Zavadil, C. Liao, *J. Electrochem. Soc.* **2019**, *166*, A1510–A1519.
- [22] J. T. Herb, C. A. Nist-Lund, C. B. Arnold, *ACS Energy Lett.* **2016**, *1*, 1227–1232.
- [23] H. Tokuda, M. Watanabe, *Electrochim. Acta* **2003**, *48*, 2085–2091.
- [24] S. Tsujioka, B. Nolan, H. Takase, B. Fauber, S. Strauss, *J. Electrochem. Soc.* **2004**, *151*, A1418–A1423.
- [25] H. Tokuda, S.-i. Tabata, M. A. B. H. Susan, K. Hayamizu, M. Watanabe, *J. Phys. Chem. B* **2004**, *108*, 11995–12002.
- [26] I. Krossing, *Comprehensive Inorganic Chemistry II (Second Edition): From Elements to Applications* **2013**, *1*, 681–705.
- [27] S. Bulut, P. Klose, I. Krossing, *Dalton Trans.* **2011**, *40*, 8114–8124.
- [28] J. Gao, M. A. Lowe, Y. Kiya, H. D. Abruña, *J. Phys. Chem. C* **2011**, *115*, 25132–25137.
- [29] X. M. Zhao, Q. Zhu, S. D. Xu, L. Chen, Z. J. Zuo, X. M. Wang, S. B. Liu, D. Zhang, *J. Electroanal. Chem.* **2019**, *832*, 392–398.
- [30] X. Xu, D. Zhou, X. Qin, K. Lin, F. Kang, B. Li, D. Shanmukaraj, T. Rojo, M. Armand, G. Wang, *Nat. Commun.* **2018**, *9*, 3870.
- [31] A. Bhide, J. Hofmann, K. A. Dürr, J. Janek, P. Adelhelm, *Phys. Chem. Chem. Phys.* **2014**, *16*, 1987–1998.
- [32] J. Kasnatscheew, B. Streipert, S. Röser, R. Wagner, I. Cekić Lasković, M. Winter, *Phys. Chem. Chem. Phys.* **2017**, *19*, 16078–16086.
- [33] E. Markevich, G. Salitra, Y. Talyosef, F. Chesneau, D. Aurbach, *J. Electrochem. Soc.* **2017**, *164*, A6244–A6253.
- [34] S. Zhang, *Energies* **2014**, *7*, 4588–4600.
- [35] Z.-Q. Jin, Y.-G. Liu, W.-K. Wang, A.-B. Wang, B.-W. Hu, M. Shen, T. Gao, P.-C. Zhao, Y.-S. Yang, *Energy Storage Mater.* **2018**, *14*, 272–278.
- [36] A. K. Haridas, J. Heo, X. Li, H.-J. Ahn, X. Zhao, Z. Deng, M. Agostini, A. Matic, J.-H. Ahn, *Chem. Eng. J.* **2020**, *385*, 123453.
- [37] M. Liu, D. Zhou, Y.-B. He, Y. Fu, X. Qin, C. Miao, H. Du, B. Li, Q.-H. Yang, Z. Lin, T. S. Zhao, F. Kang, *Nano Energy* **2016**, *22*, 278–289.
- [38] Y. Lu, Z. Tu, L. A. Archer, *Nat. Mater.* **2014**, *13*, 961–969.
- [39] L. Qin, H. Xu, D. Wang, J. Zhu, J. Chen, W. Zhang, P. Zhang, Y. Zhang, W. Tian, Z. Sun, *ACS Appl. Mater. Interfaces* **2018**, *10*, 27764–27770.
- [40] G. Bieker, M. Winter, P. Bieker, *Phys. Chem. Chem. Phys.* **2015**, *17*, 8670–8679.
- [41] X. Huang, Z. Wang, R. Knibbe, B. Luo, S. A. Ahad, D. Sun, L. Wang, *Energy Technol.* **2019**, *7*, 1801001.
- [42] S. Ma, P. Zuo, H. Zhang, Z. Yu, C. Cui, M. He, G. Yin, *Chem. Commun. (Camb.)* **2019**, *55*, 5267–5270.
- [43] A. Y. S. Eng, D.-T. Nguyen, V. Kumar, G. S. Subramanian, M.-F. Ng, Z. W. Seh, *J. Mater. Chem. A* **2020**, *8*, 22983–22997.
- [44] F. Scholz, *Electroanalytical Methods, Vol. 1*, Springer, **2010**.
- [45] D. Kumar, D. K. Kanchan, S. Kumar, K. Mishra, *Mater. Sci. Technol.* **2019**, *2*, 117–129.
- [46] I. Bauer, M. Kohl, H. Althues, S. Kaskel, *Chem. Commun. (Camb.)* **2014**, *50*, 3208–3210.
- [47] Y. Tao, Y. Wei, Y. Liu, J. Wang, W. Qiao, L. Ling, D. Long, *Energy Environ. Sci.* **2016**, *9*, 3230–3239.
- [48] X. Tao, J. Wang, C. Liu, H. Wang, H. Yao, G. Zheng, Z. W. Seh, Q. Cai, W. Li, G. Zhou, C. Zu, Y. Cui, *Nat. Commun.* **2016**, *7*, 11203.
- [49] A. K. Timbola, C. D. Souza, C. Soldi, M. G. Pizzolatti, A. Spinelli, *J. Appl. Electrochem.* **2007**, *37*, 617–624.
- [50] J.-j. Wu, *Int. J. Electrochem. Sci.* **2016**, *11*, 5165–5179.
- [51] Z. Li, J. Zhang, Y. Lu, X. W. Lou, *Sci. Adv.* **2018**, *4*, 1687.
- [52] J. Ding, H. Zhou, H. Zhang, L. Tong, D. Mitlin, *Adv. Energy Mater.* **2018**, *8*, 1701918.
- [53] X. Yu, A. Manthiram, *ChemElectroChem* **2014**, *1*, 1275–1280.
- [54] G. W. Luther, *Geochim. Cosmochim. Acta* **1991**, *55*, 2839–2849.
- [55] H. Zhang, T. Diemant, B. Qin, H. Li, R. Behm, S. Passerini, *Energies* **2020**, *13*, 836.
- [56] L. Li, R. Jacobs, P. Gao, L. Gan, F. Wang, D. Morgan, S. Jin, *J. Electrochem. Soc.* **2016**, *138*, 2838–2848.
- [57] W. Weppner, R. A. Huggins, *J. Electrochem. Soc.* **1977**, *124*, 1569–1578.
- [58] B. J. Lindberg, K. Hamrin, G. Johansson, U. Gelius, A. Fahlman, C. Nordling, K. Siegbahn, *Phys. Scr.* **1970**, *1*, 286–298.
- [59] C.-P. Yang, Y.-X. Yin, Y.-G. Guo, L.-J. Wan, *J. Electrochem. Soc.* **2015**, *137*, 2215–2218.
- [60] Q. Yang, T. Yang, W. Gao, Y. Qi, B. Guo, W. Zhong, J. Jiang, M. Xu, *Inorg. Chem. Front.* **2020**, *7*, 4396–4403.
- [61] S. Wei, S. Xu, A. Agrawal, S. Choudhury, Y. Lu, Z. Tu, L. Ma, L. A. Archer, *Nat. Commun.* **2016**, *7*, 11722.
- [62] R. Aghaei, A. Eshaghi, *J. Alloys Compd.* **2017**, *699*, 112–118.
- [63] A. Salama, M. El-Sakhawy, S. Kamel, *Int. J. Biol. Macromol.* **2016**, *93*.

Manuscript received: June 1, 2021

Revised manuscript received: June 24, 2021

Accepted manuscript online: July 14, 2021

Version of record online: July 28, 2021

Batteries & Supercaps

Supporting Information

Ultra-Stable Cycling of High Capacity Room Temperature Sodium-Sulfur Batteries Based on Sulfurated Poly (acrylonitrile)

Saravanakumar Murugan, Stefan Niesen, Julian Kappler, Kathrin Küster, Ulrich Starke, and Michael R. Buchmeiser*

Table S1. Combustion elemental analysis of Na[B(hfip)₄].

Element	Calculated (%)	Found (%)
C	29.64	29.62
H	3.5249	3.536
C : H	8.4087	8.3766

Table S2. Combustion elemental analysis of a SPAN cathode.

Element	wt.%				Atomic ratio
	S	C	N	H	C/S
S@PAN	38.18	41.07	13.66	1.113	2.9

Table S3. Comparison of SPAN cathodes, electrolytes, and their literature-known performance in RT Na-S batteries.

Cathodes	Electrolyte	Current density	Initial discharge capacity (mAh g _s ⁻¹)	Discharge capacity (mAh g _s ⁻¹) (cycles)	Capacity retention (%)	reference
SPAN	1 M NaClO ₄ in EC:DMC	0.1 mA.cm ⁻²	1455	1111 (18)	76	[1]

SPAN – tellurium doped (Te _{0.04} S _{0.96} @pPAN)	1 M NaClO ₄ in EC:DMC + 10 wt.% FEC	6 A.g ⁻¹	1067	970 (600)	90	[2]
SPAN – selenium doped (Se _{0.08} S _{0.92} @pPAN)	1 M NaClO ₄ in PC:EC	0.4 A.g ⁻¹	1185	770 (500)	65	[3]
SPAN	1 M NaClO ₄ in EC:DMC	0.83 A.g ⁻¹ 1	1195	1000(1000)	83	[4]
SPAN-polystyrene- SeS ₂	1 M NaClO ₄ in EC:DMC + 5 wt.% FEC	1 A.g ⁻¹	1043	800(400)	76.7	[5]
SPAN web	1 M NaPF ₆ in EC:DEC	0.167 A.g ⁻¹	342	266(200)	77.7	[6]
Free-standing SPAN	1 M NaClO ₄ in PC:EC	0.167 A.g ⁻¹	890	717(200)	80.5	[7]

Iodine doped SPAN	1 M NaClO ₄ in EC:DMC + 8 wt.% FEC	0.167 A.g ⁻¹	1787	850(100)	47.6	[8]
SPAN (electrospun PAN)	0.8 M NaClO ₄ in EC:DEC	1.67 A.g ⁻¹ 1	1158	487(500)	42	[9]
SPAN (our work)	1 M NaB(hfip) ₄ in EC:DMC + 13 wt% FEC	5.025 A.g ⁻¹ (3 C)	1360	1070(1000)	78.7	

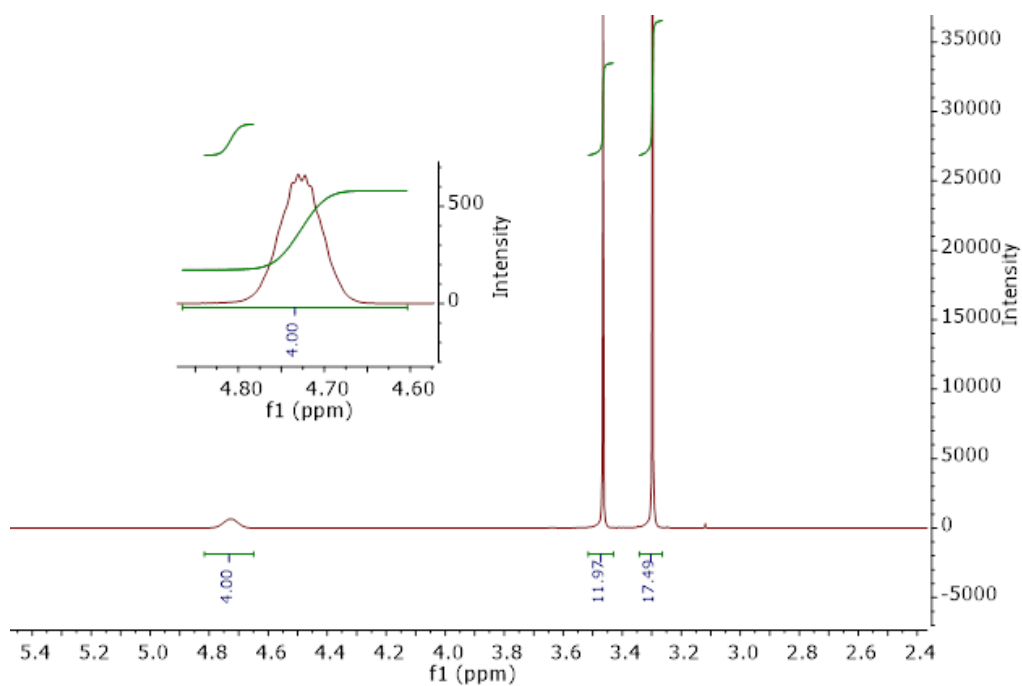


Fig. S1. ¹H NMR spectrum of Na[B(hfip)₄] in CD₃CN.

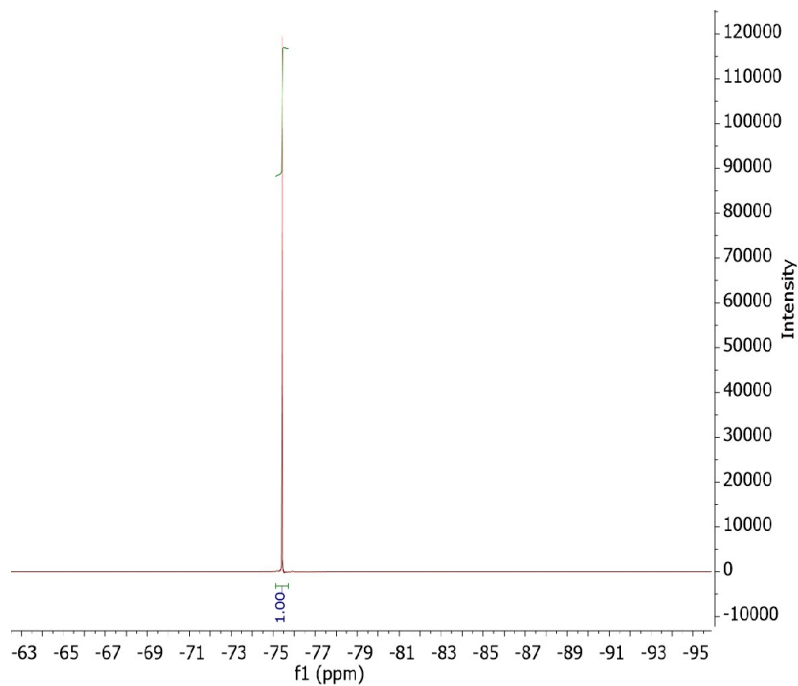


Fig. S2. ^{19}F NMR spectrum of $\text{Na}[\text{B}(\text{hfip})_4]$ in CD_3CN .

The synthesis of $\text{Na}[\text{B}(\text{hfip})_4]$ yielded pure salt with 3 DME molecules coordinated to Na^+ . Removal of the solvent by heating under vacuum ($> 50\text{ }^\circ\text{C}$) results in decomposition [1].

Pristine SPAN cathode

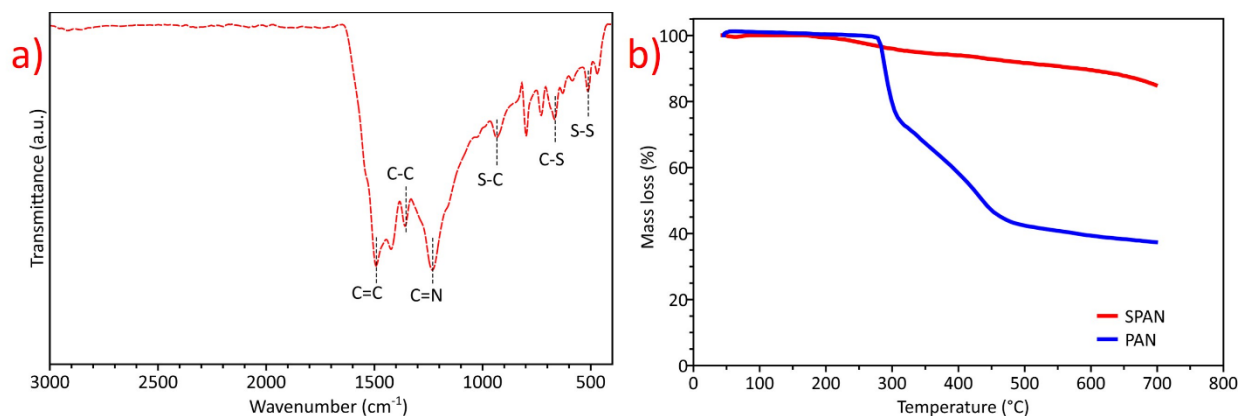


Fig. S3. Structure and composition analysis of a SPAN composite. a) Fourier-transform infrared spectroscopy (FTIR) of SPAN material, b) thermogravimetric analysis (TGA) of PAN and the SPAN composite.

FTIR reveals (Fig. S3a) covalently bound sulfur in the cyclized PAN matrix by the presence of S-S and C-S stretching bonds at 513 cm^{-1} and 663 cm^{-1} , respectively. Symmetric C=N, C=C stretching bonding at 1229 cm^{-1} and 1493 cm^{-1} respectively, shows that cyclization results in a conjugated pyridine-like backbone. Fig. S3b shows the TGA of both PAN and SPAN composite. During the synthesis of the SPAN composite, a total mass loss of 14 wt% was observed due to H_2S elimination between $300\text{ }^\circ\text{C}$ and $570\text{ }^\circ\text{C}$. A major weight loss ($\sim 6\text{ wt\%}$) begins only above $570\text{ }^\circ\text{C}$, indicating thermally stable, covalently bound short-chain sulfur molecules. In contrast, PAN shows a rapid weight between $270\text{ }^\circ\text{C}$ and $300\text{ }^\circ\text{C}$ due to dehydrogenation. Above $300\text{ }^\circ\text{C}$, the disintegration of the polymer chains occurs, which leads to another significant weight loss ($\sim 36\text{ wt\%}$).

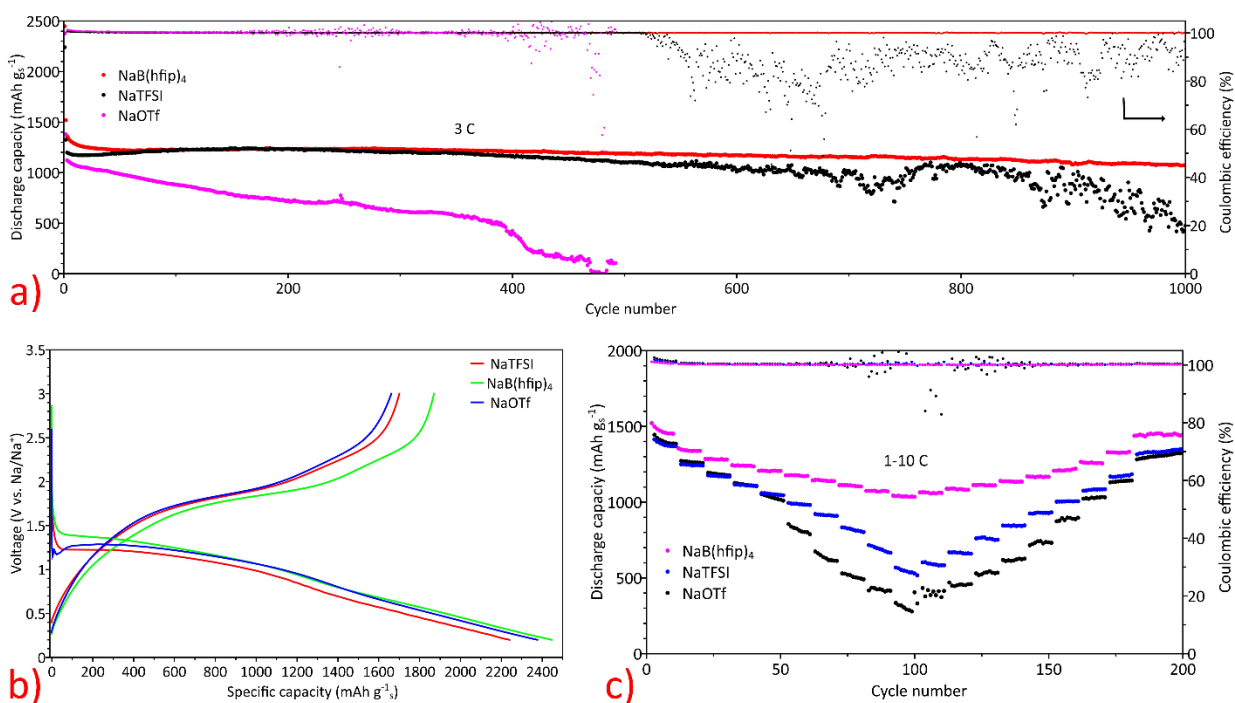


Fig. S4. Comparison of NaB(hfip)₄ with commercially used Na battery salts such as sodium bis(trifluoromethylsulfonyl)imide (NaTFSI), sodium trifluoromethanesulfonate (NaOTf), a) long term galvanostatic cycling at 3 C; b) voltage profile evaluation of the 1st cycle at 0.3 C; c) rate capability performance from 1 to 10 C.

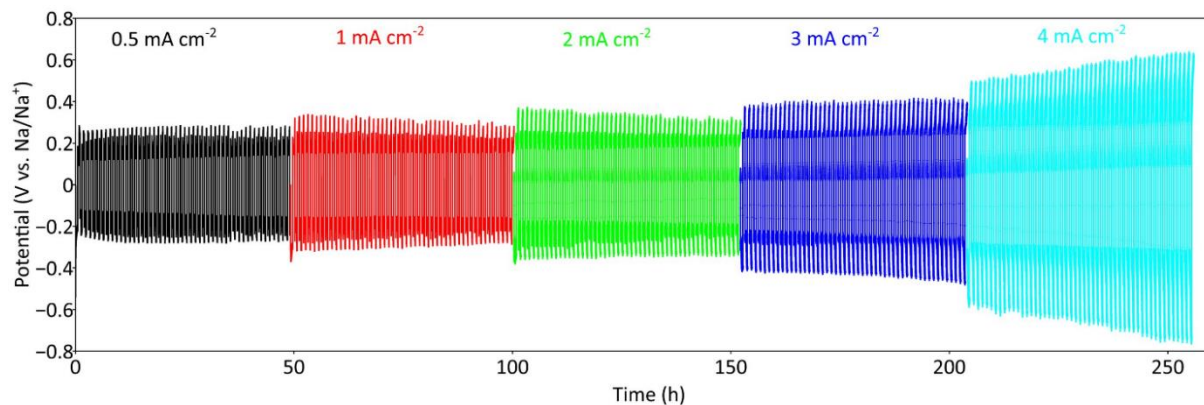


Fig. S5. Galvanostatic cycling of a symmetric Na||Na cell and its response over time with varying current density.

Randles–Ševčík equation

$$i_p = 0.4463 nFAc \left(\frac{nFvD}{RT} \right)^{1/2} \quad \text{Equation S1}$$

i_p indicates the peak current (A), which increases linearly with the square root of the scan rate v ($V s^{-1}$), whereas n is the number of electrons involved in the redox reaction, F is the Faraday constant ($Coulombs mol^{-1}$), A is the electrode surface area (cm^2), c is the concentration of the Na^+ ions in the electrolyte ($mol cm^{-3}$), D is the diffusion coefficient of the oxidized species ($cm^2 s^{-1}$), R is the universal gas constant ($J mol^{-1} K^{-1}$), and T is the temperature (K).

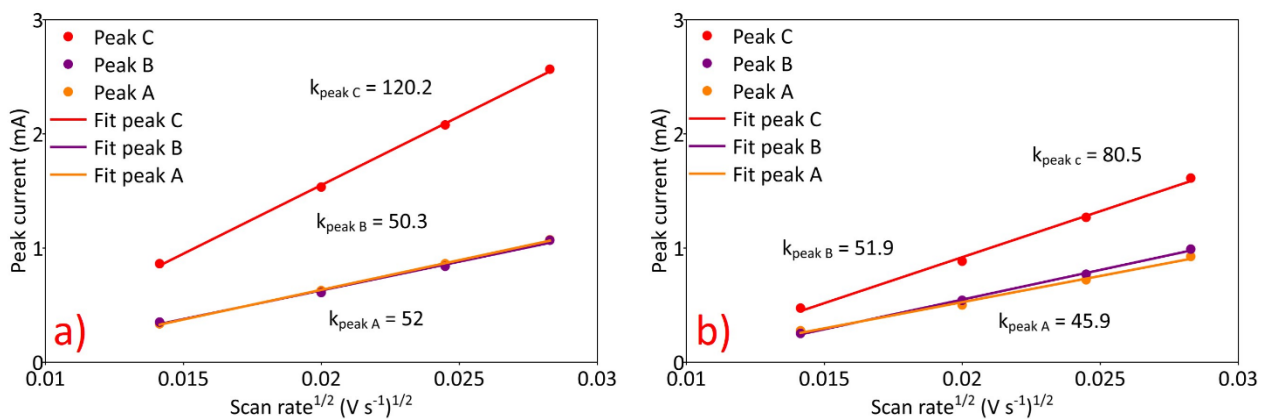


Fig. S6. Peak current vs. square root of scan rate from CV measured between peak A (orange), peak B (purple), peak C (red), k – slope of the respective peak), a) 0.2 - 3 V; b) 0.5 - 3 V.

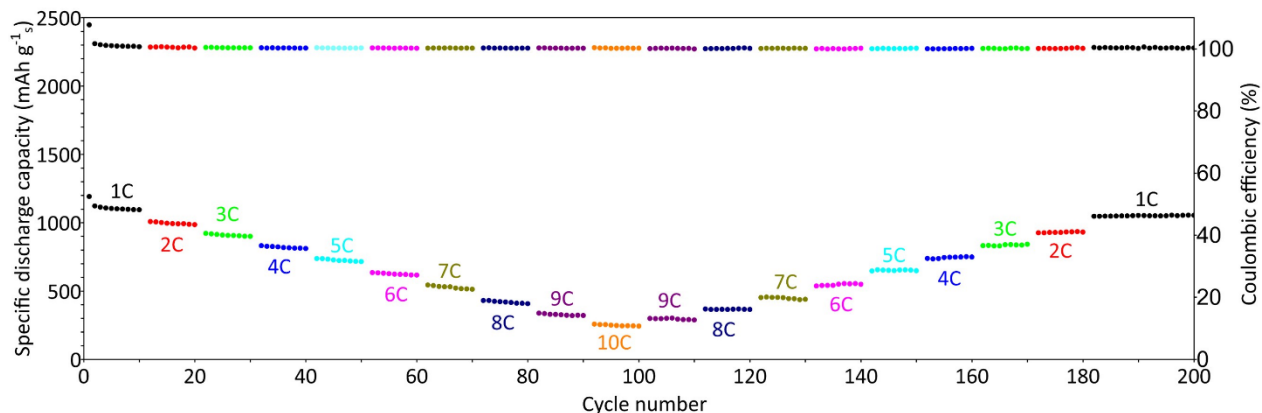


Fig. S7. The rate capability of a Na-SPAN cell cycled between 0.5 - 3 V with a C - rate varying between 1 - 10 C.

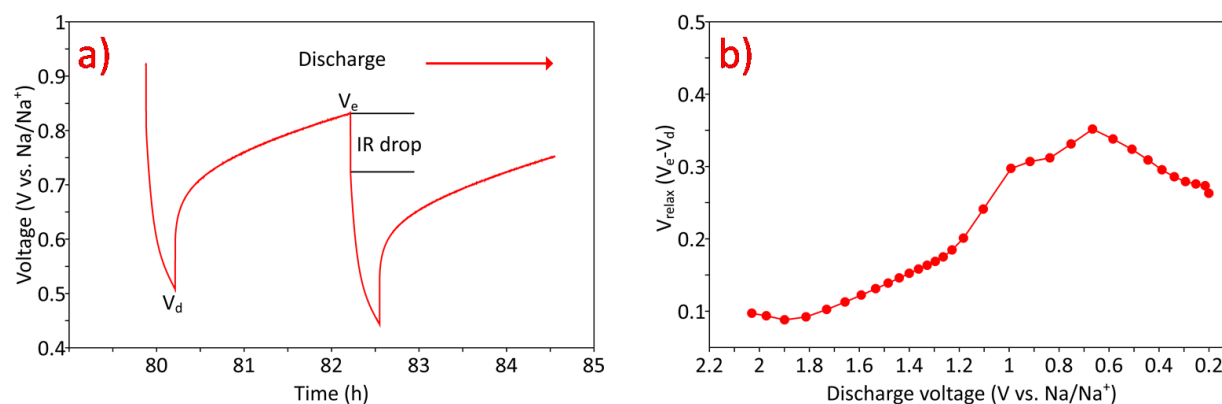


Fig. S8. Galvanostatic intermittent titration technique (GITT), a) an example voltage profile during discharge (IR drop - the electrical potential difference between electrodes, V_e - potential after relaxation, V_d - potential at the end of the constant current pulse during discharge); b) calculated relaxation voltage (potential difference between the end of two sequential open-circuit relaxation periods; $V_e - V_d$) at each transient voltage step.

Weppner and Huggins equation

$$D_{Na}^+ = \frac{4}{\pi\tau} \left(n_m V_m / A \right)^2 \left(\Delta E_s / \Delta E_t \right)^2$$

Equation S2

τ denotes the duration of the current pulse applied (s), n_m denotes the number of moles (mol), V_m denotes the molar volume of the active material ($\text{cm}^3 \text{mol}^{-1}$) and A denotes a contact area of electrode/electrolyte (cm^2). ΔE_s , ΔE_t are the steady-state and constant current pulse voltage changes, respectively.

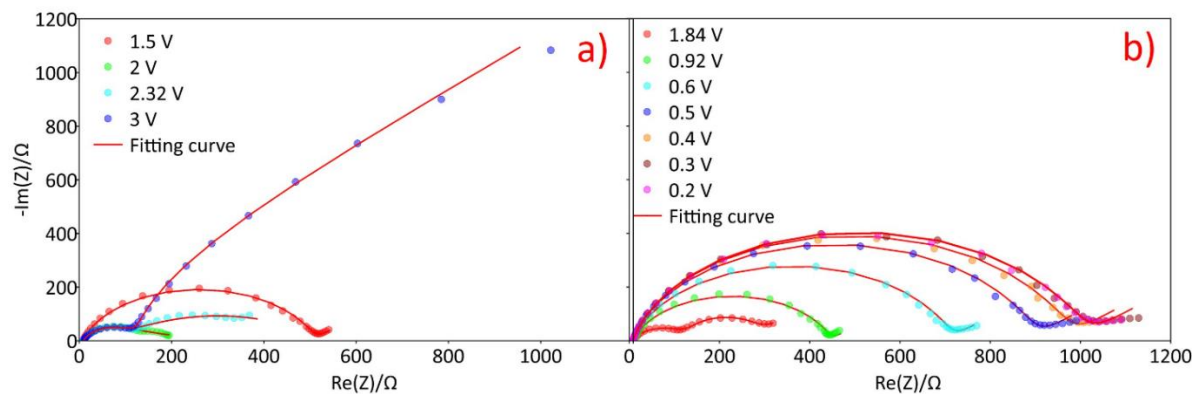


Fig. S9. Impedance spectroscopy of a full cell cycled between 0.2 – 3 V, a) charge and; b) discharge.

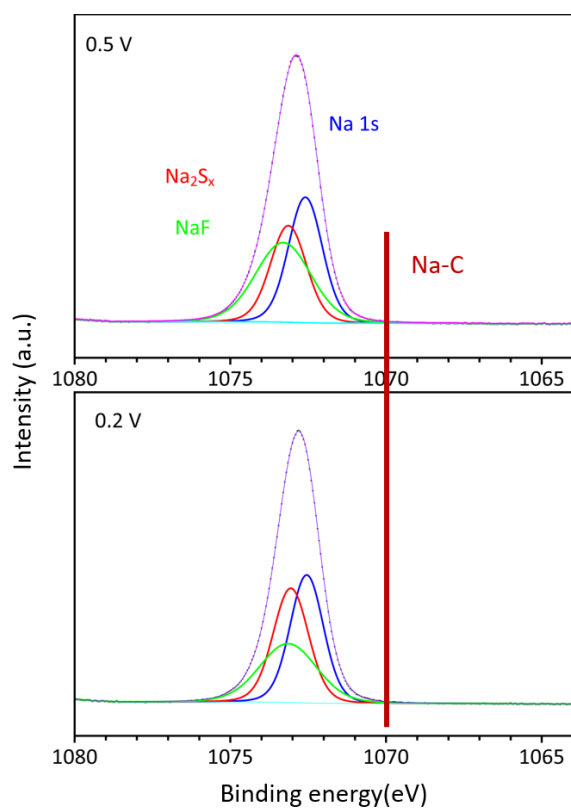


Fig. S10. Na 1s *ex-situ* XPS spectra of a SPAN cathode at a DCP of 0.5 V (top) and 0.2 V (bottom), respectively.

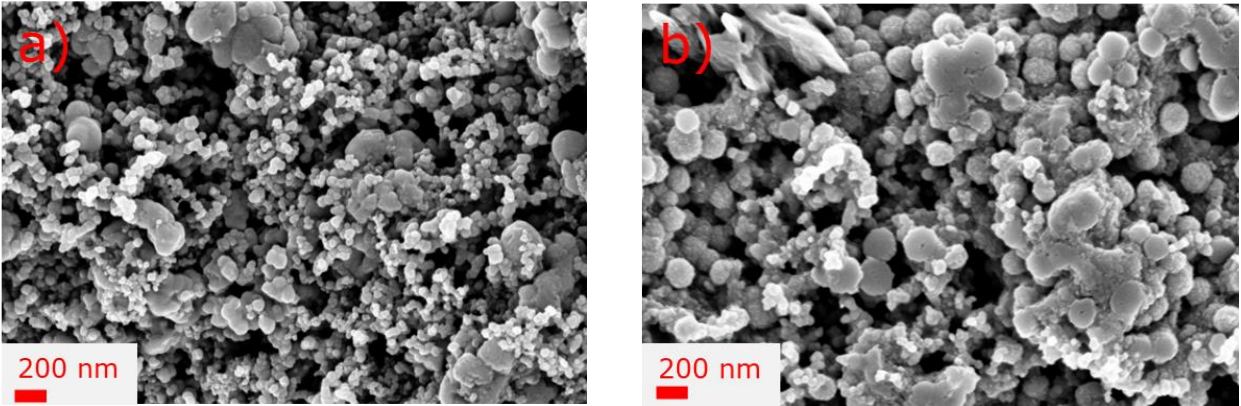


Fig. S11. Scanning electron microscopy images of a SPAN cathode, a) pristine; b) discharged to 0.2 V.

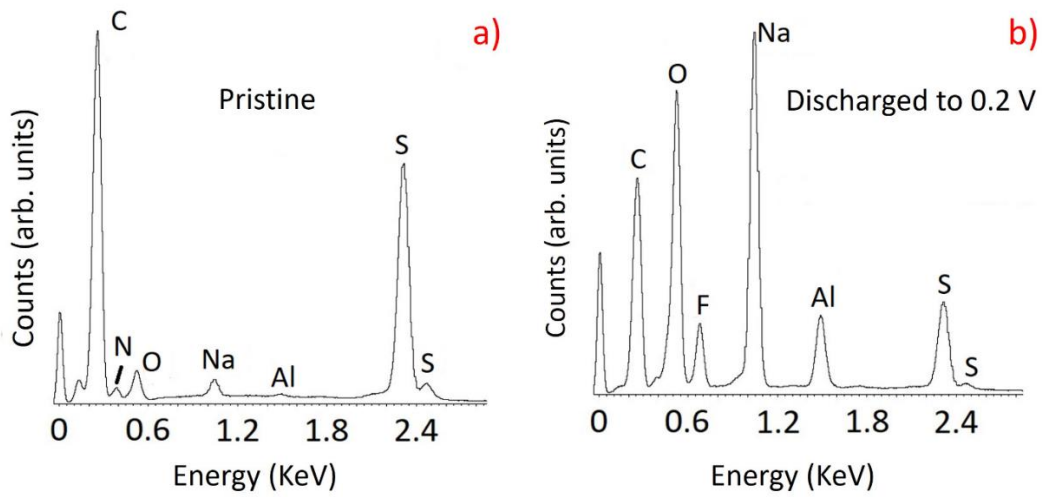


Fig. S12. EDX characterization of a SPAN cathode, a) pristine state and; b) discharged to 0.2 V.

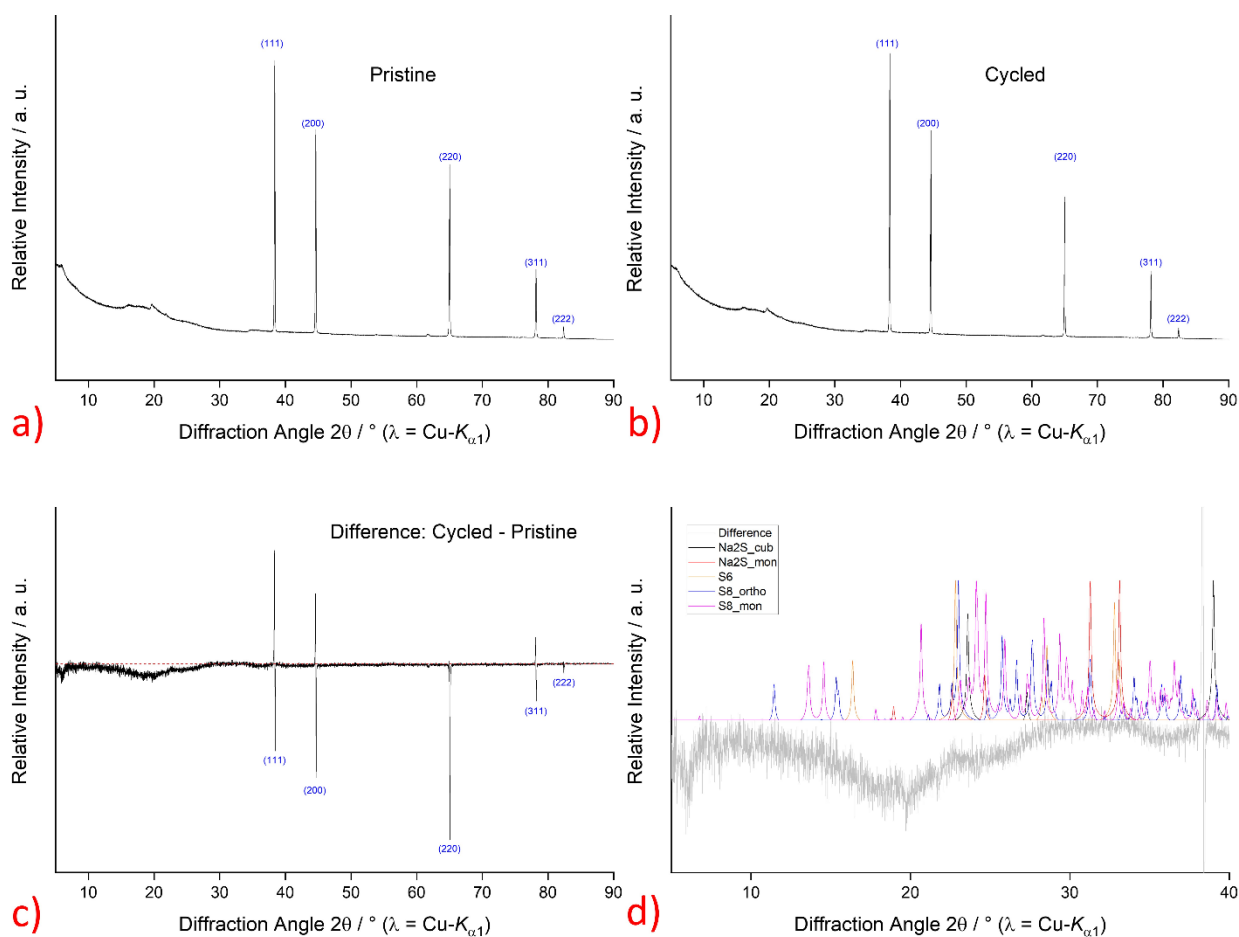


Fig. S13. X-ray powder diffraction pattern of an SPAN cathode, a) pristine; b) charged cathode cycled 10 times; c) difference in signal intensities between cycled and pristine cathode; d) reference XRD patterns of the various sulfur phases and sodium sulfides (limited to the region that contains the strongest reflections only for a better separation of literature phases).

References

- [1] S. Bulut, P. Klose, I. Crossing, *Dalton Trans.* **2011**, 40, 8114-8124.
- [1] J. Wang, J. Yang, Y. Nuli, R. Holze, *Electrochem. Commun.* **2007**, 9, 31-34.
- [2] S. Li, Z. Zeng, J. Yang, Z. Han, W. Hu, L. Wang, J. Ma, B. Shan, J. Xie, *ACS Appl. Energy Mater.* **2019**, 2, 2956-2964.
- [3] L. Wang, X. Chen, S. Li, J. Yang, Y. Sun, L. Peng, B. Shan, J. Xie, *J. Mater. Chem. A* **2019**, 7, 12732-12739.
- [4] A. Y. S. Eng, D.-T. Nguyen, V. Kumar, G. S. Subramanian, M.-F. Ng, Z. W. Seh, *J. Mater. Chem. A* **2020**, 8, 22983-22997.
- [5] Z. Li, J. Zhang, Y. Lu, X. W. Lou, *Sci. Adv.* **2018**, 4, 1687.

- [6] I. Kim, C. H. Kim, S. h. Choi, J.-P. Ahn, J.-H. Ahn, K.-W. Kim, E. J. Cairns, H.-J. Ahn, *J. Power Sources* **2016**, *307*, 31-37.
- [7] X. Huang, J. Liu, Z. Huang, X. Ke, L. Liu, N. Wang, J. Liu, Z. Guo, Y. Yang, Z. Shi, *Electrochim. Acta* **2020**, *333*, 135493.
- [8] S. Ma, P. Zuo, H. Zhang, Z. Yu, C. Cui, M. He, G. Yin, *Chem Commun (Camb)* **2019**, *55*, 5267-5270.
- [9] T. H. Hwang, D. S. Jung, J.-S. Kim, B. G. Kim, J. W. Choi, *Nano Letters* **2013**, *13*, 4532-4538.

3.3 Publication “A sodium bis(perfluoropinacol) borate-based electrolyte for stable, high-performance room temperature sodium-sulfur batteries based on sulfurized poly(acrylonitrile)”

The chemical stability of the salt is one of the main aspects of an electrolyte for battery applications. Thermodynamical stability of the complex is defined as the ability of the metal ion to selectively form a complex with another molecule (i.e., metal-ligand bond). Bidentate ligands are bound to the metal ion through multiple binding sites. Therefore, monodentate ligands are thermodynamically less stable than their bidentate counterparts due to the chelating effect.^[315] Bidentate salts such as LiBOB have been used as a stand-alone salt or as an additive in commercial applications due to their excellent oxidation stability, wide electrochemical window, and ability to withstand high operating temperatures. Similarly, NaBOB and NaDFOB were tested for SIBs which were able to demonstrate good ionic conductivity, low viscosity, and a wide electrochemical window.



Figure 31. Sodium or lithium salt of BOB and DFOB anion.^[169, 316, 317, 318]

In this work, a bidentate ligand-containing salt, sodium bis(perfluoropinacol)borate, (Na-PPB); NaB[O₂C₂(CF₃)₄]₂, was synthesized to demonstrate the excellent electrochemical properties of Na-PPB in carbonate-based electrolytes. As expected, the bidentate salt, Na-PPB, was able to outperform its monodentate equivalent under harsh chemical and electrochemical conditions. Electrochemical tests and DFT calculations were carried out by the group of Prof. Johannes Kästner and are included in this study to highlight the enhancement in cell performance. Furthermore, the decomposition tests were also taken into consideration to evaluate the safety and easy handling, storage, and transport of the electrolyte.

Publication:

Murugan, S.; Klostermann, S. V.; Frey, W.; Kästner, J.; Buchmeiser, M. R., A sodium bis(perfluoropinacol) borate-based electrolyte for stable, high-performance room temperature sodium-sulfur batteries based on sulfurized poly(acrylonitrile). *Electrochem. Commun.* **2021**, *132*, 107137.

Author Contributions: **Saravanakumar Murugan:** Conceptualization, Data curation, Formal analysis, Investigation, Methodology, Validation, Visualization, Writing - original draft, Writing - review & editing. **Sina V. Klostermann:** Data curation, Formal analysis, Validation, Visualization, Writing - review & editing. **Wolfgang Frey:** Investigation (single-crystal X-ray structures), Data curation, Formal analysis. **Johannes Kästner:** Funding acquisition, Resources, Supervision. **Michael R. Buchmeiser:** Funding acquisition, Methodology, Project administration, Resources, Supervision, Validation, Writing - original draft, Writing - review & editing.

Reprinted with permission from Ref. ^[319], (open access).



A sodium bis(perfluoropinacol) borate-based electrolyte for stable, high-performance room temperature sodium-sulfur batteries based on sulfurized poly(acrylonitrile)

Saravanakumar Murugan^a, Sina V. Klostermann^b, Wolfgang Frey^c, Johannes Kästner^b, Michael R. Buchmeiser^{a,d,*}

^a Institute of Polymer Chemistry, University of Stuttgart, 70569 Stuttgart, Germany

^b Institute for Theoretical Chemistry, University of Stuttgart, 70569 Stuttgart, Germany

^c Institute of Organic Chemistry, University of Stuttgart, 70569 Stuttgart, Germany

^d German Institutes of Textile and Fiber Research (DITF), 73770 Denkendorf, Germany

ARTICLE INFO

Keywords:

Sodium-sulfur batteries
Sulfur-polyacrylonitrile cathode
Bidentate ligands
Weakly coordinating anion
Hydrolysis
Potential energy barrier

ABSTRACT

Sodium bis(perfluoropinacol)borate, $\text{NaB}[\text{O}_2\text{C}_2(\text{CF}_3)_4]_2$ (Na-PPB), as part of the electrolyte is introduced to room temperature (RT) sodium-sulfur batteries based on a sulfurized poly(acrylonitrile) (Na-SPAN) cathode. Na-PPB was stable under atmospheric conditions for 20 days and showed no sign of degradation. Na-SPAN full cells based on a Na-PPB electrolyte demonstrated excellent oxidation stability against various current collectors and delivers a high discharge capacity of $>950 \text{ mAh/g}_{\text{sulfur}}$ with 100 % coulombic efficiency over 500 cycles.

1. Introduction

Lithium-ion technology currently dominates electrochemical energy storage applications. Because of the scarcity of lithium and the impractical energy density of standard Li-ion batteries (LIB), researchers started to look beyond Li-ion technology. Moreover, high costs and limited lifetime so far impede their use in large-scale energy storage. On the other hand, high-temperature sodium-sulfur (HT Na-S) batteries with solid β -alumina electrolytes (760 Wh/kg) have been widely used for grid applications for almost two decades. However, working at high temperatures entails serious safety issues and operating costs [1–3]. Thus, research on room-temperature (RT) Na-S batteries with a theoretical gravimetric energy density of 1274 Wh/kg is gaining increasing attention.

The electrolytes used in such Na-S batteries strongly affect the reaction kinetics at the electrodes. Specifically, the salt used in the electrolyte governs both ion mobility and anode stability. So far, the choice of electrolyte salts for sodium-ion batteries (NIBs) is limited to NaClO_4 , NaPF_6 , NaCF_3SO_3 , NaTFSI , NaFSI , NaBF_4 , and NaAsF_6 , which are analogous to the salts used in LIBs [4]. These salts suffer from disadvantages such as sensitivity towards moisture, limited electrochemical window,

explosiveness (NaClO_4), corrosive behavior towards aluminum-based current collectors (NaTFSI , NaCF_3SO_3 , NaFSI), or toxicity (NaAsF_6). Currently, RT Na-S batteries use similar electrolytes to NIBs [5–7], though with the limited overall performance of the final batteries. It is therefore essential to develop novel, stable, highly conductive, and non-corrosive electrolytes for RT Na-S batteries [8].

So far, the use of sulfur-based cathodes employing simple sulfur-carbon composites results in the formation of long-chain polysulfides upon reaction with sodium ions during discharge in ether-based electrolytes. These long-chain polysulfides are retained by carbon-based materials only through weak physical adsorption and can therefore easily dissolve in the electrolyte, which results in a severe polysulfide shuttle effect and self-discharge of the battery [9]. On the other hand, long-chain polysulfides react with carbonate-based electrolytes reducing the overall performance of the cell [10]. Several alternatives were considered to mitigate this phenomenon such as the formation of stable solid electrolyte interphases (SEIs), modifications of the cathode architecture or the separator, the use of tailored polymer electrolytes, or hosts to retain polysulfides [11–13]. In sulfurized poly(acrylonitrile) (SPAN) the sulfur is covalently bound to the composite backbone, which eliminates the above-mentioned issues [14]. The use of SPAN in a RT Na-S

* Corresponding author.

E-mail address: michael.buchmeiser@ipoc.uni-stuttgart.de (M.R. Buchmeiser).

<https://doi.org/10.1016/j.elecom.2021.107137>

Received 18 August 2021; Received in revised form 22 September 2021; Accepted 30 September 2021

Available online 7 October 2021

1388-2481/© 2021 The Author(s). Published by Elsevier B.V. This is an open access article under the CC BY license (<http://creativecommons.org/licenses/by/4.0/>).

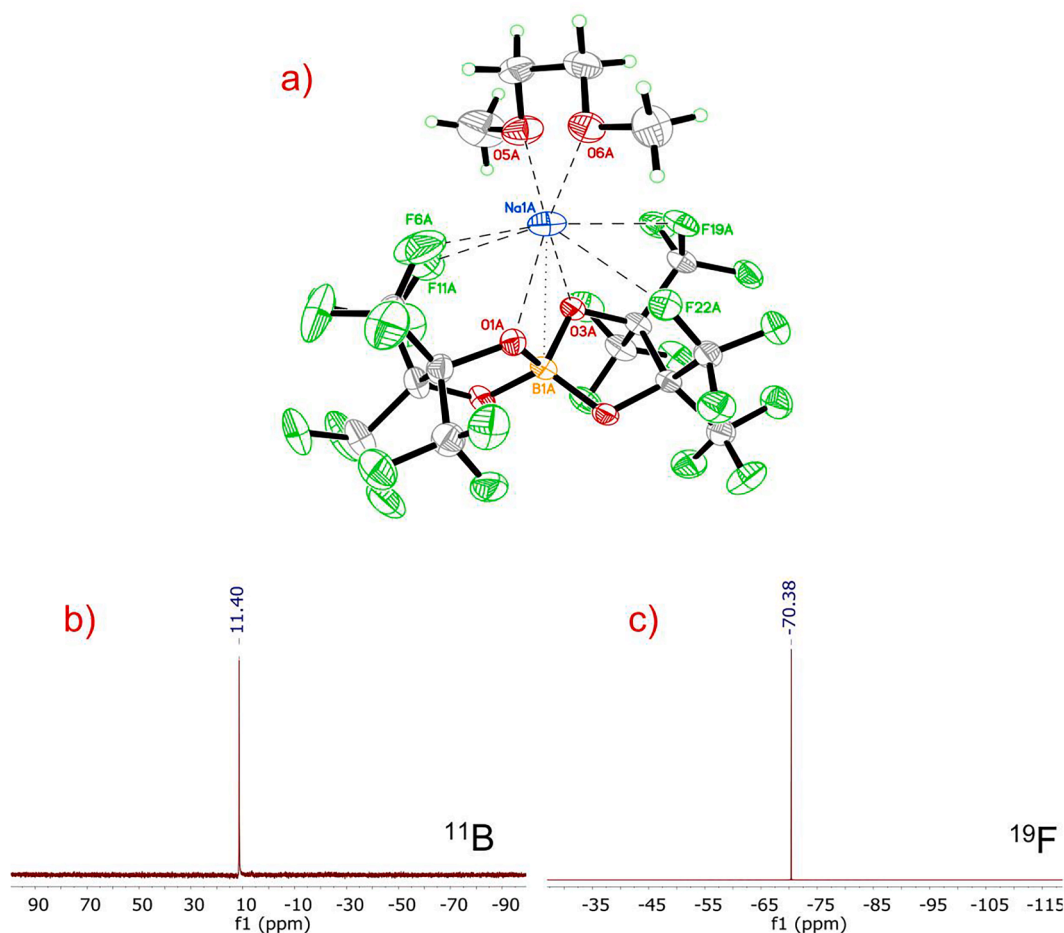


Fig. 1. a) Structure of Na-PPB as determined by single-crystal X-ray analysis; b) ^{11}B - and c) ^{19}F NMR spectra of Na-PPB in CD_3CN .

battery was first reported by Wang *et al.*, where the high compatibility of SPAN with the sodium anode and a high initial discharge capacity of 655 $\text{mAh/g}_{\text{cathode}}$ were demonstrated [15]. Since then, SPAN-based composite cathodes, together with different electrolytes, have been used for RT Na-S batteries [16–20].

Here, we outline the use of the sodium salt of a fluorinated, weakly coordinating anion (WCA), ‘bis(perfluoropinacol) borate’ (Na-PPB) as an electrolyte salt for SPAN-based RT Na-S batteries. It possesses a wide electrochemical window, a high oxidation potential, high solubility, and its chemical and electrochemical stability allows for realizing RT Na-S batteries with high discharge capacity and high coulombic efficiency.

2. Experimental

2.1. Synthesis of $\text{Na}[\text{B}(\text{O}_2\text{C}_2(\text{CF}_3)_4)_2]$ (Na-PPB)

A modified synthetic route under inert conditions was developed [21]. NaBH_4 (1 g, 26.43 mmol) was pulverized inside a glovebox and then transferred to a Schlenk flask filled with 50 mL of 1,2-dimethoxyethane (DME). The solution was cooled to 0 °C under constant stirring. Then, hexafluoro-2,3-bis(trifluoromethyl)-2,3-butanediol (18 g, 55.5 mmol) was added dropwise over a period of 1 h. After complete addition, the solution was slowly heated at 20 °C/h to reflux and then refluxed for 24 h. Then, DME was removed under vacuum followed by three-fold co-evaporation with pentane. The residuals were suspended in pentane and filtered. The final product was dried at RT under vacuum (10^{-3} mbar) for 24 h and 12 h under ultra-high vacuum (10^{-9} mbar) at 30 °C. A pure white salt was obtained in 90% yield. NMR (CD_3CN) and elemental analysis confirmed sufficient purity (Table S1, S.I.).

2.2. Cathode fabrication and electrochemical characterization

SPAN was synthesized according to the literature [21–22]. The cathode slurry was prepared by mixing 70 wt% SPAN, 20 wt% carbon black, and 10 wt% Na-CMC binder in water using a planetary mixer (Thinky, Japan) and coating on a carbon-coated aluminum foil with a wet thickness of 300 μm . The final sulfur content in SPAN was 40.12 wt % (Table S2, S.I.). The average sulfur loading per cathode was 0.73 mg. Cell fabrication was carried out inside an Ar-filled glove box with Swagelok-T-type cells. 1 M Na-PPB in propylene carbonate with 10 wt% fluoroethylene carbonate (FEC) was used as an electrolyte. For linear-sweep voltammetry (LSV) (using Biologic VMP3) carried out at 1 mV s^{-1} , sodium metal was used both as a reference and counter electrode employing different metal sheets as working electrodes (Pt, Cu, Al, SS, and Al/C). The sodium metal was cut from the block, rolled to the desired thickness and then punched into 12 mm discs. Full Na-SPAN cells were fabricated by placing the following in order: sodium anode, two glass fiber separators, and SPAN cathode. The potential window for cyclic voltammetry (CV) was set between 0.5 and 3 V using a scan rate of 0.1 mV s^{-1} . Galvanostatic cycling and rate capability testing (one pre-formation cycle at 0.3 C) were carried out on a BasyTec XCTS-LAB systems, Germany, at 2C and 1–4C, respectively, using a voltage window between 0.5 and 3 V vs. Na/Na^+ .

2.3. Density functional calculations

Binding energies of the Na-PPB and the Na-hfip salt were calculated with the Gaussian 09 software [23] package using density functional theory. The initial geometries were optimized at the B3LYP/6-31 + G

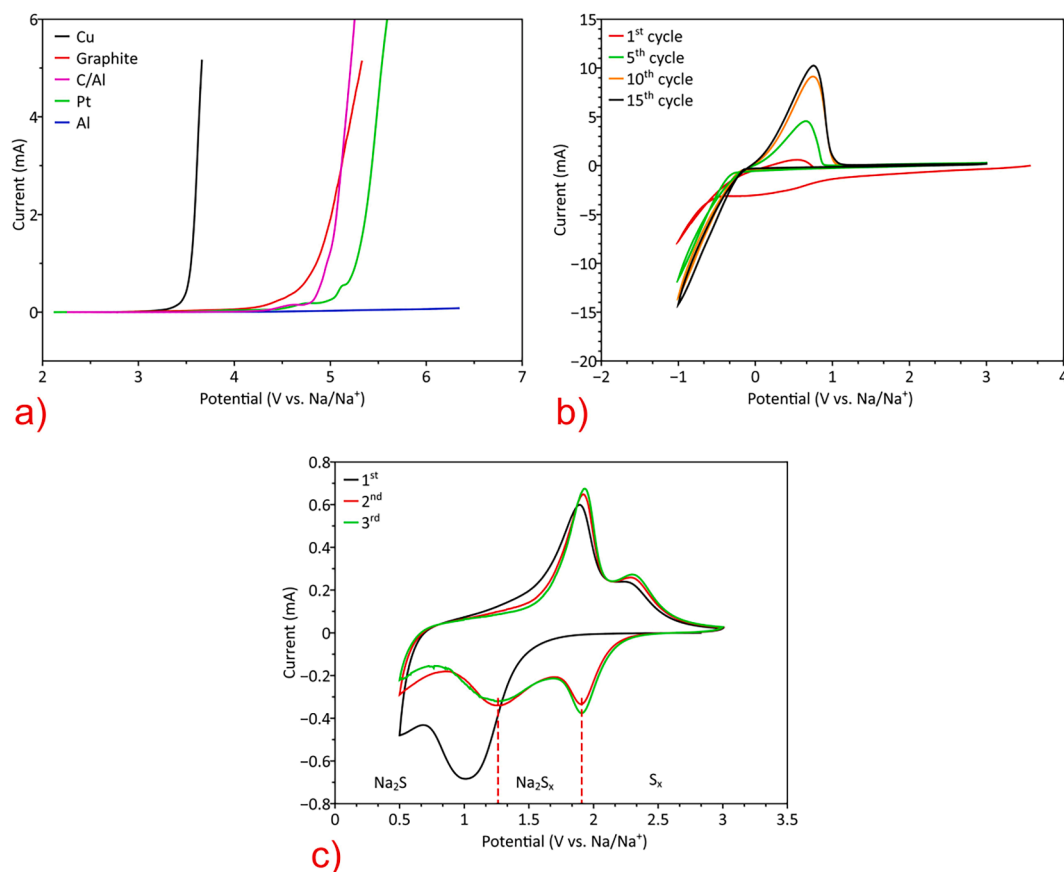


Fig. 2. Electrochemical performance of a Na-PPB-based electrolyte measured with Na as counter and reference electrode, a) LSV of different working electrodes scanned at 1 mV s^{-1} with Cu (black), graphite (red), carbon-coated aluminum (pink), Pt (green), and Al (blue); b) plating and stripping test with graphite as working electrode scanned at 1 mV s^{-1} showing the 1st (red), 5th (green), 10th (orange), and 15th (black) cycle; and c) CV of a Na-SPAN full cell recorded at 0.1 mV s^{-1} at the 1st (black), 2nd (red), and 3rd (green) cycle. (For interpretation of the references to colour in this figure legend, the reader is referred to the web version of this article.)

(2d,p) level. On these optimized geometries, single-point energies were calculated at the B3LYP/6-311 + G(2df,2p) level. Binding energies include zero-point vibrational energies (ZPE). Reaction paths were obtained by performing nudged elastic band (NEB) calculations at the B3LYP-D3(BJ)/def2-SVP level in Turbomole V.7.4 [24] performed in ChemShell [25–26] via DL-FIND [27].

3. Results and discussion

3.1. Synthesis and characterization of Na-PPB

The $\text{p}K_a$ value of perfluoropinacol (5.95 vs. 18 for pinacol) facilitates the deprotonation by NaBH_4 [28]. The reaction between NaBH_4 and perfluoropinacol resulted in Na-PPB in 90% isolated yield. Na-PPB was analyzed by single-crystal X-ray analysis, NMR, and elemental analysis to ensure purity. Single crystals formed by slowly diffusing pentane into a chloroform solution of Na-PPB at -30°C . Single-crystal X-ray analysis showed that the unit cell contains one DME-solvated Na^+ ion weakly coordinated to four fluorine and two oxygen atoms of the counter anion (Fig. 1a). The boron atom is coordinated by two bidentate perfluoropinacolate groups. The ^{11}B and ^{19}F NMR spectra show signals at $\delta = 11.40$ and $\delta = 70.38$ ppm, respectively, in line with the results of single-crystal X-ray analysis (Fig. 1b and 1c).

3.2. Electrochemical characterization

The oxidative stability of the electrolyte was determined by linear sweep voltammetry (LSV) applying a potential sweep at the rate of 1 mV

s^{-1} . As shown in Fig. 2a, the Na-PPB-based electrolyte exhibited remarkable oxidative stability on Al ($>5.5 \text{ V}$) compared to Cu (3.25 V). Carbon-coated aluminum foil, Pt, and graphite showed oxidation stabilities of 4.58 V , 4.5 V , and 4.25 V , respectively. The high oxidation potential of Na-PPB by far surpasses other commercially available sodium salts used in the literature (Table S3) [11,29]. The resistance of Na-PPB towards oxidation is attributed to the presence of the electron-withdrawing CF_3 groups, which reduce the electron density at both, carbon and boron, and lower the HOMO level, corroborating the results from Fig. S1 (S.I.) [30]. The plating and stripping behavior of the Na-PPB-based electrolyte on a graphite electrode strongly improved during the first 10 cycles (Fig. 2b). The overpotentials during plating and stripping at the 5th cycle were -0.26 V and -0.13 V , respectively. Further cycling resulted in a decreased plating overpotential (-0.17 V for the 10th cycle and -0.14 V for the 15th cycle) and increased current density. This enhancement in plating is attributed to the deposition of Na onto Na nucleated during the first cycle. Finally, a full cell using Na-SPAN as cathode was assembled for CV measurements. During the first cycle (Fig. 2c), only one reduction peak was observed at 1 V , which was shifted to a higher potential (1.92 V) during the 2nd cycle with the appearance of a new peak at 1.25 V . The first reduction peak indicates the reduction of sulfur in the SPAN backbone to form short-chain polysulfide intermediates at 1.92 V , followed by sodiation at 1.25 V to give the final discharge product Na_2S [31]. Similarly, during charging, the formed sulfides are reoxidized to short-chain sulfides at 1.92 V , which then reattach to the SPAN backbone at 2.3 V .

To show the electrochemical performance of the Na-PPB-based electrolyte in a Na-SPAN full cell, both stress tests and long-term

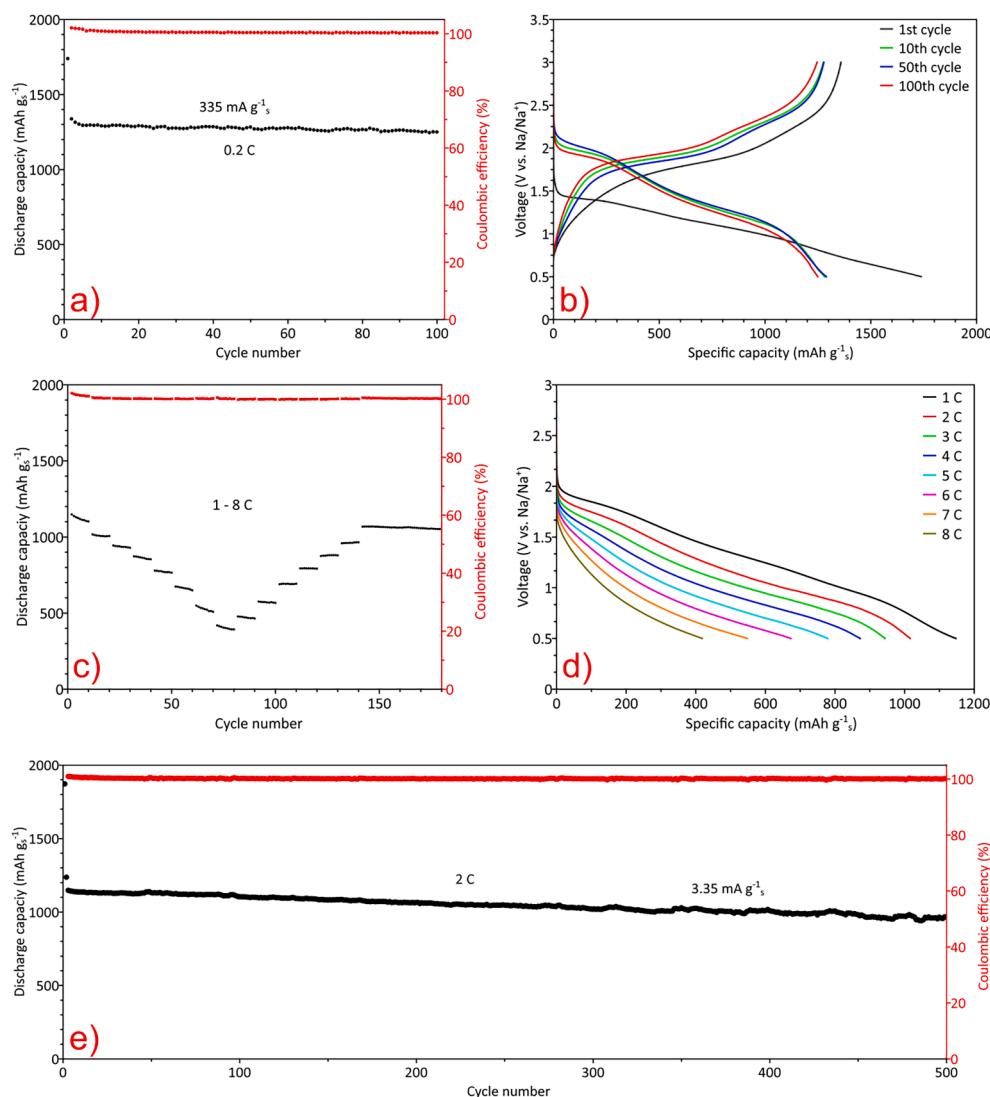


Fig. 3. Galvanostatic cycling measurements of a Na-SPAN full cell with a Na-PPB-based electrolyte, a) cycling at low C-rate (0.2C) for 100 cycles; b) voltage profiles at 0.2C during the 1st (black), 10th (green), 50th (blue), and 100th (red) cycle; c) stress test performed between 1 and 8C and the corresponding voltage profiles of the first cycle at each C-rate (d); e) long term cycling at 2C, discharge capacity (black) and coulombic efficiency (red) for the first 500 cycles. (For interpretation of the references to colour in this figure legend, the reader is referred to the web version of this article.)

cycling were carried out under defined conditions. Cells were cycled against Na metal between 0.5 and 3 V at a low C-rate (0.2C). The discharge capacity curve (Fig. 3a) showed high capacity ($>1250 \text{ mAh/g}_{\text{sulfur}}$), indicating full conversion of SPAN-bound sulfur to $\text{Na}_2\text{S}/\text{Na}_2\text{S}_2$. During the first cycle (Fig. 3b) irreversible Na^+ insertion, SEI layer formation, and irreversible reduction of short conjugated carbon bonds in SPAN fragments lead to high initial discharge capacity ($1738 \text{ mAh/g}_{\text{sulfur}}$) [32–34]. The voltage vs. specific capacity curve revealed two distinct discharge plateaus at 1.9 V and 1.1 V, implying multi-step conversion reactions. The overpotential decreased upon cycling until the 50th cycle, then insignificantly increased at the 100th cycle, demonstrating high compatibility of the Na-PPB electrolyte with both Na and SPAN cathode. Upon cycling at high C-rates of 1C up to 8C the full Na-SPAN cell demonstrated 1147, 1016, 943, 872, 778, 673, 548, and 418 $\text{mAh/g}_{\text{sulfur}}$, respectively (Fig. 3c and d). During reversal to the initial C-rate (1C), the capacity almost fully restored to the initial value ($1067 \text{ mAh/g}_{\text{sulfur}}$, suggesting high-stress endurance of the cathode and the electrolyte. Fig. 3e shows the long-term galvanostatic cycling at 2C. The Na-PPB-based electrolyte showed a stable and high initial discharge capacity of $1146 \text{ mAh/g}_{\text{sulfur}}$ and maintained $>950 \text{ mAh/g}_{\text{sulfur}}$ for 500 cycles with an average capacity decay of 0.016 % per cycle. The cell maintained an average coulombic efficiency of 99.8%. This high performance of the Na-SPAN cell shows that Na-PPB salt is electrochemically stable.

Unlike a monodentate ligand-containing salt such as sodium tetrakis (hexafluoroisopropoxy) borate $\text{NaB}[\text{OH}(\text{CF}_3)_2]_4$ (Na-hfip), Na-PPB is chemically stable due to its unique structure based on a bidentate ligand. We conducted a symmetrical $\text{Na} \parallel \text{Na}$ test to compare the overpotential of both salts. No significant differences in overpotential were observed except for a high plating overpotential of the Na-hfip salt (Fig. S2a and S2b, S.I.). The coulombic efficiency during stripping and plating of Na was calculated by chronopotentiometry analysis. A constant high cathodic current density of 1 mA cm^{-2} was applied until the capacity reached 0.5 mAh cm^{-2} and an anodic current of 1 mA cm^{-2} was applied until the potential reached 1 V. Fig. S3a (S.I.) shows a coulombic efficiency during the first cycle of $\sim 50\%$, which increased up to 89.5% after the 50th cycle. Fig. S3b (S.I.) shows an insignificant increase in overpotential during cycling, indicating that the Na-PPB electrolyte had stable Na plating/stripping potentials. Na-PPB exhibited exceptionally high stability under atmospheric conditions. To analyze the hydrolysis resistance of salts, we kept both salts in the air for 20 days. Upon addition of CD_3CN , Na-PPB formed a clear solution whereas, Na-hfip was partially insoluble resulting in a milky white solution. Partially insoluble particles suggest a decomposition reaction that occurred between the salt and atmospheric moisture. Fig. S4a and b (S.I.) show the ^{19}F NMR spectra of both salts exposed to air for 20 days. Na-PPB still showed a single peak whereas Na-hfip showed a new fluorine peak at $\delta = -75.9 \text{ ppm}$, indicating the formation of decomposition products. We

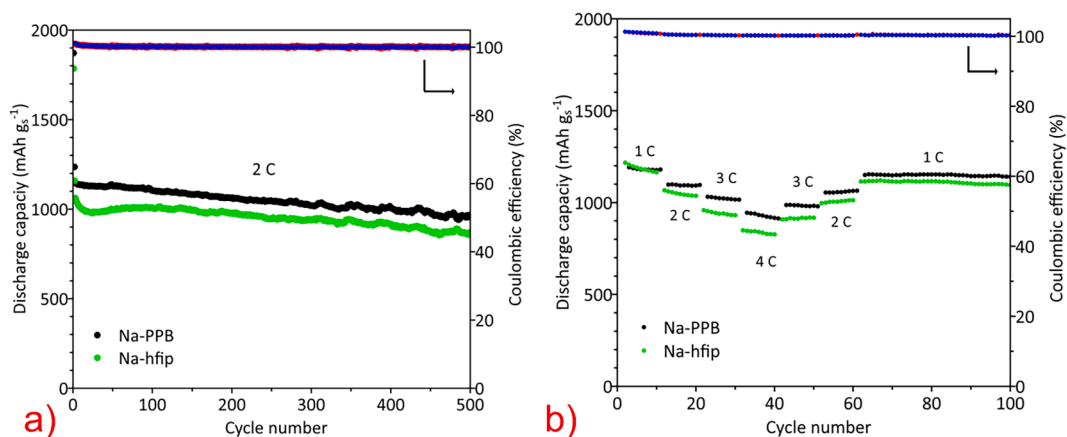


Fig. 4. Galvanostatic test comparison between a Na-PPB and a Na-hfip based electrolyte, a) long term cycling at 2C; b) rate capability assessment performed between 1 and 4C.

Table 1

Binding energies E_{bind} of the WCA with the Na^+ cation in Na-PPB and Na-hfip.

Compound	E_{bind} in $\text{kJ}\cdot\text{mol}^{-1}$
Na-PPB	-369.4
Na-hfip	-374.6

attribute this high stability of the Na-PPB salt to the thermodynamic stability of bidentate over monodentate ligands [35]. Salt decomposition and morphological changes were analyzed in detail by comparing both salts before and after exposure to air for 20 days (Tables S4 and S5, S.I.).

3.3. Theoretical analysis

A comparison of the galvanostatic electrochemical tests for the Na-PPB and Na-hfip electrolyte, respectively, revealed a lower capacity and lower stress endurance of the Na-hfip salt-based electrolyte (Fig. 4a and b). Generally, the Na^+ ion mobility in an electrolyte, which is fostered by the use of WCAs, plays an important role in the conversion reaction that occurs on the cathode. To elucidate the better performance of the Na-PPB salt-based electrolyte, density functional (DFT) calculations were carried out to investigate the energy needed for Na^+ ion movement. The binding energies of Na^+ solvated by DME to the PPB and hfip anion, respectively, were calculated (Table 1). The small difference

in the binding energy of 5.2 kJ mol^{-1} between the Na-PPB and the Na-hfip salt, however, does not explain the better performance of the Na-PPB salt-based electrolyte.

Hence, we compared the barriers responsible for Na^+ mobility in the electrolyte. The relevant re-orientation is the movement of Na^+ around the anion. To receive a minimum energy path (MEP) on the potential energy surface (PES) between two local minima of the coordination to the anions, NEB calculations of both the Na-PPB and the Na-hfip based electrolyte were performed (Fig. S5, S.I.). Interestingly, the barrier for Na^+ ion movement within the Na-hfip electrolyte is rather high ($136.9 \text{ kJ mol}^{-1}$), which leads to a decreased Na^+ mobility. In contrast, for the Na-PPB electrolyte, the barrier is significantly lower (74.3 kJ mol^{-1}) and can easily be overcome at room temperature, which results in higher Na^+ ion mobility and, consequently, in a better electrochemical performance.

To analyze the effect of salt hydrolysis on electrochemical performance, both Na-PPB and Na-hfip were left under ambient atmospheric conditions for two days in a petri dish. The electrolytes were prepared by adding propylene carbonate and 10 wt% FEC to the corresponding salt under constant stirring. Insoluble particles of the Na-hfip salt were filtered off before injecting the solution into the cell. Rapid degradation of the Na-hfip cell was observed in the discharge curve (Fig. 5a), indicating decomposed Na-hfip adversely affects the cell performance. By contrast, the Na-PPB-based cell showed high rate capability and stable cycling. The voltage profile (Fig. 5b) confirmed the reduced overpotential of the Na-PPB electrolyte, illustrating good electrochemical

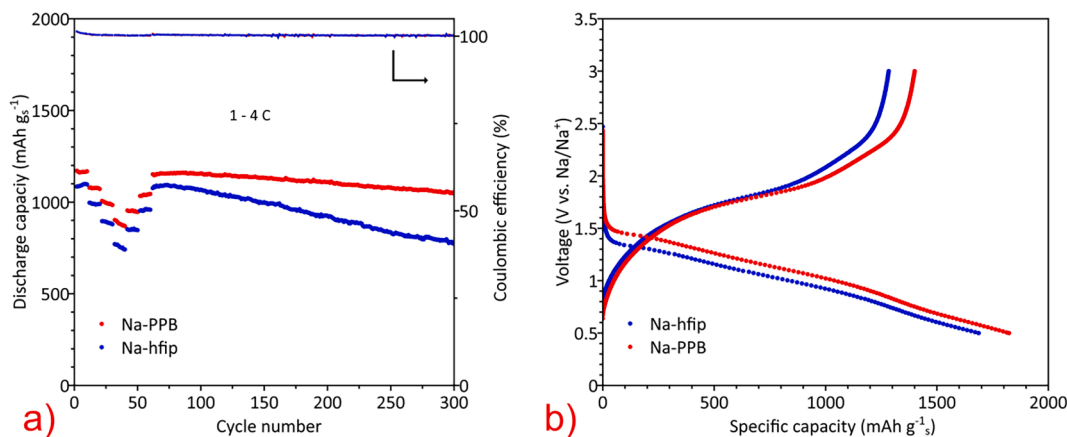


Fig. 5. Electrochemical analysis of Na-PPB and Na-hfip after exposure to air for 2 days, a) rate performance of Na-PPB (red) and Na-hfip (blue) between 1 and 4C; b) voltage profile of both salts during the first discharge and charge cycle. (For interpretation of the references to colour in this figure legend, the reader is referred to the web version of this article.)

reaction kinetics compared to Na-hfip.

4. Conclusions

In summary, a new type of electrolyte salt based on a weakly coordinating anion (Na-PPB) for RT Na-SPAN batteries has been developed. Na-PPB was synthesized in bulk via a one-pot reaction. NMR spectroscopy reveals high purity of the salt and stability even under ambient atmospheric conditions. Single-crystal X-ray analysis confirmed the molecular structure of Na-PPB with Na⁺ coordinated by one DME molecule. The electrolyte containing Na-PPB with PC + 10 wt% FEC showed high oxidative stability on Al current collector exceeding 5.5 V. In a Na-SPAN cell, the Na-PPB electrolyte allows for an initial and final discharge capacity (500 cycles) of 1140 mAh/g_{sulfur} and 965 mAh/g_{sulfur} respectively, obtained at 2C (3.35 A/g_{sulfur}). The excellent electrochemical performance and good chemical stability of Na-PPB offers access to the design of novel electrolyte salts for RT Na-SPAN batteries.

CRedit authorship contribution statement

Saravanakumar Murugan: Conceptualization, Data curation, Formal analysis, Investigation, Methodology, Validation, Visualization, Writing – original draft, Writing – review & editing. **Sina V. Klostermann:** Data curation, Formal analysis, Validation, Visualization, Writing – review & editing. **Wolfgang Frey:** Data curation, Formal analysis. **Johannes Kästner:** Funding acquisition, Resources, Supervision. **Michael R. Buchmeiser:** Funding acquisition, Methodology, Project administration, Resources, Supervision, Validation, Writing – original draft, Writing – review & editing.

Declaration of Competing Interest

The authors declare that they have no known competing financial interests or personal relationships that could have appeared to influence the work reported in this paper.

Acknowledgments

We gratefully acknowledge funding and support from the German Federal Ministry for Economic Affairs and Energy [BMW, project no. S50400, *FiMaLiS*]. We thank the Deutsche Forschungsgemeinschaft [DFG, German Research Foundation] for supporting this work by funding – [EXC2075 – 390740016] under Germany's Excellence Strategy. We acknowledge the support of the Stuttgart Center for Simulation Science (SimTech). The authors also acknowledge support by the State of Baden-Württemberg through bwHPC and the German Research Foundation (DFG) through grant no [INST 40/575-1 FUGG (JUSTUS 2 cluster)].

Appendix A. Supplementary data

Supplementary data to this article can be found online at <https://doi.org/10.1016/j.elecom.2021.107137>.

References

- [1] S.S. Berbano, I. Seo, C.M. Bischoff, K.E. Schuller, S.W. Martin, *J. Non-Cryst. Solids* 358 (2012) 93–98.
- [2] K. Hueso, M. Armand, T. Rojo, *Energy Environ. Sci.* 6 (2013) 734–749.
- [3] R. Okuyama, H. Nakashima, T. Sano, E. Nomura, *J. Power Sources* 93 (2001) 50–54.
- [4] V. Aravindan, J. Gnanaraj, S. Madhavi, H.-K. Liu, *Chem. Eur. J.* 17 (2011) 14326–14346.
- [5] S. Zhang, Y. Yao, Y. Yu, *ACS Energy Lett.* 6 (2021) 529–536.
- [6] Y.-X. Wang, B. Zhang, W. Lai, Y. Xu, S.-L. Chou, H.-K. Liu, S.-X. Dou, *Adv. Energy Mater.* 7 (2017) 1602829.
- [7] Y. Wang, Y. Zhang, H. Cheng, Z. Ni, Y. Wang, G. Xia, X. Li, X. Zeng, *Molecules* 26 (2021) 1535.
- [8] S. Murugan, S. Niesen, J. Kappler, K. Küster, U. Starke, M.R. Buchmeiser, *Batter. Supercaps*, <https://doi.org/10.1002/batt.202100125>.
- [9] B. Zhang, J. Wu, J. Gu, S. Li, T. Yan, X.-P. Gao, *ACS Energy Lett.* 6 (2021) 537–546.
- [10] T. Yim, M.-S. Park, J.-S. Yu, K.J. Kim, K.Y. Im, J.-H. Kim, G. Jeong, Y.N. Jo, S.-G. Woo, K.S. Kang, I. Lee, Y.-J. Kim, *Electrochim. Acta* 107 (2013) 454–460.
- [11] X. Xu, D. Zhou, X. Qin, K. Lin, F. Kang, B. Li, D. Shanmukaraj, T. Rojo, M. Armand, G. Wang, *Nat. Commun.* 9 (2018) 3870.
- [12] N. Wang, Y. Wang, Z. Bai, Z. Fang, X. Zhang, Z. Xu, Y. Ding, X. Xu, Y. Du, S. Dou, G. Yu, *Energy Environ. Sci.* 13 (2020) 562–570.
- [13] S. Wei, S. Xu, A. Agrawal, S. Choudhury, Y. Lu, Z. Tu, L. Ma, L.A. Archer, *Nat. Commun.* 7 (2016) 11722.
- [14] T. Leberher, M. Frey, A. Hintennach, M.R. Buchmeiser, *RSC Adv.* 9 (2019) 7181–7188.
- [15] J. Wang, J. Yang, Y. Nuli, R. Holze, *Electrochem. Commun.* 9 (2007) 31–34.
- [16] Z. Li, J. Zhang, Y. Lu, X. Lou, *Sci. Adv.* 4 (2018) 1687.
- [17] L. Wang, X. Chen, S. Li, J. Yang, Y. Sun, L. Peng, B. Shan, J. Xie, *J. Mater. Chem. A* (2019) 7.
- [18] X. Chen, L. Peng, L. Wang, J. Yang, Z. Hao, J. Xiang, K. Yuan, Y. Huang, B. Shan, L. Yuan, J. Xie, *Nat. Commun.* 10 (2019) 1021.
- [19] S. Ma, P. Zuo, H. Zhang, Z. Yu, C. Cui, M. He, G. Yin, *Chem. Commun.* 55 (2019) 5267–5270.
- [20] Y. Hu, B. Li, X. Jiao, C. Zhang, X. Dai, J. Song, *Adv. Funct. Mater.* 28 (2018) 1801010.
- [21] S. Bulut, P. Klose, I. Krossing, *Dalton Trans.* 40 (2011) 8114–8124.
- [22] M. Frey, R. Zenn, S. Warneke, K. Küster, A. Hintennach, R. Dinnebier, M. Buchmeiser, *ACS Energy Lett.* (2017) 2.
- [23] M. J. Frisch, G. W. Trucks, H. B. Schlegel, G. E. Scuseria, M. A. Robb, J. R. Cheeseman, G. Scalmani, V. Barone, G. A. Petersson, H. Nakatsuji, X. Li, M. Caricato, A. V. Marenich, J. Bloino, B. G. Janesko, R. Gomperts, B. Mennucci, H. P. Hratchian, J. V. Ortiz, A. F. Izmaylov, J. L. Sonnenberg, Williams, F. Ding, F. Lipparini, F. Egidi, J. Goings, B. Peng, A. Petrone, T. Henderson, D. Ranasinghe, V. G. Zakrzewski, J. Gao, N. Rega, G. Zheng, W. Liang, M. Hada, M. Ehara, K. Toyota, R. Fukuda, J. Hasegawa, M. Ishida, T. Nakajima, Y. Honda, O. Kitao, H. Nakai, T. Vreven, K. Throssell, J. A. Montgomery Jr., J. E. Peralta, F. Ogliaro, M. J. Bearpark, J. J. Heyd, E. N. Brothers, K. N. Kudin, V. N. Staroverov, T. A. Keith, R. Kobayashi, J. Normand, K. Raghavachari, A. P. Rendell, J. C. Burant, S. S. Iyengar, J. Tomasi, M. Cossi, J. M. Millam, M. Klene, C. Adamo, R. Cammi, J. W. Ochterski, R. L. Martin, K. Morokuma, O. Farkas, J. B. Foresman, D. J. Fox, Wallingford, CT, 2016.
- [24] S.G. Balasubramani, G.P. Chen, S. Coriani, M. Diedenhofen, M.S. Frank, Y. J. Franzke, F. Furche, R. Grotjahn, M.E. Harding, C. Hättig, A. Hellweg, B. Helmich-Paris, C. Holzer, U. Huniar, M. Kaupp, A.M. Khah, S.K. Khani, T. Müller, F. Mack, B. D. Nguyen, S.M. Parker, E. Perlt, D. Rappoport, K. Reiter, S. Roy, M. Rückert, G. Schmitz, M. Sierka, E. Tapavicza, D.P. Tew, C.V. Wüllen, V.K. Voora, F. Weigend, A. Wodyński, J.M. Yu, *J. Chem. Phys.* 152 (2020), 184107.
- [25] P. Sherwood, A.H. de Vries, M.F. Guest, G. Schreckenbach, C.R.A. Catlow, S. A. French, A.A. Sokol, S.T. Bromley, W. Thiel, A.J. Turner, S. Billeter, F. Terstegen, S. Thiel, J. Kendrick, S.C. Rogers, J. Casci, M. Watson, F. King, E. Karlsen, M. Sjøvoll, A. Fahmi, A. Schäfer, C. Lennartz, *J. Mol. Struct.* 632 (2003) 1–28.
- [26] S. Metz, J. Kästner, A.A. Sokol, T.W. Keal, P. Sherwood, *Wiley Interdiscip. Rev. Comput. Mol. Sci.* 4 (2014) 101–110.
- [27] J. Kästner, J.M. Carr, T.W. Keal, W. Thiel, A. Wander, P. Sherwood, *J. Phys. Chem. A* 113 (2009) 11856–11865.
- [28] J. Luo, Y. Bi, L. Zhang, X. Zhang, T.L. Liu, *Angew. Chem.* 58 (2019) 6967–6971.
- [29] J. Wu, J. Liu, Z. Lu, K. Lin, Y.-Q. Lyu, B. Li, F. Ciucci, J.-K. Kim, *Energy Storage Mater.* 23 (2019) 8–16.
- [30] K.-C. Lau, T. Seguin, E. Carino, N. Hahn, J. Connell, B. Ingram, K. Persson, K. Zavadil, C. Liao, *J. Electrochem. Soc.* 166 (2019) A1510–A1519.
- [31] A.Y.S. Eng, D.-T. Nguyen, V. Kumar, G.S. Subramanian, M.-F. Ng, Z.W. Seh, *J. Mater. Chem. A* 8 (2020) 22983–22997.
- [32] Z.-Q. Jin, Y.-G. Liu, W.-K. Wang, A.-B. Wang, B. Hu, M. Shen, T. Gao, P.-C. Zhao, Y.-S. Yang, *Energy Storage Mater.* (2018) 14.
- [33] W. Wang, Z. Cao, G. Elia, W. Wahyudi, E. Abou-hamad, A.-H. Emwas, L. Cavallo, L. Li, *ACS Energy Lett.* 3 (2018).
- [34] S. Zhang, *Energies* 7 (2014) 4588–4600.
- [35] A.N. Srivastava, *Stability and Applications of Coordination Compounds*, Intech, 2020.

Supporting Information

to

A sodium bis(perfluoropinacol) borate-based electrolyte for stable, high-performance room temperature sodium-sulfur batteries based on sulfurized poly(acrylonitrile)

Table S1. Combustion elemental analysis of Na-PPB.

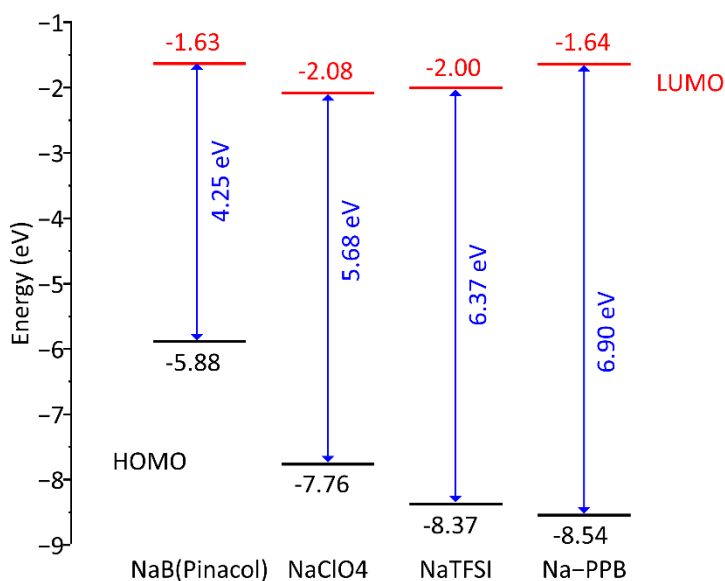
Element	Calculated (%)	Found (%)
C	24.38	24.21
H	1.279	1.318
C : H	19.062	18.361

Table S2. Combustion elemental analysis of an SPAN cathode.

Element	wt.%				Atomic ratio
	S	C	N	H	C/S
SPAN	40.24	42.36	13.43	0.9883	2.81

Table S3. Comparison of oxidation potentials of the various existing electrolyte system for RT Na-S batteries.

Salt / molar	Solvent	Working electrode	Oxidation potential V (vs. Na ⁺ /Na)
NaTFSI / 2M	PC:FEC (1:1) + 10 mM InI ₃	SS	5.2 ^[1]
NaTFSI / 2M	TMP:FEC (7:3)	SS	4.6 ^[2]
NaB(hfip) ₄ / 1M	EC:DMC + FEC (1:1) + 13 wt.%	Pt	4.65 ^[3]
NaCF ₃ SO ₃ / 1M	Triglyme	Carbon-coated Al	4.0 ^[4]
Na-PPB / 1M	PC + (FEC, 10 wt.%)	Al	>5.5 (This work)

**Figure S1.** Comparison of HOMO and LUMO energy levels of sodium bis(pinacol) borate, NaClO₄, NaTFSI, and Na-PPB.

The calculation of the HOMO and LUMO energy levels was performed with the Gaussian 09 software package using DFT. All energies are calculated at the B3LYP/6-31+G(2d,p) level. We compared the HOMO energy levels of different salts to validate the high oxidation resistance of

Na-PPB. Thus, commercially available salts such as NaClO₄ and NaTFSI and a non-fluorinated sodium bis(pinacol) borate HOMO energy levels were calculated and compared with Na-PPB. From Figure S1, it is evident that Na-PPB has a lower HOMO energy level (-8.54 eV) than its counterparts. It is reasonable to associate oxidative stability of the molecule to their HOMO energy level since oxidation results in losing of an electron from its HOMO. The electron-withdrawing group in the molecule is responsible for lowering the HOMO energy level which in turn increases stability against oxidation. Based on the calculation results, Na-PPB has excellent oxidation stability compared to commercially available sodium salts.

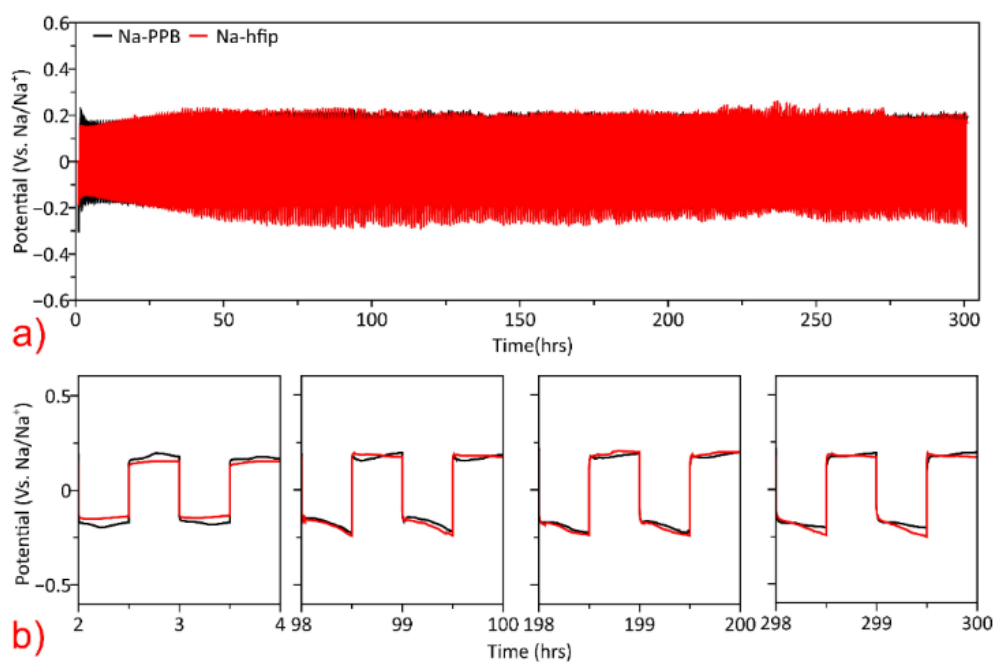


Figure S2. Na||Na symmetrical cell voltage profile at 1 mA cm⁻² (0.5 mAh cm⁻²) for Na-PPB and Na-hfip.

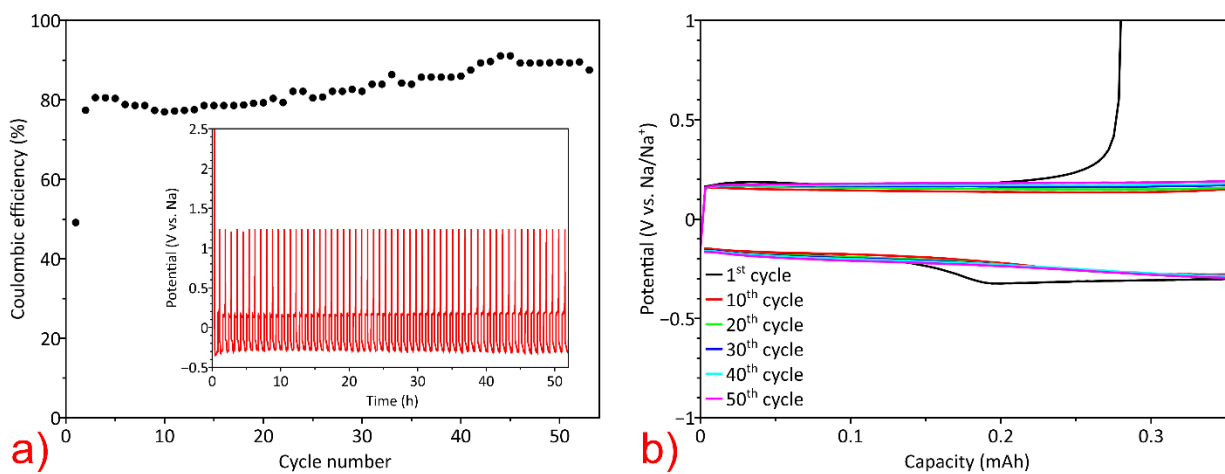


Figure S3. Cycling performance of a Na-PPB electrolyte with graphite as a working electrode, a) coulombic efficiency (inset: chronopotentiogram); b) comparison of voltage versus capacity plot at various cycles.

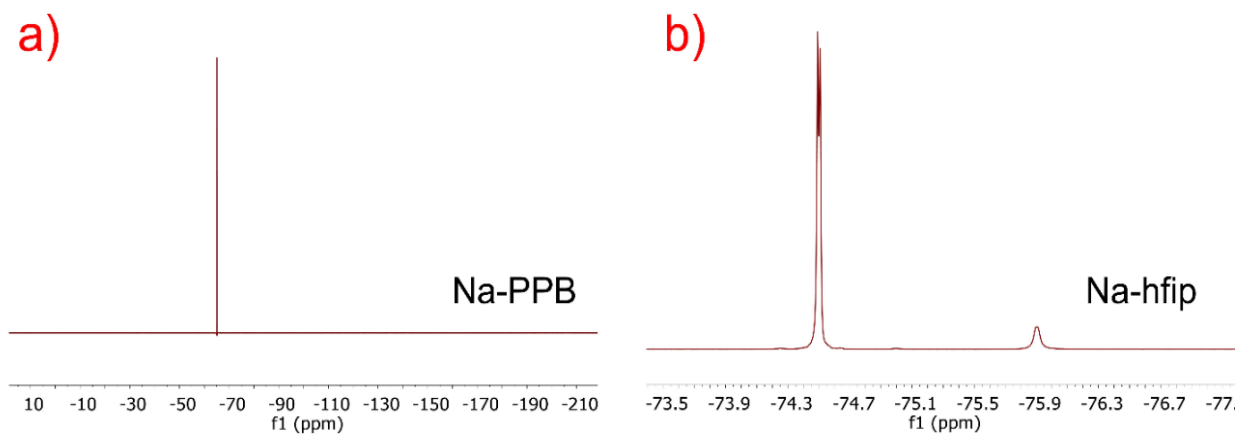


Figure S4. ^{19}F -NMR spectra of a) Na-PPB and b) Na-hfip kept under ambient conditions for 20 days.

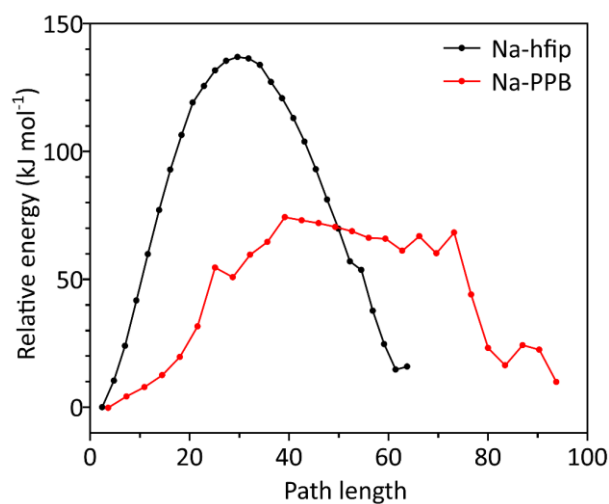


Figure S5. Energy profile along the reaction path (NEB calculations) of both salts, representing the potential barrier between two local minima of the respective salt.

Table S4. Comparison of the morphological changes of Na-hfip and Na-PPB after exposure to air for 20 days.

Samples	Na-hfip	Na-PPB
Pristine		
After exposure to air for 20 days		
Remarks	Color changed to pure white and loss of material	Almost similar to the initial state except for a slight color change

Table S5. Comparison of the weight loss of Na-PPB and Na-hfip after exposure to air for 20 days.

Sample	Initial weight (g)	Weight (g) after 20 days in air	Weight loss (%)
Na-PPB	0.0686	0.0491	28
Na-hfip	0.1347	0.0128	91

Table S6. Comparison of cycling performance of RT Na-S systems with various sulfur-based cathodes.

Cathode system	Electrolyte	C - rate / current	Capacity (mAh g ⁻¹)	Cycle life	Coulombic efficiency (%)
Electrospun SPAN	0.8 M NaClO ₄ in EC + DEC (v = 1:1)	1 C	153	500	99.93 ^[5]
SPAN cathode	1 M NaClO ₄ in EC + DMC (v = 1 : 1) + 8 wt% FEC	0.5 C	1000	1000	~100 ^[6]
Selenium-doped SPAN	1 M NaClO ₄ in PC + PC (v = 1:1)	0.4 A g ⁻¹	~770	500	~100 ^[7]
Tellurium-doped SPAN	1 M NaClO ₄ in PC + DMC (v = 1:1) + 10 wt% FEC	0.5 A g ⁻¹	~970	600	~100 ^[8]
Iodine-doped SPAN	1 M NaClO ₄ in EC + DEC (v = 1 : 1) + 8 wt% FEC	2 C	674	500	>99 ^[9]
S / C composite	1.5 M NaClO ₄ + 0.3 M NaNO ₃ in tetraglyme	-	400	20	- ^[10]
Sulfur in slit micropore	1 M NaClO ₄ in EC + PC (v = 1 : 1) + 2 wt% FEC	1 C	~640	2000	~100 ^[11]
SPAN cathode	1 M Na-PPB in PC + 10 wt%FEC	2 C	>950	500	>99.8 (This work)

References

- [1] X. Xu, D. Zhou, X. Qin, K. Lin, F. Kang, B. Li, D. Shanmukaraj, T. Rojo, M. Armand, G. Wang, *Nat. Commun.* **2018**, *9*, 3870.
- [2] J. Wu, J. Liu, Z. Lu, K. Lin, Y.-Q. Lyu, B. Li, F. Ciucci, J.-K. Kim, *Energy Storage Mater.* **2019**, *23*, 8-16.
- [3] S. Murugan, S. Niesen, J. Kappler, K. Küster, U. Starke, M. R. Buchmeiser, *Batter. Supercaps*, <https://doi.org/10.1002/batt.202100125>.
- [4] D. Di Lecce, L. Minnetti, D. Polidoro, V. Marangon, J. Hassoun, *Ionics* **2019**, *25*, 3129-3141.
- [5] T. H. Hwang, D. S. Jung, J.-S. Kim, B. G. Kim, J. W. Choi, *Nano Letters* **2013**, *13*, 4532-4538.
- [6] A. Y. S. Eng, D.-T. Nguyen, V. Kumar, G. S. Subramanian, M.-F. Ng, Z. W. Seh, *J. Mater. Chem. A* **2020**, *8*, 22983-22997.
- [7] L. Wang, X. Chen, S. Li, J. Yang, Y. Sun, L. Peng, B. Shan, J. Xie, *J. Mater. Chem. A* **2019**, *7*, 12732-12739.
- [8] S. Li, Z. Zeng, J. Yang, Z. Han, W. Hu, L. Wang, J. Ma, B. Shan, J. Xie, *ACS Appl. Energy Mater.* **2019**, *2*, 2956-2964.
- [9] S. Ma, P. Zuo, H. Zhang, Z. Yu, C. Cui, M. He, G. Yin, *ChemComm* **2019**, *55*, 5267-5270.
- [10] X. Yu, A. Manthiram, *ChemElectroChem* **2014**, *1*, 1275-1280.
- [11] Q. Guo, S. Li, X. Liu, H. Lu, X. Chang, H. Zhang, X. Zhu, Q. Xia, C. Yan, H. Xia, *Adv. Sci.* **2020**, *7*, 1903246.

4 Gel polymer electrolyte for sodium sulfur batteries

4.1 Introduction

LEs have played a key role in transforming the energy storage sector for several decades by successful commercialization of LIB technology and also promoting research beyond LIB batteries. LE technology was successful due to its high ionic conductivities ($>1 \text{ mS cm}^{-1}$), good contact with electrodes, and ease of fabrication and characterization. However, the usage of harmful solvents leads to leakage and even combustion or explosion. Lithium dendrite growth is inevitable in LEs caused by uneven deposition of the lithium ions. On the other hand, solid polymer or inorganic solid electrolytes can prevent dendrite formation and electrolyte leakage.^[320] However, reduced ion mobility limits the ionic conductivity (10^{-5} to $10^{-2} \text{ mS cm}^{-1}$) in solid electrolytes. As an electrolyte with two states, liquid and solid, and a mixture of liquid and solid components, GPE shows a synergistic advantage such as high ionic conductivity and good interfacial contact through the liquid medium and good mechanical properties from its solid contents. GPEs are divided into two types namely, heterogeneous (phase-separated) and homogeneous (uniform) gel. The homogeneous gel contains a uniform polymer matrix with interconnected pores. These pores absorb and swell in presence of the liquid electrolyte where the ion conduction takes place. This is the reason for the high ionic conductivity in GPE ($>1 \text{ mS cm}^{-1}$). Heterogeneous GPEs are synthesized by adding inorganic fillers such as TiO_2 , Al_2O_3 , and SiO_2 to the polymer matrix. Many polymer systems were employed as the solid component in GPEs such as PEO,^[321] poly(vinylidene fluoride) (PVDF),^[322] poly(methyl methacrylate) (PMMA),^[323, 324] poly(acrylonitrile) (PAN),^[325] poly(vinyl alcohol) (PVA),^[326] poly(vinylidene fluoride-*co*-hexafluoropropylene) (PVDF-HFP)^[327, 328] and poly(acrylic acid) (PAA)^[329] due to their good affinity towards liquid electrolytes. The distinct types of electrolytes and their properties required to be used in LIB are listed in Table 5. In an early research phase, Feuillade et al. introduced a quasi-solid state GPE in 1975 by using a binary polymer-salt system.^[198] Apart from traditional electrolytes, various ionic liquids were used as a novel type of liquid electrolytes for GPEs. GPEs are not a new type of electrolyte, therefore, research focused on optimizing the properties such as ionic conductivity, mechanical strength, LE / GPE composition, and interfacial contact.^[330]

4. Gel polymer electrolyte for sodium sulfur batteries

Achieving high ionic conductivity and mechanical strength for GPEs is challenging since the presence of liquid components ultimately degrades the mechanical strength by swelling or soaking the polymer host. The amount of liquid present in the polymer host controls the ionic conductivity, the higher the liquid amount, the better the ionic conductivity. To attain the balance between them, it is necessary to design a polymer host, which can absorb a high amount of LE but at the same time maintains structural integrity.^[331]

Table 5. The main properties of the primary electrolytes used in LIBs (reproduced with permission from Ref. ^[332]).

Electrolyte properties	Liquid	Gel	Solid
Ionic conductivity	>1 mS cm ⁻¹ (high)	>0.1 mS cm ⁻¹ (medium)	<0.1 mS cm ⁻¹ (low)
Interfacial properties	Good	Medium	Poor
Electrochemical stability	Poor	Poor	Good
Thermal stability	Poor	Poor	Good
Dimension stability	Poor	Medium	Good
Safety	Poor	Medium	Good

For example, mixing nanoparticles and crosslinking the polymer enhances the mechanical strength and ensures high conductivity.^[332, 333, 334, 335, 336] Kil et al.^[337] synthesized UV-curable composite GPEs by mixing LEs and trivalent monomer and Al₂O₃ nanoparticles with a particle size of ~300 nm. The polymer host maintained structural integrity by crosslinking and the introduction of the Al₂O₃ nanoparticles increases the mechanical strength as well as the ion movement. Liao et al. developed a GPE with Al₂O₃ doped in PEO and PVDF-HFP polymer with poly(propylene) as a polymer matrix. The addition of nanoparticles increased the ionic conductivity from 2.7 mS cm⁻¹ to 3.8 mS cm⁻¹.^[338] Though the addition of an LE ensures interfacial contact to some extent, achieving full contact with GPE is much more challenging. Therefore, the GPEs and electrodes require a unique design concept of the interface, processing, and fabrication. Usually, GPEs are prepared by wetting the polymer matrix several times before fabrication to ensure the complete penetration of LE and good interfacial contact. Hung et al.^[339] proposed a roll-to-roll fabrication of the GPE for supercapacitors. Owing to the

good contact between electrodes and electrolyte, the device showed superior performance on par with LEs.

The LEs in lithium metal batteries (LMBs) experience severe challenges. The reaction between LEs and lithium metal leads to the formation of an unstable native SEI layer. This SEI layer breaks up on cycling due to the stress on the Li metal forcing the Li to react with the LE again. This repetitive process continuously consumes Li, resulting in low coulombic efficiency, reduced capacity, and early failure of the cell.

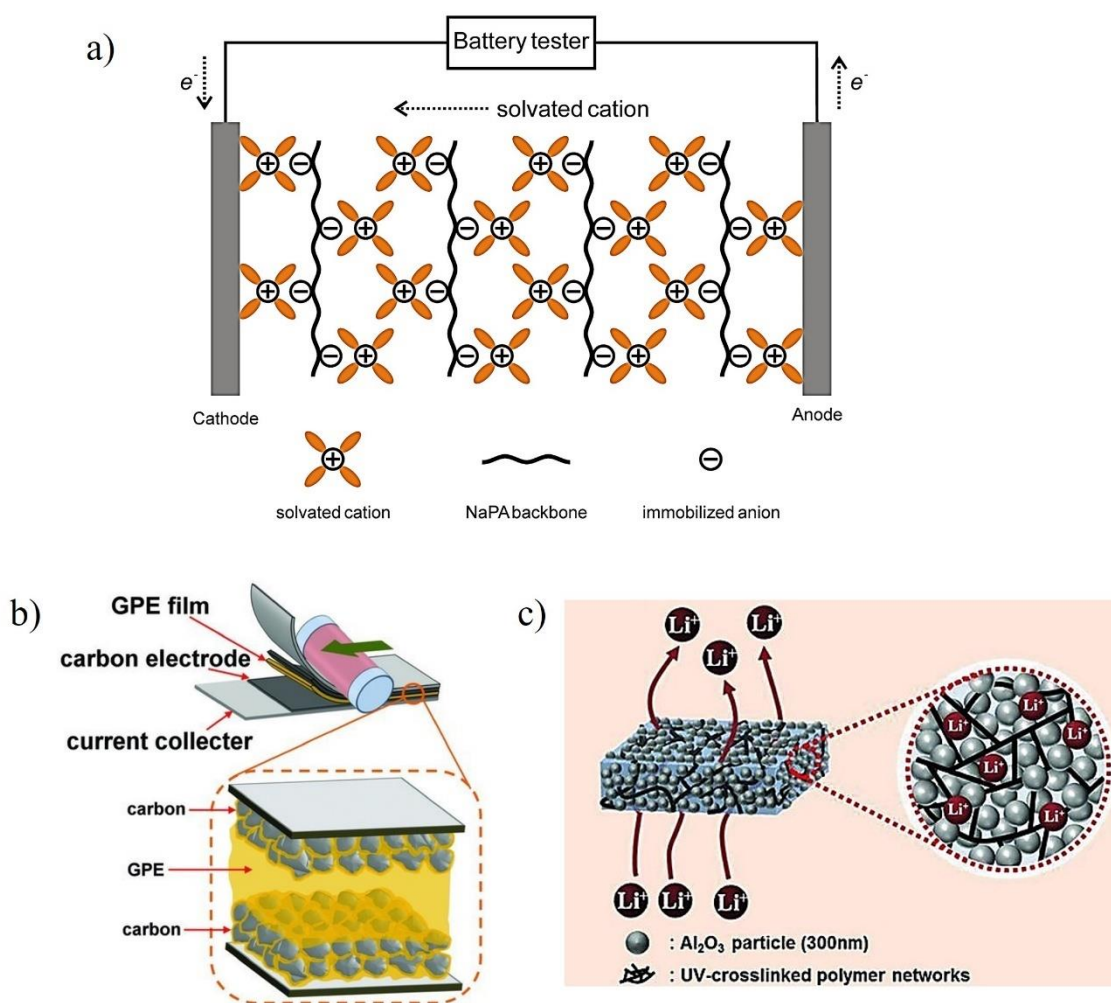


Figure 32. a) Schematic drawing of Na⁺ ion movement in SIC-GPE (reproduced with permission Ref. ^[340]); b) graphical illustration of a roll-to-roll assembly of a supercapacitor with GPE film (reproduced with permission Ref. ^[339]); c) schematic diagram of a flexible, printable, and conformable crosslinked GPE (reproduced with permission Ref. ^[337]).

On the other hand, nonuniform plating/stripping contributes to dendrite formation and subsequent short-circuiting of the cell in LEs. SPEs might avert all the shortcomings of

4. Gel polymer electrolyte for sodium sulfur batteries

the LEs such as safety and stability but suffer from low ionic conductivity. The batteries with SPEs can cycle only at low C-rates (<0.2 C) and at elevated temperatures (>60 °C). On the other hand, the low ionic conductivity of SPEs can be overcome by adding plasticizers to the polymer host. Uniform and stable nucleation and growth of Li on the anode is a genuine issue considering the safety of the battery. Conventional SPEs lack cation movement due to the interaction between cations and Lewis acid sites in the polymer chain, leading to an ion transference number <0.5 .^[341, 342] Both anions and cations move in opposite directions during the application of the electric field; however, the anions tend to accumulate near the anode creating concentration gradients because the behavior of the electrode is blocking. This leads to concentration polarization thus resulting in poor cell performance such as voltage hysteresis, increased internal impedance, side reactions, and cell failure. Therefore, a novel type of GPE with cation transference number reaching unity was developed by using single-ion conducting gel polymer electrolytes (SIC-GPE). Several advantages such as excluded concentration gradient even at the liquid phase, ca. 100% active electrode material utilization,^[343] and prevention of dendrite growth^[344] make SIC-GPE a perfect alternate for dual ion conducting SPEs.^[345] Two basic methods are followed while synthesizing SIC-GPEs: 1) polymerization of the electrolyte salt and 2) modification of the existing polymer. Alteration of the existing polymer by including the anionic group of Li/Na salt into the polymer backbone. The lithium-based SIC polymer can be synthesized by functionalization of the sodium precursor. For example, lithium poly[(4-styrenesulfonyl)(trifluoromethanesulfonyl)imide] (LiPSTFSI) is usually obtained through polymerization of LiSTFSI or by modification of sodium poly(styrenesulfonate) (NaPSS). These SIC-GPEs can absorb a huge amount of electrolyte solvents without losing their mechanical strength and can be blended with other polymers such as PEO, PVDF, and PVDF-HFP to improve their mechanical properties. Oh et al. synthesized a microporous SIC-GPE based on aromatic poly(arylene ethers) with pendant lithium perfluoroethyl sulfonates. The electrolyte exhibits very high ionic conductivity of >1 mS cm⁻¹ and transference numbers near unity.^[346, 347] Wang et al. synthesized a polymeric sodium tartaric acid borate-based SIC-GPE which exhibits a high Na⁺ transference number of 0.88 and high oxidation voltage of 4.5 V vs. Na/Na⁺. The low concentration polarization due to the restricted anion movement leads to excellent plating and stripping cycles up to 600 h.^[348]

Even though SIC-GPE provides several advantages, from the practical standpoint, the noticeable benefit appears only at impractically high currents (i.e., where the concentration polarization occurs). In other words, during the cycling of the traditional cells, the concentration polarization is imperceptible. Moreover, the lower ohmic resistance and better kinetics under practical conditions (Figure 33) render dual ion GPE a good choice of electrolyte for commercial purposes.

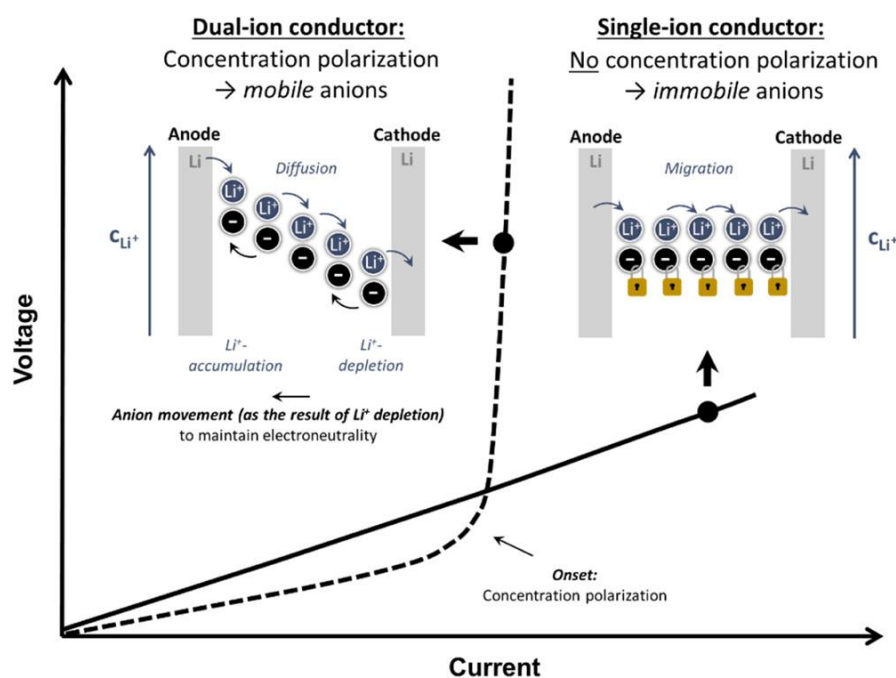


Figure 33. Illustration of symmetric Li||Li cell with single and dual ion conductor (reproduced with permission Ref. [349]).

An alternate method of synthesizing a GPE for LIBs or SIBs is by crosslinking single or several monomers either by *ex situ* or *in situ* polymerization. This type of dual ion conducting GPE exhibits high ionic conductivity, enhanced dimensional stability, good mechanical strength, and reduced dendrite formation. Moreover, crosslinked GPEs offer a durable polymer membrane with good absorption of the liquid electrolyte. For example, Lu et al.^[350] developed a 3D crosslinked polymer network (3D-GPE) with poly(ethylene glycol) diglycidyl ether (PEGDE) and diamino-poly(propylene oxide) (DPPO), which ensures the fast ion transport across the electrode (Figure 34a and c). The symmetrical cell with Li||3D-GPE||Li cycled for over 900 h while maintaining a stable and extremely low overpotential. The full cell containing LiFePO₄/3D-GPE/Li delivered a high discharge capacity of 73 mAh g⁻¹ at 20 C. Similarly, Gao et al.^[351] synthesized a crosslinked GPE with methyl methacrylate (MMA) and tetraethylene glycol dimethacrylate (TEGDMA) by free radical polymerization for SIBs. The MMA and

4. Gel polymer electrolyte for sodium sulfur batteries

TEGDMA were dissolved in the liquid electrolyte which comprises $\text{NaClO}_4 + \text{PC}$ and FEC followed by a drop casting on a cellulose membrane and then heated to 70°C for 6 h (Figure 34b, d). The full cell containing $\text{Na}_3\text{V}_2(\text{PO}_4)_3/\text{GPE}/\text{Sb}$ cell was able to cycle steadily compared to the liquid electrolyte.

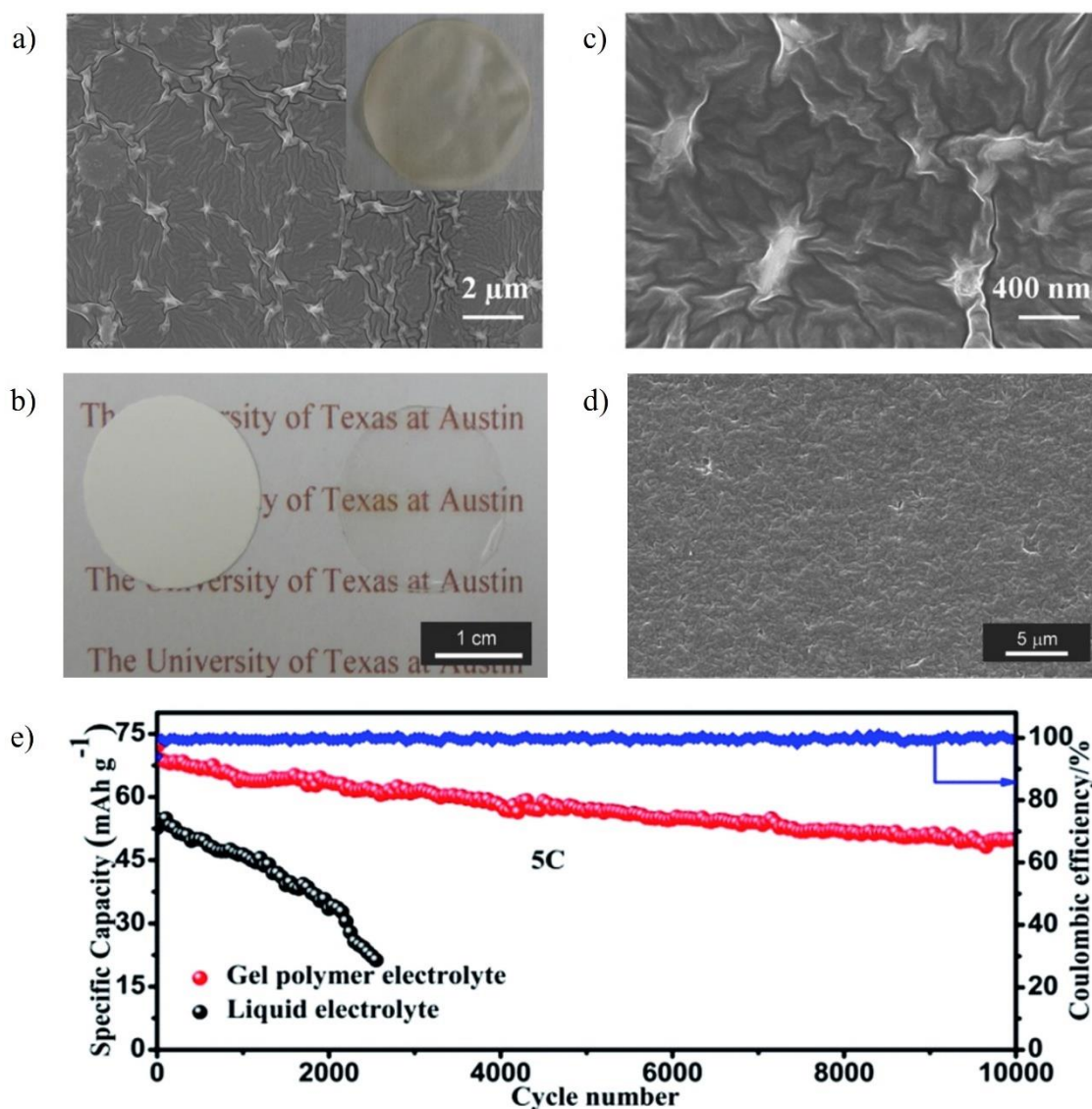


Figure 34. a, b) SEM image of crosslinked PEGDE-based 3D-GPE membrane (inset: optical photograph) (reproduced with permission Ref. ^[350]); c) visual image of the cellulose membrane (left) and the GPE electrolyte of PMMA-loaded cellulose (right); d) SEM image of cellulose membrane with cross-linked PMMA (reproduced with permission Ref. ^[351]); e) long-term cycling of $\text{Na}_3\text{V}_2(\text{PO}_4)_3/\text{GPE}/\text{Sb}$ cell at 5 C (reproduced from Ref. ^[352] with permission from the Royal Society of Chemistry).

The phosphorus containing GPEs possess improved ionic conductivity and high flame retardancy. Zheng et al. synthesized a GPE with MMA and trifluoroethyl methacrylate

(TFMA) crosslinked by a phosphonate-containing monomer. Figure 34e shows the long-term cycling performance of a Na full cell containing a GPE demonstrating excellent cycle stability up to 10000 cycles at 5 C yet retaining 69.2 % of its original capacity. On the other hand, the liquid electrolyte-containing cell degraded within 2500 cycles. The cell also showed a very little overpotential compared to the liquid electrolyte.^[352]

In the case of MSBs, the active material, sulfur, comprises several difficulties compared to LIBs or SIBs. Therefore, GPE-based electrolytes should possess additional advantages such as good mechanical strength, good affinity towards polysulfides, and better contact with cathode active material. They should also accompany volume changes and have confinement capability towards discharged products in the electrode. Wang et al.^[95] were the first to develop the concept of GPEs in lithium-sulfur batteries in 2002. The heterogeneous GPE was synthesized by mixing SiO₂ filler with the PVDF-HFP polymer in an acetone and ethanol solution. The resulting slurry was cast on a glass plate and then soaked in the liquid electrolyte. The polymer film was able to absorb 70 wt.% of the electrolyte, which facilitates fast ion transport. This GPE reduced polysulfide dissolution and enhanced battery performance. Similarly, in 2006, Park et al.^[123] combined a GPE based on PVDF-tetraglyme-NaCF₃SO₃ and a sulfur cathode for RT SSBs. The cell delivered an initial discharge capacity of 489 mAh g⁻¹ with two voltage plateaus at 2.28 V and 1.28 V. In both Na and Li – sulfur batteries, GPE helps to alleviate the “polysulfide shuttle” by a physical barrier or/and by chemical adsorption (Figure 35). Electrolyte pores can be modified to block some polysulfides by the addition of nanoparticles and pore-making agents and by creating multidimensional structures. In addition, the GPE viscosity alone can prohibit the polysulfide crossover. For example, Jeddi et al.^[353] developed a GPE by mixing PVDF-HFP and PMMA as a polymer host and mesoporous silica as a filler to control polysulfide movement within the electrolyte. The electrolyte offers two unique characteristics such as immobilization of the electrolyte within the polymer matrix during cycling and nanometer-sized silica facilitating lithium ion movement by forming a porous mesh. Adding special groups to the GPE benefits the formation of chemical bonds with the polysulfides which blocks the shuttle effect of the polysulfides. For example, a GPE membrane with PEO and LiTFSI absorbs the polysulfides thereby reducing the diffusion of polysulfides and self-discharge.^[354]

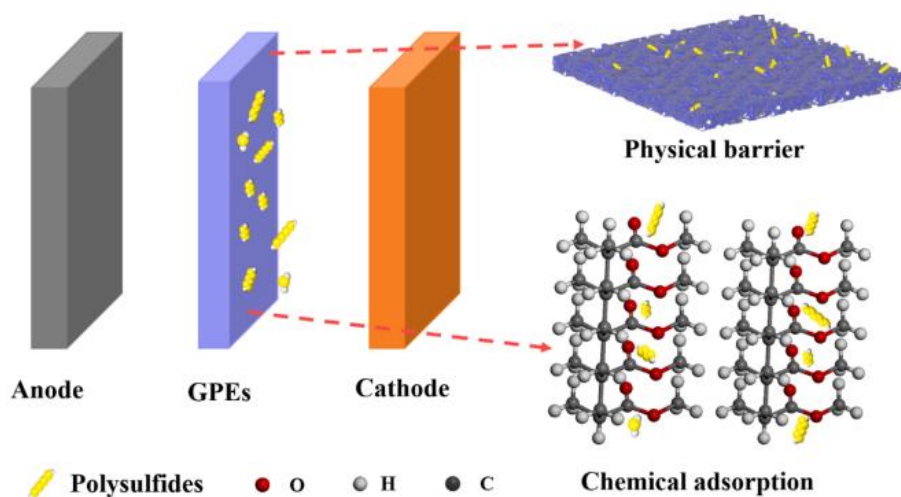


Figure 35. Polysulfide blocking mechanism by GPEs in sulfur-based cathodes (reproduced with permission Ref. ^[355]).

Similarly, Qu et al.^[356] developed a sandwich-structured GPE, “NCP-CPEs” with nano carbon black and cellulose nonwoven/poly(ethylene glycol)-*block*-poly(propylene glycol)-*block*-poly(ethylene glycol) (PEG-PPGPEG) (Figure 36). The cathode side was coated with nano carbon black, which acts as a second current collector thereby enhancing the electron transfer during the conversion of final sulfides and also preventing the polysulfide shuttle. Additionally, the hydroxyl groups in the cellulose membrane have a strong binding capacity toward polysulfides, which helps in retaining polysulfides on the cathode side. Finally, the PEG-PPGPEG layer on the side of the anode protects the Li metal and ensures uniform Li plating and stripping. This full cell with GPE demonstrated an excellent cycling performance at 4 C up to 1500 cycles with a pure sulfur cathode.

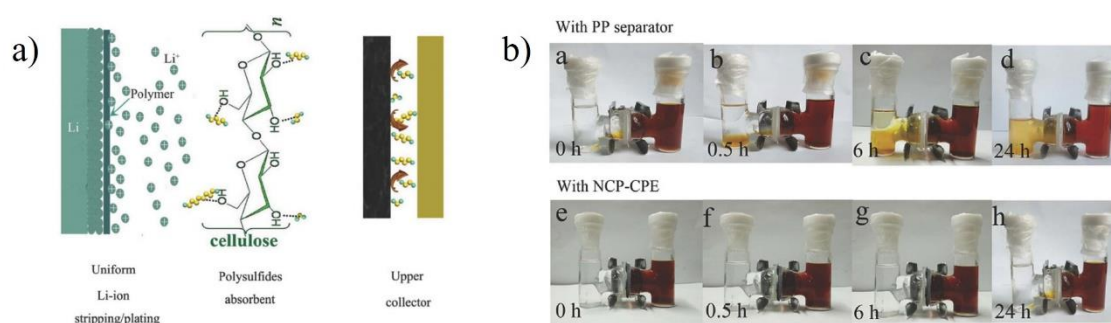


Figure 36. a) Graphical illustration of an interaction mechanism between polysulfides and NCP-CPEs; b) optical images of polysulfide dissolution comparison in (a-d) PP separator and (e-h) NCP-CPEs separator (reproduced with permission from Ref. ^[356], open access).

4.2 Publication “Stable Cycling of Room-Temperature Sodium-Sulfur Batteries Based on an In Situ Crosslinked Gel Polymer Electrolyte”

GPE preparation strategies include gelation, polymerization, and cross-linking, which can be divided into two different types: *In situ* and *ex situ* methods (Figure 37). In an *ex situ* preparation, GPEs were prepared before the cell assembly (i.e) free-standing polymer membranes. This method provides excellent safety but it faces a similar challenge as SSEs: the GPEs cannot infiltrate the cathode pores, which results in poor interfacial contact and increased interfacial impedance. On the other hand, GPEs prepared via *in situ* methods resolve the interfacial contact issue between electrolyte and electrode. In this method, the liquid precursor containing monomeric units is injected into the separator and progressively transformed into a quasi-solid state or GPE with the help of temperature or the initiator.

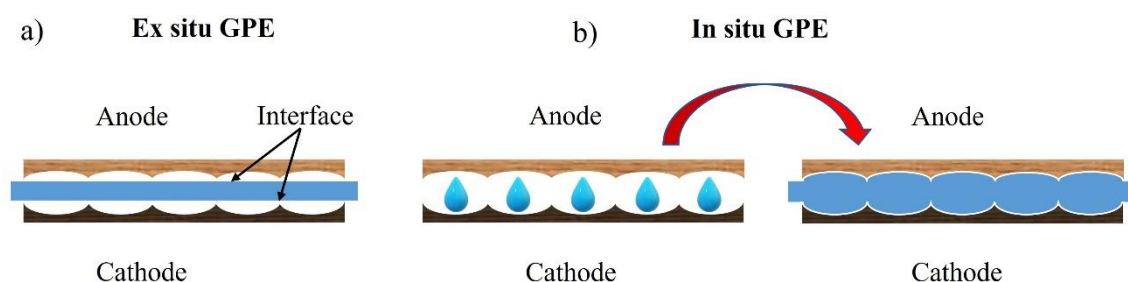


Figure 37. Schematic illustration of interfacial contact between electrode and electrolyte in a) *ex situ* and b) *in situ* synthesis of GPE.

Several attempts were made to improve the battery performance of sulfur-based cathodes in LSBs and SSBs. For example, pentaerythritol tetraacrylate (PETEA)-based GPE was synthesized by free radical polymerization for an LSB via *in situ* polymerization. The tetra-functional monomer yielded a highly viscous crosslinked GPE which was able to retain the liquid electrolyte in their matrix. The GPE showed a high ionic conductivity value of 11.3 mS cm^{-1} at room temperature which is close to that of the liquid electrolyte (11.9 mS cm^{-1}). The crosslinked PETEA network blocks the movement of the anions thereby increasing the lithium-ion transference number. The transference number of the lithium cation was 0.47 for GPE compared to the LE (0.35). The pure sulfur electrodes with GPE were cycled with an excellent discharge capacity and high rate capability. Finally, the high-strength GPE mitigated the polysulfide migration across the electrodes by forming a flexible passivation layer on the cathode. Additionally, the GPE was able to sustain huge volume changes exerted during cycling (Figure 38a).

4. Gel polymer electrolyte for sodium sulfur batteries

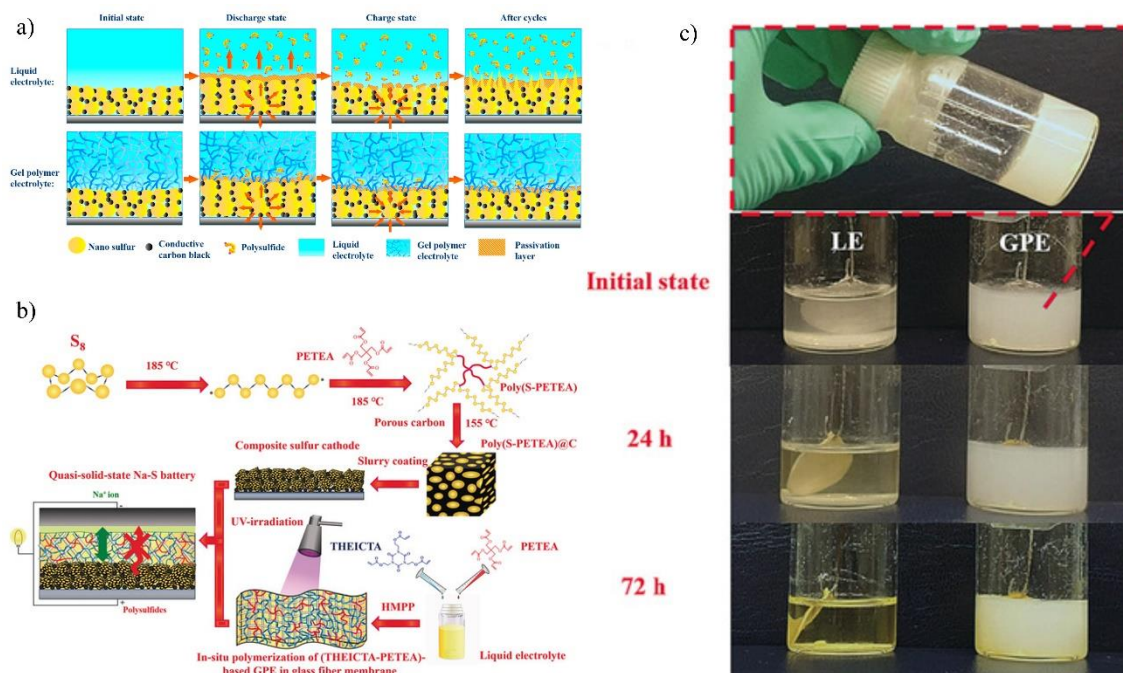


Figure 38. Inhibition of the polysulfides from the pure sulfur cathode by confinement of the PETEA-based GPE (reproduced with permission Ref. [357]); b) graphical illustration of the preparation of the GPE based on PETEA; and c) optical images of Na polysulfides evolution and diffusion in LE and GPE at various time intervals (reproduced with permission Ref. [358]).

Similarly, RT SSB with PETEA-based GPE was synthesized with crosslinked sulfur cathode by *in situ* polymerization (Figure 38b). Several synthesis steps were followed to obtain a crosslinked sulfur cathode and quasi-solid-state electrolyte by combining heating and ultraviolet light (UV)- irradiation to initiate the radical polymerization of C=C bonds. PETEA and tris[tris[2-(acryloyloxy)ethyl] isocyanurate] (THEICTA) were dissolved in a liquid electrolyte together with an initiator to form a precursor solution. Later the precursor solution was infiltrated into a glass fiber membrane and subjected to UV irradiation. As shown in Figure 38c, the diffusion of polysulfides was observed by placing Na metal foil in LE and GPE. After heating to 60 °C for 72 h, the LE turns yellow color, indicating sulfur dissolution into the LE and reaction with Na metal to generate soluble polysulfides. On the other hand, GPE retains its milky white color, implying that the dissolution of the polysulfides has been significantly decreased in the GPE.

In this study, a trifunctional pentaerythritol triacrylate (PETA) based GPE was synthesized by *in situ* crosslinking to ensure good contact between SPAN and Na electrodes and electrolytes. PETA-based GPE offers both chemical and physical barriers,

which can alleviate self-discharge and locally confine the discharged product. DFT studies were carried out by the group of Prof. Johannes Kästner to calculate the binding energy between PETA and polysulfides and also molecular electrostatic potential mapping was performed to identify the source of the ion transport in GPE and LE. Finally, a pouch containing GPE-based SSB full cell was subjected to various mechanical deformation tests.

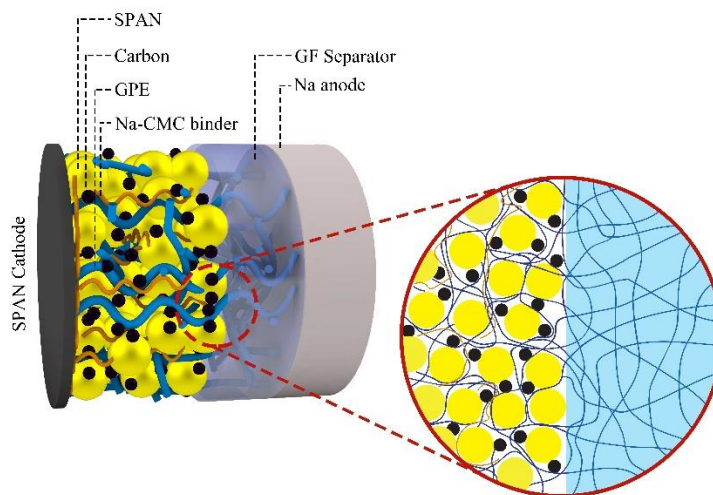


Figure 39. Schematic illustration of GPE containing Na-SPAN full cell (reproduced with permission from Ref. ^[359], open access).

Publication:

Murugan, S.; Klostermann, S. V.; Schützendübe, P.; Richter, G.; Kästner, J.; Buchmeiser, M. R., Stable Cycling of Room-Temperature Sodium-Sulfur Batteries Based on an In Situ Crosslinked Gel Polymer Electrolyte. *Adv. Funct. Mater.* **2022**, *32*, 2201191.

Author Contributions: **Saravanakumar Murugan**: Conceptualization, Data curation, Formal analysis, Investigation, Methodology, Validation, Visualization, Writing - original draft, review & editing. **Sina V. Klostermann**: Investigation (DFT calculations), Validation, Writing - review & editing. **Peter Schützendübe**: Data curation, Formal analysis (XPS measurements). **Gunther Richter**: Resources (SEM, XPS), Supervision. **Johannes Kästner**: Funding acquisition, Resources, Supervision. **Michael R. Buchmeiser**: Funding acquisition, Project administration, Resources, Supervision, Validation, Writing - review & editing.

Reprinted with permission from ^[359], (open access).

Stable Cycling of Room-Temperature Sodium-Sulfur Batteries Based on an In Situ Crosslinked Gel Polymer Electrolyte

Saravanakumar Murugan, Sina V. Klostermann, Peter Schützendübe, Gunther Richter, Johannes Kästner, and Michael R. Buchmeiser*

High-temperature sodium-sulfur battery (HT Na–S) technology has attracted substantial interest in the stationary energy storage sector due to its low cost and high energy density. However, the currently used solid electrolyte (β -alumina) is expensive and can only be operated at high temperatures, which compromises safety. On the other hand, liquid electrolytes in room temperature sodium-sulfur batteries (RT Na–S) are susceptible to dendrite formation and polysulfide shuttle. Consequently, an electrolyte with both solid (shuttle blocking) and liquid (ionic conductivity) properties to overcome the above-mentioned issues is highly desired. Herein, a high-performance quasi-solid state crosslinked gel polymer electrolyte (GPE) prepared in situ using pentaerythritol triacrylate (PETA) exhibiting high ionic conductivity of 2.33 mS cm^{-1} at $25 \text{ }^\circ\text{C}$ is presented. The GPE-based electrolyte shows high stability resulting in a high discharge capacity of $>600 \text{ mAh g}_s^{-1}$ after 2500 cycles with an average Coulombic efficiency of 99.91%. Density functional theory calculations reveal a weak interaction between the Na^+ ions and the oxygen molecules of the PETA moiety, which leads to a facile cation movement. The crosslinked polymer network is tightly connected to the cathode and can confine sulfides, thereby facilitating the conversion process.

1. Introduction

The electrochemical energy storage sector has seen significant development.^[1,2] Lithium-ion batteries (LIBs) are becoming indispensable in a wide range of energy storage applications such as portable electronic devices, electric vehicles, and stationary grid applications, to name just a few.^[3–5] Peak power performance, gravimetric energy density, cycle life, and safety are the most important parameters for cells used in large-scale energy storage devices. LIBs for grid storage applications are increasingly used in recent years due to their high energy density (NMC–200 Wh kg^{-1}), long cycle life (3000 cycles at a depth-of-discharge [DOD] of 80%), and high energy efficiency (95%).^[6,7] However, price fluctuations of the raw materials, capital costs, and rapid material degradation demand alternative technologies. High-temperature sodium-sulfur (HT Na–S) batteries with high gravimetric energy density (760 Wh kg^{-1}) have

been in use for grid energy storage applications due to their ultra-long cycle life (up to 5000 cycles or 15 years). Sodium appears to be a better option for energy storage for large-scale applications since it is naturally abundant, and cheaper than lithium. The use of sulfur as a cathode material in batteries has its advantages such as low costs, natural abundance, environmental benignity, and a high theoretical energy density of 1672 mAh g^{-1} . Additionally, HT Na–S batteries use β -alumina operated at $300\text{--}350 \text{ }^\circ\text{C}$ as a solid electrolyte.^[8] At this temperature, however, both sodium and sulfur exist in the molten state, which entails serious safety issues including explosion.^[9]

Consequently, many attempts have been made to reduce the operating temperature and develop room-temperature sodium-sulfur (RT Na–S) batteries.^[10] As a result of the formation of Na_2S during discharge as a final product instead of intermediate polysulfides in HT Na–S, the gravimetric energy density reaches up to 1274 Wh kg^{-1} in RT Na–S batteries.^[11–13] However, RT Na–S batteries experience issues similar to those observed in their lithium counterparts such as dissolution of polysulfides in ether-based electrolyte solvents, shuttling of polysulfides, electrolyte incompatibility with the anode, self-discharge, and huge volume changes (ca. 260% vs 80% for Li) on the cathode.^[14] Moreover, polysulfide anions react with carbonate solvents due

S. Murugan, M. R. Buchmeiser
Institute of Polymer Chemistry
University of Stuttgart
Pfaffenwaldring 55, 70569 Stuttgart, Germany
E-mail: michael.buchmeiser@ipoc.uni-stuttgart.de

S. V. Klostermann, J. Kästner
Institute for Theoretical Chemistry
University of Stuttgart
Pfaffenwaldring 55, 70569 Stuttgart, Germany
P. Schützendübe, G. Richter
Materials Central Scientific Facility
Max Plank Institute for Intelligent Systems
Heisenbergstr. 3, 70569 Stuttgart, Germany

M. R. Buchmeiser
German Institutes of Textile and Fiber Research (DITF)
Körschtalstr. 26, 73770 Denkendorf, Germany

 The ORCID identification number(s) for the author(s) of this article can be found under <https://doi.org/10.1002/adfm.202201191>.

© 2022 The Authors. Advanced Functional Materials published by Wiley-VCH GmbH. This is an open access article under the terms of the Creative Commons Attribution License, which permits use, distribution and reproduction in any medium, provided the original work is properly cited.

DOI: 10.1002/adfm.202201191

to their nucleophilic nature, which significantly affects cell capacity. To overcome the reaction between the active species and carbonate solvents, substantial research efforts have been dedicated to cathode modifications, separator architecture, binder modifications, and artificial (SEI) layer formation. Sulfurized poly(acrylonitrile) (SPAN) cathodes can completely avoid soluble intermediates (MS_x , $2 \leq x \leq 4$, M = Li or Na) in carbonate solvents by using short sulfur chains covalently bound to the polymeric matrix.^[15–17] SPAN-based cathodes were first proposed for lithium-sulfur (Li–S) batteries due to their low cost, ease of synthesis, high specific capacity, high energy density, and suppression of the polysulfide shuttle.^[18,19]

Another approach to eliminating the dissolution of polysulfides in metal-sulfur batteries entails the use of gel polymer electrolytes (GPEs). The high viscosity of GPEs compared to liquid electrolytes (LEs) suppress the dissolution of polysulfides. Since a GPE comprises, an LE trapped inside the polymer matrix, it can avoid electrolyte leakage, dendrite formation, and internal short-circuiting.^[20,21] Moreover, GPEs also provide a synergistic effect on both liquid and solid electrolytes such as high ionic conductivity ($>10^{-3}$ S cm^{-1}) and high safety.^[22] Commonly, ex situ polymerized GPEs are prepared by solvent casting (heterogeneous) and phase inversion (homogeneous) techniques. During solvent casting, both the electrolyte salt and the polymer are dissolved in a suitable solvent and cast on a Teflon medium to evaporate the solvent subsequently obtaining a thin polymer electrolyte. However, casting and evaporation of the solvent should be controlled under inert conditions to avoid hydrolysis of the salt.^[23] In phase inversion, a porous polymer is immersed in a liquid electrolyte to form a gel. Both techniques require complex synthetic steps, which impede the adoption of GPEs in commercial energy storage applications.^[24,25]

Herein, we report the easy one-step synthesis of GPEs for RT Na-SPAN batteries by in situ polymerization.^[26] A liquid electrolyte solution containing 1 M of sodium tetraphenylborate (NaTPB), propylene carbonate (PC), and 7 wt.% fluoroethylene carbonate (FEC) was crosslinked via in situ free radical polymerization of pentaerythritol triacrylate (PETA) initiated by azobisisobutyronitrile (AIBN, 1 wt.%). So far, only a few reports exist on the in situ preparation of GPEs for Na–S batteries. Since the polymerization takes place on the surface of the Na anode as well as on the surface of the porous SPAN cathode, good interfacial contact is ensured. We found that as-synthesized GPEs have higher ionic conductivity than LEs at higher temperatures. The polymer matrix in the electrolyte locally constrains the discharge products, thereby avoiding the blockage of cathode pores by insulating crystallites and also enhancing the conversion process. As-prepared GPEs in Na-SPAN full cell exhibit extremely stable cycling over 2500 cycles with a discharge capacity >600 mAh g_s^{-1} at 2 C and an average CE of 99.91%.

2. Results and Discussion

2.1. Synthesis and Characterization of the GPE

The GPE was synthesized by free radical polymerization of a precursor solution containing PETA and the LE using AIBN as

a thermal initiator at 70 °C (Figure 1a). This way, a crosslinked, viscous, translucent polymeric network with encapsulated LE was obtained (Figure 1b).^[27] To verify the confinement capability of the GPE for the LE, a swelling method was used to calculate the crosslinking density of the PETA-derived polymer (Equations S1–S3, Supporting Information).^[28] According to these measurements, poly-PETA shows high crosslinking density with low molecular weight polymer chains between the individual crosslinks (Table S1, Supporting Information). Importantly, poly-PETA can form a high gel content even at low concentrations in the LE. When combining an LE and PETA, the highly cross-linked poly-PETA network can effectively confine the LE and prevent leaking (Figure S1, Supporting Information).

The GPE was polymerized under inert conditions on a glass plate and subjected to a vacuum to completely evaporate the solvent. This dried GPE was then characterized by scanning electron microscopy (SEM) to visualize the surface texture. SEM pictures at different magnifications (Figure S2, Supporting Information) revealed a smooth surface where the polymer network acts as an ion-conductive matrix while the LE inside allows for ion motion (Figure 1c). For the in situ polymerization inside Swagelok cells, polymerization was carried out for 6 h at 70 °C to ensure maximum monomer conversion. To confirm polymerization, both PETA and the final GPE were subjected to Fourier-transform infrared spectroscopy (FTIR, Figure 1d). Signals at 1470 and 1407 cm^{-1} (CH_2 , bending), 1263 cm^{-1} (C–O, antisymmetric stretching), and 1174 cm^{-1} (C–O, symmetrical stretching) appeared for all three samples.^[29,30] The signal at 1722 cm^{-1} (C=O, stretching) of PETA shifts to higher energy (1739 cm^{-1}) and is weaker than in the monomer. Additionally, the bands at 1633 and 1618 cm^{-1} represent stretching vibrations of the C=C double bond,^[31,32] which almost disappeared in the final GPE. Quantification of the FTIR signals revealed a high degree of double bond conversion ($>99.7 \pm 5\%$,^[33] Figure S3 and Equation S4, Supporting Information). The thermal stability of the GPE and LE were compared using thermogravimetric analysis (TGA, Figure 1e). At the beginning of heating, both the GPE and the LE behave similarly, yet at 220 °C a weight loss of up to 85 wt.% was observed for the LE compared to 64 wt.% for the GPE. This weight loss begins at 212 °C by evaporation of volatile compounds at a faster rate for the LE compared to the GPE. Above this temperature, the GPE shows a reduced weight loss of at least up to 400 °C. Complementary, the weight loss at constant temperature (23 °C) and atmospheric pressure was measured as a function of time for both the GPE and the LE. Figure S4, Supporting Information shows that the GPE and LE exhibit weight losses of up to ≈ 6 and ≈ 14 wt.% after 24 h, respectively, which indicates that the solvents (PC and FEC) in the LE are more volatile compared to those encapsulated in the polymeric matrix.

2.2. Electrochemical Characterization

The anodic stability of the GPE was evaluated by linear sweep voltammetry (LSV) against various metal electrodes. As shown in Figure 2a, the GPE possesses high oxidative stability against an aluminum (Al, >6 V), carbon paper (3.3 V), graphite

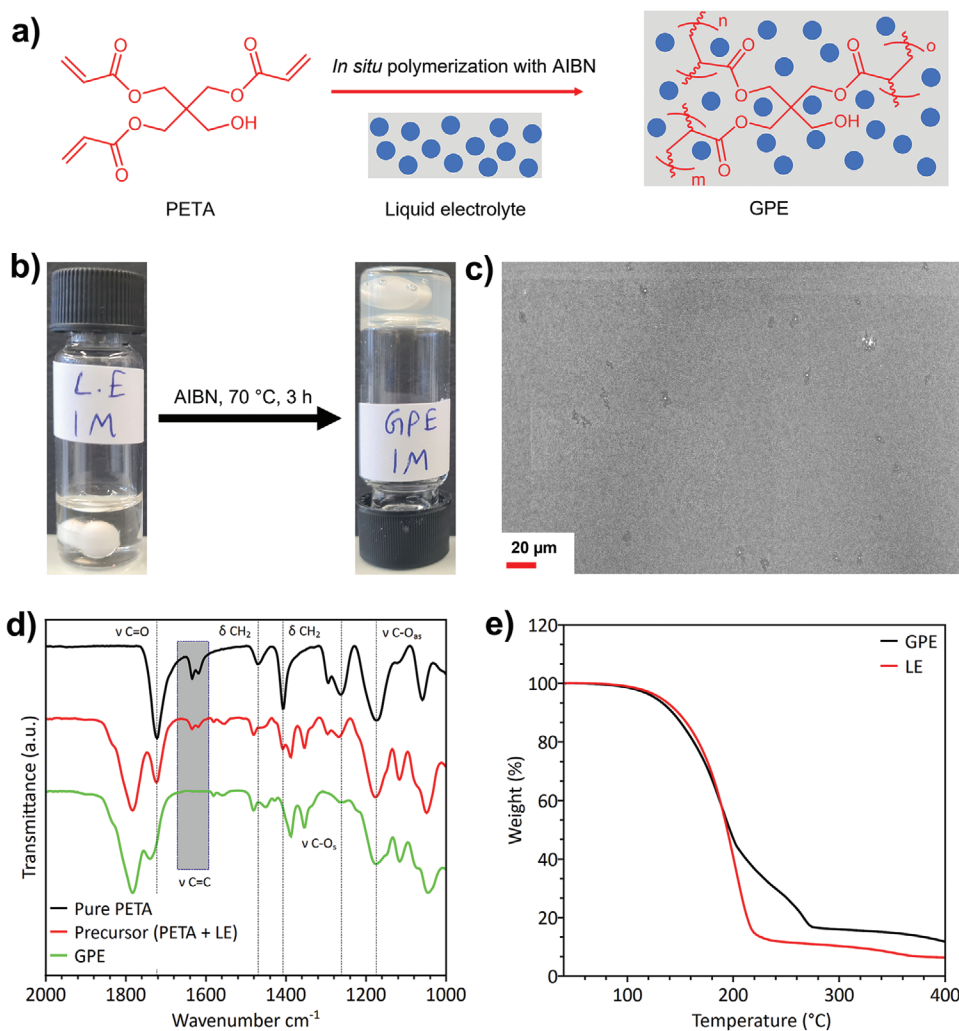


Figure 1. a) Synthesis of the GPE; b) visual image of the precursor solution (left) and the GPE (right); c) secondary electron SEM image of a dried GPE polymerized on a glass plate; d) FTIR spectra of PETA (black), the precursor solution (red) and the final GPE (green); e) TGA of the LE and the final GPE.

(3.45 V), platinum (Pt, 3.55 V), and stainless steel (SS, 4.2 V) current collector. Notably, the anodic stability of the GPE electrolyte against Al reported here is the highest for Na batteries published so far.^[34–36] Since the ion movement in the electrolyte is crucial for the kinetics during the redox reaction,^[37] the ionic conductivity of both the LE and the GPE was measured with the help of blocking SS electrodes at various temperatures (Figure 2b). The bulk resistance of both the GPE and LE was extracted from the impedance spectroscopy data in the high-frequency region (Table S2, Supporting Information). Usually, the ionic conductivity of a GPE is lower than the one of the LE due to the increased viscosity, which impedes ion movement. However, a PETA-based GPE showed an ionic conductivity (σ) of $2.33 \times 10^{-3} \text{ S cm}^{-1}$ at 25 °C, virtually identical (within experimental error) to the one of the LE ($2.32 \times 10^{-3} \text{ S cm}^{-1}$). This can well be expected in view of the low polymer content (1.5 wt.%). At elevated temperature (40 °C), the ionic conductivity of the GPE was $3.77 \times 10^{-3} \text{ S cm}^{-1}$, thereby significantly exceeding the one of the LE ($3.39 \times 10^{-3} \text{ S cm}^{-1}$). These findings suggest that the polymer segmental motion at high-temperature influences

ionic conductivity. A plot of $\log \sigma$ versus T^{-1} was non-linear, indicating a strong coupling between polymer segmental relaxation and ionic motion.^[38] This behavior can be well described by the Vogel–Tamman–Fulcher (VTF) type equation (Equation S5, Supporting Information).^[39,40] By employing the VTF equation for non-linear curve fitting, the pseudo-activation energy (E_a) can be obtained. The E_a value obtained for the GPE (73.5 meV) is virtually identical to the one for the LE (73.9 meV), implying that ion transport across the polymer chains is as fast as in an LE.

The low activation energy of the GPE suggests that the polymeric matrix promotes ion motion in the electrolyte. Generally, cations are stabilized by the coordination of solvent molecules, which then transport the cations across the electrodes. The coordination number of the cation affects its mobility.^[41,42] To elucidate the coordination of the cation by the solvent and PETA, respectively, molecular electrostatic potential (MEP) and binding energy calculations were carried out. MEP calculations revealed the favorable binding sites for Na⁺ by mapping the charge distribution^[43] in PC and PETA, respectively. Figure 2c,d

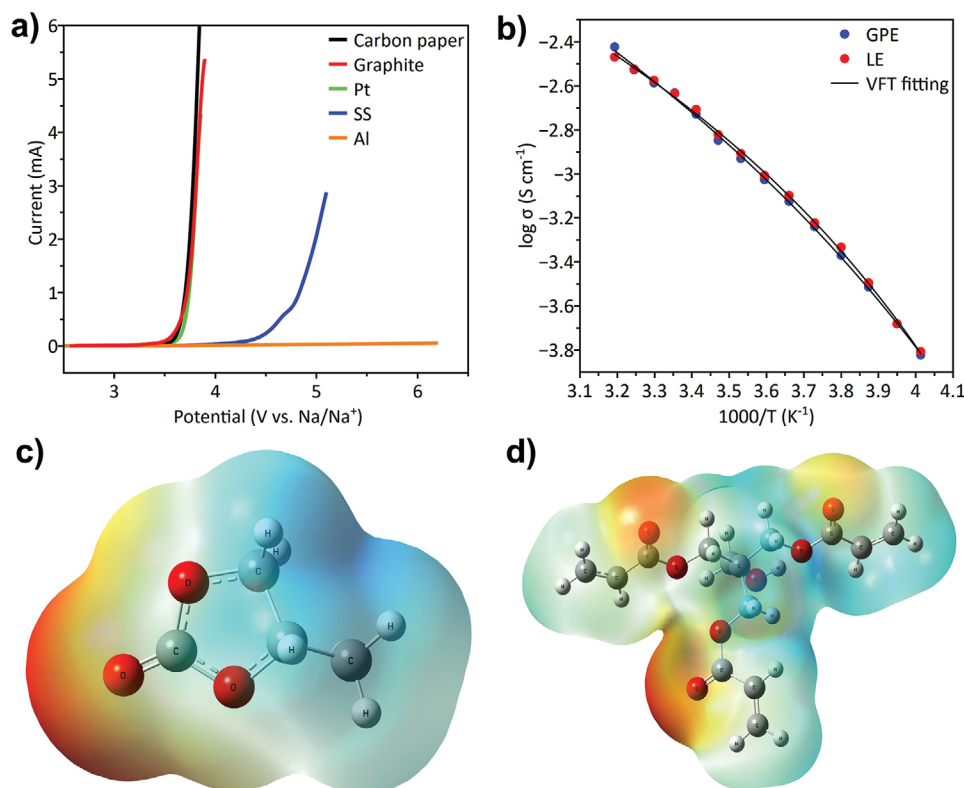


Figure 2. Characterization of the GPE. a) Oxidative stability of the GPE determined by linear sweep voltammetry (LSV) at a scan rate of 1 mV s⁻¹ against carbon paper, graphite, Pt, SS, and Al; b) ionic conductivities of the GPE (black dots) and the LE (red dots) measured with a blocking SS electrode at various temperatures. Molecular electrostatic potential (MEP) mapping of possible binding sites (colored in red) of Na⁺ with, c) PC; and d) PETA.

shows the electrostatic potential response of the PC solvent molecule (in the LE) and of the ester groups of PETA (also present in the GPE) towards Na⁺. The Van der Waals surface is colored red for a negative electrostatic potential, which attracts Na⁺, and blue for positive electrostatic potential. Clearly, the MEP on the Van der Waals surface of the carbonyl oxygen atom in PC interacts with Na⁺ stronger than the ester groups in PETA. Moreover, PC shows strong single-site coordination, whereas multiple coordination occurs in PETA, indicating an overall weaker interaction of Na⁺ with PETA. Notably, Na⁺ does not prefer coordination with the carboxylate and hydroxyl groups. Thus, when placed close to the C–O–C or -OH groups in density functional theory (DFT) simulation, Na⁺ spontaneously moves to the nearest -C=O group as the preferred coordination site. The different coordination possibilities and their respective binding energies are summarized in Figure S5a–d and Table S3, Supporting Information. DFT calculations based on the same coordination numbers always reveal stronger binding energy between Na⁺ and PC of -427.4 kJ mol⁻¹ compared to the binding of Na⁺ to PETA (-316.9 kJ mol⁻¹). It is, therefore, reasonable to assume that, despite the higher viscosity of GPEs compared to LEs (Figure S6, Supporting Information), the weaker coordination of Na⁺ to the PETA-derived polymer is responsible for the high Na⁺ mobility in the GPE. Ultimately, DFT calculations also suggest that weak coordination of Na⁺ to the ester groups in PETA promotes ion hopping.

Generally, both the cation and anion contribute to the current transport across electrodes. An ionic current preferentially

carried by the cation significantly reduces the concentration polarization caused by the accumulation of anions near the electrode, which in turn affects the rate at which the battery operates.^[44,45] A combination of chronoamperometric and alternating current (AC) impedance spectroscopy was used to obtain the Na⁺ transference number (T_{Na^+}) of the GPE and the LE (Equation S6 and Figure S7, Supporting Information). The T_{Na^+} of the GPE was 0.44 and thus higher than the T_{Na^+} of the LE (0.33). This high T_{Na^+} value of the GPE indicates that the movement of the anion is restricted by the polymer network due to the interaction between the bulky anion with delocalized charges and the polymer chains. This reduces the cell's polarization and leads to dendrite-free, stable Na deposition.^[46–48]

To identify the redox potentials of Na-SPAN cells, cyclic voltammetry (CV, Figure S8a,b, Supporting Information) was performed at a scan rate of 0.1 mV s⁻¹.^[49] Both the GPE and the LE show similar redox potentials and current densities, indicating that the performance of the GPE-containing cell is not hampered by the high viscosity of the polymeric matrix. Reduction of sulfur to Na₂S_x (x = 3–4) occurs at 1.77 V and an additional broad reduction peak around 1.20 V indicates the conversion of Na₂S_x to Na₂S. Likewise, during oxidation Na₂S is converted into Na₂S_x at 2.0 V and then reattach to the SPAN composite in the fully charged state above 2.3 V.^[50] To determine reaction kinetics at the sulfur cathode, CV measurements were carried out by increasing the scan rate stepwise from 0.2 to 1.2 mV s⁻¹. The resulting graph (Figure 3a,b) shows an increase in peak current density and potential shift (polarization) with an increasing

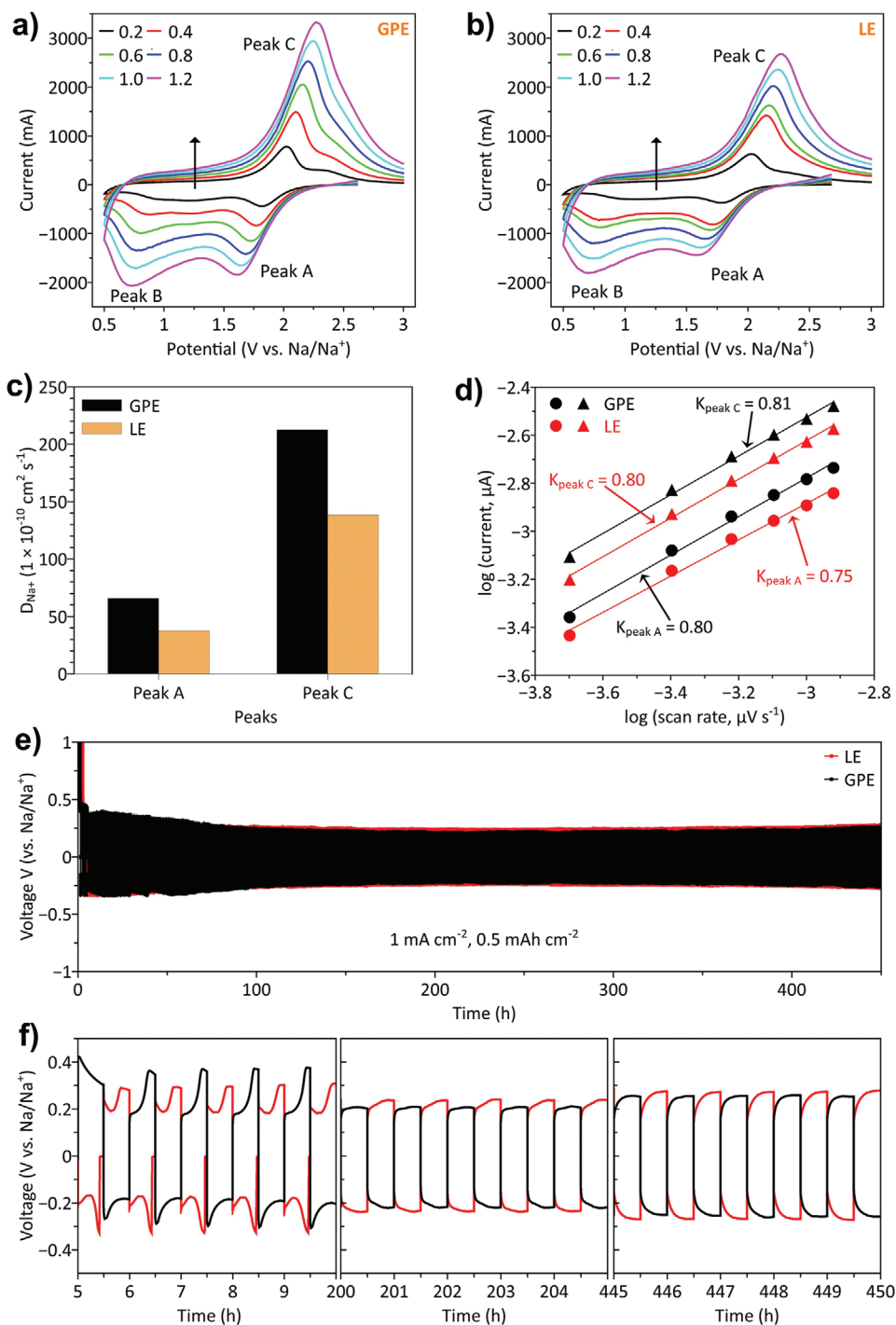


Figure 3. Cyclic voltammogram of a Na-SPAN cell at different scan rates. a) GPE and b) LE; c) calculated values of the Na⁺ ion diffusion coefficient (D_{Na^+}) for the main anodic and cathodic peaks (peak A and peak C) for a GPE and an LE; d) calculated slope (K) values for the peaks A and C based on the double logarithmic plot of peak current versus scan rate; e) overpotential voltage profile at 1 mA cm⁻² (0.5 mAh cm⁻²); f) expanded view of overpotential at various intervals.

scan rate. The GPE displayed enhanced peak current density and sharper peak shapes compared to the LE at similar scan rates, indicating fast electrode kinetics at the cathode. A diminished reduction peak current (peaks A and B) was observed for the LE in contrast to the sharp peak in the GPE, specifying sluggish reaction kinetics during the reduction in the LE.^[51,52] The

Na⁺ diffusion coefficient (D_{Na^+}) was determined by using the Randles–Sevcik equation based on the relation between peak current (i) versus square root of the scan rate (\sqrt{v}) (Figure S8c,d, Supporting Information).^[53,54] Since peak B is broad for the LE, only peaks A and C were taken into consideration to maintain the accuracy of the D_{Na^+} value. The apparent diffusion

coefficients (Figure 3c) in peaks A and C for the GPE (65×10^{-10} and $212 \times 10^{-10} \text{ cm}^2 \text{ s}^{-1}$) were slightly higher than those for the LE (37×10^{-10} and $138 \times 10^{-10} \text{ cm}^2 \text{ s}^{-1}$), suggesting facile ion movement in the GPE network. A double logarithmic plot (Figure 3d) shows a higher k value (slope) for both the cathodic peak (A) and the anodic peak (C) for the GPE, corroborating the results from CV and suggesting faster reaction kinetics at the electrodes in GPE-based cells. This enhanced reaction kinetics for the GPE can be explained as follows. In the case of the LE, the final discharge products, $\text{Na}_2\text{S}_2/\text{Na}_2\text{S}$, can deposit throughout the cathode, thereby blocking the pores, which leads to an increase in overpotential during long-term cycling (Figure S9a,b, Supporting Information). In contrast, in the GPE, the cathode pores are (partially) blocked or even filled with polymer but the polymer itself can confine $\text{Na}_2\text{S}_2/\text{Na}_2\text{S}$ locally, resulting in an efficient conversion of the active material. To support this theory, SEM pictures together with energy-dispersive X-ray (EDX) spectra of a pristine cathode, a discharged SPAN cathode with an LE, and a discharged SPAN cathode with a GPE after 600 cycles were recorded (Figure S10a–c, Supporting Information). EDX images show several agglomerated sulfur spots with the LE (Figure S10b, Supporting Information) whereas the GPE (Figure S10c, Supporting Information) shows no clustered sulfur spots, indicating that sulfur reduction results in a homogeneous distribution of $\text{Na}_2\text{S}_2/\text{Na}_2\text{S}$ throughout the polymer.

The overpotential for deposition and dissolution of Na^+ during cycling was analyzed using a symmetric $\text{Na}||\text{Na}$ cell (Figure 3e,f). The GPE showed an increased overpotential during the first 60 cycles, attributable to the formation of a pseudo-SEI layer on the Na surface.^[55] After ca. 100 cycles, the GPE showed a reduced and stable overpotential up to the 450th cycle, resulting from the breakage of the pseudo-SEI layer during cycling and the successful formation of a stable SEI layer. The pseudo-SEI formation on the Na anode in the GPE is likely to occur via the polymerization of PETA by Na during cell fabrication. The polymerization initiates from the sodium surface and propagates through the precursor solution (Figure S11a, Supporting Information). Changes in the surface morphology of the sodium anode during cell fabrication can be visualized by dropping a small piece of Na anode into the LE and precursor solution for 2 h, followed by examining the Na surface SEM. Figure S11b–d, Supporting Information shows an SEM image of elemental Na, Na in an LE, and Na in the precursor solution. The SEM images show that the precursor solution forms a smooth layer (SEI) on sodium (Figure S11d, Supporting Information) whereas, uneven film formation was observed in the LE (Figure S11c, Supporting Information). This smooth layer on the Na surface generated from the precursor solution leads to the initial overpotential during deposition/dissolution. The formation of a thin polymer layer also increases the cell's impedance as shown in Figure S12a, Supporting Information. We surmise that the polymer layer ruptures and is replaced by a stable SEI layer during subsequent cycles (Figure S12a,b, Supporting Information). Thus, the concomitant formation of a stable SEI layer leads to the reduction in resistance of the cell after the 50th cycle. To further validate the formation of a polymer layer in GPE-containing cells, impedance measurements of a symmetrical $\text{Na}||\text{Na}$ cell with an LE were carried out (Figure S12c,d, Supporting Information). And

indeed, the GPE-based cell shows interfacial resistance, attributable to the polymer layer, while the LE exhibits only bulk and charge transfer resistance. The SEM image of the Na anode surface before and after cycling of a symmetrical cell is shown in Figure S13a–d, Supporting Information. Even after 450 h, only agglomeration of Na but no dendrite structures were observed.

2.3. Cycling Performance of Na-SPAN Full Cells

To demonstrate the advantages of GPEs, we further investigated their application in RT Na-SPAN batteries. Full cells containing metallic Na as an anode, SPAN as cathode, and an in situ polymerized GPE were cycled at 0.2 C to identify the reduction steps involved (Figure 4a,b). Two voltage plateaus during discharge at 1.7 and 1.0 V and one major plateau during the charge at 2.0 V were observed, corroborating the CV results obtained (Figure S7a, Supporting Information). Figure 4c compares the rate capabilities of a GPE and an LE in Na/electrolyte/SPAN cells at C-rates between 1 and 4 C. The GPE-based cell exhibited a stable capacity of 962, 850, 725, and 590 mAh g_s^{-1} at 1, 2, 3, and 4 C, respectively, whereas LE-based cells delivered a capacity of only 922, 805, 692, and 564 mAh g_s^{-1} at these C-rates. This enhanced performance of GPE-based cells points towards improved electrode kinetics resulting from the rapid movement of Na^+ ions between the electrodes. Both GPE- and LE-based cells maintain a good reversible capability when the C-rate returns to 1 C. A comparison of the long-term galvanostatic cycling performance of GPE- and LE-based cells is shown in Figure 4d. Cells were cycled at 2 C (3.35 mA g_s^{-1}) in a potential window between 0.5–3 V at room temperature (23 °C). An initial discharge capacity of 1577 mAh g_s^{-1} for GPE-based cells at 0.3 C versus 1556 mAh g_s^{-1} for LE-based cells was observed. Both values point towards irreversible side reactions, which lead to CE $>100\%$ (Figure 4e).^[56] This initial increase in CE is accompanied by an irreversible discharge capacity that likely arises from the reduction of SPAN, SEI formation, and irreversible sodium ion insertion.^[57] For the first 200 cycles, GPE-based cells showed a steady increase in discharge capacity, which we hypothesize to be related to the formation of ion channels (slow activation process) in the GPE. The Na^+ movement between the electrodes is greatly affected by the viscosity of the electrolyte. Since GPEs have higher viscosities than LEs (Figure S6, Supporting Information), we surmise that this increase in discharge capacity during the activation process is due to the slow movement of Na^+ between the GPE and the cathode and vice versa.^[58] Figure S14a,b and Table S4, Supporting Information shows that an increase in the PETA content (1.5, 5, and 10 wt.%) in the electrolyte adversely affects the activation process and subsequent cycling. Increasing the salt concentration to 2 M in the GPE resulted in a gradual increase in discharge capacity up to 250 cycles, indicating an extended activation period (Figure S14c, Supporting Information). Similarly, a Na–S cell containing 1.5 wt.% PETA showed a decrease in overpotential from the 45th to the 200th cycle (Figure S15a,b, Supporting Information). GPE-based Na-SPAN cells showed excellent cycling performance with a high discharge capacity of 1013 mAh g_s^{-1} at the 250th cycle maintaining $> 600 \text{ mAh g}_s^{-1}$ for up to 2500 cycles (Figure 4d). From the initial discharge (2 C, 787 mAh g_s^{-1}), the cell exhibited

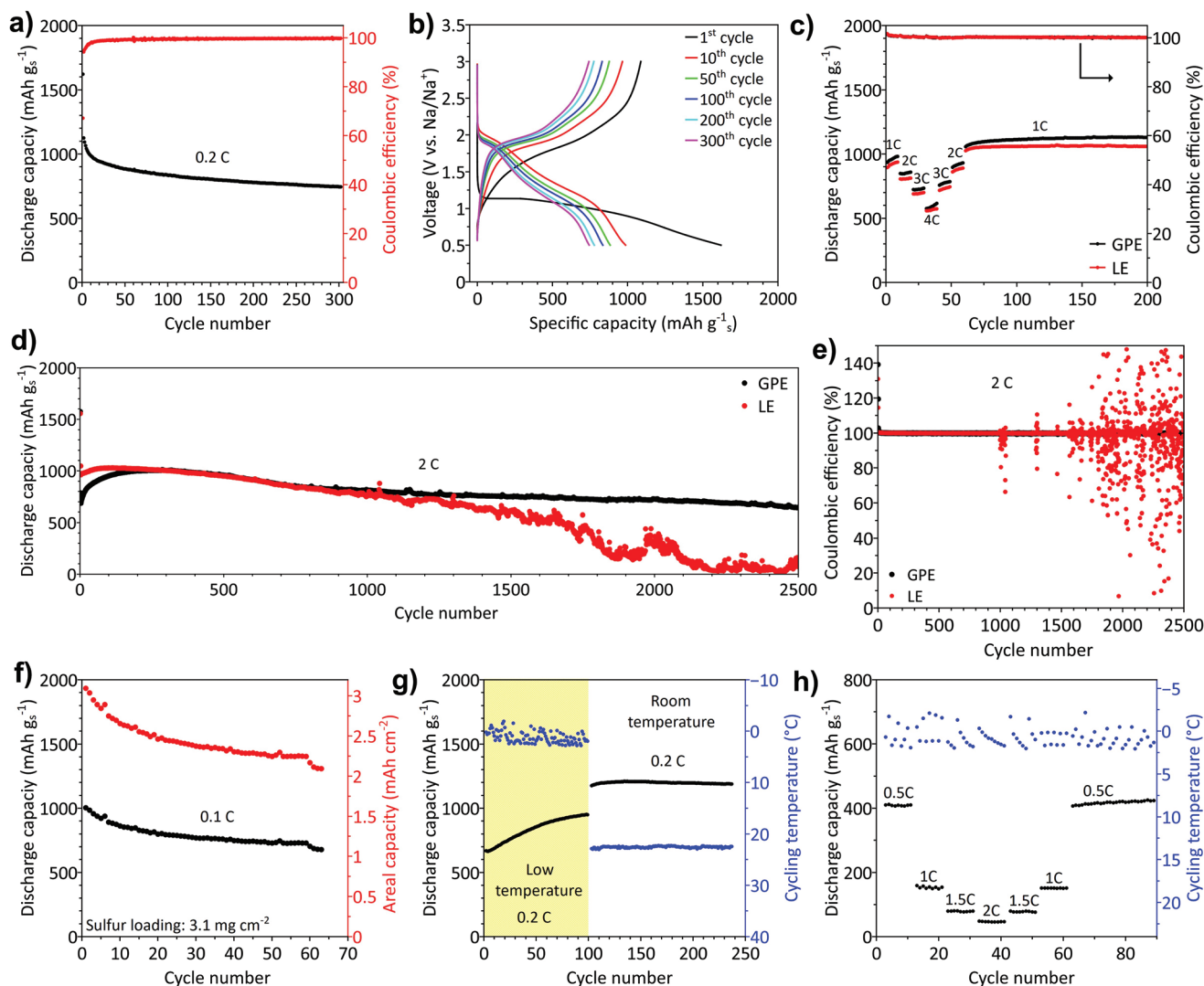


Figure 4. Electrochemical performance of a Na-SPAN full cell. a) Galvanostatic cycling of a GPE-based cell at 0.2 C and b) its corresponding voltage profiles at various cycles; c) rate performance of a GPE-based cell from 1 to 4 C; d) comparison of extended galvanostatic cycling of a GPE- and LE-based cell at 2 C and its e) Coulombic efficiency; f) galvanostatic cycling of a GPE-based Na-SPAN full cell with increased sulfur loading of 3.1 mg cm^{-2} at 0.1 C; g) low ($0 \text{ }^\circ\text{C}$) and room temperature ($23 \text{ }^\circ\text{C}$) galvanostatic cycling of a GPE-based full cell; h) rate capability assessment of a GPE-based full cell at $0 \text{ }^\circ\text{C}$.

a capacity decay of only 0.0091% per cycle resulting in a discharge capacity of 644 mAh g^{-1} at the 2500th cycle. The cell also showed a stable CE over 2500 cycles with an average CE_{avg} of 99.91%. In contrast, LE-based cells showed a gradual decrease in discharge capacity accompanied by unstable cycling after 1000 cycles (Figure 4e). X-ray photoelectron spectroscopy (XPS) was employed to monitor the product formation at the end of the charge/discharge cycles. Cells were stopped at 0.5 V (after discharge) and 3 V (after charge) and transferred to the XPS chamber. Figure S16 (Supporting Information) shows the sulfur species formed during charging and discharging. The pristine SPAN shows two signals for the S–S/C–S_x and C–S bonds at 164.0 and 162.3 eV, respectively. Sulfate species are observed at 167–172 eV. During discharge, the formation of Na₂S at 159.6 eV was observed.^[30,50] The signal observed at 161.5 eV overlaps with the signal for the C–S bonds (162.3 eV) and is assigned to Na₂S₂ and unreacted C–S bonds in the SPAN cathode. After charging,

the C–S, Na₂S, and Na₂S₂ signals disappear but the signal for the C–S_x/S–S bond at 164.0 eV reappears, indicating successful reoxidation during charging.^[17]

High sulfur loading in the cell is one of the most vital parameters that govern the feasibility of SPAN batteries in practical applications. Figure S17a,b, Supporting Information shows the cycling and rate performance of GPE-based cells with a sulfur loading of 0.88 mg per cathode. The cell showed an increased capacity of 968 mAh g^{-1} at the 2nd cycle at 0.5 C and a discharge capacity of 913, 439, 157, and 87 mAh g^{-1} at 0.5, 1, 1.5, and 2 C, respectively. Increasing the sulfur loading to 3.5 mg per cathode by increasing the sulfur content in the cathode to 90 wt.% delivered a discharge capacity of 986 mAh g^{-1} in the 2nd cycle at 0.1 C (Figure 4f). As cycling proceeded, a reversible discharge capacity of 680 mAh g^{-1} was retained at the end of the 63rd cycle with a capacity retention of 68.9%. Throughout cycling, the areal capacity of the cathode stayed above 2 mAh cm^{-2} .

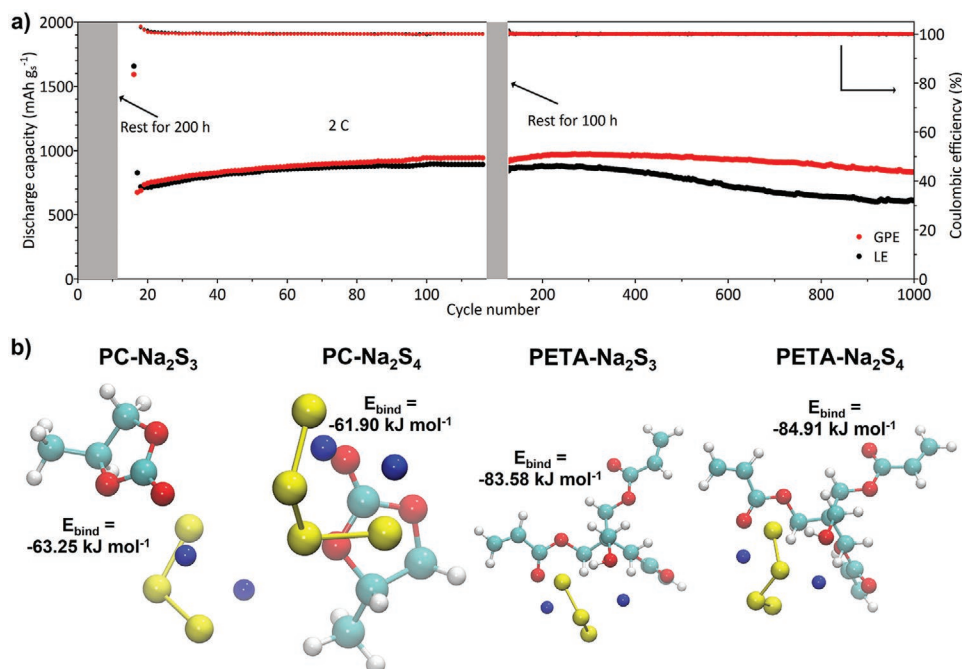


Figure 5. Comparison of the self-discharge of a GPE and an LE. a) Initial rest for 200 h, cycling at 2 C for 100 cycles, then rested for a further 100 h followed by cycling at 2 C until 1000 cycles; b) Computed binding energies of $\text{Na}_2\text{S}_3/\text{Na}_2\text{S}_4$ with PETA and PC. (White – hydrogen, Red – oxygen, Yellow – sulfur, Dark blue – sodium, Light sky blue – carbon).

The impact of temperature on the electrochemical performance of GPE-based cells was examined by cycling a full cell close to 0 °C at 0.2 C and then reversing the temperature to room temperature (23 °C). Figure 4g shows the increase in discharge capacity from 669 to 951 mAh g_s^{-1} up to 100 cycles, indicating a strong activation process due to the restricted movement of Na^+ ions at low temperatures. Upon reversing to room temperature, the cell showed a stable capacity of 1190 mAh g_s^{-1} . To further demonstrate their capability to work at near 0 °C temperature, the rate performance of a GPE-based Na-SPAN cell was investigated at discharge rates of 0.5, 1, 1.5, and 2 C at which the cells delivered a discharge capacity of 408, 154, 77, and 46 mAh g_s^{-1} at 0 °C (Figure 4h). When the C-rate was reversed to 0.5 C, the cell retained its initial capacity of 408 mAh g_s^{-1} .

Next, the self-discharge propensity of GPE- and LE-based full cells was addressed (Figure 5a). Na-SPAN cells were stored for 200 h and then cycled at 2 C for 100 cycles. Subsequently, the cells were stopped in the charged state (3 V) with a resting period of 100 h, followed by a cycling process over 1000 cycles. GPE- and LE-based cells showed a similar trend in discharge capacity over the first 100 cycles. However, from the 101st cycle on, LE-based cells displayed an accelerated degradation in discharge capacity due to loss of active material. Accordingly, the capacity retention between the 101st and the 1000th cycle of GPE-based cells was 90%, whereas LE-based cells exhibited only 73%. Clearly, the polymeric matrix of GPEs restricts the diffusion of intermediates or Na_2S towards the anode, thereby providing robust protection against the self-discharge of the cell.

Poly-PETA not only inhibits the diffusion of intermediate polysulfides via a physical barrier but also by preferred interaction. $\text{Na}_2\text{S}_3/\text{Na}_2\text{S}_4$ are the intermediates formed in

the SPAN cathode.^[50] To validate the favorable interaction between $\text{Na}_2\text{S}_3/\text{Na}_2\text{S}_4$ and PETA, DFT calculations were carried out (Figure 5b). Na_2S_4 and Na_2S_3 show stronger interaction towards PETA with binding energies of -84.91 and -83.58 kJ mol^{-1} than with PC and FEC. When comparing PC and FEC alone, the interaction with the intermediate polysulfides is stronger for FEC. Thus, the binding energy values of PC- Na_2S_3 (-63.25 kJ mol^{-1}) and PC- Na_2S_4 (-61.90 kJ mol^{-1}) are lower than that of FEC- Na_2S_3 (-68.94 kJ mol^{-1}) and FEC- Na_2S_4 (-67.76 kJ mol^{-1}). The GPE contains PC, FEC, and PETA in decreasing order (wt.%); the strong binding energy of $\text{Na}_2\text{S}_3/\text{Na}_2\text{S}_4$ with PETA indicates that the polysulfides are immobilized by the crosslinked polymer network, thereby suppressing diffusion in the electrolyte. A static adsorption test was carried out to support the DFT calculations on the preferable interactions between PETA and Na_2S_4 . 0.005 M of Na_2S_4 solution was prepared in DME by adding the required amount of Na_2S and S_8 . Poly-PETA was added and the mixture was allowed to stand for more than 6 h. After this time, the color of the solution changed from green to light yellow (Figure S18a, Supporting Information). The solution was filtered and UV-vis absorption spectra were measured at various time intervals. The resulting solution showed two broad peaks around ≈ 265 – 295 nm, indicating a mixture of s_2^{2-}/s_6^{2-} while the peak at 418 nm corresponds to a mixture of s_4^{2-}/s_6^{2-} .^[59,60] The graph depicting absorption intensity versus time (Figure S18b, Supporting Information) shows that absorption intensity first decreases gradually but stabilizes after 6 h compared to the parent Na_2S_4 solution. This indicates that the polysulfide species are adsorbed by poly-PETA via preferred interaction, corroborating the DFT calculations.

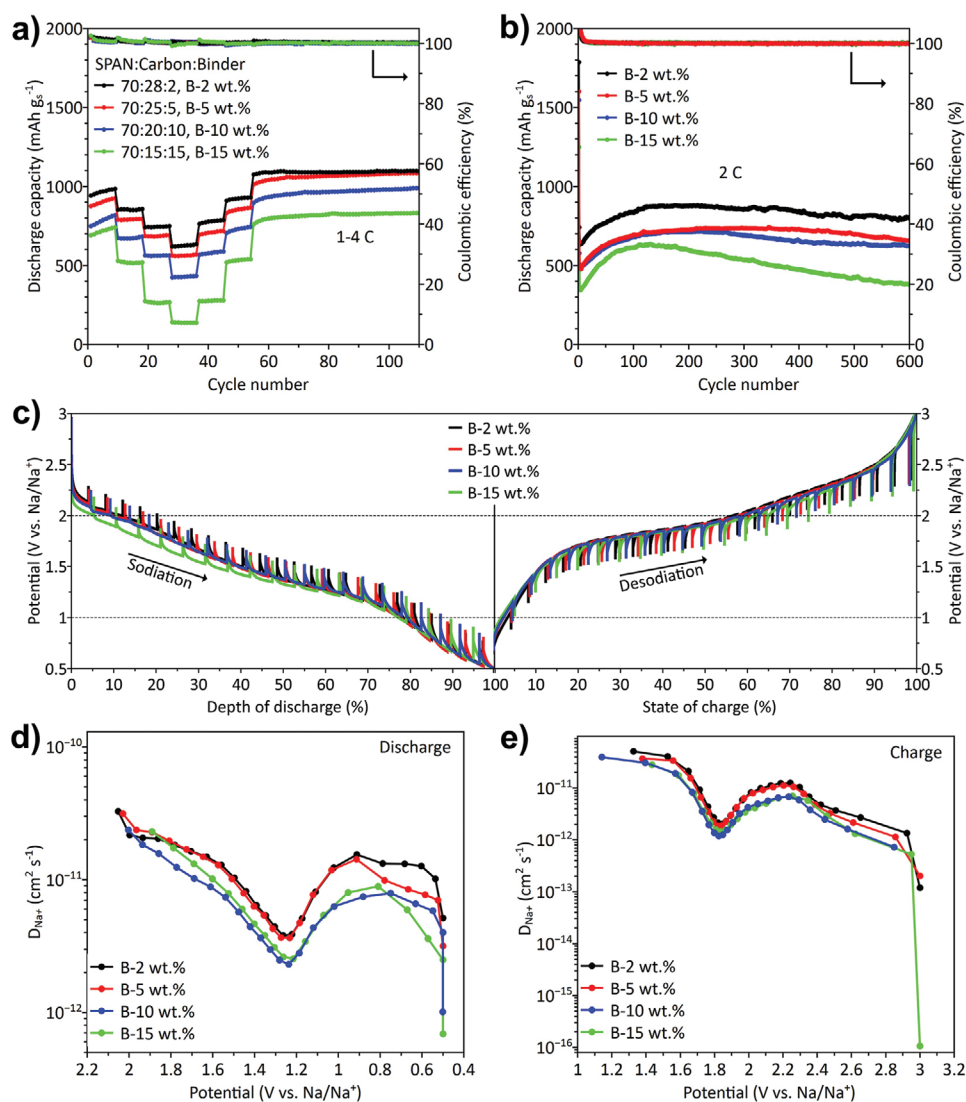


Figure 6. Electrochemical influence of the binder quantity (B – 2, 5, 10, 15 wt.%) on a GPE-containing Na-SPAN cell. a) Rate capability; b) galvanostatic cycle stability; c) GITT analysis of SPAN cathodes with varying binder content; apparent diffusion coefficient D_{Na^+} versus cell potential during, d) discharge; and e) charge.

2.4. Confinement Properties of GPEs

Binders are an indispensable part of cathodes. They help in the physical retainment of the cathode components, thereby preventing volume expansion and polysulfide dissolution.^[61] The ratio of active material to binder obviously affects the electrochemical performance of a cell. While the use of large amounts of binder prevents the diffusion of the electrolyte into the porous structure of a cathode, ultimately leading to poor cycling performance, low amounts of binder result in active material dissolution and poor adhesion of the active material during volume expansion.^[62,63] Therefore, it is essential to optimize the binder content in a way that does not compromise the cathode's electrical and ionic conductivity. To realize the GPEs confinement abilities, SPAN cathodes were fabricated with varying amounts of the binder.

SEM and EDX images of cathodes with different binder (Na-CMC) content shown in Figure S19a–d, Supporting

Information reveal that a reduction in the binder content resulted in high porosity of the cathode. This way, a low amount of binder in the cathode facilitates the penetration of the GPE into the cathode's pores. **Figure 6a** shows the rate performance of GPE-based Na-SPAN cells with SPAN cathodes containing different amounts of the binder at C-rates between 1 and 4 C. Cathodes containing 2 wt.% binder showed the highest discharge capacity (625 mAh g^{-1}) compared to cathode containing 15 wt.% binder (140 mAh g^{-1}). Similarly, galvanostatic long-term cycling (Figure 6b) revealed high discharge capacities for cathodes containing 2 wt.% binder, whereas cathodes with high binder content showed fast degradation. Figure S20a–d, Supporting Information shows plots of current density versus potential at different scan rates for cathodes containing different amounts of the binder. A reduction in binder significantly enhances the current density and leads to sharp peaks, pointing towards improved reaction kinetics at the cathode.

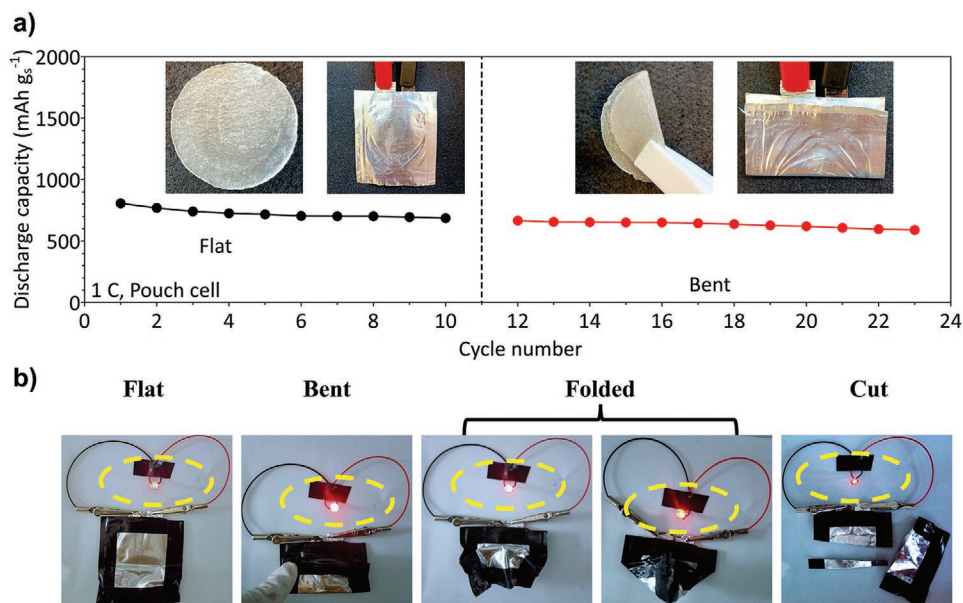


Figure 7. Performance of a flexible Na-SPAN battery based on a GPE. a) Galvanostatic cycling performance of a pouch cell during the flattening and bending test (inset: glass fiber membrane with in situ formed GPE and the corresponding pouch cell – in the flat (left) and bent (right) state); b) optical images of the GPE-containing flexible Na-SPAN cell in the flat, bent, folded and cut states, which all power the LED.

The difference in potential (ΔV) from the CV curve (peak C – peak A, Table S5, Supporting Information) and during cycling (1st, 100th, and 300th cycle at 2 C, Figure S21a–c, Supporting Information) signifies that cathodes containing 2 wt.% binder experience reduced polarization, which in turn promotes high-capacity utilization. The excellent electrochemical performance of cathodes with a low amount of binder (2 wt.%) is not only influenced by the increased carbon content (electronic conductivity) but also by higher ionic conductivity due to the larger amounts of the GPE that are in contact with the active material.

Finally, GITT measurements (Figure 6c) were carried out to determine the diffusion coefficient of Na⁺ in the cathode as well as the charge and discharge kinetics.^[52,64,65] During discharge, the initial discharge potential of cathodes containing 2 wt.% binder was 2.7 V versus Na/Na⁺, whereas, those containing 15 wt.% binder started at a lower potential of 2.4 V, suggesting that larger overpotentials are required to reduce the sulfur with increasing amounts of binder. A similar trend was observed during charging. At 50–100% state of charge, the potential curve of cathodes containing 15 wt.% binder displayed an increased potential loss at each relaxation cycle compared to cathodes containing 2 wt.% binder. This is likely a result of an impeded Na⁺ ion movement in the insulating binder environment. To prove this hypothesis, the diffusion coefficient of Na⁺ (Figure 6d,e) was calculated by the transient voltage method developed by Weppner and Huggins.^[66,67] During sodiation, the Na⁺ ions tend to diffuse faster at low binder content (2 wt.%); good contact between the GPE and the active material promotes ion mobility. Thus, at a discharge potential of 1.2 V, at which intermediate polysulfides are formed, the sodium diffusion coefficient (D_{Na^+}) of a cathode containing 2 wt.% binder was 3.87×10^{-12} versus 2.53×10^{-12} for a cathode containing 15 wt.% binder. At the end of sodiation and desodiation, cathodes with 15 wt.% binder display sluggish Na⁺ ion diffusion,

indicating poor conversion at the cut-off potentials. These data suggest that a lower binder amount in the cathode provides a higher degree of conversion, which helps in achieving high-rate capability with Na-SPAN full cells.

A comparison of the present system with other, existing liquid and gel polymer electrolytes in terms of ionic conductivity, capacity, cycling stability, and cathode materials used is given in Table S6, Supporting Information.

2.5. Application of GPEs in Flexible Batteries

Finally, to assess the potential application of a GPE-based flexible Na-SPAN battery, as proof of concept, a laboratory-scale pouch cell measuring $4 \times 4 \text{ cm}^2$ (Figure 7a) was fabricated. The glass fiber separator was placed on a thin sodium anode, which was rolled onto the stainless-steel current collector. The soft packaged pouch cell was sealed and subjected to galvanostatic cycling at a rate of 1 C. First, the cell was cycled in its original flat state, later, cycling was continued by folding the pouch cell to 180°. Due to the good contact between the GPE and the electrodes, the cell was able to deliver a first discharge capacity of 807 mAh g⁻¹ and 668 mAh g⁻¹ in the flat and bent states, respectively. Even after bending, the cell was still able to maintain its capacity for the rest of the cycles. Moreover, the GPE-containing glass fiber membrane showed good mechanical stability and flexibility even after multiple bending cycles. Equally important, the pouch cell was able to light a light-emitting diode (LED) when tested under intentional flattening, bending (180°), and folding (Figure 7b). This mechanically robust pouch cell was further able to deliver current to the LED even after cutting it into three separate pieces. As outlined above, both the GPE-filled pores of the cathode and the initially formed polymer layer on the Na anode enhance the adhesion

between the electrolyte and the electrodes. This improved interfacial contact obviously allows to withstanding extreme deformations without affecting performance.

3. Conclusion

In summary, we developed a novel crosslinked GPE based on PETA for use in room temperature sodium-sulfur batteries. The as-prepared gel polymer electrolyte shows high ionic conductivity of 2.33 mS cm^{-1} at $25 \text{ }^\circ\text{C}$ in a Na-SPAN battery. DFT studies revealed strong one-site coordination of Na^+ to the propylene carbonate-based solvent, which restricts the free ion movement in the liquid electrolyte. By contrast, the interaction of Na^+ with the PETA-based polymer in the GPE is weak, which facilitates ion hopping, leading to high ionic conductivity. The GPE maintains ultra-stable cycling of 2500 charge-discharge cycles with discharge capacities $>600 \text{ mAh g}_s^{-1}$ at 2 C, ultimately achieving an average CE of 99.91%. In contrast, the liquid electrolyte exhibits degrading capacity accompanied by unstable CE after 1000 cycles. The confinement properties of the crosslinked GPE were studied by varying the amount of binder in the cathode between 2 and 15 wt.%. Cathodes containing 2 wt.% of binder showed improved rate capability, discharge capacity, and a higher diffusion coefficient compared to cathodes with higher binder contents. Results suggest that the reduction in the amount of binder leads to better contact between the GPE and the active material, which in turn favors rapid ion movement in the interfaces with the active material. The advantages of GPEs outlined here are expected to pave the path to the successful use of Na-S batteries in flexible energy storage devices.

4. Experimental Section

Preparation and Characterization of GPEs: NaTPB ($\geq 99.5\%$ purity, Sigma-Aldrich) was dried under vacuum at $120 \text{ }^\circ\text{C}$ overnight. PC ($\text{C}_4\text{H}_6\text{O}_3$, 99.7% purity) and FEC ($\text{C}_3\text{H}_3\text{FO}_3$, $\geq 99\%$ purity) battery grade solvents were purchased from Sigma-Aldrich. The preparation of PETA-based GPEs was carried out in an inert sealed glass vial for characterization of the GPE. The precursor solution containing 1.5 wt.% of PETA (abcr) and 0.5 wt.% of azobisisobutyronitrile (AIBN, Sigma-Aldrich) was mixed with liquid electrolyte (1 M NaTPB in PC and 7 wt.% FEC) under constant stirring for 1 h. Then the precursor solution was filtered through a syringe filter to remove any impurities and kept in an oven at $70 \text{ }^\circ\text{C}$ for 3 h to obtain a translucent GPE block.

SEM (Zeiss Gemini 500) was used to analyze the sample's surface by applying an electron acceleration voltage of 3.5 keV. EDX was carried out on a Bruker Nano using an acceleration voltage of 5 keV. Thermal degradation was measured via thermogravimetric analysis (TGA, PerkinElmer) under a constant nitrogen flow (19.8 ml min^{-1}) using a heating rate of $20 \text{ }^\circ\text{C min}^{-1}$ from room temperature to $400 \text{ }^\circ\text{C}$.

Cathode Preparation: The SPAN active material was synthesized according to the literature.^[6] Briefly, 2.0 g of poly(acrylonitrile) (PAN, $M_w = 150\,000 \text{ g mol}^{-1}$, $\bar{D} = 3.6$, Sigma-Aldrich) was placed in a quartz tube together with sulfur (ca. 20 g, Carl Roth) and the mixture was deoxygenized with nitrogen. The tube was heated to $150 \text{ }^\circ\text{C}$ to compact the sulfur and then transferred to a furnace (Nabertherm, Germany) to further increase the temperature to $550 \text{ }^\circ\text{C}$ for 3 h under a constant nitrogen flow (200 L h^{-1}). To remove excess sulfur, the SPAN was subjected to Soxhlet extraction with toluene for 48 h. Elemental analysis revealed a sulfur content of $40.24 \pm 0.03 \text{ wt.}\%$. The composite

cathode was prepared by mixing 70 wt.% of SPAN, 20 wt.% of carbon (C-65 MTI corporation), and 10 wt.% of Na-CMC binder (high viscosity, Sigma-Aldrich) in water using a planetary mixer (Thinky, Japan) at 2000 rpm for 15 min. The resulting slurry was coated (wet thickness, $300 \mu\text{m}$) on a carbon-coated aluminum foil ($16 \mu\text{m}$, MTI Corporation) with the help of a blade coater (Erichsen, Germany). After drying at $60 \text{ }^\circ\text{C}$ overnight, the cathode was punched into disks 12 mm in diameter. The average sulfur content per cathode was 0.7–0.8 mg. Pure metallic sodium was cut and rolled on a polyethylene surface and then pressed into 12 mm disks.

In situ Polymerization of Precursor Solution and Cell Assembly: The cell assembly was carried out in an argon-filled glovebox (O_2 , $\text{H}_2\text{O} < 0.1 \text{ ppm}$). Swagelok-type cells were used for in situ polymerization and subsequent electrochemical characterization. First, sodium metal was placed inside the cell container on a stainless-steel stem followed by a single glass fiber sheet ($\varnothing = 13 \text{ mm}$, Whatman). To maintain accurate conditions, $80 \mu\text{L}$ precursor solution were injected into the glass fiber separator for all cells. The SPAN cathode was wetted with precursor solution before placing it into the cell compartment. The assembled cells were aged for 2 h before placing them inside an oven at $70 \text{ }^\circ\text{C}$. To ensure steady-state temperature throughout the cell, 6 h of heating was maintained. Finally, cells were cooled to room temperature followed by resting at OCV for 2 h to maintain a constant voltage before testing.

Electrochemical Characterization: A Biologic VMP3 analyzer (France) was used for LSV, CV, potentiostatic electrochemical impedance spectroscopy (PEIS), galvanostatic intermittent titration technique (GITT), and overpotential measurements. Galvanostatic long-term cycling tests and rate performance tests were conducted using BasyTec XCTS-LAB systems (Germany). LSV was conducted applying a scan rate of 1 mV s^{-1} in a three-electrode setup with platinum, copper, carbon paper, graphite, and stainless steel working electrodes (all vs Na/Na^+). CV measurements were conducted between 0.5–3 V using SPAN as a working electrode and sodium as a reference and counter electrode. Ionic conductivity measurements were carried out using PEIS between 0.5 Hz and 500 kHz applying an alternating current amplitude of 10 mV using SS blocking electrodes. Cells were measured between -25 to $40 \text{ }^\circ\text{C}$ using temperature intervals of $5 \text{ }^\circ\text{C}$ and rested for 4 h at each temperature to attain thermal equilibrium. The resulting impedance curve was fitted using the built-in Z-fit library. GITT of Na-S cells was performed at different cycles by cycling the cell at 0.1 C for 20 min, followed by a 2 h relaxation period until the battery was fully charged/discharged. Symmetric $\text{Na}||\text{Na}$ cells with a GPE were measured to obtain the plating/stripping overpotential at defined current densities. Galvanostatic charge/discharge was conducted at different C-rates (1 C = 1672 mA g_s^{-1}) between 0.5–3 V versus Na/Na^+ . Unless mentioned otherwise, all cells were subjected to one preformation cycle at 0.3 C prior to testing.

Statistical Analysis: All electrochemical tests were carried out with the help of two identical cell setups. The standard deviation was calculated for each data point and the maximum value was taken into account. The standard deviation (%) for all long-term cycling tests (at 2 C) and for cycling at 0.2 C was $<6\%$ and $<4\%$ for the rate capability tests (1–4 C).

Computational Details: Binding energies of the molecular geometries were calculated with the Gaussian 09 software package^[6] using DFT. Geometries were optimized on the B3LYP/6-31+G(2d,p) level. On these optimized geometries, single-point energies were calculated at the B3LYP/6-311+G(2df,2p) level. Binding energies include zero-point vibrational energies (ZPE) and are related to the energies of the separated compounds. Molecular electrostatic potential (MEP) maps were computed on the B3LYP/6-31+G(2d,p) level.

Supporting Information

Supporting Information is available from the Wiley Online Library or from the author.

Acknowledgements

The authors thank H. David (Max Planck Institute for Intelligent Systems, Stuttgart) for assistance with SEM. The authors thank J.V. Musso and J. Kappler for fruitful discussions and S. Athreya for assisting with 3D designs. The authors acknowledge support by the state of Baden-Württemberg through bwHPC and the German Research Foundation (DFG) through grant no INST 40/575-1 FUGG (JUSTUS 2 cluster). The authors also thankfully acknowledge financial support from the German Federal Ministry for Economic Affairs and Energy (BMWi, project no. 03ETE003A, FiMaLiS).

Open access funding enabled and organized by Projekt DEAL.

Conflict of Interest

The authors declare no conflict of interest.

Data Availability Statement

The data that support the findings of this study are available from the corresponding author upon reasonable request.

Keywords

gel polymer electrolytes, in situ polymerized electrolytes, polysulfide confinements, room-temperature sodium-sulfur batteries, sulfurized poly(acrylonitrile)

Received: January 28, 2022

Revised: April 29, 2022

Published online: May 31, 2022

- [1] D. D. Sarma, A. K. Shukla, *ACS Energy Lett.* **2018**, *3*, 2841.
 [2] M. Nentwich, B. Störr, J. Hanzig, *Phys. Sci. Rev.* **2019**, *4*, 20180038.
 [3] M. Armand, P. Axmann, D. Bresser, M. Copley, K. Edström, C. Ekberg, D. Guyomard, B. Lestriez, P. Novák, M. Petranikova, W. Porcher, S. Trabesinger, M. Wohlfahrt-Mehrens, H. Zhang, *J. Power Sources* **2020**, *479*, 228708.
 [4] S. Chu, A. Majumdar, *Nature* **2012**, *488*, 294.
 [5] Z. P. Cano, D. Banham, S. Ye, A. Hintennach, J. Lu, M. Fowler, Z. Chen, *Nat. Energy* **2018**, *3*, 279.
 [6] B. Dunn, H. Kamath, J.-M. Tarascon, *Science* **2011**, *334*, 928.
 [7] H. C. Hesse, M. Schimpe, D. Kucevic, A. Jossen, *Energies* **2017**, *10*, 2107.
 [8] K. B. Hueso, M. Armand, T. Rojo, *Energy Environ. Sci.* **2013**, *6*, 734.
 [9] K. B. Hueso, V. Palomares, M. Armand, T. Rojo, *Nano Res.* **2017**, *10*, 4082.
 [10] C.-W. Park, J.-H. Ahn, H.-S. Ryu, K.-W. Kim, H.-J. Ahn, *Electrochem. Solid-State Lett.* **2006**, *9*, A123.
 [11] Z. W. Seh, J. Sun, Y. Sun, Y. Cui, *ACS Cent. Sci.* **2015**, *1*, 449.
 [12] P. Adelhelm, P. Hartmann, C. L. Bender, M. Busche, C. Eufinger, J. Janek, *Beilstein J. Nanotechnol.* **2015**, *6*, 1016.
 [13] S. Zhang, Y. Yao, Y. Yu, *ACS Energy Lett.* **2021**, *6*, 529.
 [14] A. Manthiram, X. Yu, *Small* **2015**, *11*, 2108.
 [15] S. Murugan, S. V. Klostermann, W. Frey, J. Kästner, M. R. Buchmeiser, *Electrochem. Commun.* **2021**, *132*, 107137.
 [16] M. Frey, R. K. Zenn, S. Warneke, K. Müller, A. Hintennach, R. E. Dinnebier, M. R. Buchmeiser, *ACS Energy Lett.* **2017**, *2*, 595.
 [17] Z.-Q. Jin, Y.-G. Liu, W.-K. Wang, A.-B. Wang, B.-W. Hu, M. Shen, T. Gao, P.-C. Zhao, Y.-S. Yang, *Energy Storage Mater.* **2018**, *14*, 272.
 [18] J. Wang, J. Yang, C. Wan, K. Du, J. Xie, N. Xu, *Adv. Funct. Mater.* **2003**, *13*, 487.
 [19] J. Wang, J. Yang, J. Xie, N. Xu, *Adv. Mater.* **2002**, *14*, 963.
 [20] S. Gao, K. Wang, R. Wang, M. Jiang, J. Han, T. Gu, S. Cheng, K. Jiang, *J. Mater. Chem. A* **2017**, *5*, 17889.
 [21] K. Xu, *Chem. Rev.* **2014**, *114*, 11503.
 [22] J. Zhou, H. Ji, J. Liu, T. Qian, C. Yan, *Energy Storage Mater.* **2019**, *22*, 256.
 [23] S. Janakiraman, A. Agrawal, R. Biswal, A. Venimadhav, *Appl. Surf. Sci.* **2021**, *6*, 100139.
 [24] H. Yin, C. Han, Q. Liu, F. Wu, F. Zhang, Y. Tang, *Small* **2021**, *17*, 2006627.
 [25] M. Liu, D. Zhou, Y.-B. He, Y. Fu, X. Qin, C. Miao, H. Du, B. Li, Q.-H. Yang, Z. Lin, T. S. Zhao, F. Kang, *Nano Energy* **2016**, *22*, 278.
 [26] J. Zheng, Y. Zhao, X. Feng, W. Chen, Y. Zhao, *J. Mater. Chem. A* **2018**, *6*, 6559.
 [27] D. Zhou, L.-Z. Fan, H. Fan, Q. Shi, *Electrochim. Acta* **2013**, *89*, 334.
 [28] G. Hoti, F. Caldera, C. Cecone, A. Rubin Pedrazzo, A. Anceschi, S. Appleton, Y. Khazaei Monfared, F. Trotta, *Materials* **2021**, *14*, 478.
 [29] A. Oueslati, S. Kamoun, F. Hlel, M. Gargouri, A. Fort, *Akademeia* **2010**, *1*, a0100.
 [30] D. Zhou, Y. Chen, B. Li, H. Fan, F. Cheng, D. Shanmukaraj, T. Rojo, M. Armand, G. Wang, *Angew. Chem., Int. Ed.* **2018**, *57*, 10168.
 [31] H.-J. Ha, Y. H. Kwon, J. Y. Kim, S.-Y. Lee, *Electrochim. Acta* **2011**, *57*, 40.
 [32] H.-J. Ha, E.-H. Kil, Y. H. Kwon, J. Y. Kim, C. K. Lee, S.-Y. Lee, *Energy Environ. Sci.* **2012**, *5*, 6491.
 [33] F. A. Settle, *Handbook of Instrumental Techniques for Analytical Chemistry*, Prentice Hall PTR, Upper Saddle River, NJ **1997**.
 [34] X. Xu, D. Zhou, X. Qin, K. Lin, F. Kang, B. Li, D. Shanmukaraj, T. Rojo, M. Armand, G. Wang, *Nat. Commun.* **2018**, *9*, 3870.
 [35] J. Wu, J. Liu, Z. Lu, K. Lin, Y.-Q. Lyu, B. Li, F. Ciucci, J.-K. Kim, *Energy Storage Mater.* **2019**, *23*, 8.
 [36] S. Murugan, S. Niesen, J. Kappler, K. Küster, U. Starke, M. R. Buchmeiser, *Batteries Supercaps* **2021**, *4*, 1636.
 [37] W. Zhang, X. Chen, Y. Wang, L. Wu, Y. Hu, *ACS Omega* **2020**, *5*, 22465.
 [38] S. B. Aziz, T. J. Woo, M. F. Z. Kadir, H. M. Ahmed, *J. Sci. : Adv. Mater. Devices* **2018**, *3*, 1.
 [39] F. Croce, M. L. Focarete, J. Hassoun, I. Meschini, B. Scrosati, *Energy Environ. Sci.* **2011**, *4*, 921.
 [40] M. A. Ratner, P. Johansson, D. F. Shriver, *MRS Bull.* **2000**, *25*, 31.
 [41] S. Han, *Sci. Rep.* **2019**, *9*, 5555.
 [42] K. Xu, A. von Cresce, U. Lee, *Langmuir* **2010**, *26*, 11538.
 [43] L. Liu, L. Miao, L. Li, F. Li, Y. Lu, Z. Shang, J. Chen, *J. Phys. Chem.* **2018**, *9*, 3573.
 [44] K. Xu, *Chem. Rev.* **2004**, *104*, 4303.
 [45] Y. Wang, L. Fu, L. Shi, Z. Wang, J. Zhu, Y. Zhao, S. Yuan, *ACS Appl. Mater. Interfaces* **2019**, *11*, 5168.
 [46] E. Quartarone, P. Mustarelli, *Chem. Soc. Rev.* **2011**, *40*, 2525.
 [47] P. Bai, J. Li, F. R. Brushett, M. Z. Bazant, *Energy Environ. Sci.* **2016**, *9*, 3221.
 [48] R. C. Agrawal, G. P. Pandey, *J. Phys. D: Appl. Phys.* **2008**, *41*, 223001.
 [49] X. Huang, Z. Wang, R. Knibbe, B. Luo, S. A. Ahad, D. Sun, L. Wang, *Energy Technol.* **2019**, *7*, 1801001.
 [50] A. Y. S. Eng, D.-T. Nguyen, V. Kumar, G. S. Subramanian, M.-F. Ng, Z. W. Seh, *J. Mater. Chem. A* **2020**, *8*, 22983.
 [51] L. Ji, M. Rao, H. Zheng, L. Zhang, Y. Li, W. Duan, J. Guo, E. J. Cairns, Y. Zhang, *J. Am. Chem. Soc.* **2011**, *133*, 18522.
 [52] Z. Li, J. Zhang, Y. Lu, X. W. Lou, *Sci. Adv.* **2018**, *4*, aat1687.
 [53] S. Bai, X. Liu, K. Zhu, S. Wu, H. Zhou, *Nat. Energy* **2016**, *1*, 16094.
 [54] L. Wang, X. Chen, S. Li, J. Yang, Y. Sun, L. Peng, B. Shan, J. Xie, *J. Mater. Chem. A* **2019**, *7*, 12732.
 [55] G. Bieker, M. Winter, P. Bieker, *Phys. Chem. Chem. Phys.* **2015**, *17*, 8670.

- [56] X.-m. Zhao, Q. Zhu, S.-d. Xu, L. Chen, Z.-j. Zuo, X.-m. Wang, S.-b. Liu, D. Zhang, *J. Electroanal. Chem.* **2019**, 832, 392.
- [57] S. S. Zhang, *Energies* **2014**, 7, 4588.
- [58] Y. Zhang, Y. Zhao, D. Gosselink, P. Chen, *Ionics* **2015**, 21, 381.
- [59] X. Yu, A. Manthiram, *Chem. - Eur. J.* **2015**, 21, 4233.
- [60] C. Zu, N. Azimi, Z. Zhang, A. Manthiram, *J. Mater. Chem. A* **2015**, 3, 14864.
- [61] L. Li, T. A. Pascal, J. G. Connell, F. Y. Fan, S. M. Meckler, L. Ma, Y.-M. Chiang, D. Prendergast, B. A. Helms, *Nat. Commun.* **2017**, 8, 2277.
- [62] M. Shaibani, M. S. Mirshekarloo, R. Singh, C. D. Easton, M. C. D. Cooray, N. Eshraghi, T. Abendroth, S. Dörfler, H. Althues, S. Kaskel, A. F. Hollenkamp, M. R. Hill, M. Majumder, *Sci. Adv.* **2020**, 6, aay2757.
- [63] M. Hagen, D. Hanselmann, K. Ahlbrecht, R. Maça, D. Gerber, J. Tübke, *Adv. Energy Mater.* **2015**, 5, 1401986.
- [64] N. Garcia-Araez, J. Dibden, N. Meddings, J. Owen, *ChemElectroChem* **2017**, 5.
- [65] S. Li, Z. Zeng, J. Yang, Z. Han, W. Hu, L. Wang, J. Ma, B. Shan, J. Xie, *ACS Appl. Energy Mater.* **2019**, 2, 2956.
- [66] W. Weppner, R. A. Huggins, *J. Electrochem. Soc.* **1977**, 124, 1569.
- [67] S. Wei, S. Xu, A. Agrawal, S. Choudhury, Y. Lu, Z. Tu, L. Ma, L. A. Archer, *Nat. Commun.* **2016**, 7, 11722.
- [68] M. J. Frisch, G. W. Trucks, H. B. Schlegel, G. E. Scuseria, M. A. Robb, J. R. Cheeseman, G. Scalmani, V. Barone, G. A. Petersson, H. Nakatsuji, X. Li, M. Caricato, A. V. Marenich, J. Bloino, B. G. Janesko, R. Gomperts, B. Mennucci, H. P. Hratchian, J. V. Ortiz, A. F. Izmaylov, J. L. Sonnenberg, Williams, F. Ding, F. Lipparini, F. Egidi, J. Goings, B. Peng, A. Petrone, T. Henderson, D. Ranasinghe, et al., *Gaussian 09*, Gaussian, Inc., Wallingford, CT **2016**.

Supporting Information

for *Adv. Funct. Mater.*, DOI: 10.1002/adfm.202201191

Stable Cycling of Room-Temperature Sodium-Sulfur Batteries Based on an In Situ Crosslinked Gel Polymer Electrolyte

*Saravanakumar Murugan, Sina V. Klostermann, Peter Schützendübe, Gunther Richter, Johannes Kästner, and Michael R. Buchmeiser**

Supporting Information

Stable Cycling of Room-Temperature Sodium-Sulfur Batteries Based on an In Situ Crosslinked Gel Polymer Electrolyte

*Saravanakumar Murugan, Sina V. Klostermann, Peter Schützendübe, Gunther Richter, Johannes Kästner, Michael R. Buchmeiser**

Swelling rate of crosslinked PETA

Crosslinked PETA (pure) was swollen by propylene carbonate until the weight of the swollen polymer remained constant.

$$\text{Swelling rate (S, \%)} = \frac{m_1 - m_0}{m_0} \cdot 100 \quad \text{Equation S1}$$

m_1 is the weight of the swollen polymer, and m_0 is the initial weight of the dry polymer.

The molecular weight between the crosslinks (M_c) and the crosslinking density (ν) was calculated using the Flory-Rehner equation.

$$M_c = \frac{V_1 \left[(V_r)^{\frac{1}{3}} - \left(\frac{2}{f} V_r \right) \right]}{-[\ln(1 - V_r) + V_r + \chi (V_r)^2]} \quad \text{Equation S2}$$

V_r is the polymer volume fraction in the equilibrium-swollen polymer, V_l is the molar volume of the solvent used for swelling, χ is the Flory-Huggins solvent-polymer interaction parameter, f is the functionality of the crosslinks.

$$M_c = \frac{\rho}{\nu} \quad \text{Equation S3}$$

ρ is the density of the polymer.

Table S1: Calculated values of S , V_r , M_c , ν

	S (%)	V_r	M_c (g mol ⁻¹)	ν (mol cm ⁻³)
Crosslinked PETA	30	0.75	100	0.0126

To mimic the GPE environment, poly-PETA was immersed in propylene carbonate until the weight of the swollen polymer remained constant. The results from Table S1 allow for correlating the decrease in molecular weight between the crosslinks with the crosslinking density, resulting in a decrease in swelling.^[1] Poly-PETA shows a high crosslinking density due to its three reactive functional groups, which can form a high percentage of gel even at a low concentration in the LE. This highly crosslinked PETA can successfully retain the LE in the polymer matrix, thus, preventing leakage.

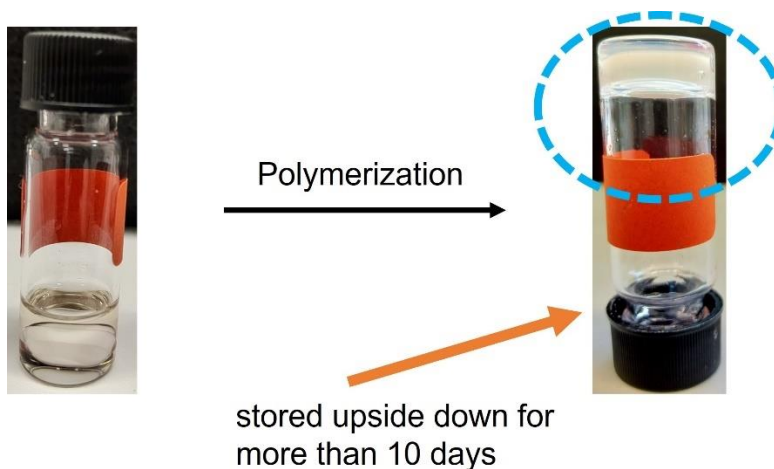


Figure S1: Polymerization and subsequent storing of the GPE upside down for more than 10 days.

The precursor solution was polymerized and stored upside down for more than ten days to observe possible LE leakage. The poly-PETA network fully contained LE even after 10 days.

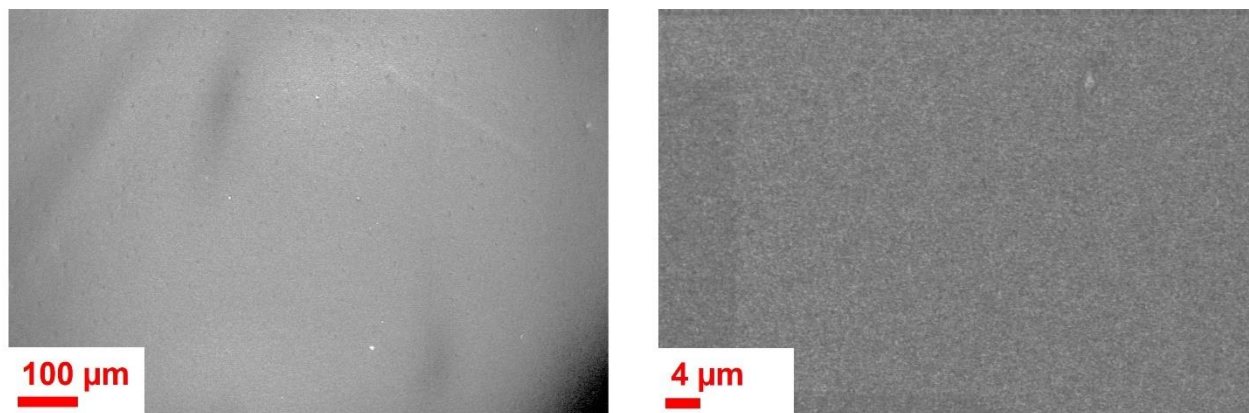


Figure S2: SEM images at different magnifications of a dried GPE polymerized on a glass plate.

FTIR - calculations

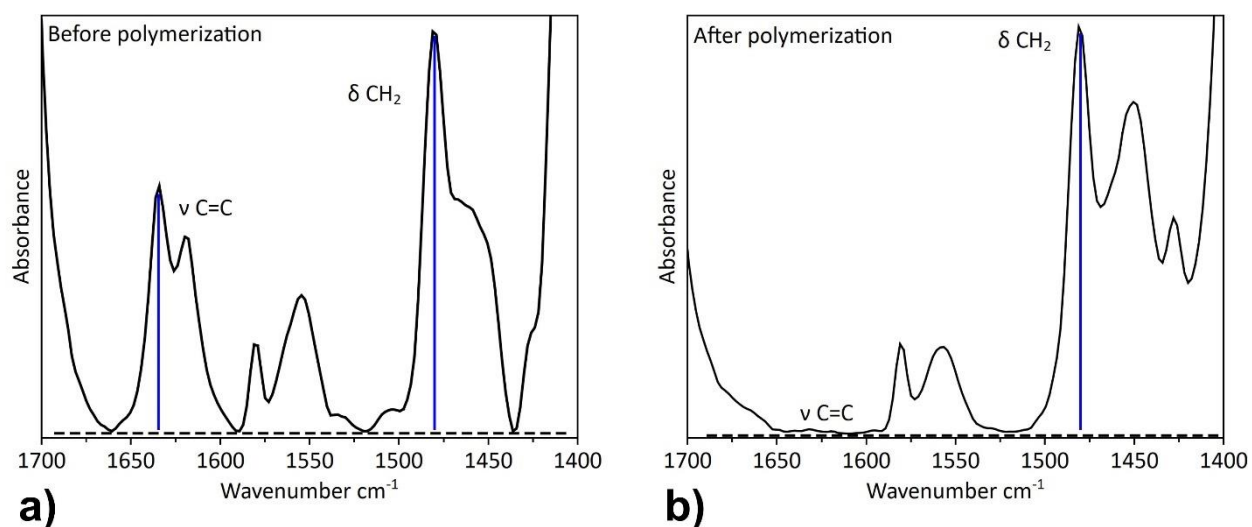


Figure S3: Comparison of the FTIR spectra of the a) precursor solution; and b) the final GPE.

Since the CH₂ bending peak at 1470 cm⁻¹ is of similar height both before and after polymerization, the degree of double bond conversion (DC, %) can be determined by comparing the CH₂ and C=C peaks. A baseline was drawn from 1406 cm⁻¹ to 1693 cm⁻¹ and the peak height was measured at 1470 cm⁻¹ and 1633 cm⁻¹, respectively.^[2]

$$DC (\%) = \left(1 - \frac{h_{1633} \times h_{1470 \text{ before}}}{h_{1633} \times h_{1470 \text{ after}}} \right) \times 100 \quad \text{Equation S4}$$

$h_{1470 \text{ before}}$ represents the height of the peak at 1470 cm^{-1} before polymerization, $h_{1470 \text{ after}}$ is the height of the peak after polymerization.

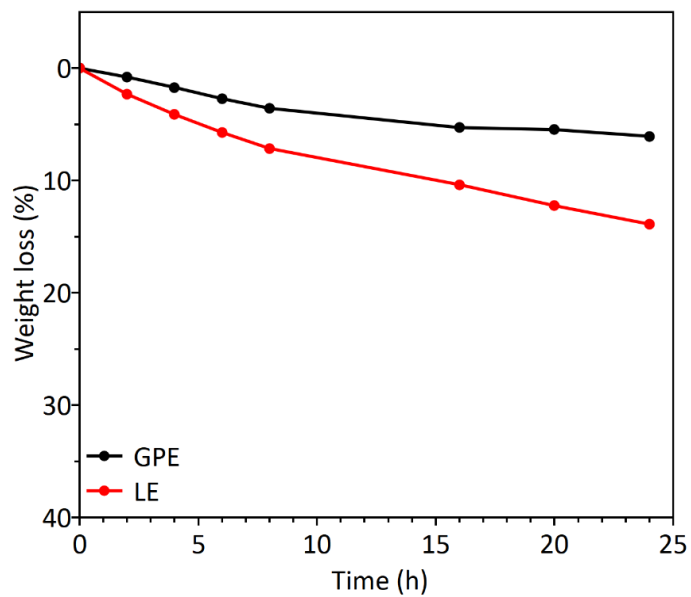


Figure S4: Weight-loss over time at $23 \text{ }^{\circ}\text{C}$ under atmospheric pressure for a GPE and an LE, both incorporated in a glass fiber separator.

Ion conductivity in gel polymer electrolytes – Vogel-Tamman-Fulcher (VTF) equation

Table S2: Experimental details and comparison of the ionic conductivities of the GPE and the LE (thickness of the electrolyte (GPE and LE) - 0.0210 cm, surface area – 1.13 cm²).

Electrolyte	Temperature (°C)	Bulk resistance (R _b , Ω)	Ionic conductivity (σ, mS cm ⁻¹)
GPE	-24	125	0.15
	-20	91	0.20
	-15	62	0.30
	-10	44	0.42
	-5	33	0.57
	0	25	0.75
	5	20	0.94
	10	16	1.2
	15	13	1.4
	20	10	1.9
	25	8	2.3
	30	7	2.6
	35	6	3.0
	40	5	3.8
	LE	-24	121
-20		90	0.20
-15		59	0.32
-10		41	0.46
-5		32	0.59
0		24	0.79
5		19	0.98
10		15	1.2
15		13	1.5
20		10	2.0
25		8	2.3
30		7	2.7
35		6	3.0
40		6	3.4

VTF fitting of the log σ vs. T⁻¹ provides a bent line, which indicates the diffusion of ion occurs from one free volume to another one. In polymer electrolyte systems, both the ions and polymer segments are in motion.

$$\sigma = AT^{-1/2} \exp\left(-\frac{E_a}{R(T-T_0)}\right) \quad \text{Equation S5}$$

σ = ionic conductivity, A = pre-exponential factor proportional to the number of charge carriers, T = temperature, E_a = pseudo-activation energy for the ion hopping process, T_o = equilibrium glass transition temperature (usually 30-50 K below T_g) where the configuration entropy or free volume disappears.

DFT simulations

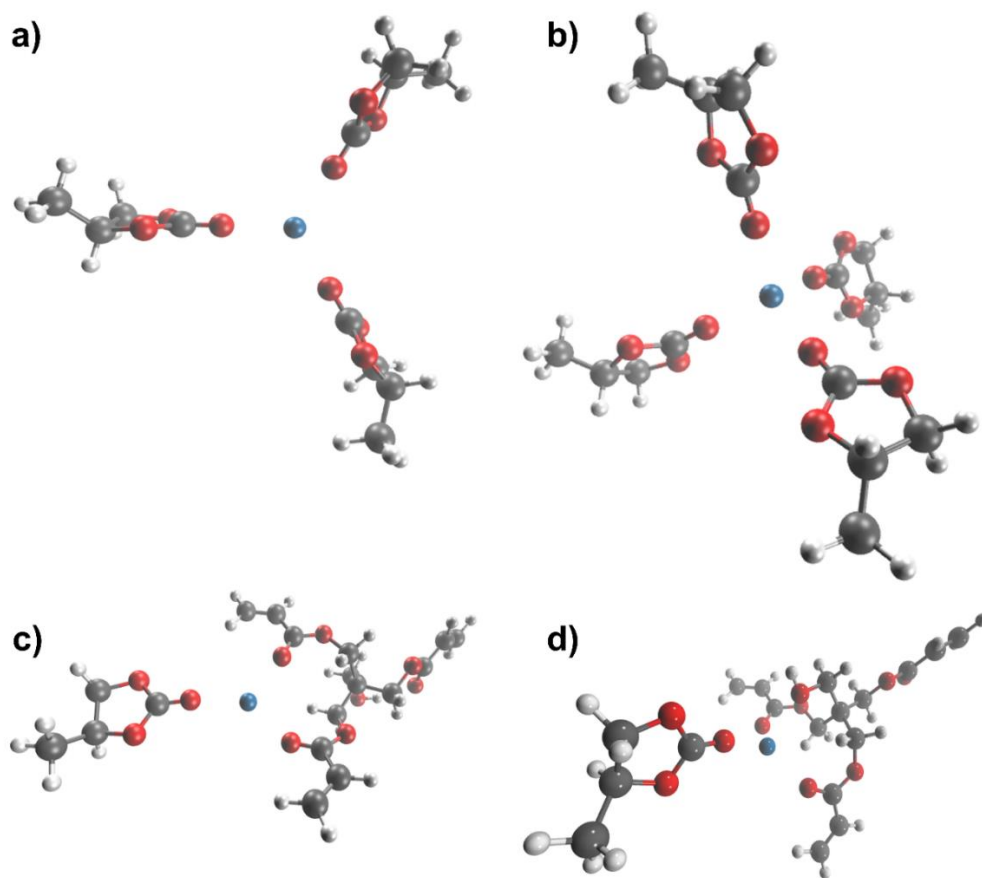


Figure S5: MEP calculations for Na⁺ with solvent (PC) and PETA. Calculated binding energies of Na⁺ and the energy of the corresponding number of solvent molecules, a) Na⁺ coordinated to three solvent (PC) molecules; b) Na⁺ coordinated to four PC molecules. The calculated energies consist of Na⁺, a solvent molecule (PC), and the energy of PETA; c) solvent-bound Na⁺ coordinated to a PETA monomer with coordination number three; d) solvent-bound Na⁺ coordinated to a PETA monomer with coordination number four. (Color code: blue - Na⁺, red - O, dark grey - C, white - H).

Table S3. Calculated binding energies of Na⁺ to PC and PETA, respectively, with different coordination numbers.

Molecule	Solvent (PC)		Monomer (PETA)	
	Coordination number			
	3	4	3	4
E_{bind} (kJ mol⁻¹)	-371.4	-427.4	-315.0	-316.9
Bond distance Na⁺⋯O (Å)	2.20, 2.20, 2.20	2.25, 2.26, 2.25, 2.25	2.19, 2.21, 2.22	2.21, 2.31, 2.39(- OH), 2.31

Since the GPE contains both the LE and a polymer matrix, it was assumed that, due to the high binding energy, Na⁺ always binds to the solvent molecule (PC) while interacting with PETA. From the above calculations, it is evident that Na⁺ has a lower binding energy to PETA. Therefore, Na⁺ movement in the GPE is not impeded by the coordination of Na⁺ to the polymeric matrix, which leads to high ionic conductivity.

Viscosity of the GPE and the LE

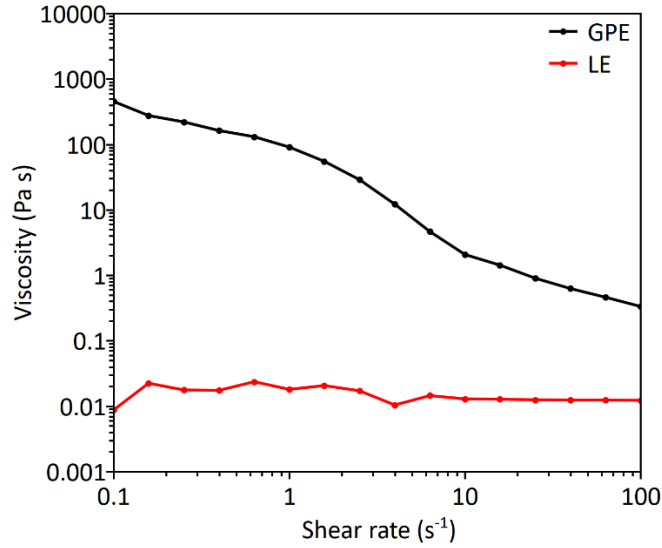


Figure S6: Viscosity vs. shear rate for the GPE and the LE.

The viscosity was measured by varying the shear rate from 0.1 to 100 s⁻¹. The LE exhibited Newtonian behavior with a viscosity of 0.01 Pa·s. The GPE showed a decrease in viscosity as the shear rate increased, indicating non-Newtonian shear-thinning of the GPE. When the shear rate was increased, the bond breakage and rearrangement of the polymer structure led to a reduction in viscosity. However, at low shear rate (0.1 s⁻¹), the viscosity of the GPE was many times higher than the one of the LE, suggesting that the GPE behaves like a solid at a low shear rate.

Transference number

$$t_{\text{Na}^+} = \frac{I_{ss}R_b^{ss}}{I_0R_b^0} \left[\frac{\Delta v - I_0R_0}{\Delta v - I_{ss}R_{ss}} \right] \quad \text{Equation S6}$$

A small direct current (DC) potential (Δv) of 10 mV was applied to a symmetric Na||Na cell and the resulting polarization current (initial (I_0) and steady-state current (I_{ss}) values) were recorded. Simultaneously, alternating current (AC) impedance was measured between 300 mHz to 800 kHz with a current amplitude of 10 mV before and after polarization; this

way, the values of the bulk (R_b^o and R_b^{ss}) and interfacial resistance (R_o and R_{ss}) were obtained.^[3-4]

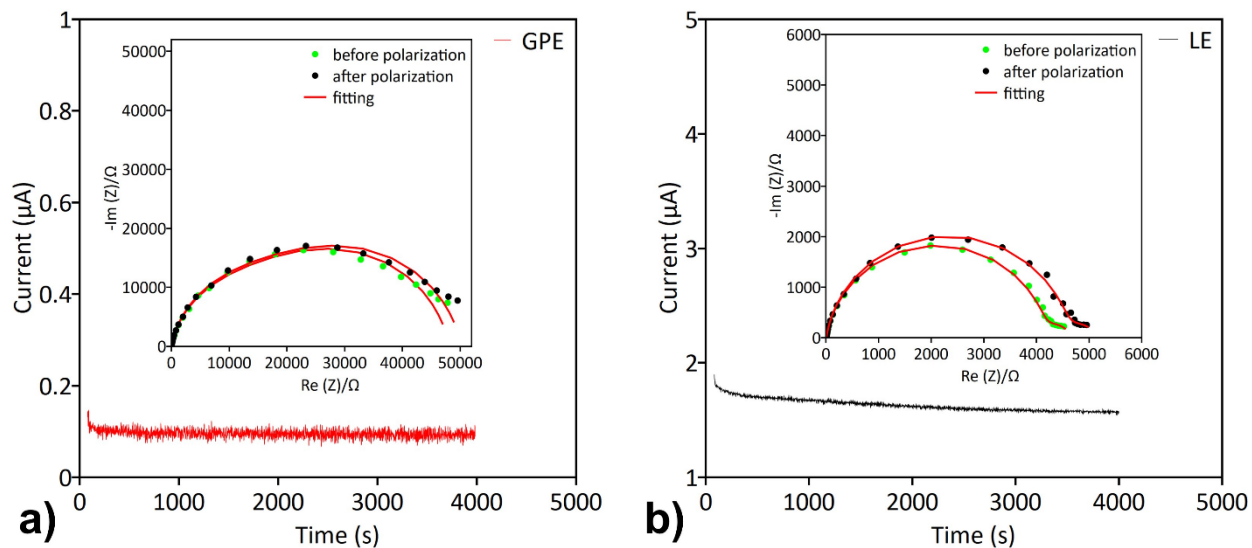


Figure S7: The chronoamperometry (polarization voltage - 10 mV) and AC impedance curve (inset, 0.5 Hz to 500 kHz at 10 mV AC amplitude) of a symmetric Na||Na cell based on a) a GPE; and b) an LE.

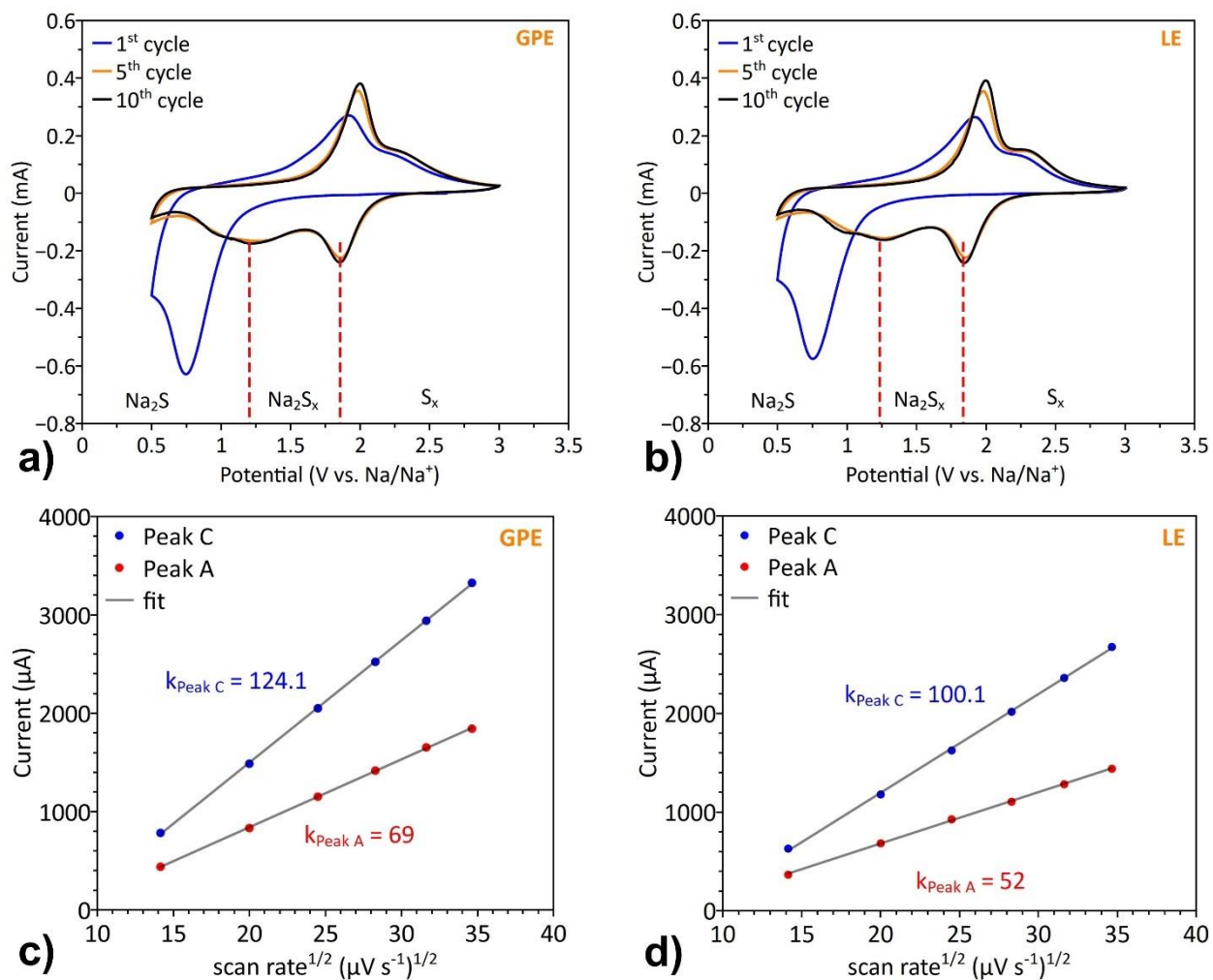


Figure S8: Comparison of the electrochemical kinetics of a GPE and an LE, a) 1st, 5th, and 10th CV cycle of a GPE; and b) an LE at 0.1 mV s⁻¹; Current vs. square root of scan rate (peak A (red) and peak B (blue)) for, c) GPE; and d) LE.

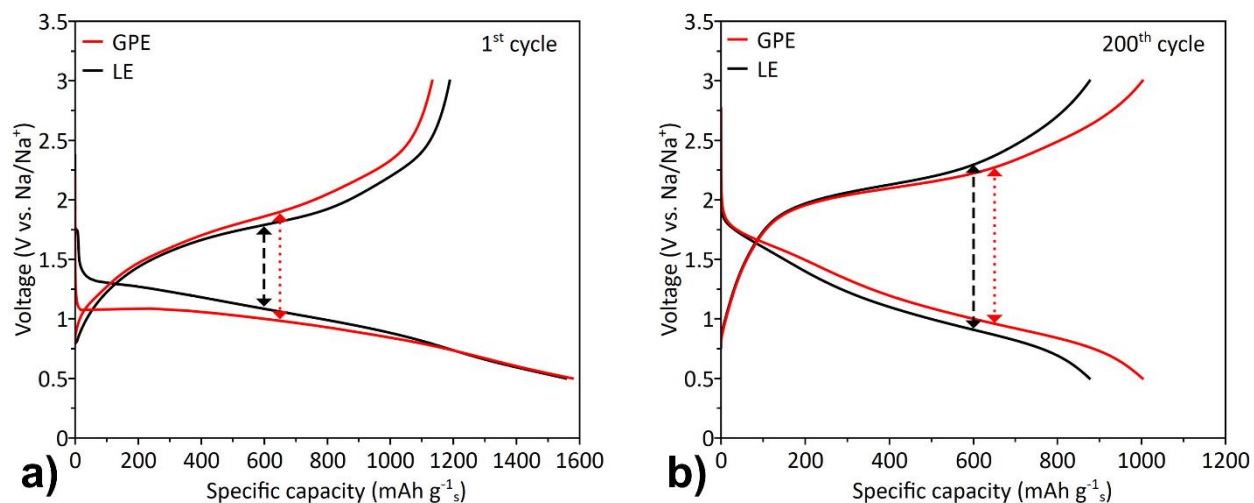


Figure S9: Comparison of the overpotential of a GPE and an LE cycled at 2 C, a) 1st cycle; and b) 200th cycle.

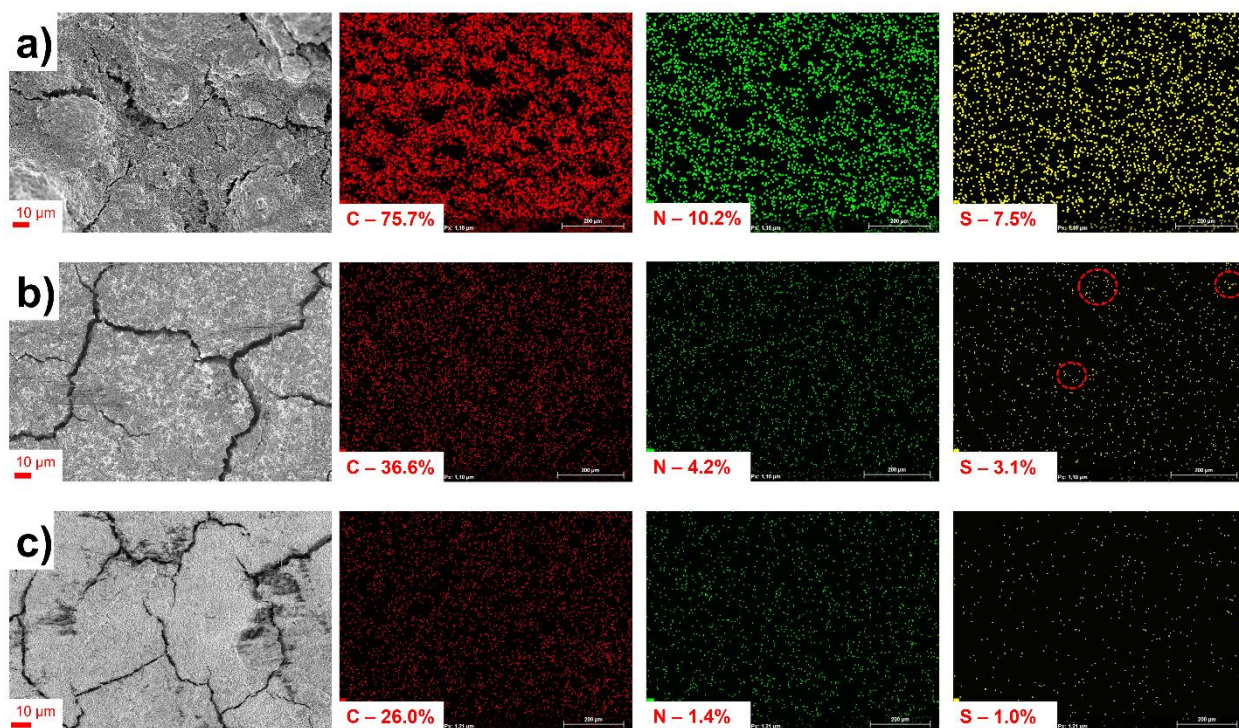


Figure S10: Scanning electron microscope images and the corresponding energy dispersive X-ray mapping of SPAN cathodes. a) Pristine SPAN before cycling; b) after discharge in an LE (red circles indicate the sulfur agglomeration spots); and c) in a GPE.

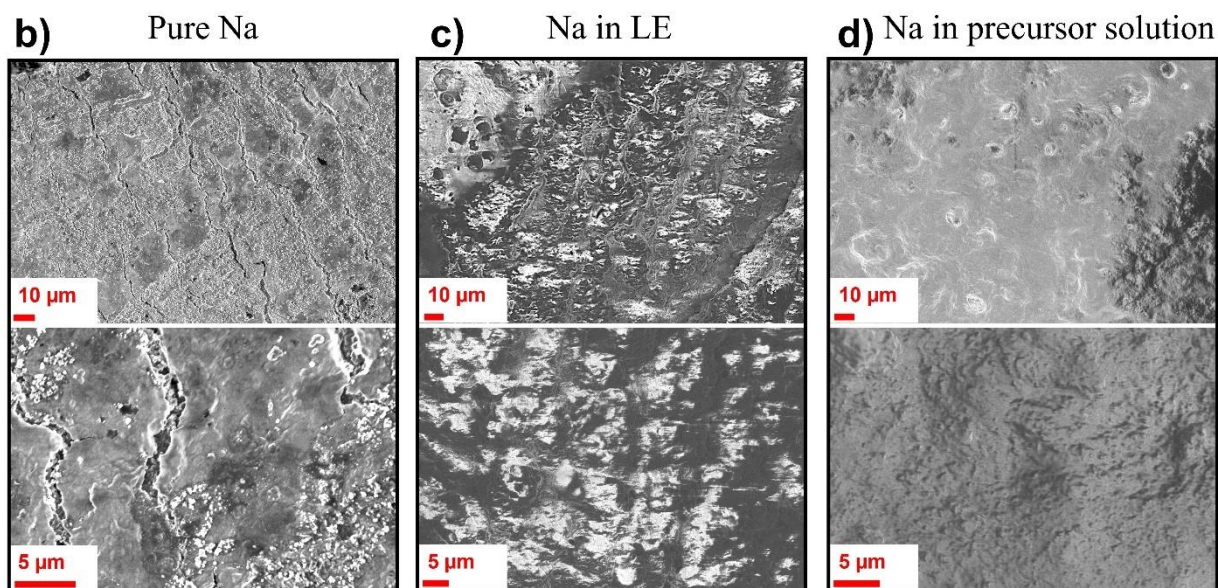
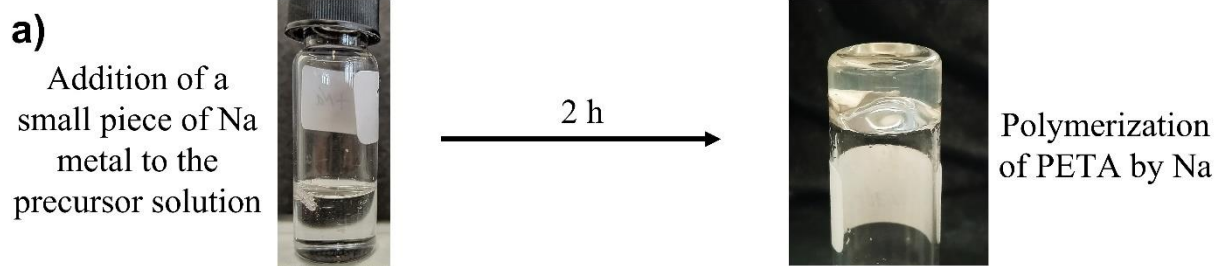


Figure S11: a) Visual images of the reaction between a Na anode and the precursor solution. Left: Na metal placed inside the precursor solution; right: polymerized gel phase. SEMs of a sodium anode b) freshly prepared, c) soaked in a liquid electrolyte, d) soaked in a precursor solution.

A piece of Na metal placed into the precursor solution (LE+PETA) initiates the polymerization from the Na surface resulting in gel formation.

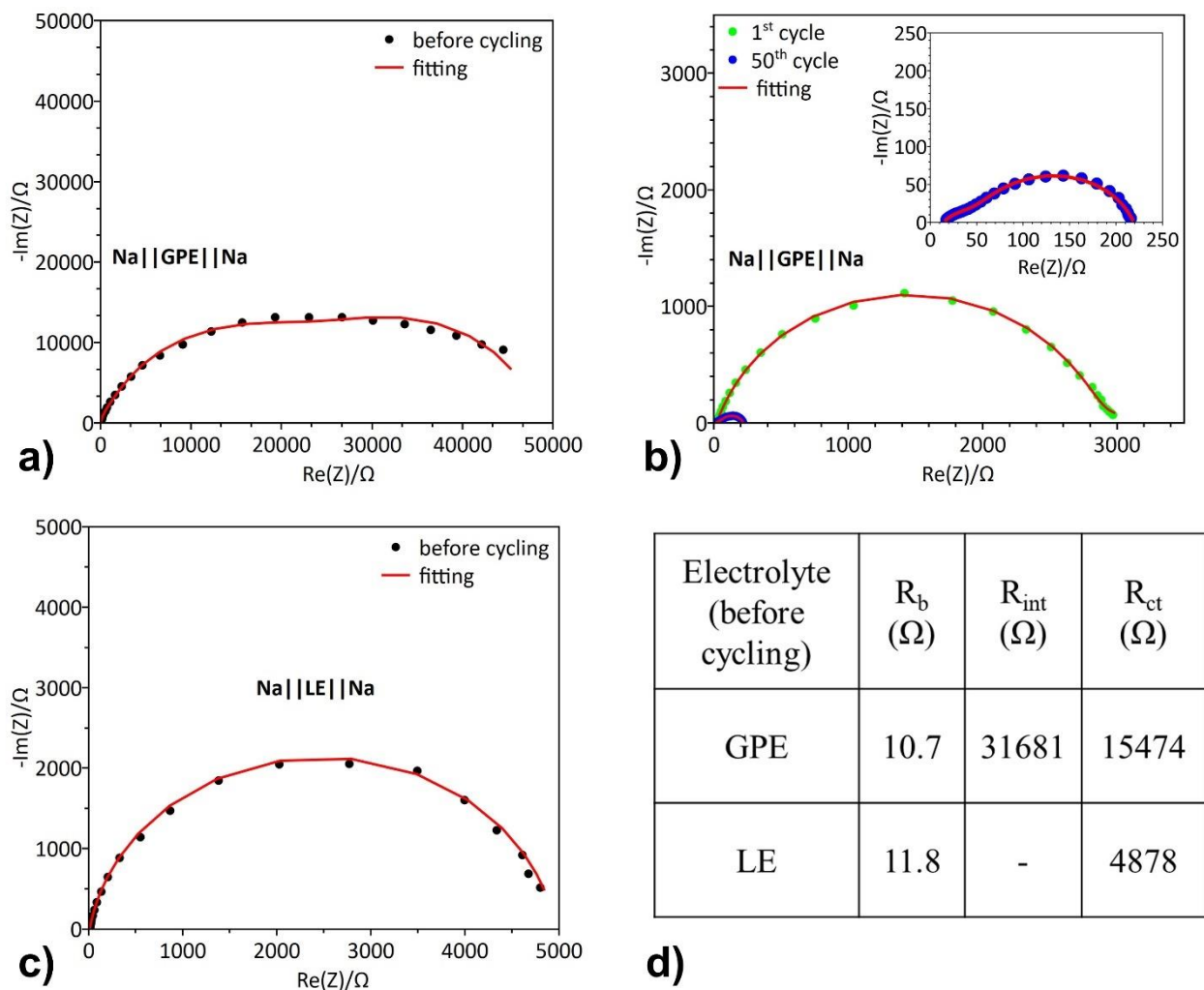


Figure S12: Impedance spectroscopy of a symmetric Na||Na cell containing a GPE. a) Before cycling (black); b) after 1st (green) and 50th (blue) cycling; c) impedance of a Na||Na cell with an LE (black); d) resistance values of a Na||Na cell with a GPE and an LE before cycling. (fitting curve – red).

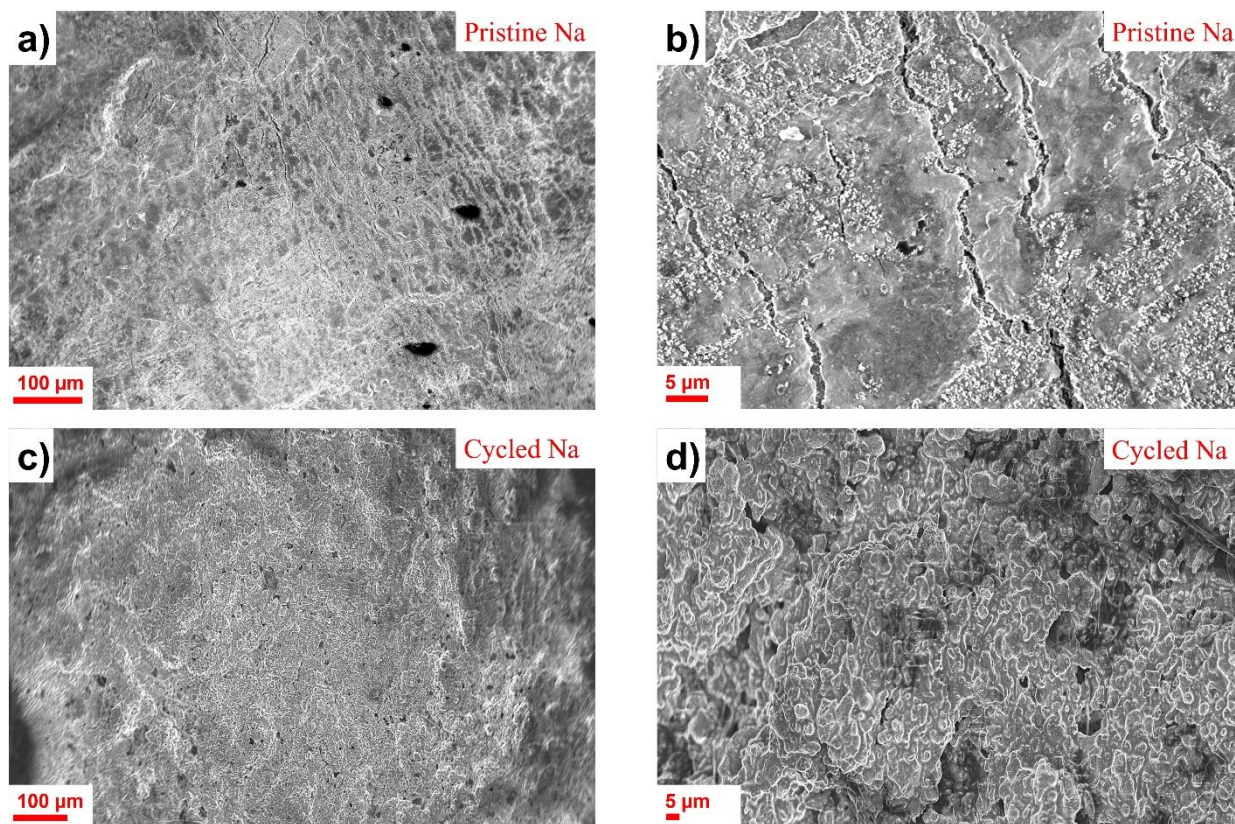


Figure S13: SEM images of a Na metal surface. a,b) Pristine Na; c,d) after 450 h of cycling in a symmetrical Na||Na cell.

SEM analysis revealed smooth and agglomerated Na particles, resembling a moss-covered surface, but no formation of dendrite needles. Moreover, the glass fiber-containing GPE was bound to the Na metal surface due to good interfacial contact. Consequently, the glass fiber separator filaments are always visible in the SEM images.

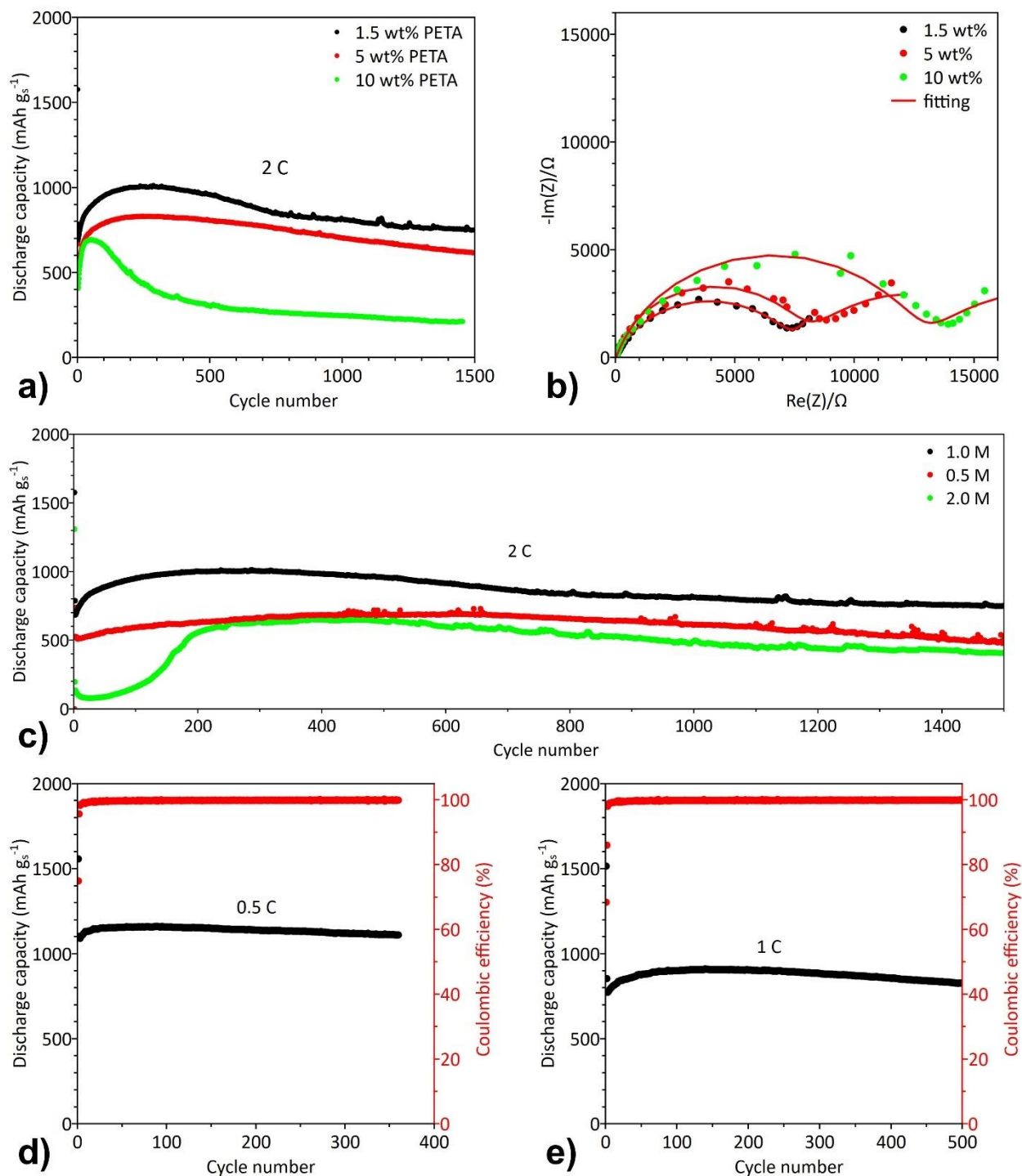


Figure S14: Electrochemical performance of a GPE under various conditions. Varying monomer content in the precursor solution, a) galvanostatic cycling of a GPE in a Na-SPAN full cell at 2 C; b) PEIS of a freshly prepared Na-SPAN full cell; c) long-term cycling of a GPE-containing Na-SPAN full cell with different salt concentration (0.5, 1, and 2 M); Galvanostatic cycle stability of a GPE (1.5 wt.%, standard) at d) 0.5 C and e) 1 C.

Table S4: Consolidated PEIS results from Figure S13b.

Monomer wt.% in the precursor solution	R_b	R_{SEI}	R_{ct}
1.5	10.2	4183	7606
5	12.5	7862	9224
10	24.0	9854	12848

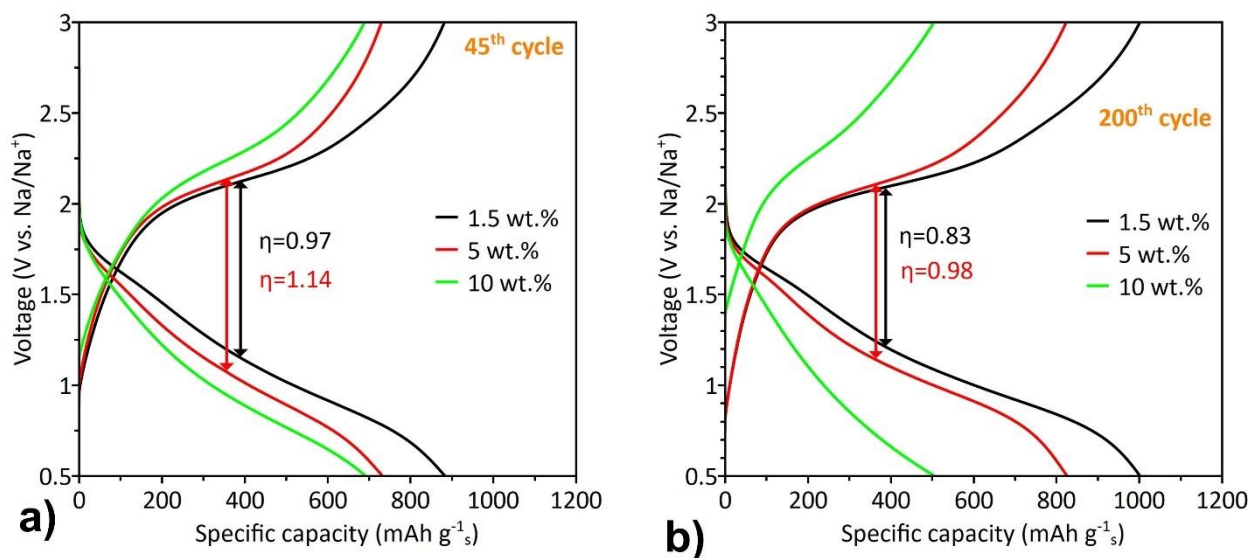


Figure S15: Comparison of the voltage profiles of a GPE prepared from various PETA concentrations, cycled at 2 C. a) 45th cycle; and b) 200th cycle.

The cell with 1.5 wt.% PETA exhibited low overpotential, which was further reduced after the 200th cycle. By contrast, cells containing 5 wt.% PETA showed an increased overpotential due to the thick interfacial layer.

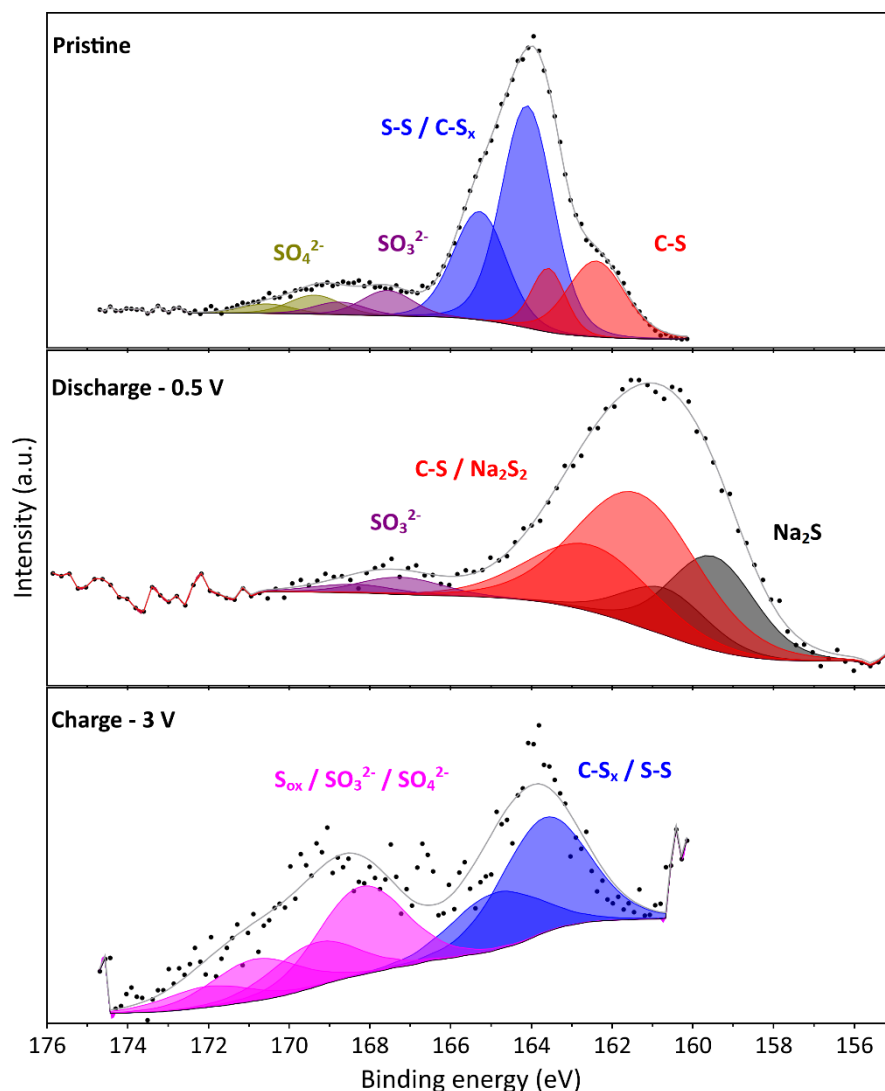


Figure S16: Sulfur S 2p *ex situ* XPS spectra of SPAN cathodes cycled with a GPE. Top to bottom: pristine, discharged to 0.5 V and charged to 3 V.

Cells were stopped at the desired state of charge/discharge, after which the cathode was characterized by XPS. XPS measurements were carried out on a Thermo VG Thetaprobe system (Thermo Fisher Scientific, USA), employing monochromatic Al K_{α} / X-ray radiation (1486.7 eV) produced with an electrical power of 100 W. The X-ray spot size on the sample was about 400 μm in diameter. A flood gun was employed to compensate for possible surface charging. No further correction of the peak positions was conducted. Survey spectra were recorded with a pass energy of 200 eV and more detailed spectra of single elemental peaks were measured in the snap scan mode.

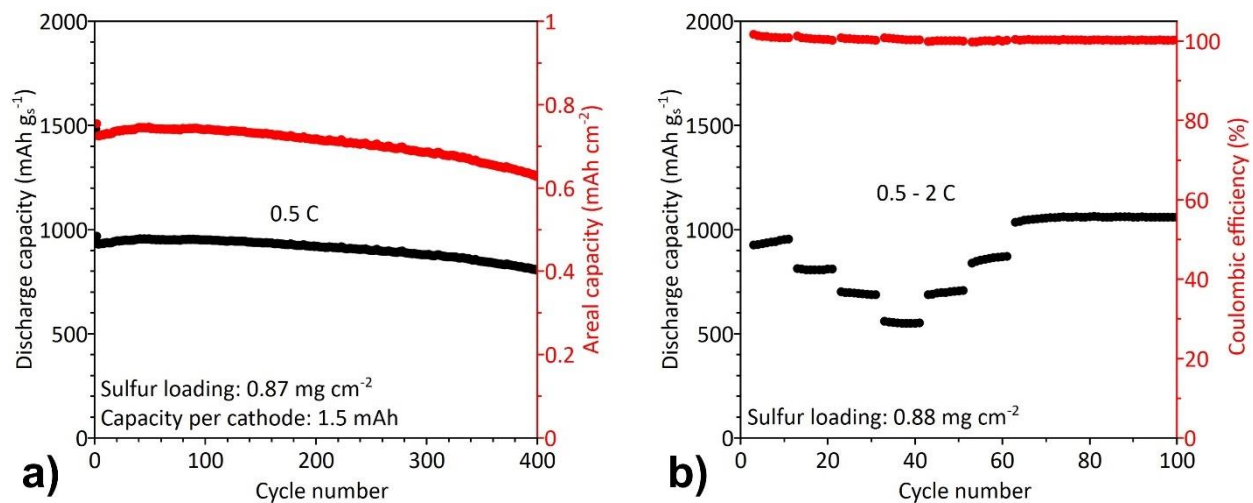


Figure S17: Galvanostatic testing of a GPE with a sulfur loading of 0.78 mg cm⁻². a) Cycling at 0.5 C; b) rate performance between 0.5 to 2 C.

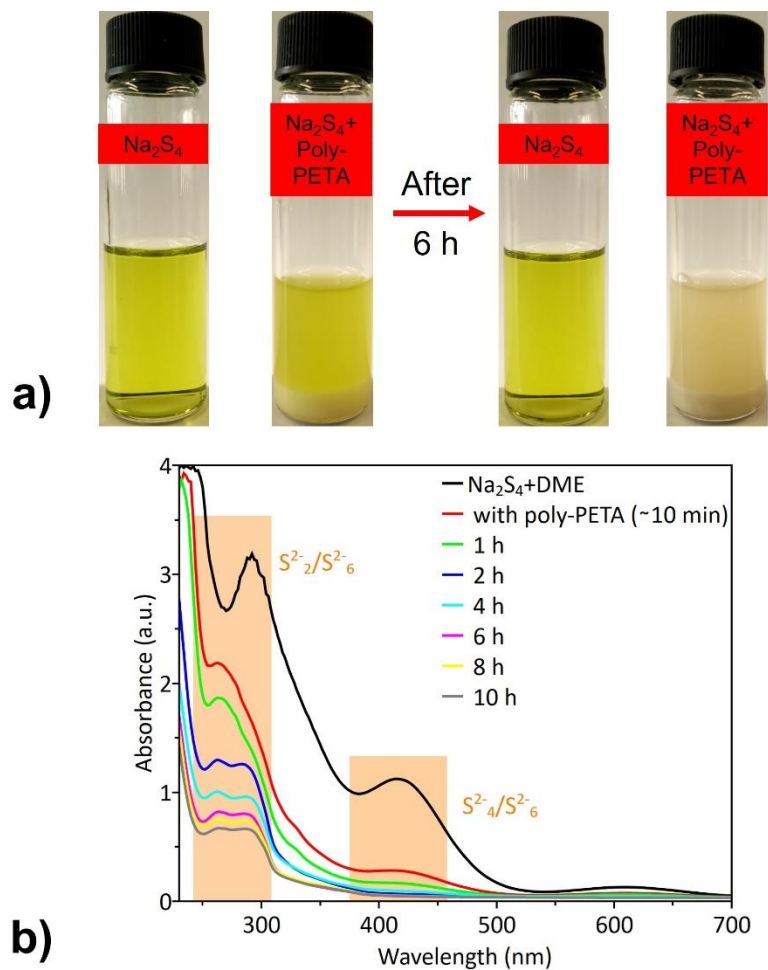


Figure S18: Absorption capability of poly-PETA. a) Digital picture of the adsorption of Na_2S_4 by poly-PETA; b) UV absorption spectra of a Na_2S_4 solution in DME and of a solution of Na_2S_4 + poly-PETA in DME recorded at various time intervals.

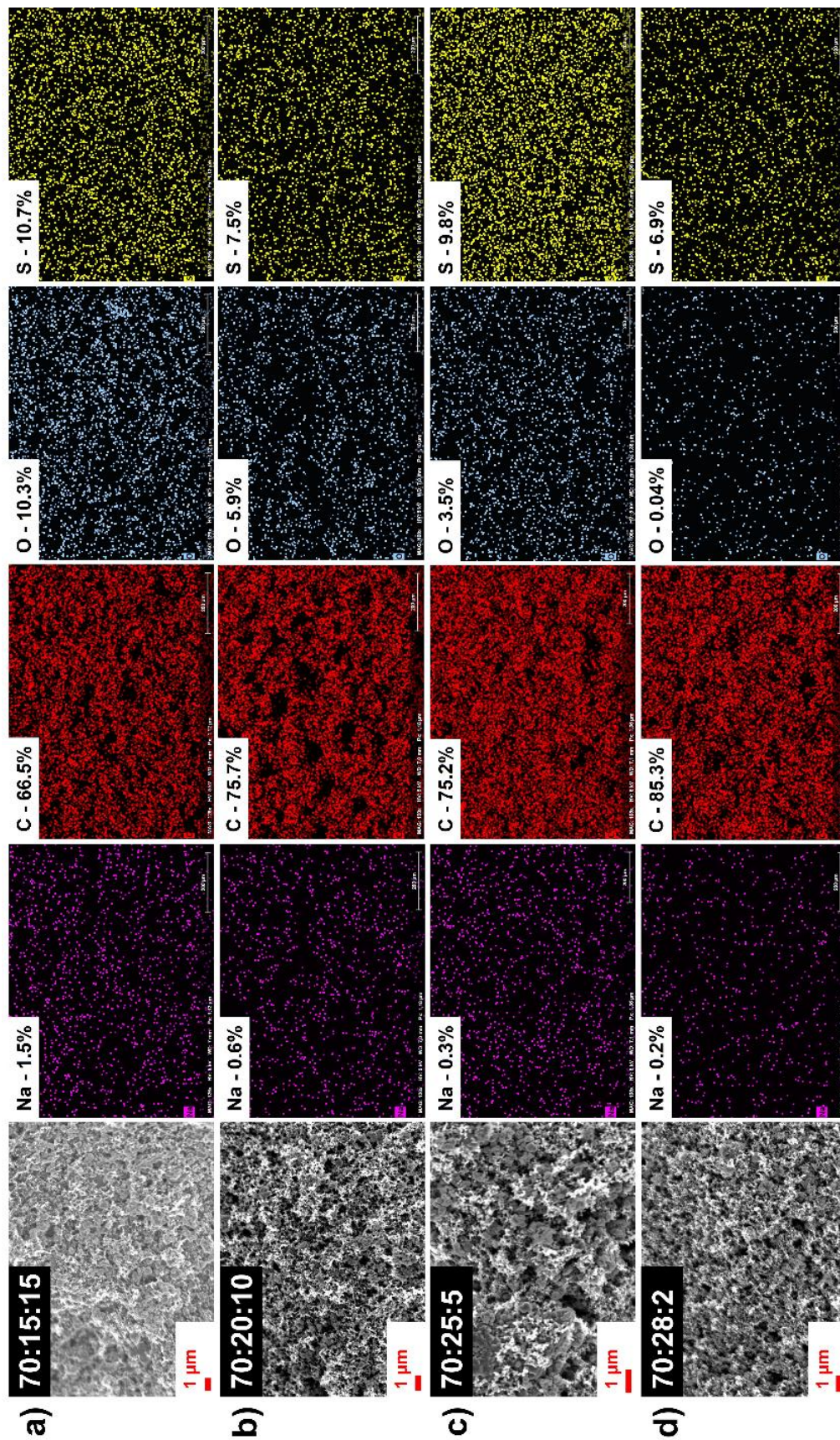


Figure S19: SEM and EDX images of an SPAN cathode containing different amounts of the binder. a) 15 wt.%; b) 10 wt.%; c) 5 wt.%; and d) 2 wt. %.

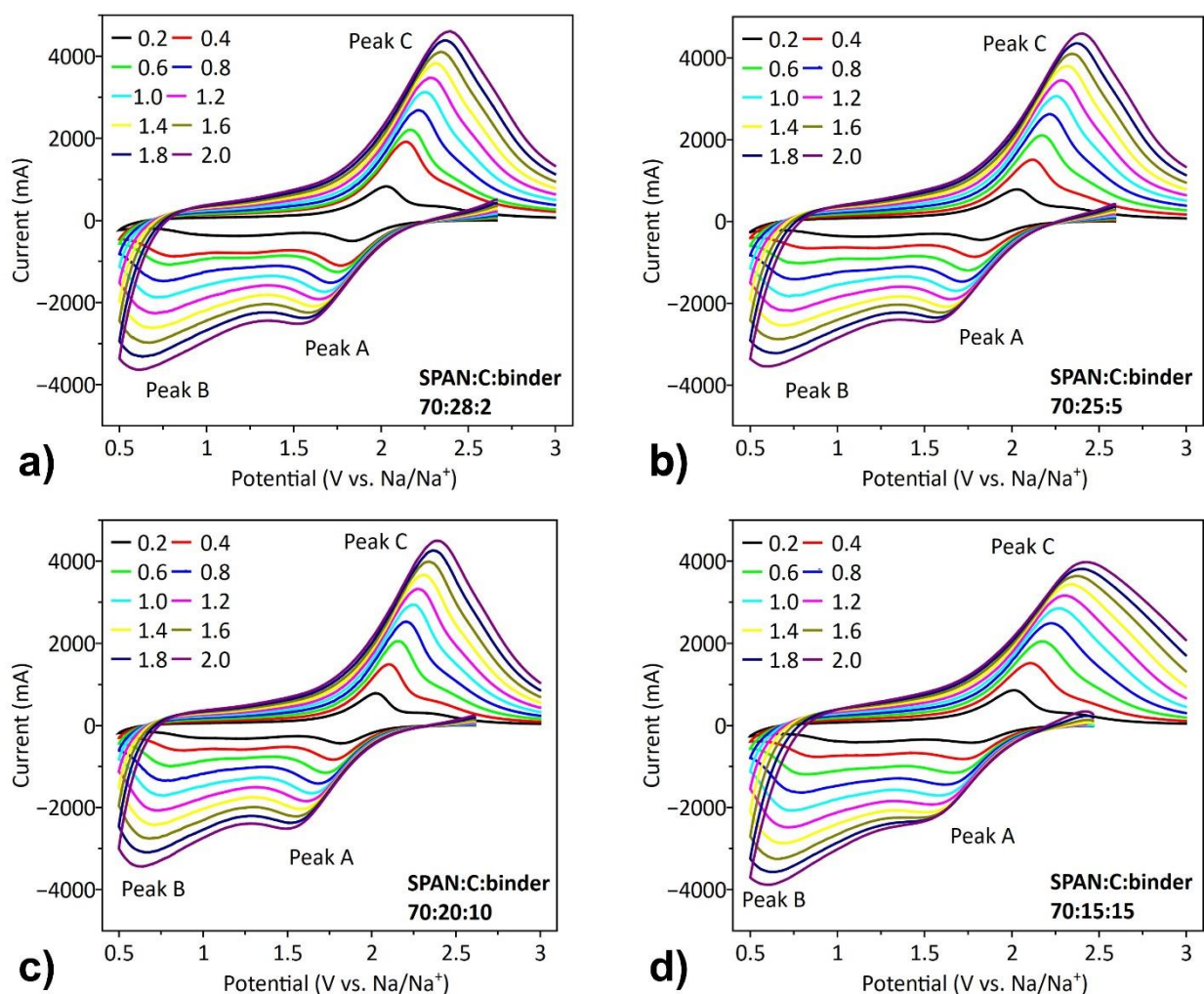


Figure S20: CV of a GPE-based SPAN cathode containing different amounts of the binder at different scan rates. a) 2 wt.%; b) 5 wt.%; c) 10 wt.%; d) 15 wt.% binder.

Table S5: Main anodic to cathodic peak potential difference (peak A – peak C, overpotential).

Cathode composition (all wt.%)	Overpotential (ΔV , peak C – peak A)
70:28:2	0.264 V
70:25:5	0.273 V
70:20:10	0.272 V
70:15:15	0.317 V

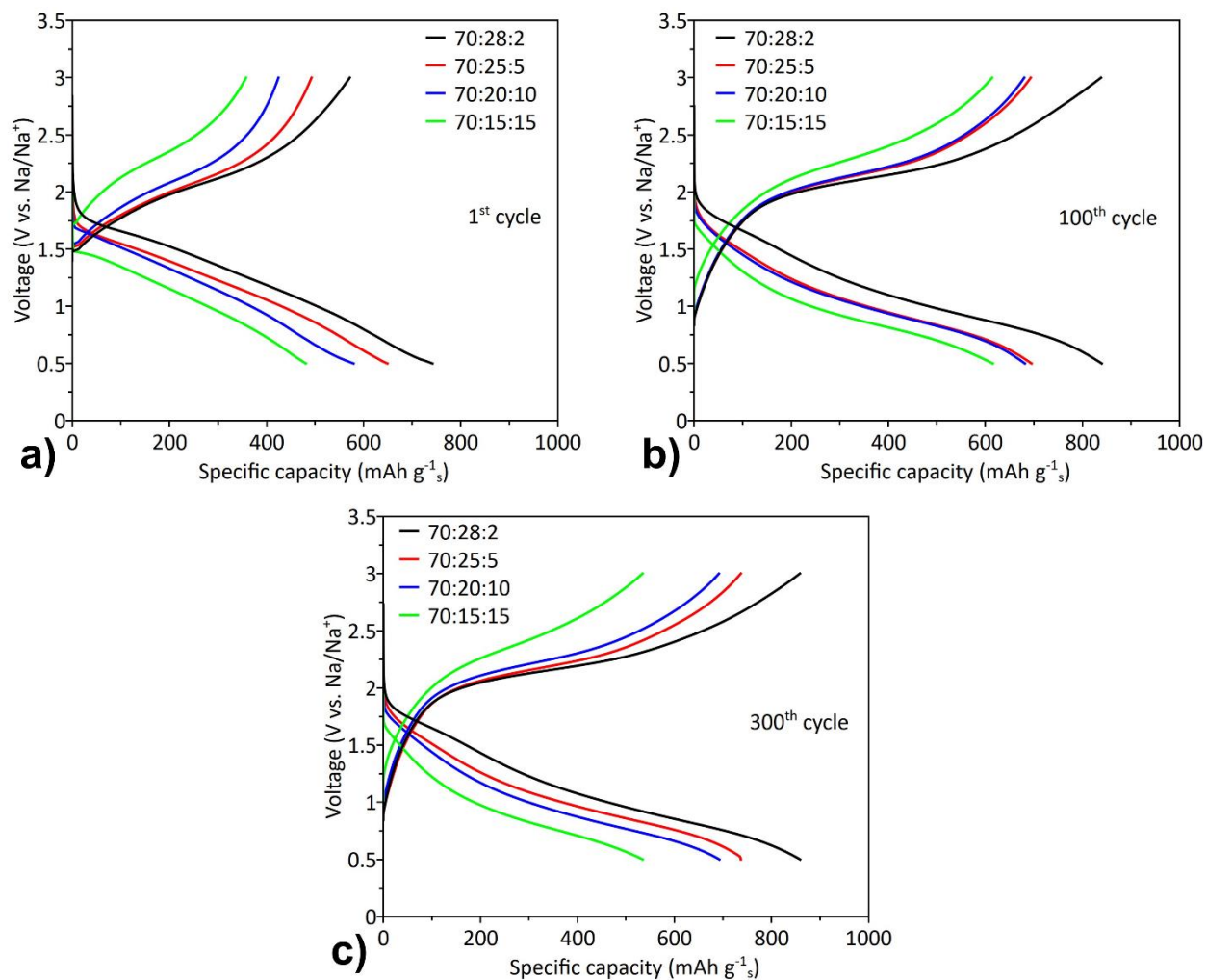


Figure S21: Voltage vs. specific capacity profiles of an SPAN cathode with 2, 5, 10, and 15 wt.% binder. a) 1st cycle; b) 100th cycle; c) 300th cycle.

Table S6: Comparison of the investigated liquid and gel polymer electrolytes for Na-S systems.

Electrolyte	Cathode	Initial capacity mAh g ⁻¹	Discharge capacity, mAh g ⁻¹ (Cycle life)	Current density, mA cm ⁻²	Ionic conductivity, mS cm ⁻¹ (25 °C)	Refs.
NaTFSI + TMP + FEC	SPAN	-	788 (300)	1 C	6	[5]
NaTFSI/InI ₃ + PC + FEC	S/MPCF	-	581 (500)	1 C	1.95	[6]
NaClO ₄ + TEGDME + FEC	S/C	-	587 (200)	200 mA g ⁻¹	-	[7]
NaFSI + DME + TTE	S/C/ CNT	922	675 (300)	0.1 C	1.98	[8]
NaClO ₄ /SiO ₂ -IL-CO ₄ + EC + PC	MCPS/C	866	600 (100)	0.5 C	□0.3	[9]
PVDF/NaTf /TEGDME	S/C	489	40 (20)	0.144	0.51	[10]
PVDF- HFP/NaTf/ TEGDME	S/C	392	36 (20)	0.288	-	[11]
PVDF- HFP/EMITf /NaTf + EC + PC	S/C	267	-	7.4	8.4	[12]
PVDF- HFP/SiO ₂ / NaTf + EC+ PC	S/C	165	21 (8)	-	2.5	[13]

PAN-NFM/NaTf/PEGDME	S/C	775	500 (40)	80 mA g ⁻¹	0.6	[14]
PVDF-HFP/NaTf/EMITf	S/C	240	150 (10)	-	5.7	[15]
GF/PETEA-THEICTA/NaTFSI + PC + FEC	Poly(S-PETEA)/S	877	736 (100)	0.1 C	3.9	[16]
NaTPB/PETA + PC + FEC	SPAN	1577 (0.3 C)	644 (2500)	2 C	2.33	Our work

References

- [1] G. Hoti, F. Caldera, C. Cecone, A. Rubin Pedrazzo, A. Anceschi, S. Appleton, Y. Khazaei Monfared, F. Trotta, *Materials* **2021**, *14*, 478.
- [2] A. M. Herrera-González, M. Caldera-Villalobos, A. A. Pérez-Mondragón, C. E. Cuevas-Suárez, J. A. González-López, *J. Chem. Educ.* **2019**, *96*, 1786-1789.
- [3] K. M. Abraham, Z. Jiang, B. Carroll, *Chem. Mater.* **1997**, *9*, 1978-1988.
- [4] J. Evans, C. A. Vincent, P. G. Bruce, *Polymer* **1987**, *28*, 2324-2328.
- [5] J. Wu, J. Liu, Z. Lu, K. Lin, Y.-Q. Lyu, B. Li, F. Ciucci, J.-K. Kim, *Energy Storage Mater.* **2019**, *23*, 8-16.
- [6] X. Xu, D. Zhou, X. Qin, K. Lin, F. Kang, B. Li, D. Shanmukaraj, T. Rojo, M. Armand, G. Wang, *Nat. Commun.* **2018**, *9*, 3870.
- [7] D. Liu, Z. Li, X. Li, X. Chen, Z. Li, L. Yuan, Y. Huang, *ACS Appl. Mater. Interfaces* **2022**, *14*, 6658-6666.
- [8] J. He, A. Bhargav, W. Shin, A. Manthiram, *J. Am. Chem. Soc.* **2021**, *143*, 20241-20248.
- [9] S. Wei, S. Xu, A. Agrawal, S. Choudhury, Y. Lu, Z. Tu, L. Ma, L. A. Archer, *Nat. Commun.* **2016**, *7*, 11722.
- [10] C.-W. Park, J.-H. Ahn, H.-S. Ryu, K.-W. Kim, H.-J. Ahn, *Electrochem. Solid-State Lett.* **2006**, *9*, a123-a125.
- [11] J.-S. Kim, H.-J. Ahn, I.-P. Kim, K.-W. Kim, J.-H. Ahn, C.-W. Park, H.-S. Ryu, *J. Solid State Electrochem.* **2008**, *12*, 861-865.
- [12] D. Kumar, *Solid State Ion.* **2018**, *318*, 65-70.
- [13] D. Kumar, M. Suleman, S. A. Hashmi, *Solid State Ion.* **2011**, *202*, 45-53.
- [14] D.-H. Lim, M. Agostini, J.-H. Ahn, A. Matic, *Energy Technol.* **2018**, *6*, 1214-1219.

- [15] D. Kumar, D. K. Kanchan, *J. Energy Storage* **2019**, 22, 44-49.
- [16] D. Zhou, Y. Chen, B. Li, H. Fan, F. Cheng, D. Shanmukaraj, T. Rojo, M. Armand, G. Wang, *Angew. Chem. Int. Ed.* **2018**, 57, 10168-10172.

5 References

- [1] O. Dimitriev, *Sustain. Energy* **2013**, *1*, 1-6.
- [2] U. S. E. I. Administration, in *World coal-fired generation declines through 2030 in the Reference case, but it remains a significant part of the worldwide generation mix*, **2021**, pp. 1-40.
- [3] Y. Ding, Z. P. Cano, A. Yu, J. Lu, Z. Chen, *Electrochem. Energy Rev.* **2019**, *2*, 1-28.
- [4] P. G. Bruce, S. A. Freunberger, L. J. Hardwick, J.-M. Tarascon, *Nat. Mater.* **2012**, *11*, 19-29.
- [5] P. Breeze, in *Power Generation Technologies (Third Edition)* (Ed.: P. Breeze), Newnes, **2019**, pp. 219-249.
- [6] B. Dunn, H. Kamath, J.-M. Tarascon, *Science* **2011**, *334*, 928-935.
- [7] A. Volta, *Trans* **1800**, *2*, 430.
- [8] G. Leclanche, *Compt. Rend* **1866**, *83*, 54-56.
- [9] C. A. Vincent, *Modern Batteries : an introduction to electrochemical power sources*, 2nd ed., Butterworth-Heinemann, Oxford, **1997**.
- [10] Y. Liang, C.-Z. Zhao, H. Yuan, Y. Chen, W. Zhang, J.-Q. Huang, D. Yu, Y. Liu, M.-M. Titirici, Y.-L. Chueh, H. Yu, Q. Zhang, *InfoMat* **2019**, *1*, 6-32.
- [11] B. R. Thomas, *Linden's Handbook of Batteries, Fourth Edition*, 4th ed., McGraw-Hill Education, New York, **2011**.
- [12] H. Wang, D. Yu, C. Kuang, L. Cheng, W. Li, X. Feng, Z. Zhang, X. Zhang, Y. Zhang, *Chem* **2019**, *5*, 313-338.
- [13] P. Adelhelm, P. Hartmann, C. L. Bender, M. Busche, C. Eufinger, J. Janek, *Beilstein J. Nanotechnol.* **2015**, *6*, 1016-1055.
- [14] M. Armand, P. Axmann, D. Bresser, M. Copley, K. Edström, C. Ekberg, D. Guyomard, B. Lestriez, P. Novák, M. Petranikova, W. Porcher, S. Trabesinger, M. Wohlfahrt-Mehrens, H. Zhang, *J. Power Sources* **2020**, *479*, 228708.
- [15] J. Verma, D. Kumar, *Nanoscale Advances* **2021**, *3*, 3384-3394.
- [16] B. L. Ellis, L. F. Nazar, *Curr. Opin. Solid State Mater. Sci.* **2012**, *16*, 168-177.
- [17] C. Vaalma, D. Buchholz, M. Weil, S. Passerini, *Nat. Rev. Mater.* **2018**, *3*, 18013.
- [18] J. F. Peters, A. Peña Cruz, M. Weil, *Batteries* **2019**, *5*, 10.
- [19] M. Okoshi, Y. Yamada, A. Yamada, H. Nakai, *J. Electrochem. Soc.* **2013**, *160*, A2160-A2165.
- [20] N. Yabuuchi, K. Kubota, M. Dahbi, S. Komaba, *Chem. Rev.* **2014**, *114*, 11636-11682.
- [21] K. M. Abraham, *J. Phys. Chem. Lett.* **2015**, *6*, 830-844.
- [22] K. M. Abraham, *ACS Energy Lett.* **2020**, *5*, 3544-3547.
- [23] A. Manthiram, *Nat. Commun.* **2020**, *11*, 1550.
- [24] R. V. Chebiam, A. M. Kannan, F. Prado, A. Manthiram, *Electrochem. Commun.* **2001**, *3*, 624-627.
- [25] S. Venkatraman, Y. Shin, A. Manthiram, *Electrochem. Solid-State Lett.* **2003**, *6*.
- [26] R. J. Gummow, A. de Kock, M. M. Thackeray, *Solid State Ion.* **1994**, *69*, 59-67.
- [27] A. Padhi, K. S. Nanjundaswamy, J. Goodenough, *J. Electrochem. Soc.* **1997**, *144*, 1188-1194.
- [28] C. Masquelier, L. Croguennec, *Chem. Rev.* **2013**, *113*, 6552-6591.
- [29] N. Nitta, F. Wu, J. T. Lee, G. Yushin, *Mater. Today* **2015**, *18*, 252-264.
- [30] C. Delmas, J.-J. Braconnier, C. Fouassier, P. Hagenmuller, *Solid State Ion.* **1981**, *3-4*, 165-169.
- [31] J.-Y. Hwang, S.-T. Myung, Y.-K. Sun, *Chem. Soc. Rev.* **2017**, *46*, 3529-3614.
- [32] E. Jónsson, P. Johansson, *Phys. Chem. Chem. Phys.* **2012**, *14*, 10774-10779.

5. References

- [33] W. Xu, J. Wang, F. Ding, X. Chen, E. Nasybulin, Y. Zhang, J.-G. Zhang, *Energy Environ. Sci.* **2014**, *7*, 513-537.
- [34] M. Winter, J. O. Besenhard, M. E. Spahr, P. Novák, *Adv. Mater.* **1998**, *10*, 725-763.
- [35] D. Aurbach, B. Markovsky, I. Weissman, E. Levi, Y. Ein-Eli, *Electrochim. Acta* **1999**, *45*, 67-86.
- [36] J. R. Dahn, T. Zheng, Y. Liu, J. S. Xue, *Science* **1995**, *270*, 590-593.
- [37] J.-F. Colin, V. Godbole, P. Novák, *Electrochem. Commun.* **2010**, *12*, 804-807.
- [38] D. A. Stevens, J. Dahn, *J. Electrochem. Soc.* **2000**, *147*.
- [39] R. Raccichini, A. Varzi, S. Passerini, B. Scrosati, *Nat. Mater.* **2015**, *14*, 271-279.
- [40] Z. Wang, S. M. Selbach, T. Grande, *RSC Adv.* **2014**, *4*, 4069-4079.
- [41] S. S. Zhang, T. R. Jow, K. Amine, G. L. Henriksen, *J. Power Sources* **2002**, *107*, 18-23.
- [42] J. Wang, Y. Yamada, K. Sodeyama, E. Watanabe, K. Takada, Y. Tateyama, A. Yamada, *Nat. Energy* **2018**, *3*, 22-29.
- [43] S. Brutti, E. Simonetti, M. De Francesco, A. Sarra, A. Paolone, O. Palumbo, S. Fantini, R. Lin, A. Falgayrat, H. Choi, M. Kuenzel, S. Passerini, G. B. Appetecchi, *J. Power Sources* **2020**, *479*, 228791.
- [44] L. G. Chagas, S. Jeong, I. Hasa, S. Passerini, *ACS Appl. Mater. Interfaces* **2019**, *11*, 22278-22289.
- [45] W. Li, J. R. Dahn, D. S. Wainwright, *Science* **1994**, *264*, 1115-1118.
- [46] W. Li, F. Zhang, X. Xiang, X. Zhang, *ChemElectroChem* **2017**, *4*, 2870-2876.
- [47] F. Baskoro, H. Q. Wong, H.-J. Yen, *ACS Appl. Energy Mater.* **2019**, *2*, 3937-3971.
- [48] L. Qiao, X. Judez, T. Rojo, M. Armand, H. Zhang, *J. Electrochem. Soc.* **2020**, *167*, 070534.
- [49] J. Serra Moreno, M. Armand, M. B. Berman, S. G. Greenbaum, B. Scrosati, S. Panero, *J. Power Sources* **2014**, *248*, 695-702.
- [50] S. Choudhury, S. Stalin, D. Vu, A. Warren, Y. Deng, P. Biswal, L. A. Archer, *Nat. Commun.* **2019**, *10*, 4398.
- [51] C. Cao, Z.-B. Li, X.-L. Wang, X.-B. Zhao, W.-Q. Han, *Front. Energy Res.* **2014**, *2*.
- [52] Y. Wang, S. Song, C. Xu, N. Hu, J. Molenda, L. Lu, *Nano Mater. Sci.* **2019**, *1*, 91-100.
- [53] K. Xu, *Chem. Rev.* **2014**, *114*, 11503-11618.
- [54] K. Naoi, E. Iwama, N. Ogihara, Y. Nakamura, H. Segawa, Y. Ino, *J. Electrochem. Soc.* **2009**, *156*, a272-a276.
- [55] K. Naoi, E. Iwama, Y. Honda, F. Shimodate, *J. Electrochem. Soc.* **2010**, *157*, a190-a195.
- [56] M. Lee, J. Hong, J. Lopez, Y. Sun, D. Feng, K. Lim, W. C. Chueh, M. F. Toney, Y. Cui, Z. Bao, *Nat. Energy* **2017**, *2*, 861-868.
- [57] Q. Li, J. Chen, L. Fan, X. Kong, Y. Lu, *Green Energy Environ.* **2016**, *1*, 18-42.
- [58] Z. Lin, Q. Xia, W. Wang, W. Li, S. Chou, *InfoMat* **2019**, *1*, 376-389.
- [59] A. Hammami, N. Raymond, M. Armand, *Nature* **2003**, *424*, 635-636.
- [60] K. Xu, *Chem. Rev.* **2004**, *104*, 4303-4418.
- [61] A. V. Plakhotnyk, L. Ernst, R. Schmutzler, *J. Fluorine Chem.* **2005**, *126*, 27-31.
- [62] T. Ohzuku, R. J. Brodd, *J. Power Sources* **2007**, *174*, 449-456.
- [63] B. Scrosati, J. Garche, *J. Power Sources* **2010**, *195*, 2419-2430.
- [64] J. B. Goodenough, Y. Kim, *Chem. Mater.* **2010**, *22*, 587-603.
- [65] M. Gao, H. Li, L. Xu, Q. Xue, X. Wang, Y. Bai, C. Wu, *J. Energy Chem.* **2021**, *59*, 666-687.

- [66] X. Wang, Z. Wen, Y. Liu, X. Wu, *Electrochim. Acta* **2009**, *54*, 4662-4667.
- [67] H. Wu, G. Zheng, N. Liu, T. J. Carney, Y. Yang, Y. Cui, *Nano Lett.* **2012**, *12*, 904-909.
- [68] M. S. Whittingham, *Proc. IEEE* **2012**, *100*, 1518-1534.
- [69] X.-B. Cheng, R. Zhang, C.-Z. Zhao, Q. Zhang, *Chem. Rev.* **2017**, *117*, 10403-10473.
- [70] X. Shen, X.-Q. Zhang, F. Ding, J.-Q. Huang, R. Xu, X. Chen, C. Yan, F.-Y. Su, C.-M. Chen, X. Liu, Q. Zhang, *Energy Mater. Adv.* **2021**, *2021*, 1205324.
- [71] K. M. Abraham, Z. Jiang, *J. Electrochem. Soc.* **1996**, *143*, 1-5.
- [72] Y. Li, J. Lu, *ACS Energy Lett.* **2017**, *2*, 1370-1377.
- [73] K. Chen, D.-Y. Yang, G. Huang, X.-B. Zhang, *Acc. Chem. Res.* **2021**, *54*, 632-641.
- [74] E. Peled, D. Golodnitsky, H. Mazor, M. Goor, S. Avshalomov, *J. Power Sources* **2011**, *196*, 6835-6840.
- [75] N. Chawla, M. Safa, *Electronics* **2019**, *8*, 1201.
- [76] S. S. Zhang, *J. Power Sources* **2013**, *231*, 153-162.
- [77] Z. W. Seh, Y. Sun, Q. Zhang, Y. Cui, *Chem. Soc. Rev.* **2016**, *45*, 5605-5634.
- [78] K. Xi, S. Cao, X. Peng, C. Ducati, R. Vasant Kumar, A. K. Cheetham, *Chem. Commun.* **2013**, *49*, 2192-2194.
- [79] K. Xi, P. R. Kidambi, R. Chen, C. Gao, X. Peng, C. Ducati, S. Hofmann, R. V. Kumar, *Nanoscale* **2014**, *6*, 5746-5753.
- [80] T. Li, J. Xu, C. Wang, W. Wu, D. Su, G. Wang, *J. Alloys Compd.* **2019**, *792*, 797-817.
- [81] J. Wang, S. Yi, J. Liu, S. Sun, Y. Liu, D. Yang, K. Xi, G. Gao, A. Abdelkader, W. Yan, S. Ding, R. V. Kumar, *ACS Nano* **2020**, *14*, 9819-9831.
- [82] R. Li, X. Sun, Y. Huang, C. Wei, G. Liang, H. Hu, J. Zou, Q. He, *J. Nanopart. Res.* **2019**, *21*, 236.
- [83] C. Weller, J. Pampel, S. Dörfler, H. Althues, S. Kaskel, *Energy Technol.* **2019**, *7*, 1900625.
- [84] Y.-X. Wang, B. Zhang, W. Lai, Y. Xu, S.-L. Chou, H.-K. Liu, S.-X. Dou, *Adv. Energy Mater.* **2017**, *7*, 1602829.
- [85] J. Gao, M. A. Lowe, Y. Kiya, H. D. Abruña, *J. Phys. Chem. C* **2011**, *115*, 25132-25137.
- [86] J. Zhou, Y. Guo, C. Liang, L. Cao, H. Pan, J. Yang, J. Wang, *Chem. Commun.* **2018**, *54*, 5478-5481.
- [87] T. Yim, M.-S. Park, J.-S. Yu, K. J. Kim, K. Y. Im, J.-H. Kim, G. Jeong, Y. N. Jo, S.-G. Woo, K. S. Kang, I. Lee, Y.-J. Kim, *Electrochim. Acta* **2013**, *107*, 454-460.
- [88] Y. Yang, G. Zheng, Y. Cui, *Chem. Soc. Rev.* **2013**, *42*, 3018-3032.
- [89] D. Liu, Z. Li, X. Li, Z. Cheng, L. Yuan, Y. Huang, *ChemPhysChem* **2019**, *20*, 3164-3176.
- [90] A. Manthiram, X. Yu, *Small* **2015**, *11*, 2108-2114.
- [91] Y.-X. Wang, W.-H. Lai, S.-L. Chou, H.-K. Liu, S.-X. Dou, *Adv. Mater.* **2020**, *32*, 1903952.
- [92] C. Lai, X. P. Gao, B. Zhang, T. Y. Yan, Z. Zhou, *J. Phys. Chem. C* **2009**, *113*, 4712-4716.
- [93] W.-J. Li, C. Han, S.-L. Chou, J.-Z. Wang, Z. Li, Y.-M. Kang, H.-K. Liu, S.-X. Dou, *Chem. Eur. J.* **2016**, *22*, 590-597.
- [94] L. Fan, R. Ma, Y. Yang, S. Chen, B. Lu, *Nano Energy* **2016**, *28*, 304-310.
- [95] J. L. Wang, J. Yang, J. Y. Xie, N. X. Xu, Y. Li, *Electrochem. Commun.* **2002**, *4*, 499-502.
- [96] J. Zhu, J. Zou, H. Cheng, Y. Gu, Z. Lu, *Green Energy Environ.* **2019**, *4*, 345-359.

5. References

- [97] X. Wang, Y. Qian, L. Wang, H. Yang, H. Li, Y. Zhao, T. Liu, *Adv. Funct. Mater.* **2019**, *29*, 1902929.
- [98] S. Xin, L. Gu, N.-H. Zhao, Y.-X. Yin, L.-J. Zhou, Y.-G. Guo, L.-J. Wan, *J. Am. Chem. Soc.* **2012**, *134*, 18510-18513.
- [99] P. Du, W. Wei, Y. Dong, D. Liu, Q. Wang, Y. Peng, S. Chen, P. Liu, *Nanoscale* **2019**, *11*, 10097-10105.
- [100] J. Wang, J. Yang, J. Xie, N. Xu, *Adv. Mater.* **2002**, *14*, 963-965.
- [101] J. Wang, J. Yang, Y. Nuli, R. Holze, *Electrochem. Commun.* **2007**, *9*, 31-34.
- [102] M. Frey, R. K. Zenn, S. Warneke, K. Müller, A. Hintennach, R. E. Dinnebier, M. R. Buchmeiser, *ACS Energy Lett.* **2017**, *2*, 595-604.
- [103] J. Fanous, M. Wegner, J. Grimminger, Å. Andresen, M. R. Buchmeiser, *Chem. Mater.* **2011**, *23*, 5024-5028.
- [104] M. Hagen, D. Hanselmann, K. Ahlbrecht, R. Maça, D. Gerber, J. Tübke, *Adv. Energy Mater.* **2015**, *5*, 1401986.
- [105] S. Wei, L. Ma, K. E. Hendrickson, Z. Tu, L. A. Archer, *J. Am. Chem. Soc.* **2015**, *137*, 12143-12152.
- [106] C.-J. Huang, J.-H. Cheng, W.-N. Su, P. Partovi-Azar, L.-Y. Kuo, M.-C. Tsai, M.-H. Lin, S. Panahian Jand, T.-S. Chan, N.-L. Wu, P. Kaghazchi, H. Dai, P. M. Bieker, B.-J. Hwang, *J. Power Sources* **2021**, *492*, 229508.
- [107] M. Kleinberg, (Ed.: PacifiCorp), KEMA, Inc, **2016**, pp. 1-34.
- [108] Z. Wen, J. Cao, Z. Gu, X. Xu, F. Zhang, Z. Lin, *Solid State Ion.* **2008**, *179*, 1697-1701.
- [109] X. Lu, G. Xia, J. P. Lemmon, Z. Yang, *J. Power Sources* **2010**, *195*, 2431-2442.
- [110] F. R. Foulkes, P. T. Choi, *Can. J. Chem. Eng.* **1978**, *56*, 236-245.
- [111] A. V. Virkar, G. R. Miller, R. S. Gordon, *J. Am. Chem. Soc.* **1978**, *61*, 250-252.
- [112] G. E. Youngblood, G. R. Miller, R. S. Gordon, *Journ J. Am. Chem. Soc.* **1978**, *61*, 86-87.
- [113] N. Baffier, J. C. Badot, P. Colomban, *Mater. Res. Bull.* **1981**, *16*, 259-265.
- [114] J. Sudworth, A. Tiley, *Sodium Sulphur Battery*, Springer Science & Business Media, **1985**.
- [115] G. Nikiforidis, M. C. M. van de Sanden, M. N. Tsampas, *RSC Adv.* **2019**, *9*, 5649-5673.
- [116] D. Kumar, S. K. Rajouria, S. B. Kuhar, D. K. Kanchan, *Solid State Ion.* **2017**, *312*, 8-16.
- [117] R. Steudel, Y. Steudel, *Chem. Eur. J.* **2013**, *19*, 3162-3176.
- [118] X. Lu, B. W. Kirby, W. Xu, G. Li, J. Y. Kim, J. P. Lemmon, V. L. Sprenkle, Z. Yang, *Energy Environ. Sci.* **2013**, *6*, 299-306.
- [119] T. Oshima, M. Kajita, A. Okuno, *Int. J. Appl. Ceram. Technol.* **2004**, *1*, 269-276.
- [120] J. L. Sudworth, *J. Power Sources* **1984**, *11*, 143-154.
- [121] Z. Wen, Y. Hu, X. Wu, J. Han, Z. Gu, *Adv. Funct. Mater.* **2013**, *23*, 1005-1018.
- [122] F. Cheng, J. Liang, Z. Tao, J. Chen, *Adv. Mater.* **2011**, *23*, 1695-1715.
- [123] C.-W. Park, J.-H. Ahn, H.-S. Ryu, K.-W. Kim, H.-J. Ahn, *Electrochem. Solid-State Lett.* **2006**, *9*.
- [124] D. Kumar, D. K. Kanchan, S. Kumar, K. Mishra, *Mater. Sci. Technol.* **2019**, *2*, 117-129.
- [125] X. Yu, A. Manthiram, *ChemElectroChem* **2014**, *1*, 1275-1280.
- [126] Y. Wang, Y. Zhang, H. Cheng, Z. Ni, Y. Wang, G. Xia, X. Li, X. Zeng, *Molecules* **2021**, *26*, 1535.
- [127] R. Carter, L. Oakes, A. Douglas, N. Muralidharan, A. P. Cohn, C. L. Pint, *Nano Lett.* **2017**, *17*, 1863-1869.
- [128] S. Xin, Y.-X. Yin, Y.-G. Guo, L.-J. Wan, *Adv. Mater.* **2014**, *26*, 1261-1265.

- [129] P. D. James Speight, *Lange's Handbook of Chemistry, Sixteenth Edition*, 16th ed. / ed., McGraw-Hill Education, New York, **2005**.
- [130] B. Zhang, C. Lai, Z. Zhou, X. P. Gao, *Electrochim. Acta* **2009**, *54*, 3708-3713.
- [131] H. Momida, T. Yamashita, T. Oguchi, *J. Phys. Soc. Jpn.* **2014**, *83*, 124713.
- [132] B.-W. Zhang, T. Sheng, Y.-D. Liu, Y.-X. Wang, L. Zhang, W.-H. Lai, L. Wang, J. Yang, Q.-F. Gu, S.-L. Chou, H.-K. Liu, S.-X. Dou, *Nat. Commun.* **2018**, *9*, 4082.
- [133] V. W.-h. Lau, I. Moudrakovski, J. Yang, J. Zhang, Y.-M. Kang, *Angew. Chem. Int. Ed.* **2020**, *59*, 4023-4034.
- [134] Y. Diao, K. Xie, S. Xiong, X. Hong, *J. Power Sources* **2013**, *235*, 181-186.
- [135] X. Yu, A. Manthiram, *Adv. Energy Mater.* **2015**, *5*, 1500350.
- [136] H. Liu, W.-H. Lai, Q. Yang, Y. Lei, C. Wu, N. Wang, Y.-X. Wang, S.-L. Chou, H. K. Liu, S. X. Dou, *Nanomicro Lett.* **2021**, *13*, 121.
- [137] D. Ma, Y. Li, J. Yang, H. Mi, S. Luo, L. Deng, C. Yan, M. Rauf, P. Zhang, X. Sun, X. Ren, J. Li, H. Zhang, *Adv. Funct. Mater.* **2018**, *28*, 1705537.
- [138] X. Yu, A. Manthiram, *J. Phys. Chem. C* **2014**, *118*, 22952-22959.
- [139] Y. Wang, Y. Hao, L.-C. Xu, Z. Yang, M.-Y. Di, R. Liu, X. Li, *J. Phys. Chem. C* **2019**, *123*, 3988-3995.
- [140] Q. Ma, G. Du, B. Guo, W. Tang, Y. Li, M. Xu, C. Li, *Chem. Eng. J.* **2020**, *388*, 124210.
- [141] Y. Dong, H. Shi, Z.-S. Wu, *Adv. Funct. Mater.* **2020**, *30*, 2000706.
- [142] Y. Li, Y. Lu, L. Chen, Y.-S. Hu, *Chin. Phys. B* **2020**, *29*, 048201.
- [143] I. Bauer, M. Kohl, H. Althues, S. Kaskel, *Chem. Commun.* **2014**, *50*, 3208-3210.
- [144] R. Dugas, A. Ponrouch, G. Gachot, R. David, M. R. Palacin, J. M. Tarascon, *J. Electrochem. Soc.* **2016**, *163*, a2333-a2339.
- [145] S. Zheng, P. Han, Z. Han, P. Li, H. Zhang, J. Yang, *Adv. Energy Mater.* **2014**, *4*, 1400226.
- [146] Q. Pang, D. Kundu, M. Cuisinier, L. F. Nazar, *Nat. Commun.* **2014**, *5*, 4759.
- [147] X. Ji, S. Evers, R. Black, L. F. Nazar, *Nat. Commun.* **2011**, *2*, 325.
- [148] S. Evers, T. Yim, L. F. Nazar, *J. Phys. Chem. C* **2012**, *116*, 19653-19658.
- [149] H. Kim, J. T. Lee, D.-C. Lee, A. Magasinski, W.-i. Cho, G. Yushin, *Adv. Energy Mater.* **2013**, *3*, 1308-1315.
- [150] Z. Qiang, Y.-M. Chen, Y. Xia, W. Liang, Y. Zhu, B. D. Vogt, *Nano Energy* **2017**, *32*, 59-66.
- [151] T. H. Hwang, D. S. Jung, J.-S. Kim, B. G. Kim, J. W. Choi, *Nano Lett.* **2013**, *13*, 4532-4538.
- [152] Z. W. Seh, J. Sun, Y. Sun, Y. Cui, *ACS Cent. Sci.* **2015**, *1*, 449-455.
- [153] Y. Zhao, L. V. Goncharova, Q. Zhang, P. Kaghazchi, Q. Sun, A. Lushington, B. Wang, R. Li, X. Sun, *Nano Lett.* **2017**, *17*, 5653-5659.
- [154] Y. Zhao, L. V. Goncharova, A. Lushington, Q. Sun, H. Yadegari, B. Wang, W. Xiao, R. Li, X. Sun, *Adv. Mater.* **2017**, *29*, 1606663.
- [155] W. Luo, Y. Zhang, S. Xu, J. Dai, E. Hitz, Y. Li, C. Yang, C. Chen, B. Liu, L. Hu, *Nano Lett.* **2017**, *17*, 3792-3797.
- [156] A. Wang, X. Hu, H. Tang, C. Zhang, S. Liu, Y.-W. Yang, Q.-H. Yang, J. Luo, *Angew. Chem. Int. Ed.* **2017**, *56*, 11921-11926.
- [157] D.-J. Lee, J.-W. Park, I. Hasa, Y.-K. Sun, B. Scrosati, J. Hassoun, *J. Mater. Chem. A* **2013**, *1*, 5256-5261.
- [158] R. Okuyama, H. Nakashima, T. Sano, E. Nomura, *J. Power Sources* **2001**, *93*, 50-54.
- [159] I. Kim, J.-Y. Park, C. H. Kim, J.-W. Park, J.-P. Ahn, J.-H. Ahn, K.-W. Kim, H.-J. Ahn, *J. Power Sources* **2016**, *301*, 332-337.

5. References

- [160] J. Zhu, C. Chen, Y. Lu, J. Zang, M. Jiang, D. Kim, X. Zhang, *Carbon* **2016**, *101*, 272-280.
- [161] H. Li, M. Zhao, B. Jin, Z. Wen, H. K. Liu, Q. Jiang, *Small* **2020**, *16*, 1907464.
- [162] D. Zhou, X. Tang, X. Guo, P. Li, D. Shanmukaraj, H. Liu, X. Gao, Y. Wang, T. Rojo, M. Armand, G. Wang, *Angew. Chem. Int. Ed.* **2020**, *59*, 16725-16734.
- [163] E. Ceylan Cengiz, Z. Erdol, B. Sakar, A. Aslan, A. Ata, O. Ozturk, R. Demir-Cakan, *J. Phys. Chem. C* **2017**, *121*, 15120-15126.
- [164] X. Yu, A. Manthiram, *J. Phys. Chem. Lett.* **2014**, *5*, 1943-1947.
- [165] G. G. Eshetu, G. A. Elia, M. Armand, M. Forsyth, S. Komaba, T. Rojo, S. Passerini, *Adv. Energy Mater.* **2020**, *10*, 2000093.
- [166] G. G. Eshetu, S. Grugeon, H. Kim, S. Jeong, L. Wu, G. Gachot, S. Laruelle, M. Armand, S. Passerini, *ChemSusChem* **2016**, *9*, 462-471.
- [167] S. Aladinli, F. Bordet, K. Ahlbrecht, J. Tübke, M. Holzapfel, *Electrochim. Acta* **2017**, *231*, 468-478.
- [168] A. Ponrouch, E. Marchante, M. Courty, J.-M. Tarascon, M. R. Palacín, *Energy Environ. Sci.* **2012**, *5*, 8572-8583.
- [169] J. Chen, Z. Huang, C. Wang, S. Porter, B. Wang, W. Lie, H. K. Liu, *Chem. Commun.* **2015**, *51*, 9809-9812.
- [170] C. Ge, L. Wang, L. Xue, Z.-S. Wu, H. Li, Z. Gong, X.-D. Zhang, *J. Power Sources* **2014**, *248*, 77-82.
- [171] A. Bhide, J. Hofmann, A. Katharina Dürr, J. Janek, P. Adelhelm, *Phys. Chem. Chem. Phys.* **2014**, *16*, 1987-1998.
- [172] L.-Z. Fan, T. Xing, R. Awan, W. Qiu, *Ionics* **2011**, *17*, 491-494.
- [173] K. Xu, S. Zhang, B. A. Poesse, T. R. Jow, *Electrochem. Solid-State Lett.* **2002**, *5*, a259.
- [174] J. Shim, K. A. Striebel, E. J. Cairns, *J. Electrochem. Soc.* **2002**, *149*, a1321.
- [175] Y. V. Mikhaylik, J. R. Akridge, *J. Electrochem. Soc.* **2004**, *151*, a1969-a1976.
- [176] H. Ryu, T. Kim, K. Kim, J.-H. Ahn, T. Nam, G. Wang, H.-J. Ahn, *J. Power Sources* **2011**, *196*, 5186-5190.
- [177] C.-W. Park, H.-S. Ryu, K.-W. Kim, J.-H. Ahn, J.-Y. Lee, H.-J. Ahn, *J. Power Sources* **2007**, *165*, 450-454.
- [178] S. Wenzel, H. Metelmann, C. Reiß, A. K. Dürr, J. Janek, P. Adelhelm, *J. Power Sources* **2013**, *243*, 758-765.
- [179] T. Welton, *Chem. Rev.* **1999**, *99*, 2071-2083.
- [180] J.-W. Park, K. Ueno, N. Tachikawa, K. Dokko, M. Watanabe, *J. Phys. Chem. C* **2013**, *117*, 20531-20541.
- [181] S. Wei, S. Xu, A. Agrawal, S. Choudhury, Y. Lu, Z. Tu, L. Ma, L. A. Archer, *Nat. Commun.* **2016**, *7*, 11722.
- [182] M. D. Tikekar, L. A. Archer, D. L. Koch, *J. Electrochem. Soc.* **2014**, *161*, a847-a855.
- [183] Z. Tu, P. Nath, Y. Lu, M. D. Tikekar, L. A. Archer, *Acc. Chem. Res.* **2015**, *48*, 2947-2956.
- [184] Y. Lu, S. S. Moganty, J. L. Schaefer, L. A. Archer, *J. Mater. Chem.* **2012**, *22*, 4066-4072.
- [185] L. X. Yuan, J. K. Feng, X. P. Ai, Y. L. Cao, S. L. Chen, H. X. Yang, *Electrochem. Commun.* **2006**, *8*, 610-614.
- [186] L. Wang, J. Liu, S. Yuan, Y. Wang, Y. Xia, *Energy Environ. Sci.* **2016**, *9*, 224-231.
- [187] S. Zhang, K. Ueno, K. Dokko, M. Watanabe, *Adv. Energy Mater.* **2015**, *5*, 1500117.

- [188] H. Shobukawa, H. Tokuda, S.-I. Tabata, M. Watanabe, *Electrochim. Acta* **2004**, *50*, 305-309.
- [189] K. Yoshida, M. Tsuchiya, N. Tachikawa, K. Dokko, M. Watanabe, *J. Electrochem. Soc.* **2012**, *159*, a1005-a1012.
- [190] Y. Ishino, K. Takahashi, W. Murata, Y. Umebayashi, S. Tsuzuki, M. Watanabe, M. Kamaya, S. Seki, *Energy Technol.* **2019**, *7*, 1900197.
- [191] K. Ueno, J.-W. Park, A. Yamazaki, T. Mandai, N. Tachikawa, K. Dokko, M. Watanabe, *J. Phys. Chem. C* **2013**, *117*, 20509-20516.
- [192] K. Ueno, K. Yoshida, M. Tsuchiya, N. Tachikawa, K. Dokko, M. Watanabe, *J. Phys. Chem. B* **2012**, *116*, 11323-11331.
- [193] T. Ould Ely, D. Kamzabek, D. Chakraborty, *Front. Energy Res.* **2019**, *7*.
- [194] J. B. Robinson, D. P. Finegan, T. M. M. Heenan, K. Smith, E. Kendrick, D. J. L. Brett, P. R. Shearing, *J. Electrochem. Energy Convers. Storage* **2017**, *15*.
- [195] Q. Wang, B. Mao, S. I. Stoliarov, J. Sun, *Prog. Energy Combust. Sci.* **2019**, *73*, 95-131.
- [196] Y. Zhao, Y. Zhang, D. Gosselink, T. N. L. Doan, M. Sadhu, H.-J. Cheang, P. Chen, *Membranes* **2012**, *2*, 553-564.
- [197] D. E. Fenton, J. M. Parker, P. V. Wright, *Polymer* **1973**, *14*, 589.
- [198] G. Feuillade, P. Perche, *J. Appl. Electrochem.* **1975**, *5*, 63-69.
- [199] S. Skaarup, K. West, B. Zachau-Christiansen, *Solid State Ion.* **1988**, *28-30*, 975-978.
- [200] W. Wiczcerek, K. Such, H. Wyciřlik, J. Płocharski, *Solid State Ion.* **1989**, *36*, 255-257.
- [201] Z. Zhang, K. Xu, X. Rong, Y.-S. Hu, H. Li, X. Huang, L. Chen, *J. Power Sources* **2017**, *372*, 270-275.
- [202] A. Hayashi, K. Noi, A. Sakuda, M. Tatsumisago, *Nat. Commun.* **2012**, *3*, 856.
- [203] J.-J. Kim, K. Yoon, I. Park, K. Kang, *Small Methods* **2017**, *1*, 1700219.
- [204] J. F. M. Oudenhoven, L. Baggetto, P. H. L. Notten, *Adv. Energy Mater.* **2011**, *1*, 10-33.
- [205] N. Anantharamulu, K. Koteswara Rao, G. Rambabu, B. Vijaya Kumar, V. Radha, M. Vithal, *J. Mater. Sci.* **2011**, *46*, 2821-2837.
- [206] C. Venkata Subba Rao, M. Ravi, V. Raja, P. Balaji Bhargav, A. K. Sharma, V. V. R. Narasimha Rao, *Iran. Polym. J.* **2012**, *21*, 531-536.
- [207] A. Manuel Stephan, S. Gopu Kumar, N. G. Renganathan, M. Anbu Kulandainathan, *Eur. Polym. J.* **2005**, *41*, 15-21.
- [208] Z. Zhang, Q. Zhang, C. Ren, F. Luo, Q. Ma, Y.-S. Hu, Z. Zhou, H. Li, X. Huang, L. Chen, *J. Mater. Chem. A* **2016**, *4*, 15823-15828.
- [209] Y. L. Ni'mah, M.-Y. Cheng, J. H. Cheng, J. Rick, B.-J. Hwang, *J. Power Sources* **2015**, *278*, 375-381.
- [210] F. Gebert, J. Knott, R. Gorkin, S.-L. Chou, S.-X. Dou, *Energy Storage Mater.* **2021**, *36*, 10-30.
- [211] B. Zhang, R. Tan, L. Yang, J. Zheng, K. Zhang, S. Mo, Z. Lin, F. Pan, *Energy Storage Mater.* **2018**, *10*, 139-159.
- [212] C. Zhao, L. Liu, X. Qi, Y. Lu, F. Wu, J. Zhao, Y. Yu, Y.-S. Hu, L. Chen, *Adv. Energy Mater.* **2018**, *8*, 1703012.
- [213] Y. Wang, W. D. Richards, S. P. Ong, L. J. Miara, J. C. Kim, Y. Mo, G. Ceder, *Nat. Mater.* **2015**, *14*, 1026-1031.
- [214] J. C. Bachman, S. Muy, A. Grimaud, H.-H. Chang, N. Pour, S. F. Lux, O. Paschos, F. Maglia, S. Lupart, P. Lamp, L. Giordano, Y. Shao-Horn, *Chem. Rev.* **2016**, *116*, 140-162.
- [215] G. S. MacGlashan, Y. G. Andreev, P. G. Bruce, *Nature* **1999**, *398*, 792-794.

5. References

- [216] R. Chen, W. Qu, X. Guo, L. Li, F. Wu, *Mater. Horiz.* **2016**, *3*, 487-516.
- [217] A. Boschini, P. Johansson, *Electrochim. Acta* **2015**, *175*, 124-133.
- [218] F. Colò, F. Bella, J. R. Nair, M. Destro, C. Gerbaldi, *Electrochim. Acta* **2015**, *174*, 185-190.
- [219] S. A. Hashmi, S. Chandra, *Mater. Sci. Eng. B* **1995**, *34*, 18-26.
- [220] A. Bitner-Michalska, G. M. Nolis, G. Żukowska, A. Zalewska, M. Poterała, T. Trzeciak, M. Dranka, M. Kalita, P. Jankowski, L. Niedzicki, J. Zachara, M. Marcinek, W. Wieczorek, *Sci. Rep.* **2017**, *7*, 40036.
- [221] A. Bhide, K. Hariharan, *Polym. Int.* **2008**, *57*, 523-529.
- [222] Y. W. Chen-Yang, H. C. Chen, F. J. Lin, C. C. Chen, *Solid State Ion.* **2002**, *150*, 327-335.
- [223] E. Peled, *J. Electrochem. Soc.* **1979**, *126*, 2047-2051.
- [224] W. Liu, P. Liu, D. Mitlin, *Adv. Energy Mater.* **2020**, *10*, 2002297.
- [225] B. Lee, E. Paek, D. Mitlin, S. W. Lee, *Chem. Rev.* **2019**, *119*, 5416-5460.
- [226] J. Lee, J. Kim, S. Kim, C. Jo, J. Lee, *Mater. Adv.* **2020**, *1*, 3143-3166.
- [227] P. Atkins, T. Overton, *Shriver and Atkins' inorganic chemistry*, Oxford University Press, USA, **2010**.
- [228] R. Mogensen, D. Brandell, R. Younesi, *ACS Energy Lett.* **2016**, *1*, 1173-1178.
- [229] R. Mogi, M. Inaba, S.-K. Jeong, Y. Iriyama, T. Abe, Z. Ogumi, *J. Electrochem. Soc.* **2002**, *149*, a1578.
- [230] X.-m. Zhao, Q. Zhu, S.-d. Xu, L. Chen, Z.-j. Zuo, X.-m. Wang, S.-b. Liu, D. Zhang, *J. Electroanal. Chem.* **2019**, *832*, 392-398.
- [231] J. Wu, J. Liu, Z. Lu, K. Lin, Y.-Q. Lyu, B. Li, F. Ciucci, J.-K. Kim, *Energy Storage Mater.* **2019**, *23*, 8-16.
- [232] R. Rodriguez, K. E. Loeffler, S. S. Nathan, J. K. Sheavly, A. Dolocan, A. Heller, C. B. Mullins, *ACS Energy Lett.* **2017**, *2*, 2051-2057.
- [233] Y. Lee, J. Lee, J. Lee, K. Kim, A. Cha, S. Kang, T. Wi, S. J. Kang, H.-W. Lee, N.-S. Choi, *ACS Appl. Mater. Interfaces* **2018**, *10*, 15270-15280.
- [234] Y. Lee, J. Lee, H. Kim, K. Kang, N.-S. Choi, *J. Power Sources* **2016**, *320*, 49-58.
- [235] Y. Lu, Y. Cai, Q. Zhang, L. Liu, Z. Niu, J. Chen, *Chem. Sci.* **2019**, *10*, 4306-4312.
- [236] W. Böhnstedt, in *Handbook of Battery Materials, Second Edition*, 2 ed., Wiley - VCH, **2007**, pp. 245-292.
- [237] R. Greef, S. E. Group, *Instrumental Methods in Electrochemistry*, E. Horwood, **1985**.
- [238] A. J. Bard, L. R. Faulkner, *Surf. technol.* **1983**, *20*, 91-92.
- [239] N. Elgrishi, K. J. Rountree, B. D. McCarthy, E. S. Rountree, T. T. Eisenhart, J. L. Dempsey, *J. Chem. Educ.* **2018**, *95*, 197-206.
- [240] G. Bontempelli, N. Dossi, R. Toniolo, in *Encyclopedia of Analytical Science (Third Edition)* (Eds.: P. Worsfold, C. Poole, A. Townshend, M. Miró), Academic Press, Oxford, **2019**, pp. 218-229.
- [241] J. Liu, J. Wang, C. Xu, H. Jiang, C. Li, L. Zhang, J. Lin, Z. X. Shen, *Adv. Sci.* **2018**, *5*, 1700322.
- [242] J.-j. Wu, *Int. J. Electrochem. Sci.* **2016**, *11*, 5165-5179.
- [243] P. M. Hallam, C. E. Banks, *Electrochem. Commun.* **2011**, *13*, 8-11.
- [244] A. Y. S. Eng, C. K. Chua, M. Pumera, *Electrochem. Commun.* **2015**, *59*, 86-90.
- [245] D. A. C. Brownson, D. K. Kampouris, C. E. Banks, *Chem. Soc. Rev.* **2012**, *41*, 6944-6976.
- [246] L. Porcarelli, C. Gerbaldi, F. Bella, J. R. Nair, *Sci. Rep.* **2016**, *6*, 19892.
- [247] M. A. Ratner, D. F. Shriver, *MRS Bull.* **2000**, *14*, 39-51.
- [248] R. C. Agrawal, G. P. Pandey, *J. Phys. D* **2008**, *41*, 223001.
- [249] E. Quartarone, P. Mustarelli, *Chem. Soc. Rev.* **2011**, *40*, 2525-2540.

- [250] Y. Seino, T. Ota, K. Takada, A. Hayashi, M. Tatsumisago, *Energy Environ. Sci.* **2014**, *7*, 627-631.
- [251] S. Xia, X. Wu, Z. Zhang, Y. Cui, W. Liu, *Chem* **2019**, *5*, 753-785.
- [252] M. A. Ratner, P. Johansson, D. F. Shriver, *MRS Bull.* **2011**, *25*, 31-37.
- [253] F. Croce, M. L. Focarete, J. Hassoun, I. Meschini, B. Scrosati, *Energy Environ. Sci.* **2011**, *4*, 921-927.
- [254] N. Binesh, S. V. Bhat, *J. Polym. Sci., Part B: Polym. Phys.* **1998**, *36*, 1201-1209.
- [255] J. Evans, C. A. Vincent, P. G. Bruce, *Polymer* **1987**, *28*, 2324-2328.
- [256] P. G. Bruce, C. A. Vincent, *J. Electroanal. Chem.* **1987**, *225*, 1-17.
- [257] M. D. Galluzzo, J. A. Maslyn, D. B. Shah, N. P. Balsara, *J. Chem. Phys.* **2019**, *151*, 020901.
- [258] S. Zugmann, H. J. Gores, in *Encyclopedia of Applied Electrochemistry* (Eds.: G. Kreysa, K.-i. Ota, R. F. Savinell), Springer New York, New York, NY, **2014**, pp. 2086-2091.
- [259] M. Siekierski, M. Bukat, M. Ciosek, M. Piszcz, M. Mroczkowska-Szerszeń, *Polymers* **2021**, *13*, 895.
- [260] Y. Okamoto, S. Tsuzuki, R. Tatara, K. Ueno, K. Dokko, M. Watanabe, *J. Phys. Chem. C* **2020**, *124*, 4459-4469.
- [261] M. E. Orazem, B. Tribollet, *New Jersey* **2008**, 383-389.
- [262] S. Wang, J. Zhang, O. Gharbi, V. Vivier, M. Gao, M. E. Orazem, *Nat. Rev. Methods Primers* **2021**, *1*, 41.
- [263] P. Horowitz, W. Hill, I. Robinson, *The art of electronics, Vol. 2*, Cambridge university press Cambridge, **1989**.
- [264] S. Rodrigues, N. Munichandraiah, A. K. Shukla, *J. Solid State Electrochem.* **1999**, *3*, 397-405.
- [265] S. Kochowski, K. Nitsch, *Thin Solid Films* **2002**, *415*, 133-137.
- [266] H. Li, D. Dzombak, R. Vidic, *Ind. Eng. Chem. Res.* **2012**, *51*, 2821-2829.
- [267] W. Choi, H.-C. Shin, J. M. Kim, J.-Y. Choi, W.-S. Yoon, *J. Electrochem. Sci. Technol* **2020**, *11*, 1-13.
- [268] C. Deslouis, C. Gabrielli, M. Keddad, A. Khalil, R. Rosset, B. Tribollet, M. Zidoune, *Electrochim. Acta* **1997**, *42*, 1219-1233.
- [269] J.-B. Jorcin, M. E. Orazem, N. Pébère, B. Tribollet, *Electrochim. Acta* **2006**, *51*, 1473-1479.
- [270] T. Pajkossy, *Solid State Ion.* **2005**, *176*, 1997-2003.
- [271] S. P. Jiang, J. G. Love, S. P. S. Badwal, *Key Eng. Mater.* **1996**, *125-126*, 81-132.
- [272] W. Weppner, R. A. Huggins, *J. Electrochem. Soc.* **1977**, *124*, 1569-1578.
- [273] M. J. Lacey, *ChemElectroChem* **2017**, *4*, 1997-2004.
- [274] M. J. Lacey, K. Edström, D. Brandell, *Chem. Commun.* **2015**, *51*, 16502-16505.
- [275] D. W. Dees, S. Kawauchi, D. P. Abraham, J. Prakash, *J. Power Sources* **2009**, *189*, 263-268.
- [276] H. Yang, H. J. Bang, J. Prakash, *J. Electrochem. Soc.* **2004**, *151*, a1247.
- [277] J. W. Dibden, N. Meddings, J. R. Owen, N. Garcia-Araez, *ChemElectroChem* **2018**, *5*, 445-454.
- [278] M. R. Busche, P. Adelhelm, H. Sommer, H. Schneider, K. Leitner, J. Janek, *J. Power Sources* **2014**, *259*, 289-299.
- [279] D. Uxa, E. Hüger, H. Schmidt, *J. Phys. Chem. C* **2020**, *124*, 27894-27899.
- [280] M. R. Rosenthal, *J. Chem. Educ.* **1973**, *50*, 331.
- [281] Z.-B. Zhou, H. Matsumoto, K. Tatsumi, *Chem. Eur. J.* **2006**, *12*, 2196-2212.
- [282] W. Beck, K. Suenkel, *Chem. Rev.* **1988**, *88*, 1405-1421.
- [283] S. H. Strauss, *Chem. Rev.* **1993**, *93*, 927-942.
- [284] C. H. Winter, X. X. Zhou, M. J. Heeg, *Inorg. Chem.* **1992**, *31*, 1808-1815.

5. References

- [285] J. Reedijk, *Comments Inorg. Chem.* **1982**, *1*, 379-389.
- [286] I. M. Riddlestone, A. Kraft, J. Schaefer, I. Krossing, *Angew. Chem. Int. Ed.* **2018**, *57*, 13982-14024.
- [287] N. A. Andreeva, V. V. Chaban, *J. Mol. Model.* **2017**, *23*, 86.
- [288] E. Y. X. Chen, S. J. Lancaster, in *Comprehensive Inorganic Chemistry II (Second Edition)* (Eds.: J. Reedijk, K. Poeppelmeier), Elsevier, Amsterdam, **2013**, pp. 707-754.
- [289] A. G. Massey, A. J. Park, *J. Organomet. Chem.* **1964**, *2*, 245-250.
- [290] J. H. Golden, P. F. Mutolo, E. B. Lobkovsky, F. J. DiSalvo, *Inorg. Chem.* **1994**, *33*, 5374-5375.
- [291] J. van den Broeke, B.-J. Deelman, G. van Koten, *Tetrahedron Lett.* **2001**, *42*, 8085-8087.
- [292] K. Fujiki, J. Ichikawa, H. Kobayashi, A. Sonoda, T. Sonoda, *J. Fluorine Chem.* **2000**, *102*, 293-300.
- [293] J. Clarke-Hannaford, M. Breedon, T. R  ther, M. Spencer, *Nanomaterials* **2021**, *11*, 2391.
- [294] I. Raabe, A. Reisinger, I. Krossing, in *Experiments in Green and Sustainable Chemistry. Edited by Herbert W. Roesky and Dietmar Kennepohl., Vol. 49*, Angew. Chem., **2009**.
- [295] I. Krossing, *Chem. Eur. J.* **2001**, *7*, 490-502.
- [296] S. M. Ivanova, B. G. Nolan, Y. Kobayashi, S. M. Miller, O. P. Anderson, S. H. Strauss, *Chem. Eur. J.* **2001**, *7*, 503-510.
- [297] Y. Sun, M. V. Metz, C. L. Stern, T. J. Marks, *Organometallics* **2000**, *19*, 1625-1627.
- [298] S. Strauss, in *Abstracts of papers of the american chemical society, Vol. 218*, Amer chemical soc 1155 16TH ST, NW, Washington, DC 20036 USA, **1999**, pp. U596-U596.
- [299] T. J. Barbarich, S. M. Miller, O. P. Anderson, S. H. Strauss, *J. Mol. Catal. A: Chem.* **1998**, *128*, 289-331.
- [300] B. G. Nolan, S. Tsujioka, S. H. Strauss, *J. Fluorine Chem.* **2002**, *118*, 103-106.
- [301] H. Kropshofer, O. Leitzke, P. Peringer, F. Sladky, *Chem. Ber.* **1981**, *114*, 2644-2648.
- [302] J. B. Lambert, S. Zhang, C. L. Stern, J. C. Huffman, *Science* **1993**, *260*, 1917-1918.
- [303] C. A. Reed, *Acc. Chem. Res.* **2010**, *43*, 121-128.
- [304] I. Krossing, in *Comprehensive Inorganic Chemistry II (Second Edition)* (Eds.: J. Reedijk, K. Poeppelmeier), Elsevier, Amsterdam, **2013**, pp. 681-705.
- [305] A. Bihlmeier, M. Gonsior, I. Raabe, N. Trapp, I. Krossing, *Chem. Eur. J.* **2004**, *10*, 5041-5051.
- [306] A. Martens, P. Weis, M. C. Krummer, M. Kreuzer, A. Meierh  fer, S. C. Meier, J. Bohnenberger, H. Scherer, I. Riddlestone, I. Krossing, *Chem. Sci.* **2018**, *9*, 7058-7068.
- [307] B. G. Nolan, *Polyfluoroalkoxyaluminates and borates as new weakly coordinating anions and as components of battery electrolytes*, Colorado State University, **2001**.
- [308] S. Bulut, P. Klose, M.-M. Huang, H. Weing  rtner, P. J. Dyson, G. Laurenczy, C. Friedrich, J. Menz, K. K  mmerer, I. Krossing, *Chem. Eur. J.* **2010**, *16*, 13139-13154.
- [309] S. Tsujioka, B. G. Nolan, H. Takase, B. P. Fauber, S. H. Strauss, *J. Electrochem. Soc.* **2004**, *151*, a1418-a1423.

- [310] V. Aravindan, J. Gnanaraj, S. Madhavi, H.-K. Liu, *Chem. Eur. J.* **2011**, *17*, 14326-14346.
- [311] P. Murmann, R. Schmitz, S. Nowak, N. Ignatiev, P. Sartori, I. Cekic-Laskovic, M. Winter, *J. Electrochem. Soc.* **2015**, *162*, a1738-a1744.
- [312] A. B. A. Rupp, I. Krossing, *Acc. Chem. Res.* **2015**, *48*, 2537-2546.
- [313] A. Shyamsunder, W. Beichel, P. Klose, Q. Pang, H. Scherer, A. Hoffmann, G. K. Murphy, I. Krossing, L. F. Nazar, *Angew. Chem. Int. Ed.* **2017**, *56*, 6192-6197.
- [314] S. Murugan, S. Niesen, J. Kappler, K. Küster, U. Starke, M. R. Buchmeiser, *Batter. Supercaps* **2021**, *4*, 1636-1646.
- [315] A. N. Srivastava, *Stability and Applications of Coordination Compounds*, **2020**.
- [316] J. Cha, J.-G. Han, J. Hwang, J. Cho, N.-S. Choi, *J. Power Sources* **2017**, *357*, 97-106.
- [317] R. Mogensen, S. Colbin, A. S. Menon, E. Björklund, R. Younesi, *ACS Appl. Energy Mater.* **2020**, *3*, 4974-4982.
- [318] D. M. C. Ould, S. Menkin, H. E. Smith, V. Riesgo-Gonzalez, E. Jónsson, C. A. O'Keefe, F. Coowar, J. Barker, A. D. Bond, C. P. Grey, D. S. Wright, *Angew. Chem. Int. Ed.*, *61*, e202202133.
- [319] S. Murugan, S. V. Klostermann, W. Frey, J. Kästner, M. R. Buchmeiser, *Electrochem. Commun.* **2021**, *132*, 107137.
- [320] V. Di Noto, S. Lavina, G. A. Giffin, E. Negro, B. Scrosati, *Electrochim. Acta* **2011**, *57*, 4-13.
- [321] Y. Ren, Z. Zhang, S. Fang, M. Yang, S. Cai, *Sol. Energy Mater. Sol. Cells* **2002**, *71*, 253-259.
- [322] H. Li, Y.-M. Chen, X.-T. Ma, J.-L. Shi, B.-K. Zhu, L.-P. Zhu, *J. Membr. Sci.* **2011**, *379*, 397-402.
- [323] N.-S. Choi, J.-K. Park, *Electrochim. Acta* **2001**, *46*, 1453-1459.
- [324] J. P. Sharma, S. S. Sekhon, *Solid State Ion.* **2007**, *178*, 439-445.
- [325] A. Subramania, N. T. Kalyana Sundaram, G. Vijaya Kumar, T. Vasudevan, *Ionics* **2006**, *12*, 175-178.
- [326] S. Çavuş, E. Durgun, *Acta Phys. Pol., A* **2016**, *129*, 621-624.
- [327] M.-S. Park, S.-H. Hyun, S.-C. Nam, S. B. Cho, *Electrochim. Acta* **2008**, *53*, 5523-5527.
- [328] H.-S. Jeong, J. H. Kim, S.-Y. Lee, *J. Mater. Chem.* **2010**, *20*, 9180-9186.
- [329] T. N. T. Tran, D. Aasen, D. Zhalmuratova, M. Labbe, H.-J. Chung, D. G. Ivey, *Batter. Supercaps* **2020**, *3*, 917-927.
- [330] X. Cheng, J. Pan, Y. Zhao, M. Liao, H. Peng, *Adv. Energy Mater.* **2018**, *8*, 1702184.
- [331] Y. Gu, S. Zhang, L. Martinetti, K. H. Lee, L. D. McIntosh, C. D. Frisbie, T. P. Lodge, *J. Am. Chem. Soc.* **2013**, *135*, 9652-9655.
- [332] Y. Wang, W.-H. Zhong, *ChemElectroChem* **2015**, *2*, 22-36.
- [333] Q. Lu, J. Fang, J. Yang, R. Miao, J. Wang, Y. Nuli, *J. Membr. Sci.* **2014**, *449*, 176-183.
- [334] V. Gentili, S. Panero, P. Reale, B. Scrosati, *J. Power Sources* **2007**, *170*, 185-190.
- [335] G. B. Appetecchi, F. Alessandrini, S. Passerini, G. Caporiccio, B. Boutevin, F. Guida-PietraSanta, *Electrochim. Acta* **2005**, *50*, 4396-4404.
- [336] Y. Li, P. S. Fedkiw, *J. Electrochem. Soc.* **2007**, *154*, a1140-a1145.
- [337] E.-H. Kil, K.-H. Choi, H.-J. Ha, S. Xu, J. A. Rogers, M. R. Kim, Y.-G. Lee, K. M. Kim, K. Y. Cho, S.-Y. Lee, *Adv. Mater.* **2013**, *25*, 1395-1400.
- [338] Y. H. Liao, X. P. Li, C. H. Fu, R. Xu, L. Zhou, C. L. Tan, S. J. Hu, W. S. Li, *J. Power Sources* **2011**, *196*, 2115-2121.

5. References

- [339] C.-W. Huang, C.-A. Wu, S.-S. Hou, P.-L. Kuo, C.-T. Hsieh, H. Teng, *Adv. Funct. Mater.* **2012**, *22*, 4677-4685.
- [340] Q. Pan, Z. Li, W. Zhang, D. Zeng, Y. Sun, H. Cheng, *Solid State Ion.* **2017**, *300*, 60-66.
- [341] H. Zhang, C. Li, M. Piszcz, E. Coya, T. Rojo, L. M. Rodriguez-Martinez, M. Armand, Z. Zhou, *Chem. Soc. Rev.* **2017**, *46*, 797-815.
- [342] L. Porcarelli, M. A. Aboudzadeh, L. Rubatat, J. R. Nair, A. S. Shaplov, C. Gerbaldi, D. Mecerreyes, *J. Power Sources* **2017**, *364*, 191-199.
- [343] M. Doyle, J. Newman, *Electrochim. Acta* **1995**, *40*, 2191-2196.
- [344] M. Rosso, C. Brissot, A. Teysot, M. Dollé, L. Sannier, J.-M. Tarascon, R. Bouchet, S. Lascaud, *Electrochim. Acta* **2006**, *51*, 5334-5340.
- [345] M. Doyle, T. F. Fuller, J. Newman, *Electrochim. Acta* **1994**, *39*, 2073-2081.
- [346] H. Oh, K. Xu, H. D. Yoo, D. S. Kim, C. Chanthad, G. Yang, J. Jin, I. A. Ayhan, S. M. Oh, Q. Wang, *Chem. Mater.* **2016**, *28*, 188-196.
- [347] J. Zhang, S. Wang, D. Han, M. Xiao, L. Sun, Y. Meng, *Energy Storage Mater.* **2019**, *24*.
- [348] P. Wang, H. Zhang, J. Chai, T. Liu, R. Hu, Z. Zhang, G. Li, G. Cui, *Solid State Ion.* **2019**, *337*, 140-146.
- [349] L. Stolz, S. Hochstädt, S. Röser, M. R. Hansen, M. Winter, J. Kasnatscheew, *ACS Appl. Mater. Interfaces* **2022**, *14*, 11559-11566.
- [350] Q. Lu, Y.-B. He, Q. Yu, B. Li, Y. V. Kaneti, Y. Yao, F. Kang, Q.-H. Yang, *Adv. Mater.* **2017**, *29*, 1604460.
- [351] H. Gao, W. Zhou, K. Park, J. B. Goodenough, *Adv. Energy Mater.* **2016**, *6*, 1600467.
- [352] J. Zheng, Y. Zhao, X. Feng, W. Chen, Y. Zhao, *J. Mater. Chem. A* **2018**, *6*, 6559-6564.
- [353] K. Jeddi, K. Sarikhani, N. T. Qazvini, P. Chen, *J. Power Sources* **2014**, *245*, 656-662.
- [354] W. Li, Y. Pang, T. Zhu, Y. Wang, Y. Xia, *Solid State Ion.* **2018**, *318*, 82-87.
- [355] Q. Yang, N. Deng, J. Chen, B. Cheng, W. Kang, *Chem. Eng. J.* **2021**, *413*, 127427.
- [356] H. Qu, J. Zhang, A. Du, B. Chen, J. Chai, N. Xue, L. Wang, L. Qiao, C. Wang, X. Zang, J. Yang, X. Wang, G. Cui, *Adv. Sci.* **2018**, *5*, 1700503.
- [357] M. Liu, D. Zhou, Y.-B. He, Y. Fu, X. Qin, C. Miao, H. Du, B. Li, Q.-H. Yang, Z. Lin, T. S. Zhao, F. Kang, *Nano Energy* **2016**, *22*, 278-289.
- [358] D. Zhou, Y. Chen, B. Li, H. Fan, F. Cheng, D. Shanmukaraj, T. Rojo, M. Armand, G. Wang, *Angew. Chem. Int. Ed.* **2018**, *57*, 10168-10172.
- [359] S. Murugan, S. V. Klostermann, P. Schützendübe, G. Richter, J. Kästner, M. R. Buchmeiser, *Adv. Funct. Mater.* **2022**, *32*, 2201191.

6 Curriculum Vitae

Personal Data

Name: Saravanakumar Murugan

Date of Birth: 01.01.1993

Place of Birth: Theni, India

Nationality: Indian

Scientific Education

03/2019 – 10/2022 Ph.D. student in the group of Professor Dr. Michael. Buchmeiser at the Institute of Polymer Chemistry at the University of Stuttgart, Germany. Topic: “Development of novel liquid and gel polymer electrolytes for room temperature sodium-sulfur batteries”.

03/2018 – 02/2019: Internship and Master’s thesis at SGL carbon, Innovation center, Meitingen, Augsburg. “Increasing the surface area of carbon materials: processing, characterization, and application of nanofibers”.

10/2016 – 01/2019: M.Sc. Materials Science (Master of Science) at the University of Stuttgart, Germany (Grade: 1.8).

06/2010 – 04/2014: Polymer Technology (Bachelor of Technology) at Anna University, Madras Institute of Technology Campus, Chennai. (Grade: 85.4%).

Publications

3. Murugan, S.; Klostermann, S. V.; Schützendübe, P.; Richter, G.; Kästner, J.; Buchmeiser, M. R., Stable Cycling of Room-Temperature Sodium-Sulfur Batteries Based on an In Situ Crosslinked Gel Polymer Electrolyte. *Adv. Funct. Mater.* **2022**, 2201191.
2. Murugan, S.; Klostermann, S. V.; Frey, W.; Kästner, J.; Buchmeiser, M. R., A sodium bis(perfluoropinacol) borate-based electrolyte for stable, high-performance room

temperature sodium-sulfur batteries based on sulfurized poly(acrylonitrile). *Electrochem. Commun.* **2021**, *132*, 107137.

1. Murugan, S.; Niesen, S.; Kappler, J.; Küster, K.; Starke, U.; Buchmeiser, M. R., Ultra-Stable Cycling of High Capacity Room Temperature Sodium-Sulfur Batteries Based on Sulfurated Poly(acrylonitrile). *Batter. Supercaps* **2021**, *4*, 1636-1646.